ULTRASENSITIVE DETECTION OF PANCREATIC CANCER BIOMARKERS BY NANOSCALE ENGINEERED FLUORESCENCE ENHANCING MATERIALS

This thesis is submitted in accordance with the requirements of Imperial College London for the degree of Doctor of Philosophy

By Zaynab Abdul Raheem Jawad MA (Cantab), MBBS, MRCS, MSc

Imperial College London, Department of Materials

Submitted 22nd January 2018; viva date 4th May 2018

ABSTRACT

Pancreatic cancer is one of the deadliest cancers in the world. The main reason is that patients do not show symptoms until the advanced stages of the disease, when it has spread to other organs. In the late stages, there is no cure for pancreatic cancer and the only feasible treatments are chemotherapy and radiotherapy, which only prolong survival by a few months. In fact, only 15% of patients present when the disease is still resectable with surgery, which is the only cure. The main reason for these poor outcomes is that there is no diagnostic test to detect the disease in the early asymptomatic stage. Nanotechnology is an emerging field that is providing solutions to some of the dilemmas in cancer. For diagnostics, nanoparticles are being used to increase the sensitivity of detecting circulating cancer biomarkers in blood using a phenomenon known as metal enhanced fluorescence. By increasing the sensitivity of detecting these biomarkers, it has been shown that lower tumour burden can be identified. Furthermore, novel biomarkers such as microRNAs are proving to be promising candidates as biomarkers for early pancreatic cancer. In this project, three different nanomaterials for metal enhanced fluorescence-based detection of biomarkers were developed and evaluated using pancreatic cancer biomarkers. The nanomaterials have been optimised for use in biosensing. The lowest limit of detection achieved using tunable gold nanotriangular arrays was 7.7×10^{-7} UmL^{-1} and 10^{-15} M for CA 19–9 and GPC-1 respectively. A concentration dependent metal enhanced fluorescent assay was achieved for microRNA-21, also for detecting pancreatic cancer. Both assays were highly specific for their respective analyte of interest. These nanomaterials show great potential as multiplexing platforms to simultaneously detect multiple biomarkers for pancreatic cancer. In future, this strategy may improve the detection of the disease in the early stages to improve patient outcomes.

Declaration of originality

I declare that this work is my own and that any references to other work are appropriately referenced.

This thesis was revised on 25th June 2020 to remove material that had been included without attribution.

Copyright declaration

The copyright of this thesis rests with the author and is made available under a Creative Commons Attribution Non-Commercial No Derivatives licence. Researchers are free to copy, distribute or transmit the thesis on the condition that they attribute it, that they do not use it for commercial purposes and that they do not alter, transform or build upon it. For any reuse or redistribution, researchers must make clear to others the licence terms of this work.

ACKNOWLEDGEMENTS

Firstly, I would like to express my sincere gratitude to my supervisor, Dr. Fang Xie, for her continuous support during my PhD study and for her patience and motivation. Her guidance and understanding helped me throughout and encouraged me to reach the end. I am extremely grateful to Professor Long Jiao, my co-supervisor, who provided me with the initial opportunity to get involved with this project which has given me the necessary research training within a highly accredited academic department. His ongoing support, both with this academic work and his mentorship of my clinical work is greatly appreciated.

I am grateful to my parents, brother, Adam, sister, Susan and husband Amer, who have provided me both moral and emotional support along this journey. I am also grateful to my other family members and friends who have supported me along the way.

With a special mention to Andrei Mihai, Peter Petrov, and the other members of the Thin Film Laboratory. It was really great to have the opportunity to carry out a major part of my research in your facilities. I will never forget your kindness and generosity. A special mention also to Ioannis Theodorou and Jing Pang, members of the research group with whom I worked closely and without whom I could not have accomplished this work.

I am also grateful to the following university staff: Cati Ware and Mahmoud Ardakani from the Harvey Flower Microstructural Characterisation Suite and Stephen Rothery and David Gaboriau from the Facility for Imaging by Light Microscopy Laboratory for their dedicated teaching and assistance.

My research was partially supported by the Armourers and Brasiers' fund that provided funding to attend conferences during the 3 years and to whom I am very thankful. I would also like to thank the Alliance Family Foundation who provided financial input and without whom this research would not have been possible.

And finally, last but by no means least, a big thank you to Dr. Fang Xie's research group both past and present… it was great sharing the laboratory with all of you during the last three years! I wish you all the best of luck in your current and future ventures.

TABLE OF CONTENTS

COMMON ABBREVATION 13

GLOSSARY OF TERMS 19

LIST OF TABLES 21

LIST OF FIGURES 23

CHAPTER 1: INTRODUCTION 28

CHAPTER 2: PANCREATIC CANCER 34

2.1 Classification 34

2.2 Epidemiology 34

2.2.1 Age and sex 36

2.2.2 Environmental risk factors 36

2.2.3 Risk of pancreatic cancer after chronic pancreatitis 37

2.2.4 Inherited pancreatic cancer 37

2.3 Genetic pathogenesis of pancreatic cancer 38

2.4 Precursor lesions of pancreatic cancer 40

2.5 Staging of pancreatic cancer 42

2.6 Clinical presentation 46

2.7 Imaging for pancreatic cancer 47

2.8 Screening for pancreatic cancer 48

2.9 Biomarkers for pancreatic cancer 50

2.9.1 CA 19-9 50

2.9.2 MicroRNAs 51

2.10 MicroRNAs in pancreatic cancer 54

2.10.1 Circulating microRNAs in pancreatic cancer 54

2.10.2 Early stage circulating microRNAs in pancreatic cancer 59

2.11 Biomarkers for pancreatic neuroendocrine tumours 61

2.12 Treatment of pancreatic cancer 61

2.13 Summary 63

CHAPTER 3: NANOTECHNOLOGY 65

3.1 Plasmonics and Metal Enhanced Fluorescence 65

3.1.1 Basic principles of fluorescence 67

3.1.2 Beer's law 69

3.1.3 Dynamics of fluorescence 71

3.1.4 Localised surface plasmon resonance 72

3.1.5 Surface plasmon polaritons 74

3.1.6 Generation of Metal Enhanced Fluorescence 74

3.1.7 The 'biological window' and other biological considerations 77

3.1.8 Which is the best metal to use? 79

3.1.9 Mie theory and modelling 79

3.1.10 Effects of changes in nanostructure 80

3.1.11 Distance dependence of metal enhanced fluorescence 82

3.2 Nanoscale fabrication 84

3.2.1 Nanoscale lithography 84

3.2.1.1 Formation of the monolayer: the 'fishing' technique 87

3.2.1.2 Control of size: Reactive ion etching 88

3.2.1.3 Metal deposition: Mantice e-beam evaporation 89

3.2.1.4 Polystyrene removal 89

3.3 Nanotechnology based biosensors for pancreatic cancer 90

3.3.1 Carbon nanotubes 90

3.3.2 Other electrochemical sensors 91

3.3.3 Quantum dots 91

3.3.4 LSPR-based sensors for microRNA 92

3.3.5 Metal enhanced fluorescence-based biosensors 92

3.4 Properties of a biosensor for pancreatic cancer 92

3.5 Immunoassays 93

3.5.1 Immunoassay structure 93

3.5.2 Antigens 94

3.5.3 Antibodies 94

3.5.4 Antigen-antibody interactions 95

3.5.5 Blocking and non-specific binding 96

3.5.6 Immunoassay support 97

3.5.7 Fluorescent linked immunosorbent assay (FLISA) 97

3.6 Bioconjugation techniques 99

3.6.1 PEGylation and chemical coupling 99

3.6.2 Conjugation to glass 101

3.6.3 Selection of gold nanotriangular arrays 101

3.7 Summary 102

CHAPTER 4: METHODS 103

4.1 Materials 103

4.2 Synthesis of gold nanotriangular arrays 104

4.3 Synthesis and characterization of gold capped polystyrene sphere arrays 105

4.4 Synthesis and characterization of gold nanostars 105

4.5 Preparation of MPTMS glass slides for synthesis of gold nanostar monolayers on glass 106

4.6 Formation of GNS self-assembled monolayers on MPTMS glass slides 107

4.7 Comparing cysteamine and APTES conjugation methods 108

4.8 Surface modification of gold nanotriangular arrays 108

4.9 CA 19-9 sandwich assay procedure 109

4.10 Tunable fluorescent immunoassay conjugation 109

4.11 Fluorescence measurement and analysis of CA 19-9 and GPC-1 assays 110

4.12 Drop dry calibration 110

4.13 Concentration dependent assay at higher concentrations 110

4.14 Specificity of CA 19-9 fluorescent immunoassay using albumin and GPC-1 111

4.15 Immobilization of fluorophore–protein conjugation monolayers onto gold nanostar substrates 111

4.16 Fluorescence measurements and analysis 112

4.17 MicroRNA assay procedure 113

4.18 Fluorescence measurement and analysis of microRNA assay 113

4.19 Analytical statistics 113

4.19.1 Validation 113

4.19.2 Limit of detection 114

4.19.3 Limit of quantification 114

4.19.4 Dynamic range 115

4.19.5 Specificity and sensitivity 115

4.20 Descriptive statistics 115

4.20.1 Mean 115

4.20.2 The null hypothesis, type I and type II errors 115

4.20.3 Power calculation 116

4.20.4 Standard deviation 116

4.20.5 Accuracy 116

CHAPTER 5: INSTRUMENTATION 117

5.1 Scanning electron microscope 117

5.2 UV-Visible Spectroscopy 121

5.3 Fluorescence spectroscopy 122

CHAPTER 6: SYNTHESIS OF NANOSTRUCTURES FOR USE AS BIOSENSORS 125

6.1 Gold nanotriangular arrays 125

6.1.1 Synthesis of gold nanotriangular arrays 125

6.1.2 SEM characterisation of gold nanotriangular arrays 127

6.2 Gold capped polystyrene sphere (GCPS) arrays 135

6.2.1 Synthesis of GCPS arrays 138

6.2.2 SEM characterisation of GCPS arrays 138

6.3 Gold nanostars (GNS) 140

6.3.1 Synthesis of gold nanostars in solution 140

6.3.2 TEM characterisation of GNS in solution 141

6.3.3 Synthesis of self-assembled monolayers of GNS on glass substrates 144

6.3.4 SEM characterisation of gold nanostars on glass substrates 144

6.4 Summary 146

CHAPTER 7: OPTICAL PROPERTIES AND METAL ENHANCED FLUORESCENCE 147

7.1 Optical properties of gold nanotriangular arrays 147

7.2 Fluorescence enhancement of nanotriangular arrays 155

7.2.1 Calculation of fluorescence enhancement factor 155

7.2.2 Experimental measurement of fluorescence enhancement 157

7.3 Optical properties of gold capped polystyrene sphere arrays 159

7.4 Fluorescent enhancement of gold capped polystyrene sphere arrays 162

7.5 Optical properties of gold nanostars 165

7.6 Fluorescent enhancement of GNS 168

7.7 Lifetime measurements of fluorophores conjugated with GNS 169

7.8 Summary 173

CHAPTER 8: PROTEIN ASSAYS 174

8.1 Gold nanotriangular arrays 176

8.1.1 Drop-dry calibration of fluorophore conjugated antibody 176

8.1.2 Conjugation of immunoassay to nanotriangular array 177

8.1.3 Traditional immunoassay methods 181

8.1.4 Development of conjugation chemistry 181

8.1.5 Conjugation of sandwich fluorescent immunoassay 182

8.1.5.1 Sandwich detection immunoassay 185

8.1.5.2 Concentration dependent assay 187

8.1.5.3 Lowering the detection limit 190

8.1.5.4 Excited state lifetime analysis 190

8.1.5.5 Specificity 191

8.1.5.6 Clinical detection of CA 19-9 protein 193

8.1.5.7 GPC-1 assay 194

8.2 Gold nanostars 196

8.2.1 Drop dry calibration 196

8.2.2 Enhancement of fluorescent immunoassay using gold nanostars 196

8.3 Summary 199

CHAPTER 9: MICRORNA ASSAYS 202

9.1 Gold capped polystyrene sphere (GCPS) array 203

9.1.1 Drop dry calibration 203

9.1.2 Calibration curve using microRNA assay for miR-21 204

9.1.3 Specificity of miR-10b on miR-21 assay 210

9.2 Summary 210

CHAPTER 10: CONCLUSIONS AND FUTURE WORK 211

COMMON ABBREVIATIONS

5-HIAA 5-Hydroxyindoleacetic acid

APTES (3-Aminopropyl)triethoxysilane

AUC area under the curve

BRCA-1 breast cancer-1

BSA bovine serum albumin

bBSA biotinylated bovine serum albumin

CA 19-9 carbohydrate antigen 19-9

CAPS International Cancer of the Pancreas Screening Consortium

CDKN2A cyclin-dependent kinase inhibitor 2A

CEA carcinoembryonic antigen

CgA chromogranin A

CNT carbon nanotube

CPS counts per second

CT computerised (axial) tomography

CTAB Cetyl trimethylammonium bromide

DDA discrete dipole approximation

DMF Dimethylformamide

DNA deoxyribonucleic acid

DR diffuse reflectance

EDC N-(3-Dimethylaminopropyl)-N'-ethylcarbodiimide

EF enhancement factor

ELISA enzyme-linked immunosorbent assay

EPR enhanced permeability and retention

EUS endoscopic ultrasound

FAMMM familial atypical multiple mole melanoma

FAP familial adenomatous polyposis

FDR first degree relative

FDTD finite-difference time-domain method

FEG field emission gun

FLISA fluorescence linked immunosorbent assay

FNA fine-needle aspiration

FPC familial pancreatic cancer

GCPS gold capped polystyrene sphere (arrays)

GNP gold nanoparticles

GNS gold nanostars

GPC-1 glypican-1

GPTS (3-Glycidyloxypropyl)trimethoxysilane

HIV human immunodeficiency virus

HMT Hexamethylenetetramine

HNPCC Hereditary nonpolyposis colorectal cancer

IFN interferon

Ig immunoglobulin

IL- interleukin

IPMN Intraductal papillary mucinous neoplasm

K_{nr} non-radiative decay

LOD limit of detection

LSPR localised surface plasmon resonance

MCN mucinous cystic neoplasm

MEF metal enhanced fluorescence

MIC-1 macrophage inhibitory cytokine-1

MIFE metal induced fluorescence enhancement

MMP matrix metalloproteinase

MPTMS (3-Mercaptopropyl)trimethoxysilane

mR- messenger RNA

MRI Magnetic resonance imaging

miR- micro RNA

MUC mucin

MWNT multi-walled nanotube

NHS N-hydroxysuccinimide

NIR-I near infra-red region I

NIR-II near infra-red region II

ns nanoseconds

NSB non-specific binding

NSL nanoscale lithography

OPT other pancreatic tumours

PanIN pancreatic intraepithelial neoplasia

PBS phosphate buffer solution

PBST phosphate buffer solution tween

PC pancreatic cancer

PDAC pancreatic ductal adenocarcinoma

PEG polyethylene glycol

PET positron emission tomography

PJS Peutz–Jeghers syndrome

PNET pancreatic neuroendocrine tumour

PS polystyrene

PSA prostate specific antigen

QCM quartz crystal microbalance

Γ radiative decay

RDE radiative decay engineering

RIE reactive ion etching

RNA ribonucleic acid

RPM rotations per minute

RT-PCR Reverse transcription polymerase chain reaction

SA streptavidin

SAM self-assembled monolayers

SEF surface enhanced fluorescence

SEM scanning electron microscope

SERS surface-enhanced Raman spectroscopy

SLE Systemic lupus erythematosus

SPP surface plasmon polariton

SPR surface plasmon resonance

SWNT single walled nanotube

TCSPC Time-correlated single-photon counting

TEM transmission electron microscopy

TNF tumour necrosis factor

TR total reflectance

UV ultraviolet

VEGF vascular endothelial growth factor

WHO World Health Organisation

GLOSSARY OF TERMS

Definitions of common scientific terms used in the thesis are described below:

Adjuvant treatment: Treatment given after surgery to remove a cancer, such as chemotherapy.

Anorexia: Loss of appetite

5-year survival rate: Percentage of patients still alive 5 years after diagnosis of the disease.

Beer's law: This law states that the concentration of a solution is directly proportional to the absorbance of the solution.

Biomarker: A biological molecule, found in blood or other bodily fluids, that is objectively measured and evaluated as an indicator of normal biological or pathological processes, or a response to treatment.

Carbon nanotubes: Nanostructures composed of graphene sheet cylinders made with single or multiple walls.

Chemoradiotherapy: A combination of chemotherapy and radiotherapy.

Chronic pancreatitis: A disease characterised by long term inflammation of the pancreas, usually causing long term pain.

Dysplasia: Cells of an abnormal type, usually preceding the development of cancer.

Electronic ground state: Lowest energy state for an electron in an atom.

Emission wavelength: The peak wavelength of light that is emitted by a fluorophore.

Enhancement factor: The increase in intensity of light emitted by a fluorophore as a result of metal enhanced fluorescence.

Excitation wavelength: The wavelength of light required to maximally excite a fluorophore.

Extinction co-efficient: The probability of absorption of a photon at a given wavelength of a substance.

Fluorescence: The emission of light by a substance that has absorbed light.

Glycosylation: The process of adding a glucose molecule to a protein.

Jaundice: An increase in the blood levels of bilirubin characterised by yellow discoloration of the skin and eyes.

Lithography: The use of a template to create a structure.

Localised surface plasmons: Oscillating electrons that exist around metal nanoparticles and produce an electromagnetic field.

Metastasis: Spread of cancer to organs distant from the primary site of origin.

Microarray: A platform used to detect multiple proteins on the same chip.

Multiplexing: Combining multiple signals on a single platform.

Nanofilm: Film with a thickness between 1 and 100 nanometres.

Nanoparticle: Particle with 2 or more dimensions measuring between 1 and 100 nanometres.

Neoadjuvant treatment: Treatment given prior to removal of a cancer.

Obstructive jaundice: A mechanism of jaundice caused by blockage of the bile ducts draining the liver.

Papillary: Finger-like projections.

Phosphorescence: The emission of light by a substance after is has absorbed light, but over a longer period of time than fluorescence.

Plasmonics: The field of science relating to the study of plasmons.

PS400Ox5Au100: Refers to recipe used to synthesise gold nanotriangles. PS400 indicates using 400 nm PS spheres for the template; Ox5 indicates 5 seconds etching time; Au100 indicates a thickness of 100 nm gold deposition.

Quantum yield: The proportion of excited electrons that decay radiatively to the ground state compared to those emitted by the non-radiative route.

Recurrence: The return of a disease after previous treatment.

Resectable: Describes a tumour that can be completely removed with surgery.

Screening: The process of identifying asymptomatic healthy individuals who are at higher risk of having a certain disease.

Signal-to-noise ratio: The ratio of the strength of a signal compared to the unwanted background interference.

Superior mesenteric artery: One of the main arteries supplying the small and large bowel.

Surface plasmons: Oscillating electrons that exist at the interface between a nanofilm and insulating material.

Tunability: The ability to alter a structure to change an important property of the structure.

UV-Vis: Spectrum of light spanning the range from ultraviolet light.

UV-Vis-NIR: Spectrum of light spanning the range from ultraviolet light to near infra-red.

LIST OF TABLES

CHAPTER 2: PANCREATIC CANCER

Table 1: Types of pancreatic cancer.

Table 2: IPMN subtype classification and morphological and immunohistochemical characteristics.

Table 3: TNM classification for pancreatic cancer.

Table 4: American Cancer Society staging of pancreatic cancer.

CHAPTER 3: NANOTECHNOLOGY

Table 1: Characteristics of common fluorophores.

Table 2: Advantages and disadvantages of different immunoassay structures.

CHAPTER 5: INSTRUMENTATION

Table 1: Three main types of electron gun available with their advantages and disadvantages.

CHAPTER 6: SYNTHESIS OF NANOSTRUCTURES FOR USE AS BIOSENSORS

Table 1: Structural parameters of gold nanotriangular arrays. a is the nanoparticle length and s is the inter-particle distance (Figure 5d). Mean value is give and standard deviation of 12 measurements.

Table 2: Morphological characteristics of the GNS. Spike aspect ratio =ratio of width to height.

CHAPTER 7: OPTICAL PROPERTIES AND METAL ENHANCED FLUORESCENCE

Table 1: Extinction peak positions of gold nanotriangular arrays produced with PS nanospheres of different increasing sizes and etching time. Increasing the duration of RIE increases the extinction and causes a monotonic red shift in the plasmon resonance. Increasing the size of the PS nanospheres also causes a red shift in the absorption peak wavelength.

Table 2: Average fluorescence enhancement and quenching factors of streptavidin conjugated Alexa Fluor 532, Alexa Fluor 647, and Alexa Fluor 790 for gold nanotriangular arrays synthesised by NSL.

Table 3: Measured peak absorption wavelengths and enhancement factors of GCPS arrays.

Table 4: Enhancement factors of gold nanostars using AF750 and AF790 fluorescent dyes.

CHAPTER 8: PROTEIN ASSAYS

Table 1: Structural parameters of nanotriangular arrays synthesised with 400 nm diameter PS nanospheres with increasing etching times. Absorption peak wavelength and corresponding enhancement factors are also given.

CHAPTER 9: MICRORNA ASSAYS

Table 1: Oligonucleotide probe sequences used in the microRNA assays.

LIST OF FIGURES

CHAPTER 2: PANCREATIC CANCER

Figure 1: The genetic pathogenesis of pancreatic cancer.

Figure 2: Schematic diagram to show the stages in protein synthesis from DNA. MicroRNAs act at the post-transcription level.

CHAPTER 3: NANOTECHNOLOGY

Figure 1: Stained glass rose window of Notre Dame de Paris. Gold nanoparticles embedded in the glass interact with light and are responsible for the vivid colours seen.

Figure 2: Potential energy diagram to show energy levels of fluorophore. The relationship between absorption and emission can be demonstrated using a potential energy diagram.

Figure 3: Jabonski diagram showing fluorescent absorption and emission processes. Intersystem crossing is a non-radiative process involving a transition between 2 electronic states with different states spin multiplicity. Radiative decay from an excited triplet state back to singlet state is known as phosphorescence, which has a longer half-life than fluorescence.

Figure 4: Intensity-wavelength curves depicting Stokes shift.

Figure 5: Diagram demonstrating vibrating localised surface plasmons and the induced associated electromagnetic wave.

Figure 6: Diagram showing the propagation of surface plasmon polaritons excited at a metal-dielectric interface.

Figure 7: Jabonski diagram showing effect of metal nanoparticle on fluorophore. K_m and k_r refer to non-radiative and radiative decay in the presence of nanomaterial respectively.

Figure 8: The biological or water window. Figure 8 (a) shows the organs of a newly sacrificed mouse under white light. SI=small intestine GB=gallbladder Bl=bladder (b) shows the same mouse under blue light excitation and green light emission filter set (c) under green light excitation and red light emission filter set (d) NIR range of excitation and emission. Excitation and emission within the NIR range shows no background autofluorescence.

Figure 9: Colloid solutions containing gold and silver nanoparticles of varying sizes. The red solution contains the smallest nanospheres at 12 nm in size. These absorb blue light of shorter wavelengths and the reflected light is red giving the observed colour.

Figure 10: Extinction efficiency of silver nanoparticles with the same volume but of different shapes. The simulated electrical field contour map for corresponding (a) sphere (b) cube, and (c) pyramid.

Figure 11: (Top) Distribution of the E-field (calculated by FDTD simulations) around and between silver nanoparticles that approximate the particle growth on glass slides. (Bottom) Dependence of E-field intensity maximum between silver particles upon the distance between particles outer

surfaces (blue balls). Solid curve is a smooth representation of the change in near field intensity upon the distance between two particles surfaces. (inset) Particle geometry parameters used in FDTD calculations.

Figure 12: SEM image showing (a) areas of imperfect PS nanosphere monolayer deposition and (b) corresponding nanoparticle arrangements.

Figure 13: Methods of antibody mediated detection.

Figure 14: Polyethylene glycol functionalised with end hydroxyl groups.

Figure 15: Reaction of amine group with NHS ester to form acylated product.

CHAPTER 5: INSTRUMENTATION

Figure 1: Scanning electron microscope.

Figure 2: Fluorolog fluorescence spectroscope.

CHAPTER 6: SYNTHESIS OF NANOSTRUCTURES FOR USE AS BIOSENSORS

Figure 1: Schematic diagram to show fabrication process of gold nanotriangular arrays. PS nanospheres are used as a template for gold deposition using e-beam evaporation. A, B and C indicate points of intervention to alter size parameters of gold nanotriangles. A: altering PS nanosphere size, B: etching of PS nanospheres C: altering gold layer depth during deposition.

Figure 2: SEM images (scale bars, 200 nm) of nanotriangular arrays synthesised using PS nanospheres of 280 nm in diameter and (a) with no etching (b) with 5 sec etching time (c) with 10 sec etching time (d) with 15 sec etching time.

Figure 3: SEM images (scale bars, 500 nm) of nanotriangular arrays synthesised using PS nanospheres of 400 nm in diameter and (a) with no etching (b) with 5 sec etching time (c) with 10 sec etching time (d) with 15 sec etching time.

Figure 4: SEM images of nanotriangular arrays synthesised using PS nanospheres of 500 nm in diameter and (a) with no etching (b) with 5 sec etching time (c) with 10 sec etching time (d) with 15 sec etching time.

Figure 5: (a)-(c) Scatter plots to show the relationship between the etching time and nanoparticle l length, a. Gold nanotriangles were synthesised using PS nanospheres of increasing diameter (a) 280 nm (b) 400 nm (c) 500 nm. (d) Schematic diagram to show the distances measured. a= nanoparticle length s= interparticle distance.

Figure 6: SEM characterisation of polystyrene nanosphere templates and gold nanohole arrays synthesised from 500 nm polystyrene nanospheres etched for 20 secs (scale bars, 500 nm) (a) polystyrene template shows weak crosslinking and reduction in size of polystyrene spheres (b) corresponding nanohole array.

Figure 7: SEM characterisation of polystyrene nanosphere templates and gold nanohole arrays synthesised from 500 nm polystyrene nanospheres etched for 25 secs (a) polystyrene template shows weak crosslinking and reduction in size of polystyrene spheres (b) corresponding nanohole array.

Figure 8: SEM characterisation of (a) polystyrene nanosphere templates and corresponding (b) gold nanotriangular arrays synthesised from 500 nm polystyrene nanospheres demonstrating slip dislocations, vacancies and areas of bilayer and monolayer.

Figure 9: Schematic diagram to show fabrication process of GCPS. PS nanospheres are used as a template for gold deposition using e-beam evaporation. A, B and C indicate points of intervention to alter size parameters of GCPS. A: altering PS nanosphere size, B: etching of PS nanospheres C: altering gold layer depth during deposition.

Figure 10: SEM images of GCPS arrays synthesised using PS nanospheres of 280 nm in diameter and (a) with 5 secs etching time (b) with 10 secs etching time (c) with 15 seconds etching time (d) and (e) side view images.

Figure 11: TEM images of (a) S-GNS and (b) L-GNS.

Figure 12: SEM images of GNS substrates fabricated through the self-assembly of (a) S-GNS and (b) L-GNS on MPTMS-coated glass slides.

CHAPTER 7: OPTICAL PROPERTIES AND METAL ENHANCED FLUORESCENCE

Figure 1: Normalised extinction spectra of Au nanotriangles. (a) 280nm and (b) 400nm (c)500nm polystyrene spheres on glass treated with RIE of duration 0 seconds to 15 seconds were used as a mask template to prepare the nanotriangles on gold. Background absorbance due to glass was measured and subtracted.

Figure 2: Extinction spectra of Ox25 and Ox30. These show no plasmon resonance peak and this size is therefore the limit of RIE for the use of metal enhanced fluorescence.

Figure 3: UV-vis of Ox10 to 15 showing no relationship between the size and absorption at this level of optimisation. Absorption spectra were obtained using a Cary 5000i UV-Vis-NIR spectrophotometer equipped with solid sample holder. Background absorbance due to glass was measured and subtracted. Plasmon absorption spectra exhibited only small inter-substrate variation.

Figure 4: Normalised extinction spectra of GCPS arrays synthesised from (a) 280nm and (b) 400nm polystyrene spheres on glass treated with RIE of duration 0 seconds to 20 seconds. Background absorbance due to glass was measured and subtracted.

Figure 5: Normalised extinction spectra of GCPS arrays synthesised from 280nm diameter PS nanospheres and increasing etching times. The 794 nm vertical line marks the emission wavelength of Dylight 800.

Figure 6: Fluorescence intensity measurements of gold capped polystyrene arrays synthesised with PS nanospheres of 280 nm diameter and increasing etching times.

Figure 7: UV-Vis spectroscopy of GNS in solution. Blue and red vertical lines show the emission wavelength of AF750 (blue) and AF790 (red).

Figure 8: UV-Vis spectrum of S-GNS (green line) and L-GNS (orange) monolayers on glass. Blue and red vertical lines show the emission wavelength of AF750 (blue) and AF790 (red).

Figure 9: Fluorescence intensity measurements of monolayers of streptavidin-conjugated (a) AF750 and (b) AF790 formed on biotinylated bovine serum albumin (bBSA)-coated glass slides and S- or L-GNS substrates.

Figure 10: Fluorescence lifetime spectra of streptavidin-conjugated (a) AF750 and (b) AF790 monolayers, immobilized on S- and L-GNS substrates, and on glass surfaces as a control.

CHAPTER 8: PROTEIN ASSAYS

Figure 1: Scatter plots to show the results of the drop dry calibration tests using nanotriangular arrays synthesised from 400 nm diameter PS nanospheres etched for 5 secs. (a) Scatter plot to compare the detection limits on glass and nanotriangular array (b) calibration plot on glass (c) calibration plot on nanotriangular array.

Figure 2: PEG-amine conjugation chemistry of immunoassay with nanostructured substrate. On the left, the blue ellipses represent the capture antibody, with amine groups binding to carboxylate groups in the PEG.

Figure 3: Scatter plot showing the difference in conjugation comparing cysteamine only (blue), APTES only (green) and APTES + cystemine (red). Combination of cysteamine and APTES dramatically improved the level on conjugation.

Figure 4: Schematic diagram to show indirect sandwich immunoassay for CA 19-9 conjugated to the nanotriangular substrate.

Figure 5: (a) shows the LSPR wavelengths of nanotriangular arrays produced with increasing etching times and excitation/emission wavelength of Dylight 800 (b) shows the relative enhancement produced by these nanotriangular arrays when compared to glass.

Figure 6: (a) Calibration curve for CA 19-9 immunoassay on nanotriangular array with line of best fit (b) Calibration curve of CA 19-9 immunoassay on blank glass controls.

Figure 7. The relationship between fluorescence intensity and CA 19-9 concentration using glass compared to gold nanotriangular arrays. Integrated fluorescent intensity was calculated and points represent the mean of four measurements.

Figure 8: Fluorescence decay curves of Dylight800 on nanostructured array (red) and glass slide (black).

Figure 9: Specificity test of CA 19-9 assay using albumin and GPC-1 as antigens.

Figure 10: Preliminary clinical validation in three donkey serum samples spiked with CA 19-9.

Figure 11: Calibration curve for GPC-1 fluorescent immunoassay on gold nanotriangular substrates. Glass control arrays have also been plotted for comparison.

Figure 12: Scatter plots to show the results of the drop dry calibration tests using gold nanostar substrates synthesised from S-GNSs (a) calibration plot on glass (b) calibration plot on nanotriangular array.

Figure 13: (a) Calibration curve for CA 19-9 fluorescent immunoassay on gold nanostar substrates (b) in comparison with glass control assay.

Figure 14: SEM images of GNS self-assembled monolayers on glass of (a) S-NS (b) L-NS showing greater aggregation of L-NS compared to S-NS.

CHAPTER 9: MICRORNA ASSAYS

Figure 1: Schematic diagram to show microRNA probe assay set-up for miR-21.

Figure 2: Calibration curve of miRNA miR-21 assay on GCPS assay shows linear relationship between the concentration of the miR-21 and the fluorescence intensity of the assay (a) with blank reading (b) without blank reading.

Figure 3: Specificity test for miR-21 assay using miR-10b as the substitute analyte.

CHAPTER 1: INTRODUCTION

Pancreatic cancer is the 10th most common cancer in the United Kingdom. The 5-year survival rates are the lowest of the 21 most common cancers in England. The percentage of men and women that are diagnosed with pancreatic cancer that are still alive 5 years later is 3.5% and 3.1% respectively[1]. The main reason for these poor outcomes is that the disease usually presents in the late stages. Usually by the time a patient has symptoms, the disease has already spread from the pancreas to other organs such as the liver. Patients that present with pancreatic cancer at such a late stage cannot undergo curative treatment. Surgery to remove all of the cancer is the only curative treatment that is currently available. However, only 15% of patients diagnosed with pancreatic cancer are suitable to undergo surgery at the time of diagnosis[2]. Pancreatic cancer is relatively resistant to other treatments such as chemotherapy and radiotherapy and these provide only minimal benefit; at most these prolong survival by a few months. The key to improving the survival of pancreatic cancer is to detect the disease in the early stages, before a patient has symptoms. This requires a highly sensitive and specific screening test, which is currently not available. A screening blood test to detect a biomarker or a panel of biomarkers expressed in the early stages would make an ideal screening test.

Cancer biomarkers are defined as biochemical substances elaborated by cancer cells due to either the cause or effect of the malignant process. The ideal biomarker should only be detected in the presence of the cancer that it is known to detect i.e. it has a high specificity, and may be found in serum, plasma, whole blood, cyst fluid, urine, saliva, stool or tissue. The biomarker for a particular cancer may be a normal product that is expressed at a higher rate in cancer cells or the products of genes that are switched on only in cancer cells. Carbohydrate antigen, CA 19-9, is the only validated tumour marker in clinical use for the evaluation of pancreatic adenocarcinoma[3]. Elevated serum levels of CA 19-9 are reported as being 79-81% sensitive and 82-90% specific in patients with pancreatic cancer with symptoms[4]. Up to 10% of the population are unable to produce CA 19-9 and the level may be

elevated in benign conditions such as gallstone disease. Therefore, it cannot be used as a standalone biomarker for screening of pancreatic cancer in the general healthy population. In clinical practice, it is used for monitoring for recurrence of the disease in patients who have had treatment and should not be used for diagnosis.

In addition to CA 19-9, other potential biomarkers are being discovered with levels that are elevated in pancreatic cancer. Exosomal GPC-1 has recently been reported as being 100% specific and 100% sensitive for the detection of pancreatic cancer[5], though this needs further validation in larger patient cohorts. MicroRNAs have an important role in controlling protein synthesis at the post-transcription level. Several microRNAs have been identified that may have future potential use as biomarkers for pancreatic cancer as the levels are elevated in patients with pancreatic cancer compared to healthy controls. These include microRNA-21, micro-RNA-10b and microRNA-196a[6][7][8]. One of the problems with detecting microRNA and other genetic markers is that the assays require an amplification step called polymerase chain reaction (PCR) which is time consuming and labour intensive.

Though currently there is no single biomarker that can be used for the diagnosis of pancreatic cancer, it has been shown that combining two or more biomarkers can increase the sensitivity and specificity of detecting the disease. Several microRNAs can be used together to increase the accuracy of detection[6] and it has also been shown that combining several microRNAs with CA 19-9 can also increase the accuracy of detection[9]. Ideally, this will require a biosensing platform that can measure several biomarkers at the same time. The ability to measure more than one biomarker simultaneously on the same biomarker detection device is known as multiplexing. This feature is offered by some nanotechnology biosensing platforms.

Nanotechnology refers to scientific applications at the nanoscale between 1 and 100 nanometres. To put this into context one nanometre is 1/100,000th of the thickness of a sheet of paper. The ability to explore science at such a small scale is showing promising applications in the fields of engineering,

chemistry and materials science. In medicine, an abundance of applications has been explored over the last three decades demonstrating a potential for great impact in the way certain diseases are managed. For example, for cancer therapy, the small dimensions of nanoparticles and their ability to enter tumour cells is beginning to revolutionise how we approach the disease by offering potentially more targeted treatments[10]. The advantage of more specific targeting of tumours is already showing its benefits in clinical trials that show greater efficacy and fewer side effects[11][12]. For cancer diagnostics, the plasmonic effect metal enhanced fluorescence (MEF), the focus of this project, is a phenomenon only displayed by metal particles of nanoscale proportions[13]. This has opened up a vast range of interesting and imaginative solutions to the problems in cancer diagnostics.

Currently the use of fluorescent molecules or fluorophores is the most common labelling technique in bio-sensing for the detection of disease biomarkers. Fluorophores emitting at wavelengths in the near infra-red range (700 - 900 nm) are used as there is less interference from the background auto-fluorescence emitted from biological samples. This range of wavelengths is known as the 'biological window'. However, the limiting factor in the use of fluorophores for biosensing is the concentration of biomarker in the tissue sample, as the signal intensity of fluorophores is generally very low, creating a high noise-to-signal ratio. These problems have been overcome by coupling of fluorophores to metal nanoparticles which amplify the fluorescent signal and thereby increase the signal-to-noise ratio[14]. This enhancement depends on the presence of an electromagnetic field that surrounds metal nanoparticles but does not exist around bulk metal structures. The electromagnetic field exists due to the presence of a cloud of electrons in a mobile fluid-like state on the surface of metal nanoparticles, which is called 'plasma' and the scientific field that studies the effects of plasma is known as 'Plasmonics'. When these electrons are disturbed, they create an electromagnetic field as they are pulled back to the equilibrium state by the electrostatic forces[14]. At certain resonating wavelengths, light can provide the energy to disturb these plasmons. When a fluorophore, that has excitation and emission wavelengths that match the resonant wavelength of the nanoparticles, is placed in close proximity to the metal nanoparticles, the intensity of light emitted by the fluorophore is increased.

This phenomenon is known as metal enhanced fluorescence (MEF). Using this technique, the sensitivity of fluorescent-based assays could be increased by increasing the signal-to-noise ratio.

Extensive research has been carried out to understand the phenomenon of MEF in detail. From this previous research, it has been established that the level of enhancement of fluorophore intensity is dependent on factors that include nanoparticle size, shape, inter-particle separation and the distance between the metal and fluorophore[15][16][17][18]. Furthermore, there are certain principles that must be in place for the enhancement to take place. For example, the optimal distance between the fluorophore and metal nanoparticle is around 10 nanometers[19]. If the distance is too small, then the fluorophore becomes quenched and the signal intensity is dampened. As the distance between the fluorophore and the metal nanoparticle is increased the intensity of fluorescence enhancement declines. Using these principles, it has been possible to engineer a range of nanostructures for MEF using a variety of materials. Using these nanomaterials, not only has significant fluorescence enhancement been demonstrated but the nanomaterials have been adapted for use with fluorescent immunoassays, including an assay for carcinoembryonic antigen (CEA)[20]. These metal enhanced fluorescent assays display greatly increased sensitivity above that of control assays using standard fluorescent immunoassays. However, while these assays displayed better detection limits than standard assays, the nanomaterials that were used lacked control of their synthesis, so that the nanomaterial structure varies from one assay to another. This may affect certain qualities that are important for a biosensor. For example, the results of the assay should be reproducible and precise. If the structure of the nanomaterial were not consistent, the repeated results of the assay would vary. Similarly, the method of synthesis of the nanomaterial should be labour efficient and require as few steps as possible. Ideally, the materials that are used for synthesis should be cheap and readily available.

The aim of this project is to develop and optimise nanostructures for MEF for the purpose of bio-sensing. These methods are novel, combining different nanostructures and methodologies. The novel

methods used in the project have been developed with cost efficiency and reproducibility in mind to make them suitable for clinical applications. In addition, the synthesis methods are highly controllable such that the nanomaterials that are developed have tuneable plasmonic properties to maximize the local electromagnetic field thus maximising the fluorescence enhancement. Another advantage of being able to control the synthesis of the nanomaterials is that the sensitivity can be controlled according to the assay that is used. If the assay required is for a less abundant biomarker, the sensitivity can be increased. On the contrary, if the normal lower limit of the biomarker of interest is high, the synthesis parameters of the nanomaterial can be altered to reduce the sensitivity. A further advantage of the nanomaterials that will be used is that they are capable of multiplexing. That is, more than one biomarker can be detected on the same biosensor. Therefore, these nanomaterials make promising candidates for detecting multiple biomarkers for pancreatic cancer and thereby potentially increasing, not only the sensitivity of detection but also the specificity of detection of pancreatic cancer in the early stages.

Once the plasmonic chip has been developed and the metal enhanced fluorescence has been optimised, the nanomaterial will be adapted for use with a fluorescent immunoassay. An assay to CA 19-9 will be used for proof of concept. Using this assay, the increase in enhancement provided by the nanomaterials will be analysed and any improvement in the sensitivity of detection of CA 19-9 will also be evaluated. Apart from sensitivity, another important characteristic of any analytical assay is specificity. The specificity of the metal enhanced fluorescent assay for CA 19-9 assay will also be demonstrated. To test the use of these nanomaterials for biosensing it will be important to use clinical samples. For this purpose, commercial samples will be tested for the initial analysis, followed by clinical samples, including plasma. Plasma is a complex matrix containing other proteins and molecules that could potentially interfere with the readout from the biosensor. Therefore, to test the usefulness of the assay for clinical use it is important to evaluate its ability to detect the biomarker of interest in biological samples. In addition to protein assays, the nanomaterials have also been used to detect microRNA, as certain microRNA has been found to be promising candidates as biomarkers for

pancreatic cancer. With the potential for multiplexing on these nanomaterials, it may be possible to combine protein and microRNA assays to these markers on the same biosensor platform to create a diagnostic test for pancreatic cancer.

Ultimately, the aim of this project is to develop nanomaterials for biosensing using metal enhanced fluorescence. The ability of the nanomaterials to increase the sensitivity of detection of protein biomarkers will also be demonstrated. Preliminary work demonstrating the use of these nanomaterials for detecting microRNA has also been carried out. This promising technology that is metal enhanced fluorescence has potential use as a cancer screening device for pancreatic cancer by detecting multiple biomarkers, on a multiplex platform. Increasing the sensitivity of detecting biomarkers for pancreatic cancer and increasing the number of biomarkers detected could increase the sensitivity and specificity of detecting the disease. Furthermore, the sensitivity of the metal enhanced fluorescence platform can be altered and adjusted according to the biomarker of interest. Potentially this could provide the overall huge benefits of earlier diagnosis, timely treatment and greatly improved patient survival for those suffering with the disease.

CHAPTER 2: PANCREATIC CANCER

Pancreatic cancer is one of the deadliest types of cancer[21]. The main reason for this is that by the time a patient has symptoms, the disease is usually so advanced that surgical resection, which is the only cure available, is unlikely to be possible. There has been an improvement in the treatment of patients with advanced disease leading to an improvement in 5-year survival rates, but it still remains that there is no way to detect the disease in the early stages. More research needs to be done to improve long term survival by improving diagnosis [22], [23], [24]. The first section of this literature review provides background information about pancreatic cancer and describes the reasons for choosing this cancer type for this project.

2.1 Classification

Pancreatic cancers are divided into endocrine and exocrine tumour subtypes (Table 1) depending on the type of cells that they originate from. Pancreatic ductal adenocarcinoma (PDAC) is the commonest type of pancreatic cancer and falls into the exocrine subtype. PDAC arises from epithelial cells in the pancreatic ducts and makes up 85% of all types of pancreatic cancer[2]. The other types of pancreatic exocrine tumour are very rare. Pancreatic endocrine tumours are collectively known as pancreatic neuroendocrine tumours (PNETs). PNETs make up less than 5% of all pancreatic tumours.

2.2 Epidemiology

Pancreatic cancer has an incidence of approximately 10 per 100,000 of the population per year in Europe and North America [25]. The 5-year survival rates are the lowest of the 21 most common cancers in England. The 5-year survival rates in England and Wales are 3.5% and 3.1% in men and women respectively.

PDAC is the most common type of pancreatic cancer. Several factors have been associated with a higher risk of developing pancreatic cancer.

Table 1: Types of pancreatic cancer

EXOCRINE PANCREATIC TUMOURS
• **Pancreatic ductal adenocarcinoma**
• **Acinar cell carcinoma**
• **Adenosquamous carcinoma**
• **Squamous cell carcinoma**
• **Signet ring cell carcinoma**
• **Undifferentiated carcinoma**
• **Undifferentiated carcinoma with giant cells**
PANCREATIC NEUROENDOCRINE TUMOURS (PNET)

2.2.1 Age and sex

Epidemiological studies show that the risk of developing pancreatic cancer increases with age. Less than 10% of cases occurs in those under the age of 55 years and the median age of onset is 71 years[21] with men having higher rates than women across all ethnic groups.

2.2.2 Environmental risk factors

Smoking, alcohol and obesity have all been identified as environmental factors that increase the risk of pancreatic cancer[26].

Smoking has the strongest evidence for being a risk factor for developing pancreatic cancer In a multinational case-control study evaluating 6,507 smokers and 12,890 controls, smokers were found to have twice the risk of developing pancreatic cancer compared to controls that had never smoked[27]. The risk increases with the number of cigarettes smoked and the duration of smoking. The higher risk was sustained after quitting in ex-smokers and declined to the level of non-smokers 20 years after quitting.

Alcohol has also been associated with a higher risk of developing pancreatic cancer[28]. While it is difficult to differentiate drinkers from smokers in epidemiological studies, two large studies have shown that there is an increased risk of developing pancreatic cancer in heavy drinkers[29][30].

Obesity has also been identified as a risk factor. In a meta-analysis of 8391 patients the relative risk of pancreatic cancer was 1.19 in obese patients compared to those of normal weight[31]. Apart from the consumption of red meat[32], no other dietary risk factors have been implicated in the development of pancreatic cancer[21].

New-onset diabetes is one way that patients may present with pancreatic cancer, particularly in patients who are not obese and in older patients with no family history of diabetes[33], [34]. However, during 6-year follow-up only 0.5% of patients with newly diagnosed diabetes developed pancreatic

cancer in one study[35]. Patients with long-standing diabetes have been shown to have double the risk of developing pancreatic cancer[36].

2.2.3 Risk of pancreatic cancer after chronic pancreatitis

Chronic pancreatitis is thought to be a rare cause of pancreatic cancer[37], [38]. One meta-analysis estimated the relative risk of pancreatic cancer to be 13.3 in those with chronic pancreatitis[39]. However, despite this high relative risk, as the incidence of chronic pancreatitis is relatively low (<5%), this is a less significant overall cause of pancreatic cancer[21].

2.2.4 Inherited pancreatic cancer

Between 5 and 10% of pancreatic cancers are thought to be inherited [40] but the underlying genetic mechanism for these has not been fully established. Susceptibility to pancreatic cancer may be inherited in three forms: (1) hereditary tumour predisposition syndromes, (2) syndromes associated with chronic pancreatitis and (3) familial pancreatic cancer (FPC)[41].

Hereditary tumour predisposition syndromes are genetic syndromes that predispose patients to certain types of cancer. Examples including Peutz-Jeghers syndrome (PJS) and Familial Atypical Multiple Mole Melanoma (FAMMM) account for 15-20% of cases of hereditary pancreatic cancer[42]. Peutz-Jeghers is an autosomal dominant condition caused by mutations in the STK11 tumour suppressor gene[43]. Affected individuals inherit a 132 times higher risk of developing pancreatic cancer. FAMMM is also autosomal dominantly inherited and caused by mutations in the tumour suppressor gene CDKN2A[44]. FAMMM leads to a skin condition that causes multiple atypical naevi (moles) and malignant melanomas (skin cancer). In addition some patients are also predisposed to developing pancreatic cancer and carry an estimated lifetime risk of 17%[45]. Mutations in breast cancer gene BRCA-1 have also been associated with a 3.5 to 10 fold increased risk of developing pancreatic cancer[46], [47]. Hereditary non-polyposis colorectal carcinoma (HNPCC) and familial adenomatous polyposis (FAP) syndromes are predominantly associated with colorectal cancer, but individuals are also at increased risk of pancreatic cancer at 8.6 fold[48] and 4.6-fold[49] respectively.

Patients with a hereditary risk of chronic pancreatitis have a 60-100-fold increased risk of pancreatic cancer. Hereditary chronic pancreatitis occurs because of mutations in the trypsinogen gene PRSS1[50].

Familial pancreatic cancer is defined as affecting families with two or more first-degree relatives with pancreatic cancer that is not caused by any other types of inherited syndrome[51]. The underlying genetic abnormalities have not yet been discovered but the inheritance appears to be autosomal dominant in up to 80% of cases[52], [53].

2.3 Genetic pathogenesis of pancreatic cancer

Understanding the steps involved when a normal cell changes into a cancerous cell is known as genetic pathogenesis. Studying the genetic pathogenesis of pancreatic cancer has provided evidence that there is an opportunity for early diagnosis of the disease. Until recently it was not understood why pancreatic cancer tends to present in the late stages, when the cancerous cells have spread to other organs. It was not clear whether the reason for the late presentation is due to the pancreatic cells gaining the ability to spread at an unusually early stage. However, genomic sequencing of pancreatic cancer metastases has provided evidence to suggest a time-lag of an average of 11.7 years from the first mutation in a normal cell to the primary cancer cell and a further 6.8 years to develop metastatic potential, i.e. the ability to spread to other organs (Figure 1)[54]. Currently, the majority of diagnosis occurs in the third and shortest phase, T_3, between the development of metastases and death. The study provides evidence that there is a window of opportunity of around a decade for diagnosing pancreatic cancer before it becomes metastatic.

Currently, a good opportunity for early intervention exists by identifying patients with lesions that have a risk of progressing into pancreatic cancer. This is possible in a small group of patients and the diagnosis is usually incidental. The lesions that are identified are called the precursor lesions of pancreatic cancer.

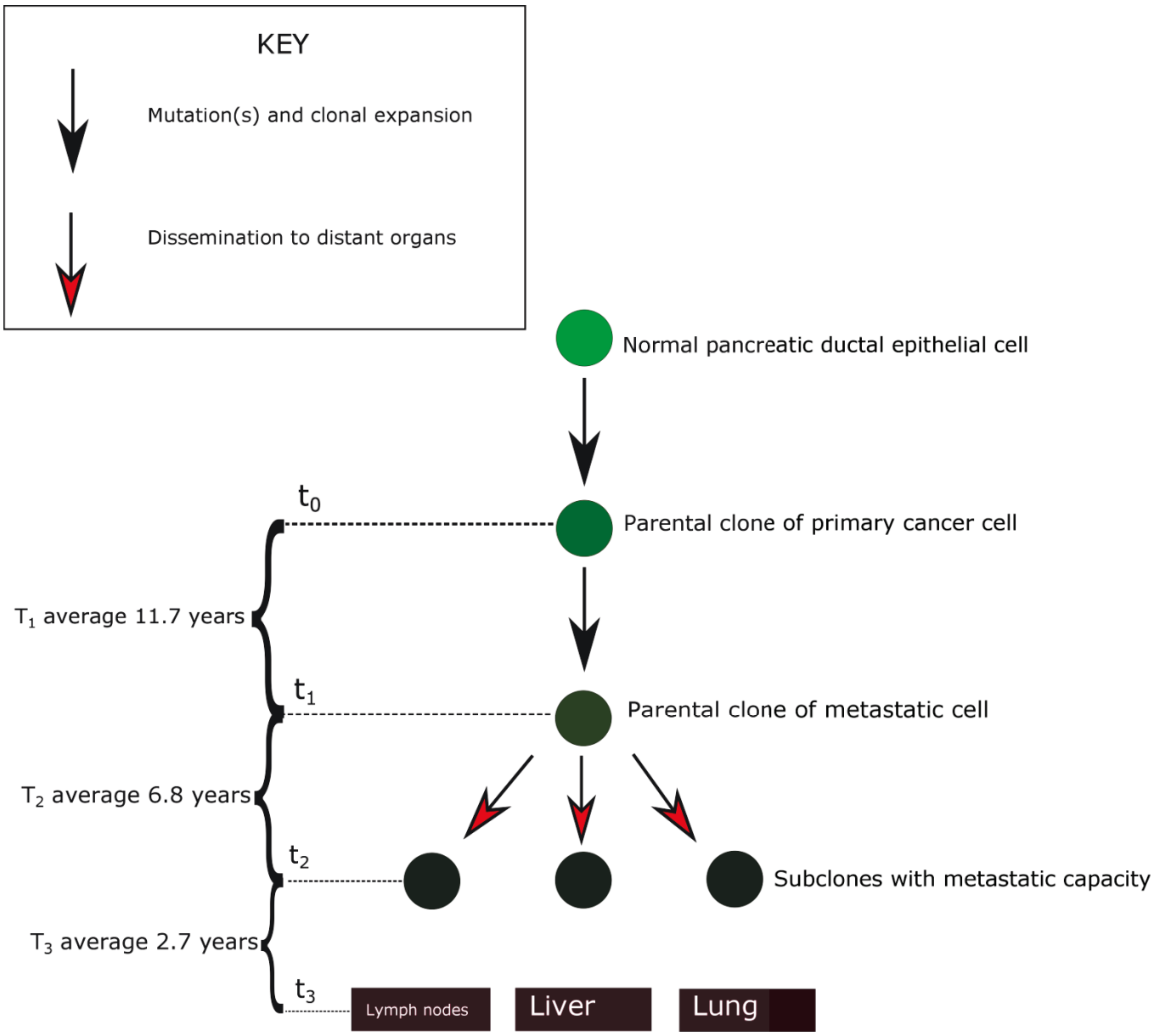


Figure 1: The genetic pathogenesis of pancreatic cancer (Adapted from ref [54]**)**

2.4 Precursor lesions of pancreatic cancer

Precursor lesions of pancreatic cancer provide an opportunity for early intervention and prevention of the disease[55], [56]. Early intervention for these lesions is an opportunity to prevent the development of pancreatic cancer. Three precursor lesions are known to develop into pancreatic cancer in time[57]. These lesions are pancreatic intraepithelial neoplasia (PanINs), intraductal papillary mucinous neoplasms (IPMN) and mucinous cystic neoplasms (MCNs).

PanIN lesions are pre-cancerous growths arising from epithelial cells within the smaller pancreatic ducts. They are either flat or papillary in shape and are classified into three grades[42]: PanIN-1(low grade) PanIN-2(intermediate grade) and PanIN-3(high grade) according to the degree of cellular and nuclear atypia or dysplasia. This morphological progression occurs in parallel with progressive genetic abnormalities[57]. A high proportion of PanIN-1 and PanIN-2 lesions have genetic alterations in the *KRAS* and *p16/CDKN2A* genes. In addition, PanIN-3 lesions and invasive adenocarcinomas have mutations in *TP53* and *SMAD4*[58]–[60].

IPMN are tumours arising from the larger pancreatic ducts, are usually papillary and produce the substance mucin. They are common tumours and are usually detected incidentally in patients undergoing investigations for other reasons. They occur in 3% of asymptomatic patients undergoing a computed tomography scan[61] and are more prevalent in the elderly population. One third of these lesions are found to have an associated focus of adenocarcinoma after resection.

IPMN are classified into subtypes based on morphological features and immunohistochemical reactivity for mucins (MUCs) as shown in Table 2.

Table 2: IPMN subtype classification and morphological and immunohistochemical characteristics.

Type	Mimicker	Atypia	MUC1	MUC2	MUC5AC
Gastric	Gastric foveolae	Mild/low grade	Not expressed	Not expressed	Expressed
Intestinal	Intestinal villous neoplasm	Moderate or severe/high grade	Not expressed	Expressed	Expressed
Pancreatobiliary	Cholangiopapillary neoplasm	Severe/high grade	Expressed	Not expressed	Expressed
Oncocytic	Oncocytic neoplasm	Severe/high grade	Expressed	Not expressed	Expressed

Although IPMN often consist of mixed morphological types, the predominate type is used for classification. The pattern of MUC expression may be used for biomarkers to differentiate the type of IPMN. For example, the absence of MUC1 and MUC2 in cystic fluid could be used to identify a low grade gastric IPMN that might not require surgery. On the other hand, the presence of MUC1 and MUC5AC would indicate a high grade pancreatobiliary or oncocytic IPMN that would require removal. These MUC biomarkers would be suitable for detection using a standard or fluorescent immunoassay.

MCNs are mucin-producing cystic lesions of the pancreas and are less common than IPMN[62]. They are more common in women and usually arise from the tail or body of the pancreas.

Being able to identify one of these precursor lesions is currently the only opportunity for early diagnosis and intervention for pancreatic cancer.

2.5 Staging of pancreatic cancer

Staging is a system used to d$_{ef}$ine how far a cancer has spread and is used to decide on the most suitable treatment. The stage also helps to determine the prognosis of the cancer.

The most commonly used staging system is called the TNM classification. T (tumour) describes the size of the primary cancer, N (lymph node) describes whether the draining lymph nodes contain cancer cells, and M (metastasis) is used to inform whether the cancer has spread to other organs. Prior to surgery, staging can be carried out radiologically using information from imaging such as CT or MRI scans. If a patient undergoes surgery, the staging is repeated to provide histological staging based on microscopic findings, which is more accurate.

The TNM classification for pancreatic cancer is shown in Table 3.

Table 3: TNM classification for pancreatic cancer.

Tumour	
Tx	Primary tumour cannot be assessed
T_0	No evidence of primary tumour
Tis	Carcinoma in situ
T1	Tumour limited to the pancreas, <2cm
T2	Tumour limited to the pancreas, >2cm
T3	Tumour extension beyond the pancreas (duodenum, bile duct, portal or superior mesenteric vein)
T4	Tumour involving the celiac axis or superior mesenteric arteries (unresectable primary tumour)
Regional lymph nodes	
N_x	Regional lymph nodes cannot be assessed
N_0	No regional lymph node metastasis
N_1	Regional lymph node metastasis
Distant metastasis	
M_x	Distant metastasis cannot be assessed
M_0	No distant metastasis
M_1	Distant metastasis present

In addition to the TNM classification, the American Cancer Society has also published a staging system as described in Table 4.

Table 4: American Cancer Society staging of pancreatic cancer.

Stage grouping	
Stage 0	Tis N0 M0
Stage IA	T1 N0 M0
Stage IB	T2 N0 M0
Stage IIA	T3 N0 M0
Stage IIB	T1-3 N0 M0
Stage III	T4
Stage IV	Any T Any N M1

2.6 Clinical presentation

One of the challenges in the diagnosis of pancreatic cancer is the late presentation of the disease. Only 7% of pancreatic tumours are confined to the pancreas at the time of presentation[62]. This is compared to 61% of breast cancers, 40% of colorectal cancers and 91% of prostate cancers[63] being confined to their respective primary organs. The pancreas is a retroperitoneal organ meaning that it is located in the back of the abdominal cavity. This is a hidden location and as such it is very difficult to feels lumps arising from this region during a clinical examination. In comparison, breast cancer may present as a lump that can be felt at an earlier stage in the disease[64], [65]. Similarly, prostate cancer can be detected during a digital rectal examination. This partially explains the better survival rates seen with breast and prostate cancer compared to pancreatic cancer.

Patients with pancreatic cancer show signs at a later stage, and when it does present the symptoms are usually non-specific including anorexia, weight loss, jaundice and abdominal pain[66]. Tumours that are situated in the head of pancreas are more likely to present with obstructive jaundice. The head of the pancreas is the area of the pancreas located adjacent to the bile ducts that drain bilirubin from the liver. Tumours located in the body and tail of the pancreas, in the region away from the bile ducts, are more likely to present with abdominal pain. Tumours in the pancreas may also lead to a reduction in the function of the pancreas (pancreatic insufficiency), though this is a less common presentation. The two major functions of the pancreas are the production of digestive enzymes and the production of insulin for blood glucose control. Lack of digestive enzymes leads to malabsorption diarrhoea (steatorrhea) and reduction in insulin production leads to new onset diabetes mellitus.

The presentation of pancreatic cancer tends to be late and non-specific. This is a major hurdle in diagnosing pancreatic cancer at an early stage. This is made worse by the fact that the current imaging techniques of the pancreas have poor sensitivity for detecting the disease.

2.7 Imaging for pancreatic cancer

The current imaging modalities available for pancreatic cancer are limited in their ability to make a diagnosis at an early stage. There are several imaging modalities in use, each of which has their limitations.

Trans-abdominal ultrasound is safe, widely available and is useful for initial assessment of the pancreas in patients with symptoms but its low sensitivity ranging between 67% and 90%[67] means it is unreliable for definitive diagnosis and lacks the ability to make an early diagnosis.

Computed tomography (CT) scan is the most commonly used imaging modality for the pancreas with a 90% sensitivity and 99% specificity[68]. However for pancreatic masses below 1.5cm the sensitivity drops to 67%[69]. The use of intravenously injected contrast dye enhances the detection of a tumour in the pancreas. Typically, a CT scan specifically to assess the pancreas is done with thin-sections (less than 3mm) and is multiphasic with images taken at different time lapses relative to the administration of the contrast dye. This includes an arterial phase to assess the involvement of nearby arteries such as the superior mesenteric artery which is required to determine whether the tumour can be safely removed completely with surgery[70][71]. The portal venous phase acquired 60 to 90 seconds after giving the contrast allows evaluation of adjacent veins particularly the mesenteric, portal and splenic veins. The pancreatic parenchymal phase is taken 35 to 50 seconds after the contrast dye is given and coincides with the peak enhancement of the pancreatic tissue thus enhancing the conspicuity of any tumours. A pancreatic tumour appears hypo-enhancing relative to the avidly-enhancing adjacent normal pancreatic tissue[72]. However, in 11 to 27% of cases there is no difference in the enhancement when comparing the lesion and the pancreatic parenchyma[73]–[75]. Another limit of CT is the exposure to ionising radiation making it unsuitable for screening.

Magnetic resonance imaging (MRI) is another imaging modality used to investigate the pancreas. In comparison to CT, MRI is better at detecting small lesions. Its use in the detection of small tumours is limited by the presence of movement artefact, its high cost and limited availability. However it has

been advocated in the screening of patients with a positive family history of pancreatic cancer detecting lesions in 40% in this group of patients[76].

Endoscopic ultrasound (EUS) has an advantage over trans-abdominal ultrasound as the pancreas is located in the retroperitoneal space which is more accessible via the endoscopic route which is through the stomach. The stomach lies in an ideal position for assessing the pancreas as it is directly in front of the pancreas. Furthermore, it can be combined with fine needle aspiration (FNA), to remove fluid that can be used for diagnosis, to increase its sensitivity. As such it is significantly more sensitive and specific than either ultrasound or CT[77]. However, it has not been taken up as a screening tool as the procedure is too invasive for the patient and thus is only used in selected cases.

PET scans can increase the sensitivity and specificity of detecting a pancreatic cancer. PET scans work on the principle that in cancer cells, there is an increase in the rate of glycolysis, the breakdown of glucose. Patients are injected with a radioactive contrast, the most commonly used being ^{18}F-fluorodeoxyglucose (^{18}F-FDG). This is phosphorylated in cancer cells and does not continue along the glycotic cycle, and therefore accumulates in these cells. A radioactive sensor and CT scan are combined to localise the distribution of the radioactive contrast in the patient. Although PET scanning can potentially increase the sensitivity and specificity of detecting pancreatic cancer, PET scans have been shown only to be useful for excluding distant metastases to decide whether a patient has resectable disease. PET scans are also used to detect disease recurrence after treatment. Furthermore, this type of imaging is not widely available.

While imaging of the pancreas may miss some early small lesions, if the imaging is done at the right time it may detect a tumour before symptoms develop. Only MRI, which is the most sensitive imaging technique, has been advocated for screening of the pancreas.

2.8 Screening for pancreatic cancer

Screening is the process of looking for disease in the general healthy population with no symptoms. The World Health Organisation (WHO) has defined several criteria for a good screening test[78].

Firstly, the disease which is being screened should be an important health problem. Secondly, there should be a test available for the disease and the test should be acceptable to be used on the general population. Thirdly, there should be a treatment for the condition. Fourthly, there should be a sufficient period of time during which intervention to treat the disease can occur. Finally, the economic implications should be considered. The cost of diagnosing and treating patients should be balanced against the cost implicated if there was no screening. These criteria pose several problems when applied to screening for pancreatic cancer.

One of the problems with developing a screening test for pancreatic cancer is that the disease has a low incidence in the general population. In the UK, the incidence rate is 16.4 per 100,000[21]. With such low incidence rates the screening test used must be highly sensitive and specific. Even using a diagnostic test that is 98% specific and 100% sensitive the number of false positives generated is very high in comparison to those that are finally diagnosed with the disease. This reduces the acceptability of the screening test unless the specificity is increased to either 99% or 100%. An option would be to screen only a sub-group of the population that has a higher incidence such as those with a familial predisposition to the disease. The International Cancer of the Pancreas Screening (CAPS) Consortium[79] have advised that first-degree relatives (FDRs) of patients with pancreatic cancer from a family with at least two affected FDRs; patients with Peutz–Jeghers syndrome; and p16, BRCA2 and hereditary non-polyposis colorectal cancer (HNPCC) mutation carriers with ≥1 affected FDR should be screened. However, the screening tests suggested are magnetic resonance imaging (MRI) and endoscopic ultrasound (EUS) which are not easily available and invasive. Furthermore, how these patients are managed once a lesion is detected is still controversial. For example, it is not clear which lesions should be kept under observation and which should be removed by surgery.

Another problem with screening for pancreatic cancer is that in some cases it is difficult to make a definite diagnosis prior to surgery. In some cases, where the suspicion is high enough, a patient will be counselled and undergo surgical removal and the final diagnosis is made when the pancreas

specimen undergoes histopathological examination. Surgery for pancreatic cancer is associated with a relatively high complication rate and mortality rate compared to surgery for other types of cancer. Therefore, screening for pancreatic cancer is controversial as it may generate an unacceptably high number of false-negative cases with patients undergoing unnecessary treatment with its associated risks of complications.

It is important that any screening test developed for pancreatic cancer should meet the criteria of being highly specific and sensitive, but not invasive[78]. This could be a blood test that detects circulating biomarkers for pancreatic cancer. Using biomarker detection would allow the screening population to be expanded to medium or low risk patients. It could also help to confirm a diagnosis in a patient with equivocal findings on imaging. While there are several circulating biomarkers that have been identified with levels that are higher in patients with pancreatic cancer[80], there is no standalone blood marker that is suitable for diagnosis.

2.9 Biomarkers for pancreatic cancer

A useful biomarker for early diagnosis should have a high specificity and sensitivity and ideally it should be able to differentiate between low-grade and high-grade dysplasia and cancer. The biomarker may be present in blood, urine, saliva, faeces or pancreatic juice[80]. CA 19-9 is the only pancreatic cancer biomarker that is in clinical use currently. It is only validated for monitoring patients to detect recurrence after treatment. microRNAs are being investigated as alternative biomarkers for diagnosis. Both types of biomarkers will be discussed.

2.9.1 CA 19-9

Carbohydrate antigen, CA 19-9, is currently the only validated biomarker for pancreatic adenocarcinoma. It is used for monitoring recurrence after treatment but is not used for diagnosis. It is reported as being 80% sensitive and 80% specific in patients with symptoms[81]. It is not produced in those with the sialyl Lewis negative genotype seen in 5–10% of population which is associated with false negative results for CA 19-9 serum levels even in the presence of advanced pancreatic cancer.

Also, the levels of CA 19-9 may be elevated in non-cancerous conditions making it unsuitable for use in a screening test in the general population or for a diagnostic test in symptomatic patients. MicroRNAs are proving to be promising candidates as biomarkers for pancreatic cancer.

2.9.2 MicroRNAs

MicroRNAs have an important role in the control of protein synthesis. The first step in protein synthesis is transcription which occurs in the cell nucleus (Figure 2). During transcription single stranded DNA acts as a template for the production of messenger RNA (mRNA). After leaving the nucleus the mRNA is used for the synthesis of proteins in a process called translation. MicroRNAs (miRNAs) are small non-coding RNA molecules around 22 nucleotides in length that regulate gene expression at the post-transcription level by targeting mRNAs. They control the synthesis of proteins either by direct cleaving of mRNA, or more commonly they bind to the 3'-untranslated regions (3'-UTRs) of target mRNAs causing target degradation or translational inhibition[82]. miRNAs have an important role in the regulation of various biological processes including proliferation, differentiation and apoptosis. Abnormalities in microRNA expression can lead to disease and cancers[83], [84].

The discovery of the first microRNA, the lin-4 gene, in *Caenorhabditis elegans* was published in 1993. The lin-4 gene has a sequence complimentary to the mRNA that encodes the lin-14 protein and inhibits its translation. The lin-14 protein controls the larval development of *C. elegans*[85], [86]. Specifically, the lin-14 protein is involved in the transition between the L1 and L2 larval stages. When its expression is repressed by the miRNA, Lin-4, in the early stages of larval development, the molecules involved in the transition between L2 and L3 can be expressed. Several years following the discovery of lin-4, let-7, another miRNA gene was discovered in the same species*, C.elegans* [87]. Let-7 also represses the Lin-14 expression to regulate late larval development[88]. The let-7 gene was later found to be conserved in many animal species. It was then discovered that microRNAs were not exclusive to worm species, but they are also present in plants, viruses and animals including humans.

Since then many more miRNAs have been discovered. In 2002, the University of Manchester set up a microRNA database (www.mirbase.org) that to date contains 28,645 entries and includes human, mouse, fly, and worm species. It is estimated that miRNAs target around 30-60% of the protein-coding genes in the human genome[83], [89].

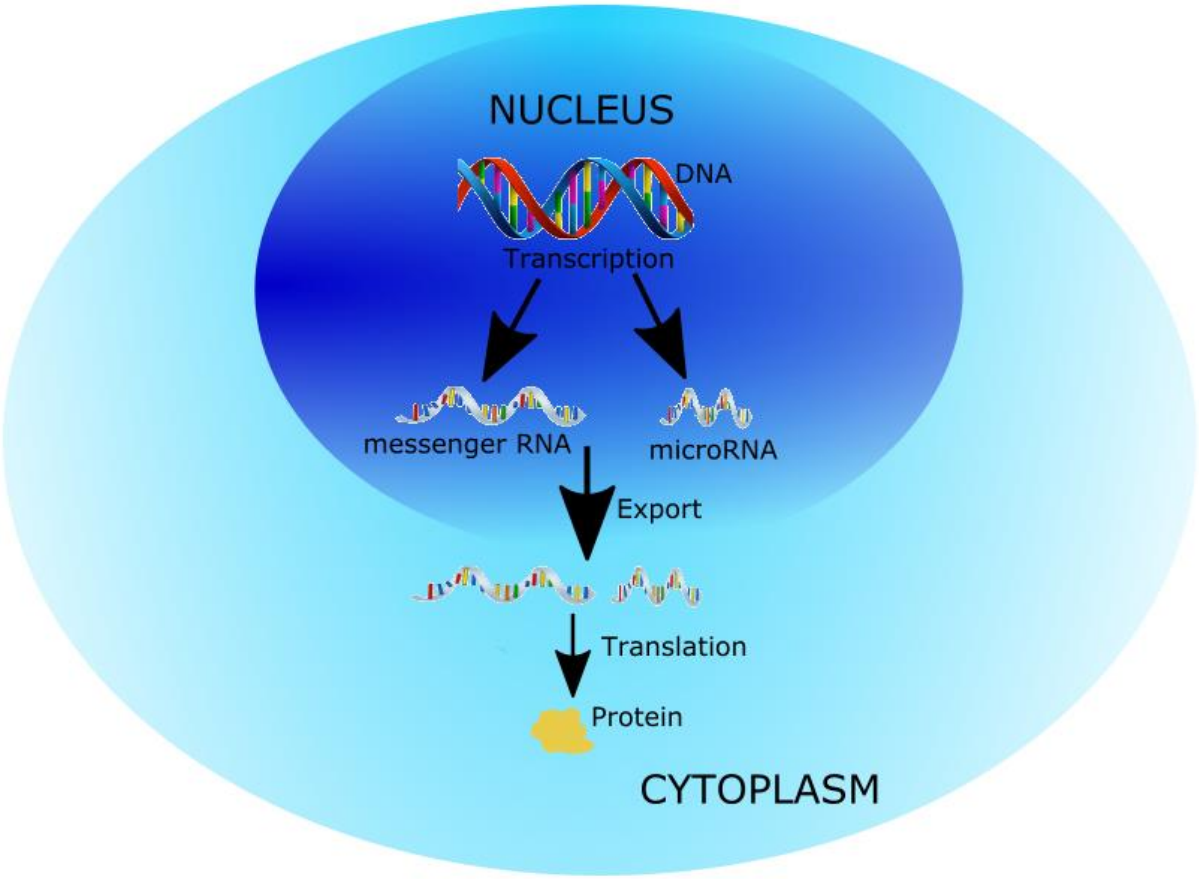


Figure 2: Schematic diagram to show the stages in protein synthesis from DNA. MicroRNAs act at the post-transcription level.

There are four known mechanisms by which microRNAs can be released by cancer cells. They may be released bound to Ago2 protein or high-density lipoprotein, or carried within exosomes or microvesicles [90], [91]. The majority of microRNAs released by pancreatic cancer cells are thought to be exosomal [91], [92]. Exosomes are tiny vesicles with a lipid bilayer wall that that are around 40-140nm in diameter. They may carry proteins, DNA, mRNA and/or microRNAs[93]. They interact with cells and have the ability to modulate various intracellular processes[94].

The up regulation of serum miRNAs in cancer was first demonstrated in patients with B-cell lymphoma[95]. Their use as a potential blood biomarker for epithelial derived cancer was first demonstrated for prostate cancer[96] and several studies show that specific miRNAs are dysregulated in different cancer types including pancreatic cancer compared to normal control patients[97], [98].

2.10 MicroRNAs in pancreatic cancer

MicroRNAs are highly stable in blood making them suitable candidates for biomarkers. This is partly due to their small size of around 22 nucleotides or approximately 7 nanometres and, for some microRNAs, protection within exosomes in bodily fluids[99]. The types of microRNAs expressed in pancreatic cancer have been studied in the pancreatic tissue, blood, biopsy and stool samples. Blood-based microRNAs have been shown to have a higher overall accuracy at detecting pancreatic cancer (91% sensitivity, 96% specificity) compared to tissue-based microRNAs (85% sensitivity, 89% specificity[100]. These circulating microRNAs would make useful biomarkers for a non-invasive screening method of diagnosing pancreatic cancer. Several studies have focused on the discovery of circulating microRNAs in pancreatic cancer.

2.10.1 Circulating microRNAs in pancreatic cancer

The first study evaluating circulating microRNAs for the diagnosis of pancreatic cancer was published in 2009[101]. Four microRNAs were studied: miR-21, miR-210, miR-155 and miR-196a.The selection of microRNAs was based on those microRNAs identified to be up regulated in previous studies in pancreatic cancer tissue or pancreatic juice. The study was a proof of principle to demonstrate

whether different levels of plasma microRNA could be used to distinguish normal controls from patients with pancreatic cancer. Of the four microRNAs, only miR-210 levels were significantly different in the two groups. However, in combination the levels of the four microRNAs demonstrated improved sensitivity and specificity to detect PC over using the single microRNAs as standalone biomarkers. This study paved the way for further work evaluating the use of other circulating microRNAs for the diagnosis of pancreatic cancer.

In another study, miR-182[102] was evaluated as a stand-alone diagnostic plasma marker and found to be expressed at significantly higher levels in patients with pancreatic cancer compared to patients with chronic pancreatitis and controls ($p<0.001$). The level of miR-182 could also distinguish between patients with pancreatic cancer and chronic pancreatitis ($p<0.05$). There was a significant correlation between circulating levels of miR-182 and clinical stage ($p<0.001$) although it could not discriminate between stage I and II disease. In combination with CA 19-9, the sensitivity and specificity were significantly higher than either marker alone.

In another study[103] miR-192 levels in plasma are used as a biomarker for pancreatic cancer and this demonstrates sensitivity and specificity of 76% and 55% respectively. The levels were significantly lower in patients with duodenal carcinoma compared to patients with pancreatic cancer. However, it could not distinguish duodenal carcinoma from normal controls. This suggests that miR-192 may be useful in a micro-RNA panel to exclude patients with duodenal carcinoma.

Morimura et al., 2011[104], studies the use of miR-18a in plasma samples from patients with pancreatic cancer. The study demonstrated a significant increase in the levels ($p<0.0001$) compared to healthy controls.

In Ali et al., 2011[105], 91 microRNAs were found to be dysregulated in the plasma from 32 patients with pancreatic cancer compared to 10 healthy volunteers. Levels of miR-21 and miR-221 were

significantly higher in pancreatic cancer patients compared to controls. The levels of miR-200b, miR-200c, let-7b and let-7d were down-regulated.

Cote et al, 2014[106] demonstrate that five microRNAs have very high accuracy (AUC>0.90) in distinguishing pancreatic cancer patients from chronic pancreatitis and normal controls. These were miR-10b, miR-30c, miR-106b, miR-155 and miR-212. When used in combination the sensitivity and specificity were 100%. The cohort number was small, but the findings are consistent with other studies that show that combinations increase the specificity and sensitivity of detecting pancreatic cancer.

A larger group consisting of 421 patients is evaluated in a Japanese study published in 2014[107]. This included patients with pancreatic cancer, biliary tract cancer, colon cancer, stomach cancer, oesophageal cancer, liver cancer and non-malignant pancreatic or biliary-tract disease as well as healthy volunteers. To differentiate pancreatic cancer patients from healthy controls, miR-125a-3p and miR-6893-5p showed the greatest significance; with the former able to detect 30 out of 33 (90.9%) patients with pancreatic cancer. 40 of 81 validated microRNA markers for pancreatic cancer had higher sensitivities than CA 19-9. However, miR-125a-3p was also highly expressed in patients with biliary tract cancer detecting 32 of 33 (97.0%) of patients. In fact, 67.9% of microRNAs detected in pancreatic cancer were also found to be markers for biliary tract cancer and none of the markers that could distinguish pancreatic from biliary tract cancers were statistically significant. These results suggest that the differentiation of pancreatic from biliary tract cancers on the basis of microRNA expression is not possible. Combining the groups of biliary and pancreatic cancers and comparing pancreaticobiliary cancers with healthy controls, 4 micro-RNAs were identified: miR-6826-5p, miR-6757-5p, miR-3131 and miR-1343-3p ($p<0.01$). To identify markers that could distinguish pancreatobiliary cancer from a heterogenous group, micro-RNAs were identified to distinguish the pancreatobiliary cohort from the other groups combined. The best marker was miR-6075 (sensitivity 63.6%, specificity 93.5%). Finally, a microRNA index of 10 micro-RNAs was tested against the single best marker to distinguish pancreatic and biliary cancers from the heterogeneous group. A combination of microRNAs increased the

accuracy to up to 91.6% when four micro-RNAs were used in combination. When the number of micro-RNAs reached 8 or 9, the accuracy started to decline suggesting the diagnostic accuracy reaches saturation.

Xu et al., 2015[108] published the results of a multiphase multicentre study to identify microRNAs present in plasma that can be used to distinguish patients with pancreatic cancer from various controls of other pancreatic tumours (OPT) including serous and mucinous cystadenomas, solid pseudopapillary tumours, intra-ductal papillary mucinous neoplasms or epithelial cysts. They also include a further control group of patients with pancreatic neuroendocrine tumours (PNET). MiR-486-5p, miR-126-3p and miR-938 were able to distinguish pancreatic cancer from normal controls. MiR-938 was also able to distinguish patients with pancreatic cancer from those with PNET (p=0.0023) and OPT (p=0.0063). When the diagnostic value of the most discriminatory miRNAs was compared with CA 19-9 there was no significant difference both when discriminating pancreatic cancer from normal controls and chronic pancreatitis. The strengths of this study are that it is multicentric and includes a large sample of patients. However, the study is limited as it did not evaluate a combination of miRNAs which has shown to outperform CA 19-9 alone in other studies.

Schultz et al, 2015[109] is a large multicentre study recruiting patients from six hospitals in Denmark. Whole blood is used instead of plasma or serum as this is thought to provide higher microRNA content. Instead of using microRNAs independently as biomarkers, several microRNAs are put together to make an index that contains microRNAs that are up- or down-regulated in pancreatic cancer compared to chronic pancreatitis and normal controls. The results suggest that using multiple microRNAs to diagnose pancreatic cancer should be used with CA 19-9 to improve the sensitivity and specificity of detection. However, one of the problems with using whole blood instead of plasma is that the levels of microRNA may be influenced by blood cells of different lineages also producing microRNA[110].

In Cao et al, 2016[111], two microRNA panels of 3 microRNAs (miR-486-5p, miR-126-3p, miR-106b-3p) and 6 microRNAs (miR-486-5p, miR-126-3p, miR-106b-3p, miR-938, miR-26b-3p, miR-1285) were

evaluated. They were both highly accurate for distinguishing pancreatic cancer from chronic pancreatitis (AUC 0.891 and 0.889, respectively). To a lesser extent they could distinguish pancreatic cancer from other pancreatic neoplasms (AUC = 0.677 and 0.737 respectively). The diagnostic value was comparable to that of CA 19-9, though this did not reach statistical significance (p=0.1 and p=0.1 respectively). The study was multi-centric, across six centres in China, and included 298 patients (156 with pancreatic cancer, 57 with chronic pancreatitis and 85 with other pancreatic neoplasms).

In Yuan et al, 2016[112], a combination of protein and microRNAs (miR-20a, miR-21, miR-25, miR-155, miR-196a, miR-210, Macrophage Inhibitory Cytokine-1(MIC-1) and CA 19-9, were evaluated in two separate indices. In a randomized setting of 260 healthy controls, 168 patients with pancreatic cancer, 132 patients with other gastrointestinal cancers and 80 patients with benign pancreatic disease, both indexes demonstrated better sensitivity for pancreatic cancer and also better specificity to distinguish pancreatic cancer from other gastrointestinal cancers than CA 19-9 and biomarkers used individually.

Another study evaluates the diagnostic accuracy of using plasma miR-16 as a standalone marker and comparing this with miR-16 in combination with CA 19-9[113]. The results show that the combination significantly increases the sensitivity, specificity and accuracy of detecting pancreatic cancer. In Liu et al., 2012[6], profiling of microRNA is carried out in blood samples from 25 patients with pancreatic cancer and compared to 25 normal controls. This showed that there is up-regulation of 44 microRNAs and down regulation of 19 microRNAs in patients with pancreatic cancer. MicroRNAs showing a p-value <0.01 were chosen to create a 7-microRNA panel which included miR-20a, miR-21, miR-24, miR-25, miR-99a, miR-185, and miR-191. The sensitivity and specificity of the panel was 89% and 100% respectively. When stratifying the results according to stage of disease, higher levels were seen in stage 3 and 4 disease. MiR-21 and miR-24 in particular were elevated in advanced stages. In another study[9], 7 predetermined plasma microRNAs (miR-16, 21, 155, 181a, 181b, 196a and 210) were tested as standalone markers. Although the levels of all seven mi-RNAs were different between pancreatic cancer patients and normal controls, only miR-16 and miR-196a levels were significantly

different to discriminate between these two groups. These two markers were then combined with CA 19-9 and a further improvement in the sensitivity and specificity was observed. The results were stratified according to tumour stage. Again, combining CA 19-9 with the miRNA panel showed a higher rate of detection of stage I tumours than using either the microRNA panel or CA 19-9 alone. This is an important finding as early diagnosis is based on finding markers that are present at an early stage.

Deng et al, 2016[114], evaluate the use of miR-25 as a stand-alone biomarker for pancreatic cancer based on its use in other cancers including prostate, ovarian and gastric adenocarcinoma. The results show significant up regulation of miR-25 in the serum from patients with pancreatic cancer compared to normal controls and compared to serum from patients with other diseases (both $p<0.0001$). A total of 1063 serum samples were collected from three national hospitals providing a large sample for the study.

In Alemar, 2016, [115], 24 serum samples from patients with pancreatic cancer were compared to 9 control samples and analysed for levels of miR-21 and miR-34a. There was a significant difference in the expression ($p<0.001$ and $p=0.001$) of the 2 microRNAs between the 2 groups. The sensitivity and specificity were 82.6% and 77.8% for miR-21 and those for miR-34a were 91.3% and 77.8% respectively. When combining the 2 microRNAs, the prediction ability increased only slightly. The sample size in this study is small but the use of miR-21 seems to concur with the results of some other studies.

2.10.2 Early stage circulating microRNAs in pancreatic cancer

Early stage detection of pancreatic cancer relies on detecting markers that are present at the early stages of the disease. In Ganepola et al., 2014 miR-642b-3p, miR-885-5p, and miR-22-3p consistently showed greater expression in early stage (IIA or IIB) pancreatic cancer compared to controls. The controls included healthy patients as well as those with a family history of pancreatic cancer. The patients with pancreatic cancer were staged according to post-operative histology. The combination of all three markers showed sensitivity and specificity both of 91%. The accuracy of detection was

better with the combination than using individual markers. Li et al, 2013[116] measure the serum levels of 735 miRNAs in patients with resectable stage I or stage II pancreatic cancer in comparison to patients with chronic pancreatitis, healthy controls and patients with pancreatic neuroendocrine tumours. miR-1290 was found to have the highest diagnostic accuracy (AUC 0.96 when compared to healthy controls). This was higher than that of CA 19-9 alone (AUC 0.86 when compared to healthy controls). There was no improvement in the accuracy when miR-1290 and CA 19-9 were combined.

In Hussein et al, 2017, [117] miR-22-3p, miR-642b-3p and miR-855-5p are demonstrated to be present at significantly higher rates in patients with pancreatic cancer even in the early stages of the disease, stage IB and IIB.

The evaluation of circulating microRNAs as biomarkers is still in its infancy. However, the studies that have been published to date show that they have a potential use for the detection of pancreatic cancer, even in the early stages. The elevated levels are thought to be due to release of tissue or organ specific microRNAs into the circulation during apoptosis or cell death due to high cell turnover, cell destruction and pathological injury[96]. The higher levels may also be due to a metabolic imbalance of microRNAs in cancer cells. Furthermore, several of the studies evaluating microRNA conclude that a combination of microRNAs increases the specificity and sensitivity of detecting pancreatic cancer. Combining CA 19-9 and relevant microRNA also increases the specificity and sensitivity of detection of pancreatic cancer compared to using individual microRNAs or CA 19-9 as a standalone marker.

The use of microRNA/s may therefore be useful biomarkers to increase the specificity of detection of pancreatic cancer which is lacking with traditional markers. However, further work needs to be carried out as in the majority of studies to date the sample sizes are small. Also, in future it will be important to identify the role of the up regulated microRNAs as some are cancer specific microRNAs while others have multiple functions, and these may be produced as part of the general inflammatory response and the levels would be expected to be elevated in other cancer types and diseases. For example, in some studies the prevalence of microRNAs found in pancreatic cancer were also evaluated in other

cancer types. Some cancers arising from the upper gastrointestinal tract appear to produce the same microRNAs as those produced in patients with pancreatic cancer. Such overlap should be taken into account when choosing biomarkers specifically for pancreatic cancer.

Also, when evaluating the results of all the studies, it is noted that there are only few microRNAs that are identified in more than one study. This suggests that there are a large number of microRNAs that are expressed and released in pancreatic cancer. The may reflect the genetic diversity of pancreatic cancers and that even cancers of the same histological type have different genetic makeup. Again, selecting the appropriate markers for diagnosis is important in making an early diagnosis.

The problem with using microRNA as a biomarker is that quantification is currently a long process as it requires an amplification step as the native levels of microRNA are small. Further work should therefore focus on better detection methods of microRNA with multiplexing being an important strategy to allow the detection of multiple microRNAs at the same time. This is in addition to the future work that needs to be carried out to improve the selection of microRNAs for diagnosing PC.

2.11 Biomarkers for pancreatic neuroendocrine tumours

The two commonly used biomarkers for pancreatic NETs are 5-hydroxyindole acetic acid (5-HIAA) and chromogranin (CgA). 5-HIAA is a breakdown product of serotonin which is produced by some NETs and excreted in the urine. It is measured in a 24 hour urine collection. CgA is a glycoprotein that is also a precursor protein that is cleaved into a large number of small bioactive peptides. Both biomarkers are used for screening and monitoring of the disease. However more studies need to be done to determine their predictive value and much research is being carried out to look for better biomarkers for pancreatic NETs.

2.12 Treatment of pancreatic cancer

The only potential cure currently available for pancreatic cancer is surgery. Curative surgery involves removing all of the disease and can only be curative if it is done at an early stage when the tumour is

small and can be removed completely. If the disease has progressed to a stage when surgery is not suitable, chemotherapy and radiotherapy are the only other treatment options available. While these treatments may be able to control the disease in the short term, the longer term benefits of chemotherapy and radiotherapy are very small[118].

Chemotherapy and radiotherapy may add only a few months to the patient's survival at most. This is because pancreatic cancer is largely resistant to these treatments. The resistance to chemotherapy and radiotherapy is a result of these treatments not being able to penetrate the cancer due to the innate structure of pancreatic tumours. Pancreatic cancers have a poor blood supply and are surrounded by a dense fibrous capsule which hinders the delivery of chemotherapy drugs. Furthermore, the development of multi-drug resistance is also more of a problem with pancreatic cancer than other types of cancer due to the overexpression of membrane transport proteins that act as drug efflux pumps. The presence of cancer stem cells also increases resistance to treatment[119]. These stem cells are responsible for tumour metastasis and recurrence and their presence leads to a high risk of relapse after treatment. These factors inherent to pancreatic cancer mean that chemotherapy and radiotherapy have low effectiveness and surgery is the only hope of cure.

While our ability to detect PC at an early stage has not improved, some recent studies have led to the improvement of survival in patients with locally advanced disease [2]. These studies have evaluated the use of adjuvant treatment in pancreatic cancer. Adjuvant treatment refers to the treatments delivered after surgery to reduce the recurrence of the disease. Until recently there were no randomised controlled trials evaluating the use of adjuvant treatment in PC. The studies that had been carried out showed equivocal data. As a result, adjuvant treatment was not routinely used. The ESPAC-1 trial from the European Study Group for Pancreatic Cancer was a landmark study showing improved median survival (22.1 months compared to 20.2 months) and median disease free survival (13.4 months compared to 6.9 months) with chemotherapy compared to no adjuvant treatment [2]. This translated to an estimated 5-year survival rate of 21 per cent in patients receiving

chemotherapy and 8 per cent in those not receiving chemotherapy. Interestingly, the trial also showed that adjuvant chemoradiotherapy (a combination of chemotherapy and radiotherapy) led to worse outcomes with a 5-year survival rate of 10 per cent in those receiving chemoradiotherapy compared to 20 per cent in those not receiving any adjuvant treatment. Therefore, in Europe, radiotherapy is not routinely used for adjuvant treatment.

Neoadjuvant treatments refer to treatments undertaken prior to surgery and can be used to downstage a tumour and make it suitable for resection or increase the likelihood of removing all of the tumour. Neoadjuvant treatment has been established in other cancers such as colorectal and oesophageal cancer, but again the role in PC has not been evaluated. Recent studies have shown that neoadjuvant therapy benefits those patients with borderline-resectable or non-resectable tumours and was able to downstage those tumours so that they were resectable in a third of cases [22].

Since surgery needs to be carried out in the early stages, the key to improving survival is early diagnosis. This is supported by evidence from large multinational population-based studies that show that the survival rates are much higher for smaller tumours in the early stages. According to the Japan Pancreatic Cancer Registry[120] size is one of the strongest prognostic factors where the 5-year survival rate of pancreatic tumours 10mm or less reached 80% compared to 4% for advanced stage IV disease. A European study shows similar results[121]. However only 15-20% of patients present with early resectable disease[122]. The success of treatment is greatly dependent on early diagnosis to improve survival in these patients.

2.13 Summary

In summary, the current available diagnostic tools for pancreatic cancer are unable to detect early stage disease as described above. Logistically, a blood screening test would be ideal for early diagnosis. However, currently there is no such test available for pancreatic cancer. A highly specific screening

test could be achieved by combining several markers in a platform with multiplex capabilities. A sensitive platform would increase the detection of markers at an early stage. One way to increase the sensitivity of detecting a biomarker for the disease is to use a technique known as metal enhanced fluorescence using nanotechnology.

CHAPTER 3: NANOTECHNOLOGY

Since the 1980s, the ability to study materials that are nanometers in size has led to the discovery of new phenomena that have potential applications in different scientific fields including medicine, chemistry and engineering. This ability to study materials at the nanoscale has come from the invention of instruments such as the scanning electron microscope (SEM). Plasmonics is one such phenomenon that is a unique property of metal nanoparticles.

3.1 Plasmonics and Metal Enhanced Fluorescence

Plasmonics describe the effects related to electrons or plasmons that surround metal nanoparticles. As a result, nanoparticles interact with light in a different way to large sized bulk materials. The plasmonic effect is a phenomenon unique to nanoparticles that has been used unknowingly for centuries for the intricate decoration of churches and precious objects (Figure 1). In recent times, an understanding of why this phenomenon occurs has developed and this has led to the ability to make it useful for applications beyond cosmetic ones.

Metal enhanced fluorescence (MEF) is thought to be a result of the plasmonic effect. It has been given many labels including metal induced fluorescence enhancement (MIFE), surface enhanced fluorescence (SEF) and radiative decay engineering (RDE). These names describe the observation that the intensity of light emitted by a fluorescent molecule increases when it is in proximity to a metal nanoparticle. This occurs due to two types of plasmonic effects: localised surface plasmon resonance (LSPR) and surface plasmon polariton (SPP).

The aim of this section is to provide a summary of the current understanding of the mechanism of MEF. It will also introduce some important concepts relevant to biosensing. Firstly, the basic principles of fluorescence will be described.

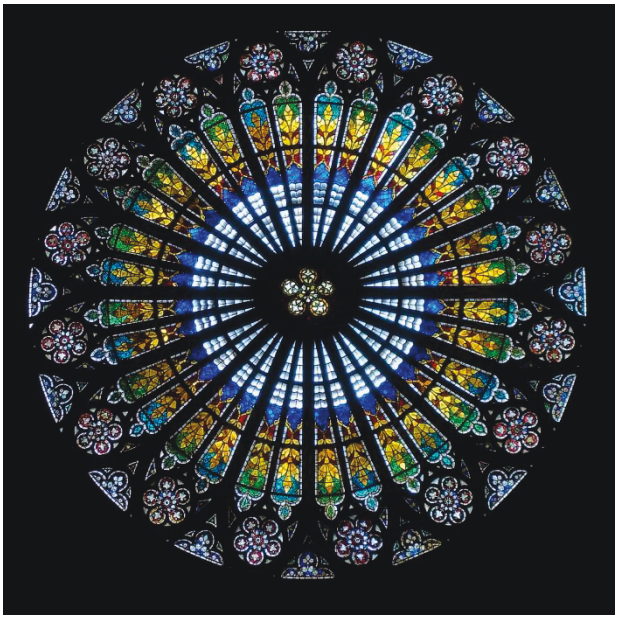


Figure 1: Stained glass rose window of Notre Dame de Paris. Gold nanoparticles embedded in the glass interact with light and are responsible for the vivid colours seen.

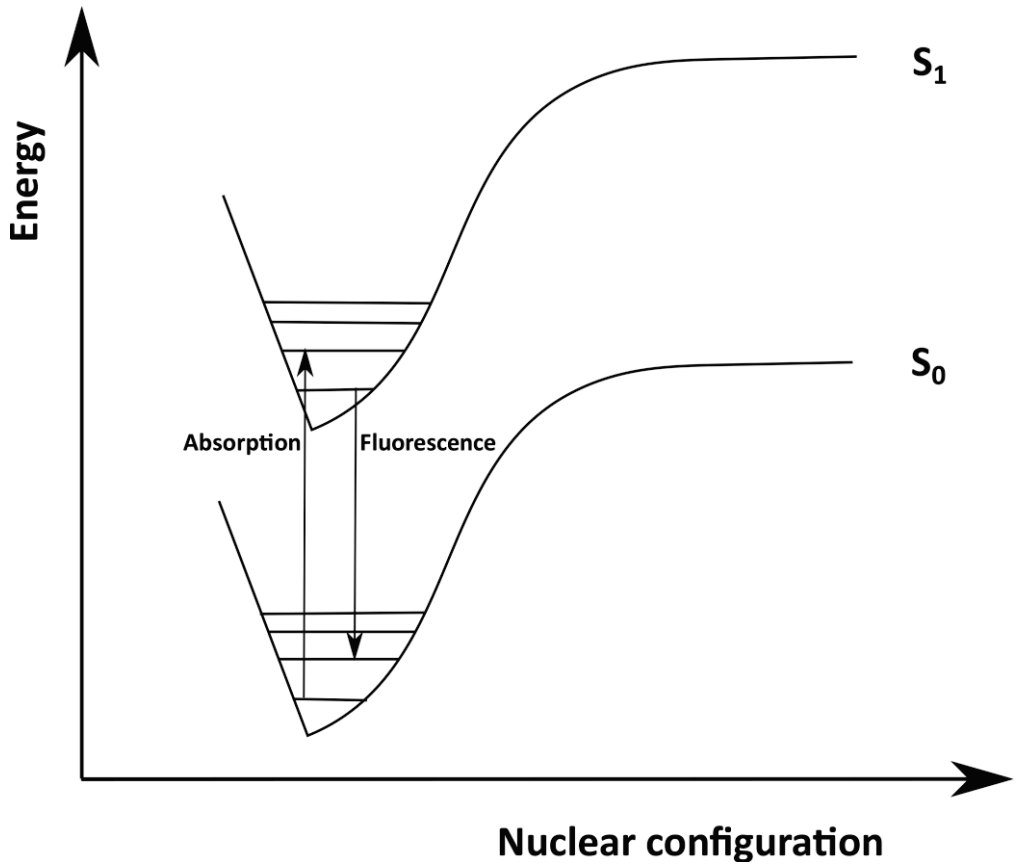


Figure 2: Potential energy diagram to show energy levels of fluorophore. The relationship between absorption and emission can be demonstrated using a potential energy diagram.

3.1.1 Basic principles of fluorescence

Fluorescent molecules or fluorophores are molecules that have the property of re-emitting light when they enter an electronically excited state by the absorption of light. Fluorophores have been extensively used in biosensing and bio-imaging applications. When a fluorophore absorbs a photon it enters an excited state whereby an electron is promoted from a lower energy orbital to a higher energy orbital [70]. When the excited electron returns to ground state it releases a photon. The characteristics of some common fluorophores are shown in Table 1.

The mechanism of energy absorption and emission is described using energy levels (Figure 2). During absorption, the energy level acquired by the electron is dependent on the amount of energy absorbed. If it acquires enough energy, an electron can assume the highest energy level, S_2. During the emission phase, the most common type of transition is between the energy level in the excited state, S_1, and the ground state S_0, when the fluorophore is not excited. It is important to note that the fluorophore cannot return to the ground state, S_0 directly from the highest energy state, S_2. As shown in Figure 3, it must always relax back to the S_1 state, after excitation to S_2, with loss of some of the energy absorbed. During the transition between the S_2 and S_1 energy levels, there is no emission of photons, hence the term non-radiative relaxation. This is in contrast to the radiative decay that occurs between S_1 and the ground state, S_0 which results in the emission of light. Hence, there is always loss of energy between the absorption and emission phases and the wavelength of emission is always red-shifted compared to the excitation wavelength[123]. This phenomenon is known as Stokes shift and is demonstrated in Figure 4. The proportion of energy emitted via the non-radiative route compared to that released via the radiative route tells us about the efficiency of the fluorophore. The time it takes for the fluorophore to release its newly acquired energy is known as the fluorescence lifetime. The typical fluorescence lifetimes are very fast in the region of around 10 nanoseconds.

Table 1: Characteristics of common fluorophores

Fluorophore name	Excitation wavelength (nm)	Emission wavelength (nm)	Extinction co-efficient ($mM^{-1}cm^{-1}$)	Colour
Alexa Fluor 430	430	545	16.0	Light green
Alexa Fluor 488	495	519	65.3	Light green
Alexa Fluor 568	578	603	63.0	Red
Alexa Fluor 647	650	665	78.9	Near-infrared*
Alexa Fluor 660	663	690	132.0	Near-infrared*
Alexa Fluor 680	679	702	184.0	Near-infrared*
Alexa Fluor 750	749	775	240.0	Near-infrared*
Alexa Fluor 790	784	814	260.0	Near-infrared*
Coumarin	432	472	44.3	Blue
Cy2	490	510	150.0	Dark green
Cy3	550	570	150.0	Yellow
Cy3.5	581	596	150.0	Red
Cy5	649	670	70.0	Near infra-red*
Cy5.5	675	694	250.0	Near infra-red*
Cy7	743	770	250.0	Near infra-red*
Dy782	783	800	170.0	
Dylight800	777	794	270.0	Near-infrared*
Fluorescein FITC	495	518	73.0	Light green
Rhodamine Red	560	580	129.0	Orange

***Wavelengths of light above 700nm are invisible to the human eye**

The use of fluorescence molecules is a popular technique that has been used for DNA sequencing and drug discovery[124]–[126]. Fluorophores attached to antibodies that target certain protein biomarkers are used in fluorescent immunoassays[127], [128]. These currently offer detection sensitivity in the picomolar range ($x10^{-12}$ M)[129].

3.1.2 Beer's law

Beer's law[130], [131] describes the linear relationship between absorbance and concentration of an absorbing species and it can be applied to fluorescence. According to Beer's law the absorbance, A, is proportional to the both the concentration, c, in molarity of the absorbing species and the sample pathlength, l, (cm) transversed by the light. It is generally independent of the intensity of the excitation light (Lambert's law) except under high intensity laser excitation. This relationship can be summarised in the equation:

$$A = \varepsilon c l \quad (1)$$

where Ɛ is the molar extinction co-efficient ($M^{-1}cm^{-1}$) that describes the probability of absorption of a photon of a given energy by the molecule.

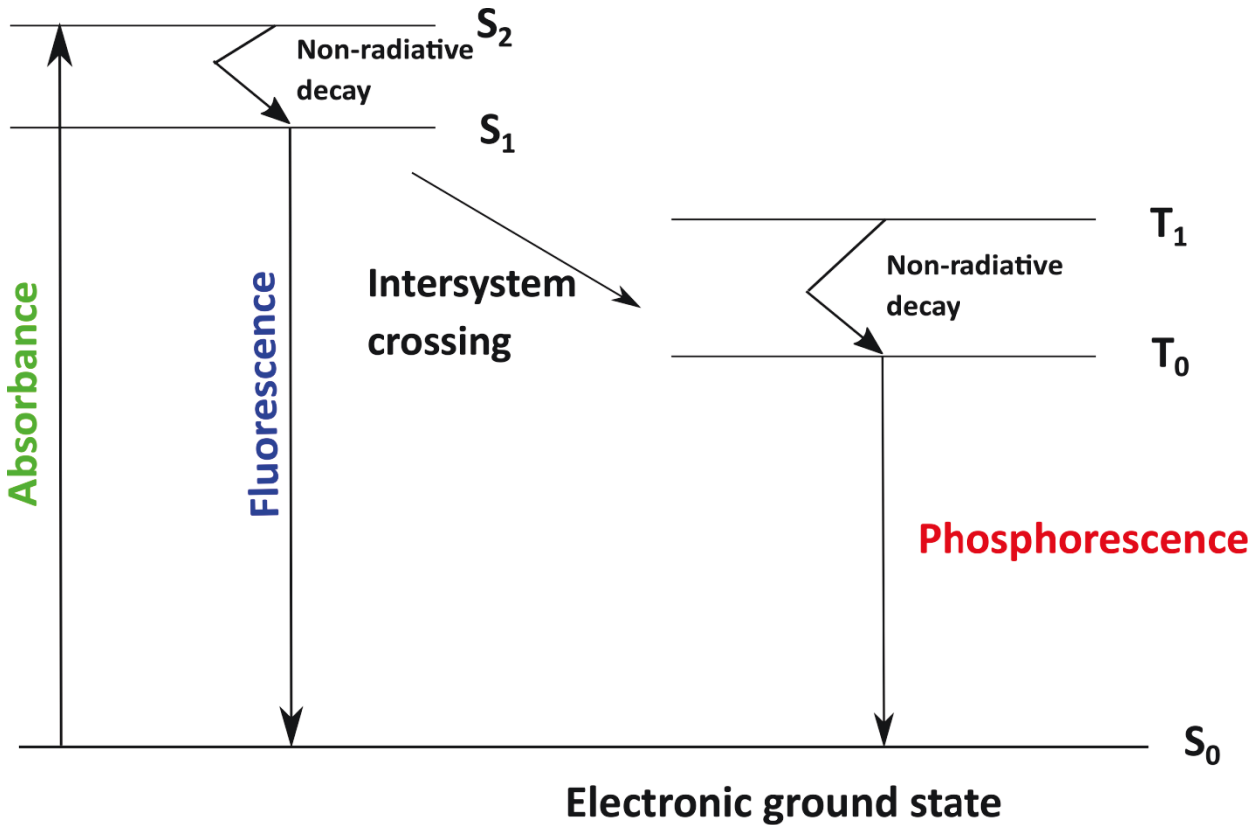


Figure 3: Jablonski diagram showing fluorescent absorption and emission processes. Intersystem crossing is a non-radiative process involving transition between 2 electronic states with different states spin multiplicity. Radiative decay from excited triplet state back to singlet state is known as phosphorescence, which has a longer half life than fluorescence.

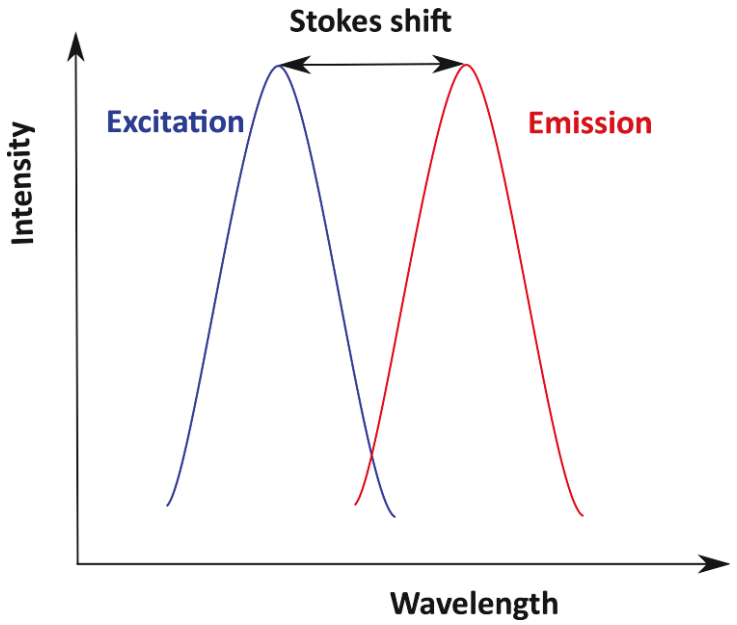


Figure 4: Intensity-wavelength curves depicting Stokes shift.

3.1.3 Dynamics of fluorescence

To understand the interactions of fluorophores with metal nanoparticles, one must firstly appreciate some basic principles of the dynamics of fluorophores.

Firstly, Γ is the *radiative decay rate* and k_{nr} *the non-radiative decay rate*[132]. The *lifetime*, τ_0, is the time taken for the fluorophore to emit its energy. The total *radiative decay rate*, $\Gamma + k_{nr}$, is the inverse of lifetime.

$$\tau_0 = \frac{1}{\Gamma + k_{nr}} \qquad (2)$$

Or,

$$\Gamma + k_{nr} = \frac{1}{\tau_0} \qquad (3)$$

Secondly, the fluorescence quantum yield, Q_0, is the proportion of excited electrons that decay radiatively to the ground state as opposed to those emitted via the non-radiative route to produce a detectable photon and can be summarised in Equation 4;

$$Q_0 = \frac{\Gamma}{(\Gamma + k_{nr})} \qquad (4)$$

The quantum yield is an important property that defines the efficiency of the fluorophore. Fluorophores with high quantum yields are observed to have high radiative decay rates. A quantum yield of 1 has no non-radiative decay channels but in reality, this cannot exist. As described previously, there is always loss of energy via non-radiative decay channels.

Thirdly, the radiative decay rate is dependent on its extinction co-efficient and is essentially independent of changes in the environment. Traditionally, interactions with fluorophores were only

known to involve alteration of the non-radiative decay rate[132]. For example, quenching processes reduce the light emitted by fluorophores by creating additional non-radiative decay channels.

The changes bought about to a fluorophore when in proximity to a metal nanoparticle are based on unique principles that fall outside these well-established rules. The metal nanoparticles are thought to alter the radiative decay rate. MEF occurs due to the presence of localised surface plasmon resonance which is unique to metal nanoparticles. In certain configurations there is also a contribution due to surface plasmon polaritons which will also be described.

3.1.4 Localised surface plasmon resonance (LSPR)

Visible light has a wavelength of between 400nm and 700nm. The size of nanoparticles is comparable to the wavelength of light. Metal nanoparticles have characteristic properties which allow them to interact with light in an unusual way owing to their size. These properties are not seen in large bulk metal structures and are unique to metal nanoparticles. One such property is called *localised surface plasmon resonance* (LSPR)[14].

Metal nanoparticles exist with a cloud of electrons on their surface which are referred to as plasma as they are in a mobile fluid-like state (Figure 5). When these electrons are disturbed, they create a dipole electric moment as they are pulled back to the equilibrium state by the electrostatic or Coulomb forces. At certain 'resonating' wavelengths, light can provide the energy to disturb these plasmons. The energy is then absorbed to create heat energy or emitted to produce light.

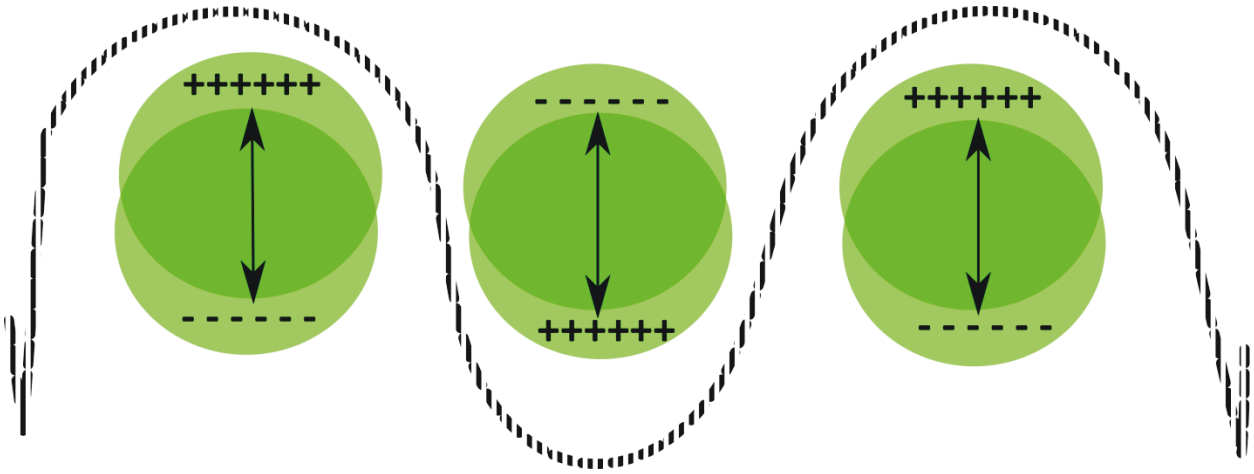


Figure 5: Diagram demonstrating vibrating localised surface plasmons and the induced associated electromagnetic wave

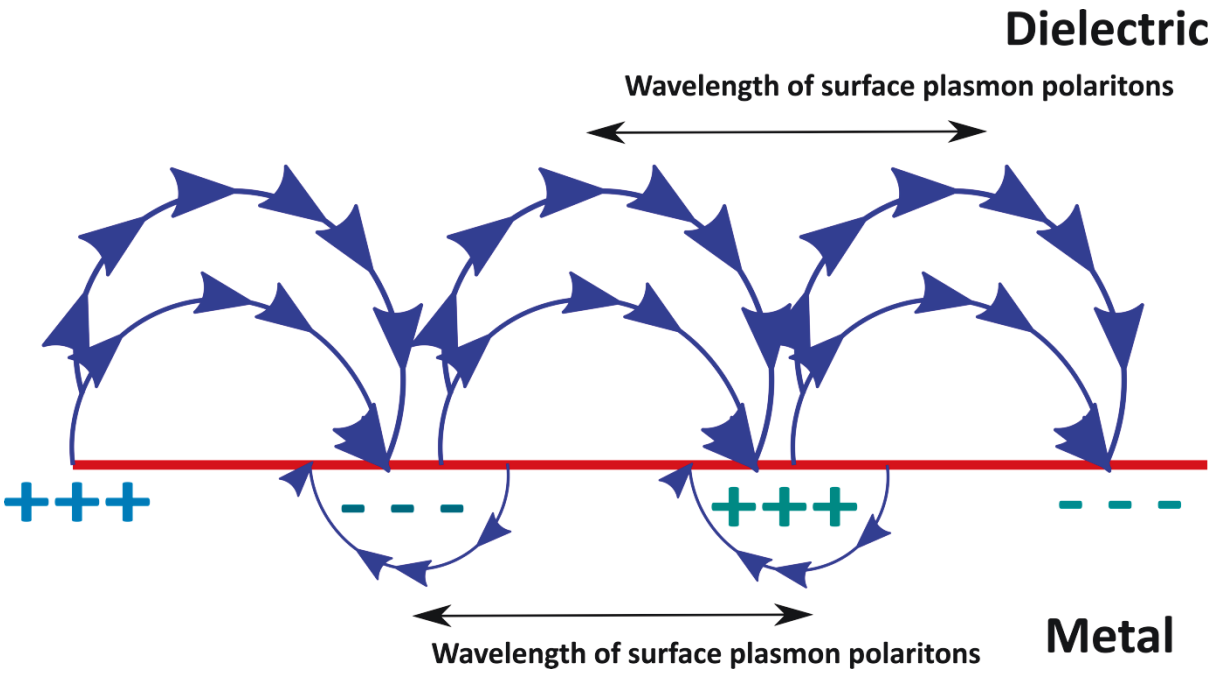


Figure 6: Diagram showing the propagation of surface plasmon polaritons excited at a metal-dielectric interface (Adapted from ref [133]**).**

The resonant wavelength can be determined by measuring the peak absorption wavelength of the metal nanoparticles using UV-Vis spectroscopy. For metal enhanced fluorescence, this absorption wavelength is an important measurement as it must overlap with the emission wavelength of the fluorophore dye to optimise the enhancement of the fluorescence.

3.1.5 Surface plasmon polaritons (SPP)

In additional to these volume plasmons, surface plasmons refer to the plasmons on the surface of thin metals that propagate along a metal-dielectric surface [134], [135](Figure 6). Dielectric surfaces are insulating and therefore do not propagate the conduction of electrons. These plasmons are another source of energy for enhancement of fluorophores. Characteristics depend on the optical properties of the interface as well as the metal. To attain this energy, similarly to LSPR, the wavelength of incoming light must match the SPP momentum. The point at which they match is known as the resonance. For basic nanostructures such as nanotriangles, only the energy from LSPR is utilised and not the SPP. To improve enhancement requires the use of more complex nanostructures to capture both energies.

3.1.6 Generation of Metal Enhanced Fluorescence (MEF)

The sensitivity of fluorescent conjugated assays is generally low. The limitation of fluorophores is that the intensity is dependent on the amount of fluorophore that remains at the end of the assay. This in turn is dependent on the amount of biomarker being tested. When the levels of biomarker are high enough there is sufficient fluorophore to produce a signal that can be used to quantify the biomarker. However, the use of fluorophores is limited in the detection of less abundant biomarkers and single molecules. MEF is a way of enhancing the signal from fluorescent molecules. MEF describes the ability of metal nanoparticles to increase the photon emission by nearby fluorophores. One of the earliest observations of this was seen when using silver island films[136] where silver was deposited on glass to produce islands of sizes below the wavelength of light in the nanometre range. We can understand why this occurs by reviewing the effect on the dynamics of the fluorophore.

If we define Γ_m as the radiative decay in the presence of metal nanoparticles, k_m as the non-radiative decay in the presence of metal nanoparticles and k_{nr} as the total non-radiative decay, then the quantum yield should be calculated as follows:

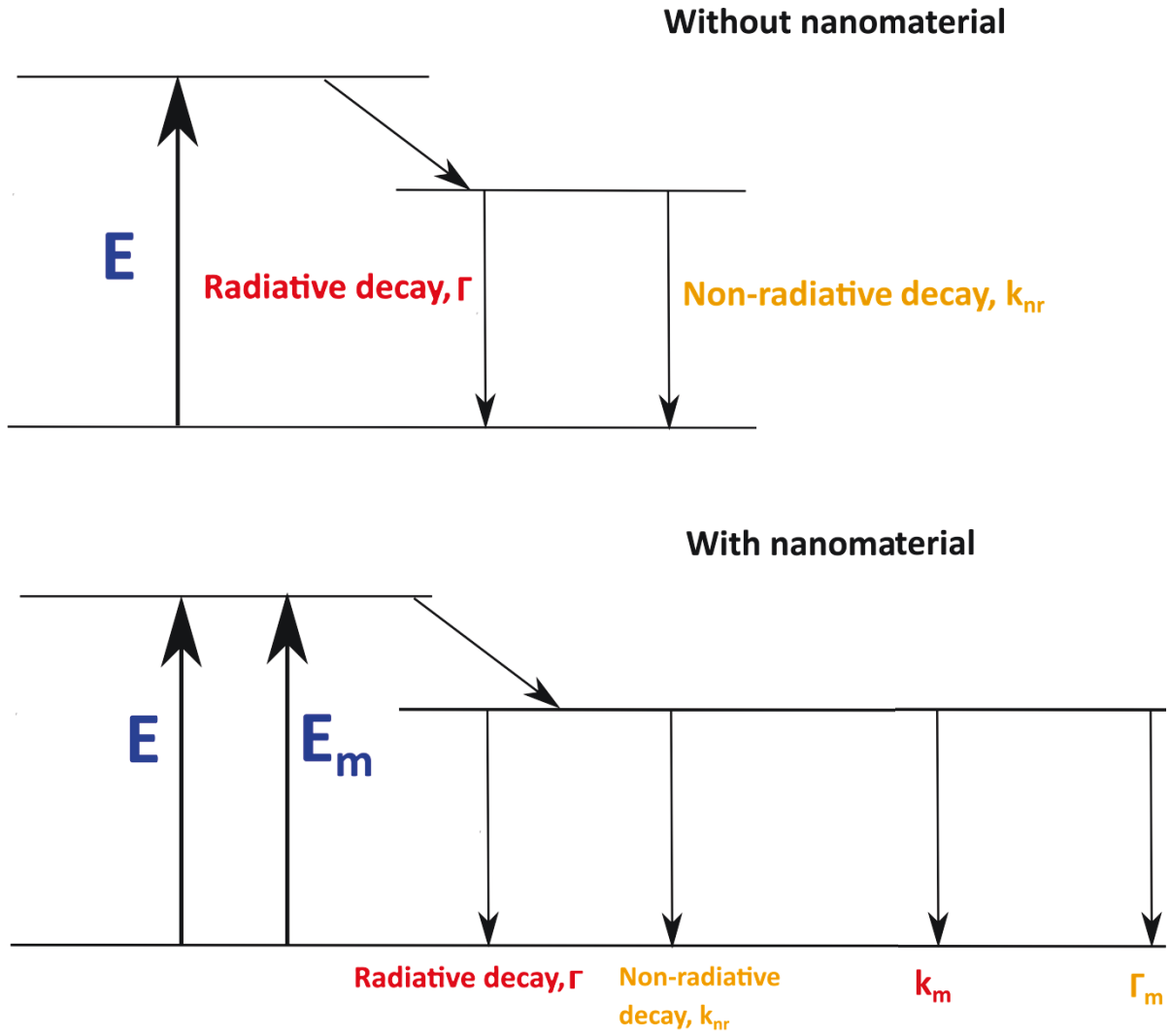
$$Q_m = \frac{\Gamma_m + \Gamma}{(\Gamma_m + \Gamma + k_{nr})} \qquad (5)$$

This is demonstrated in the Jabonski diagram in Figure 7.

Thus, the lifetime is calculated by the following equation:

$$\tau_m = \frac{1}{\Gamma + \Gamma_m + k_{nr}} \qquad (6)$$

As the value of the radiative decay rate with the metal nanoparticles increases, the quantum yield increases but the lifetime decreases. In one early study, the lifetime of deposited fluorophores was found to decrease by as much as 100 times[136]. From previous understanding of fluorescence, a reduction in lifetime should always be associated with a decrease in intensity. The reduction in intensity occurs because the lifetime decreases as a result of an increase in the non-radiative decay. On the contrary, with metal enhanced fluorescence an increase in intensity by 5 times was observed.



E excitation

E_m metal-enhanced excitation

Km non-radiative decay rate in presence of metal nanoparticle

$Γ_m$ radiative decay rate in presence of metal nanoparticle

Figure 7: Jabonski diagram showing effect of metal nanoparticle on fluorophore. (Adapted from ref [132]**).**

In turn, the reduced lifetime increases the photostability as the fluorophore has less time to undergo interactions with other molecules such as oxygen free-radicals which would thereby interfere with and reduce the fluorescence emission further. The fluorescence enhancement effect is larger for fluorophores with low quantum yields.

3.1.7 The 'biological window' and other biological considerations

There are a few considerations to take into account when dealing with fluorescence enhancement in biological tissues[137]. Firstly, when using fluorescence for biosensing applications the 'biological window' or 'water window' describes the range of wavelengths of light amongst which the fluorescence emission wavelength should fall. The range occurs between 700 and 1000 nanometres, in the near infra-red (NIR) range. Biological samples have their own natural fluorescence emission or auto-fluorescence. This gives a background fluorescence 'noise' amongst the fluorescence being detected from the fluorophore. This is illustrated in Figure 8. Using the biological window avoids this background signal and improves the signal-to-noise ratio which in turn maximises the fluorescence enhancement.

Secondly, when light falls on biological samples, some of this is lost as it is absorbed by the tissues. The same occurs to the light emitted by fluorophores which then reduces the intensity of light emitted as a signal. In the NIR range, haemoglobin is the dominant absorber accounting for up to 64% of the total absorbance[137]. If possible highly absorbent species such as haemoglobin should be removed from the sample.

Thirdly, scattering occurs when photons are deflected from the parallel axis of their pathway. The amount of scattering is dependent on the tissue type. There are 2 types of scattering depending on the size of the interacting particles which in tissue depends on the surface quality. Mie scattering refers to light scattering after interactions with particles that are comparable to the wavelength of light, whereas Rayleigh scattering occurs after interactions with particles much smaller or much larger than the wavelength of light. The amount of scatter from different tissues can be described by

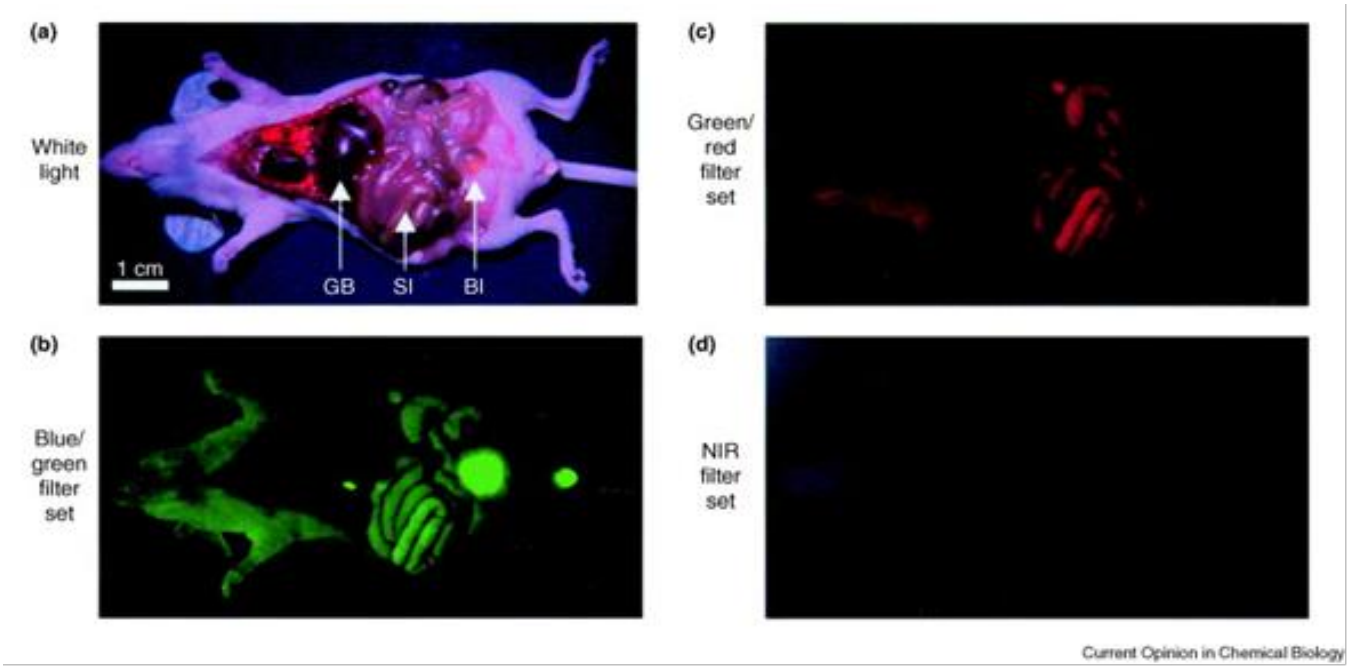


Figure 8: The biological or water window. (a) Shows the organs of a newly sacrificed mouse under white light. SI=small intestine GB=gallbladder BI=bladder (b) shows the same mouse under blue light excitation and green light emission filter set (c) under green light excitation and red emission filter set (d)NIR range of excitation and emission. Excitation and emission within the NIR range shows no background autofluorescence (Taken with permission from ref [137]**).**

the scatter co-efficient which is dependent on its composition and is another source of fluorescent signal loss that must be considered in biological applications.

3.1.8 Which is the best metal to use?

Several factors must be considered when deciding which metal to use to synthesise the metal nanoparticles used for MEF.

Most importantly, the metal that is used determines the resonant wavelength of the nanoparticles for LSPR. Also, the metal must be selected to allow that wavelength to fall within the biological window. Gold, silver and aluminium are ideal for biosensing as they satisfy these criteria. Another factor to consider is the interband transition wavelength. Interband transitions are wavelength channels that act as a mechanism of energy loss within this system. The interband absorption of aluminium falls at a wavelength of light of 827nm. This coincides with the water window and makes this not useful for biosensing compared to gold and silver which have an interband absorption of 506-521nm and 318-321 nm respectively.

Another important material property is the chemical stability. Exposure to air, oxygen and humidity changes the composition of metals and hence the optical properties. Tarnishing of metals can also lead to energy losses. While silver is unstable in air, gold is much more stable maintaining its original composition despite such changes in the environment. The surface chemistry is also well understood to allow binding to other molecules for conjugation[138], [139]. This makes gold the most suitable material for biosensing applications and is the material of choice in this project.

3.1.9 Mie theory and modelling

Modelling allows us to predict the electromagnetic field associated with localised surface plasmons. Mie theory is the easiest approach to do this and estimates that the field is dependent on the dimensions of the nanoparticles, the material and the nanoparticle environment. More complex structures can be modelled using discrete dipole approximation (DDA) and finite-difference time-domain method (FDTD)[118], [140]. These can be used to build computational models to draw the

electric field map and plan the development of nanostructures. Mie theory also allows us to predict the effect of changes in the size and shape of nanoparticles on the electric field pattern and the subsequent effect of fluorescence enhancement.

3.1.10 Effects of changes in nanostructure

Calculations based on both modelling and experimental studies show that increasing the size of metal nanoparticles causes a red shift in peak absorption wavelength as well as broadening of the peak. The strength and size of the induced electric field also gets larger as the nanoparticle size increases[141]. This effect can be demonstrated using nanoparticles in solution (metal colloids) (Figure 9).

Shape also has an interesting effect on the absorption wavelength and surrounding electromagnetic field. Haes et al [141] demonstrate that a change in shape from hemispheres to triangles increases the maximum absorption wavelength. Using modelling, the study shows the effects of more complex changes in shape on the local electromagnetic field (Figure 10). The figures demonstrate that the electric field surrounding the nanoparticles reduces quickly within nanometres of the edge of the nanoparticle. The electromagnetic field concentrates around sharp edges and corners.



Figure 9: Colloid solutions containing gold and silver nanoparticles of varying sizes. The red solution contains the smallest nanospheres at 12 nanometres in size. These absorb blue light of shorter wavelengths and the reflected light is red giving the observed colour. (Taken from nanoComposix.com).

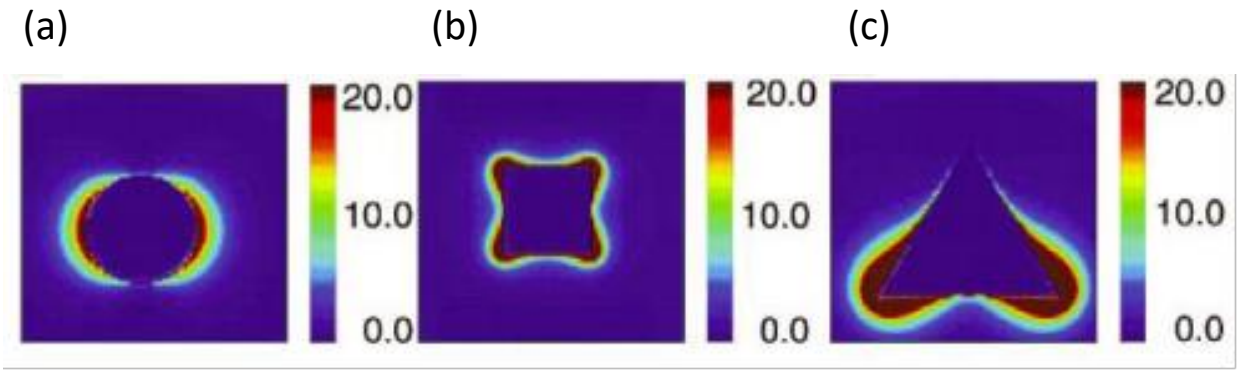


Figure 10: Extinction efficiency of silver nanoparticles with the same volume but of different shapes. The simulated electrical field contour map for corresponding (a) sphere, (b) cube, and (c) pyramid (Taken with permission from ref [141]**).**

3.1.11 Distance dependence of metal enhanced fluorescence

One of the important factors affecting the level of enhancement is the distance between the fluorophore and the metal surface as the localised electric field intensity is dependent on distance. Several studies have examined this concept in detail. For silver nanoparticles the maximum enhancement was observed at a distance of up to 13nm[142]. In addition, the enhancement factor was inversely proportional to (distance)^6. For distances beyond the maximal enhancement, the enhancement factor was inversely proportional to (distance)^3. The distance of maximum enhancement was dependent upon the size of the nanoparticle. In silver island films (SIFs) the distance between adjacent nanoparticles also has an effect on the enhancement factor with the field reaching a maximum intensity at an interparticle distance of 10nm (Figure 1)[19][143]. Similar results have been achieved using aluminium nanostructures[144], [145]. In addition to the near field enhancement, it has also been demonstrated that there is a second enhancement peak at a distance as far as 60-70nm[146]. These observations must be taken into account when designing a biosensor device.

In this section the basic principles of metal enhanced fluorescence have been discussed and aspects that are essential to its biological applications and the development of a biosensor have also been described. In the next section, the practical aspects of fabrication of nanostructures will be covered.

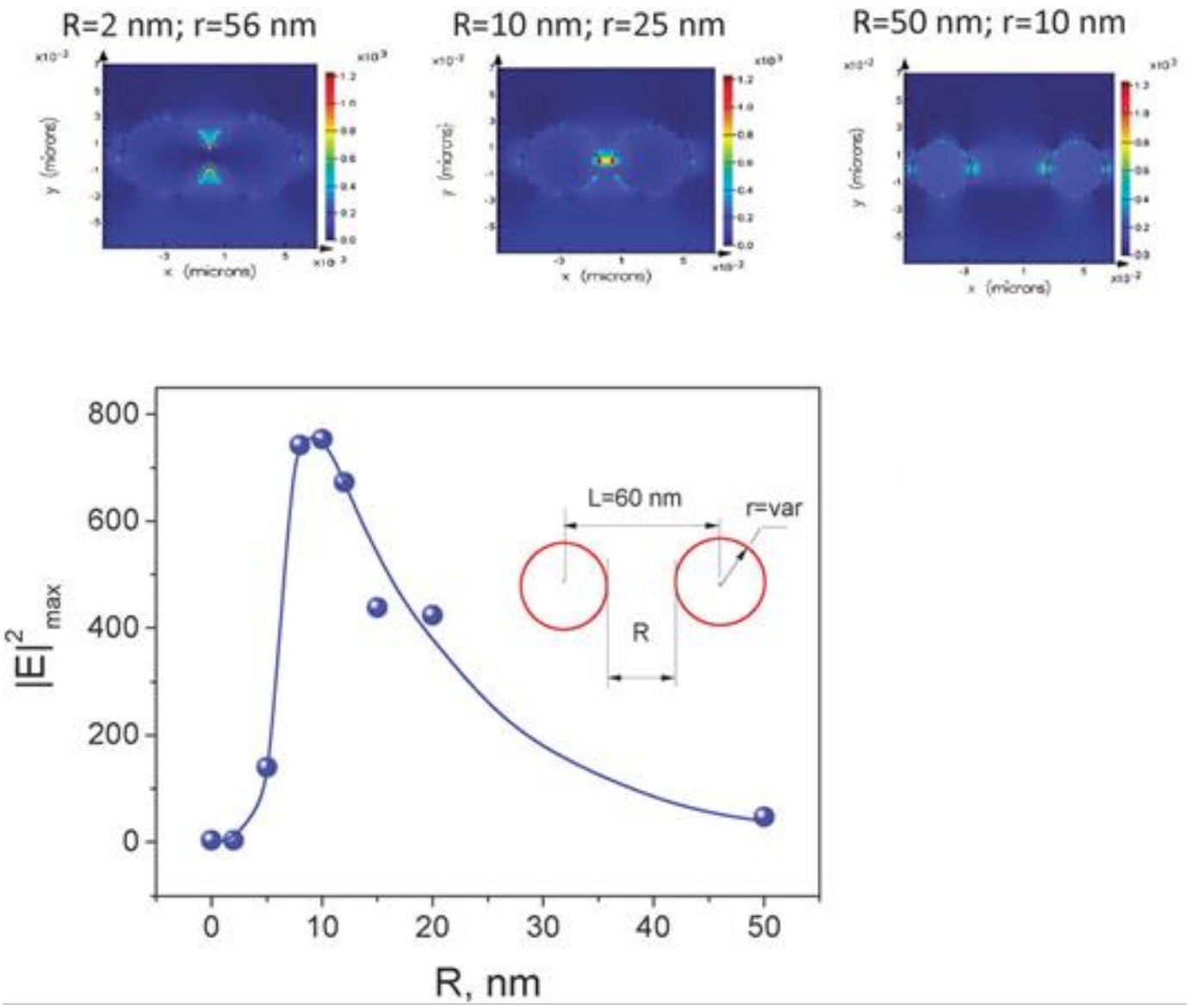


Figure 11: (Top) Distribution of the E-field (calculated by FDTD simulations) around and between silver nanoparticles that approximate the particle growth on glass slides. (Bottom, left) Dependence of E-field intensity maximum between silver particles upon the distance between particles outer surfaces (blue balls). Solid curve is a smooth representation of the change in near-field intensity upon the distance between two particles surfaces. (Inset): Particle geometry parameters used in FDTD calculations. (Taken with permission from ref [143]**).**

3.2 Nanoscale fabrication

Nanotechnology has a wide range of applications. Since this field of science has emerged, there has been a demand to be able to fabricate nanostructures with high precision so that the applications of nanotechnology can be developed to their full potential.

One group of fabrication techniques is known as lithography. Lithography describes the use of a mask template to create a structure on a substrate[147]. Material is deposited through the mask and the template is removed to leave behind the desired structure. One example of lithography-based fabrication used in nanotechnology is electron beam lithography. Electron beam lithography uses an electron beam to alter the solubility of an electron sensitive material through a mask template. The material is immersed in a solvent (developing stage) to create the final structure. While this gives excellent control over the structure details, it is a slow and expensive process. When considering fabrication of nanoparticles for a biosensor, important qualities to consider when choosing a fabrication process are reproducibility and quick and easy production. Nanoscale lithography is a fabrication method that is cheap and efficient and does not require any expensive equipment.

3.2.1 Nanoscale lithography

The technique of nanoscale lithography (NSL) is derived from a process called “Natural lithography” which was first described by Fischer and Zingsheim in 1981[148]. In their paper they describe the use of polystyrene latex nanospheres for contact imaging with visible light. Nanospheres are polystyrene spheres of nanoscale proportions. The nanoparticles produced were triangular shaped, taking the form of the spaces that are in between the nanospheres. In 1982, Deckman et al.[149], used a monolayer of nanospheres as a deposition and etch mask. Van Duyne[150] developed double layer masks and characterised these with atomic force microscopy. NSL has been used to produce basic nanoparticle structures as well as build up more complex structures by combining it with other techniques such as etching.

The NSL technique is an inexpensive method of producing relatively large areas of nanoparticle arrays. In addition, this method also allows the size, shape and inter-particle spacing[94] to be changed. As described previously, the ability to change the nanoparticle structural characteristics is important as this has an effect on the electromagnetic field for fluorescence enhancement.

However, one of the challenges with this technique is in creating the mask template with the nanospheres. Ideally the template should consist of a monolayer of nanospheres to produce the highest quality nanoparticles. Also, the monolayer should have a surface area that is large enough to cover the biosensing platform, usually a glass substrate. SEM characterisation can be used to assess the quality of the nanostructures. With less well-suited techniques, the monolayer is disrupted by defective areas including point defects (vacancies) and line defects (slip dislocations) and unintended areas of bilayer which will affect the quality of the final sample (Figure 12). These problems have been partly overcome using various deposition techniques including spin coating [150]and thermoelectrically cooled angle coating[151]. With current techniques defect-free areas of up to 100 μm^2 have been achieved.

Previous work by Xie et al., 2013[152] demonstrates an alternative reproducible method for forming the nanosphere monolayer template using polystyrene (PS) nanospheres. After formation of the monolayer, deposition of metal of a determined thickness through this and onto the substrate was carried out. Removal of the mask leaves behind triangular shaped nanoparticles or nanotriangles. Nanotriangles are the most basic structures developed using this technique by metal deposition at a 90-degree angle. Other shapes have been produced by altering the angle of deposition including crescent moons[153][154], nanorings and nanorods[155]. In addition, the size of the nanospheres could be altered prior to metal deposition using etching processes which causes changes in the size and inter-particle separation of these nanotriangles[152]. If the nanospheres are reduced significantly in size, the nanotriangles coalesce to form nanoholes[156]. The method of PS nanosphere deposition used by Xie et al [152]is

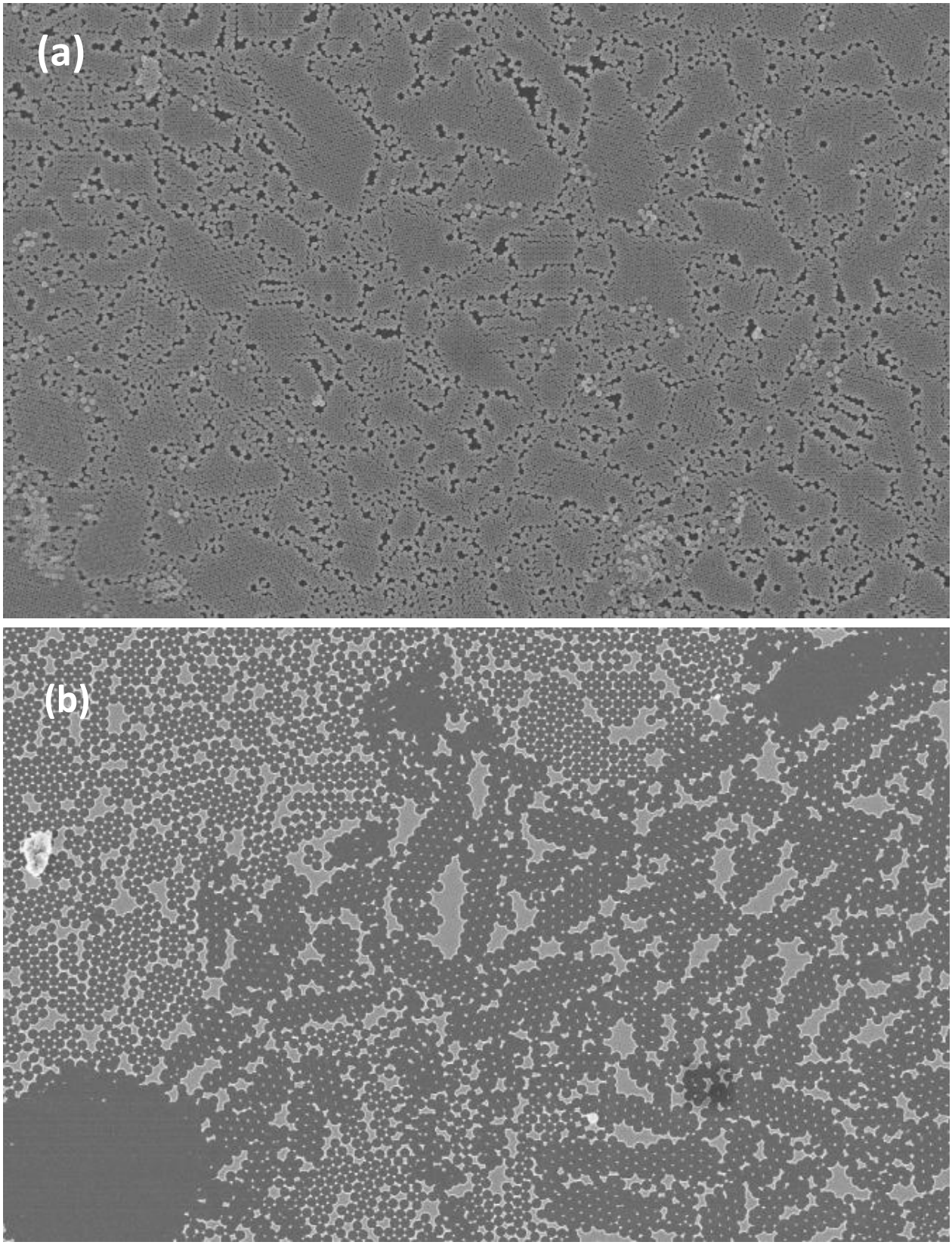


Figure 12: SEM image showing (a) areas of imperfect PS nanosphere monolayer deposition and (b) corresponding nanoparticle arrangements.

referred to as the ‘fishing' technique and is described in detail below. The nanoparticles produced were high throughout, reproducible, stable and cost effective and therefore ideal for bio-sensing substrate fabrication. Using geometric calculations structural data such as particle size and the distance between the perpendicular bisectors of the nanotriangles could be calculated[157].

3.2.1.1 Formation of the monolayer: the fishing technique

The fishing technique is a simple and cheap method of producing the PS nanosphere template for synthesis of nanotriangle arrays on the surface of a substrate[152]. What makes this technique so attractive for biosensing is that the size of the nanotriangles can be altered to change the enhancement factor. This property is known as tunability. One of the advantages of tunability is the ability to produce different enhancements depending on the required sensitivity of the biosensor.

The fishing method is based on an air-water interface transfer method[158], [159]. Using this method, the surface tension of the PS nanospheres on the surface of water creates packed layers which can then be transferred to the substrate. The PS nanospheres are firstly suspended in a 1:1 ethanol solution. Ethanol is used as a solvent as it evaporates quickly. The polystyrene solution is pipette dropped onto a rectangular shaped piece of silicon wafer suspended vertically with its lower edge submerged in a bath of nanopure water. As the PS nanosphere solution drops down the silicon wafer, the ethanol evaporates and leaves a monolayer of dried PS nanospheres on the surface. The silicon wafer is treated with UV ozone prior to use to make the surface hydrophilic and encourage spreading of the PS nanosphere solution so that it forms a homogenous monolayer on the surface of the silicon wafer. Bathing the lower edge of the silicon wafer in water during the drying process allows the surface tension to draw the ethanol solution downwards and spread the polystyrene on the surface of the silicon wafer. This aids distribution of the PS nanospheres and avoids clumping into bilayers or heavier deposits. Once the silicon wafer has dried and all the ethanol has evaporated, the dry PS nanosphere monolayer is carefully transferred to the surface of a second bath of nanopure water. The PS nanospheres float on the surface. Surfactant solution is added to reduce the surface tension and

compress the PS nanospheres. This helps to reduce any slip dislocations and vacancies. It also encourages precipitation of bilayer and aggregates of nanospheres leaving behind a better quality monolayer on the surface. Clean glass substrates are then used to "fish" areas of monolayer from the surface of the bath and these are left to air dry. Prior to using the glass substrate for the fishing process, these are treated with UV ozone to remove surface hydrocarbons and make the surface hydrophilic. This aids transfer of the PS nanospheres to the surface of the glass by reducing repelling forces which may cause damage to the monolayer. At the end of this process hexagonally packed nanospheres are assembled onto the substrate and are ready for metal deposition through the interstices of the mask.

Prior to metal deposition, the inter-particle spacing and size of individual nanotriangles can be altered by changing the size of the PS nanospheres. The tunability offered using this technique allows modifications to be made in the nanoparticle structure to change the fluorescence enhancement factor. Reactive ion etching (RIE) has been used previously to alter the diameter of the PS nanospheres.

3.2.1.2 Control of nanoparticle size: Reactive Ion Etching

Reactive ion etching (RIE) is a process whereby accelerated ion particles are used to etch the surface of a specimen within a vacuum chamber. The ion beam is generated from inert gas atoms and acceleration is provided by a strong electrical field. Oxygen is the most commonly used inert gas. The etching is a result of chemical and mechanical forces. Chemical etching occurs due to chemical reactions taking place between the material and the ion particles. Physical etching is due to the physical bombardment of the material by the ions. The effect of RIE on the PS nanosphere monolayer is to reduce the size of the PS nanospheres while maintaining their position[104]. This increases the space between the nanospheres, which in turn increases the size of the nanotriangles after metal deposition. It also has the secondary effect of creating bridges between the PS nanospheres which

cross links them[105]. In the mask template this maintains the separation of the nanoparticles and is necessary to avoid the production of large gold islands which do not produce a plasmonic effect.

The ability to modify the nanoparticle size in this way allows one to tune the size of the nanotriangles to alter the metal enhancement effect[160]. This is an important property for biosensing as the nanoparticles can be tailored for use within the biological window and match a particular fluorophore.

3.2.1.3 Metal deposition: Mantis e-beam evaporation

This method of metal deposition works by evaporation of the metal within a vacuum chamber which is then deposited directly onto the surface of a substrate with very precise thickness control provided by a quartz crystal microbalance (QCM) device. An electron beam is focused on the metal source (usually pure metal pellets held in a crucible) to increase its temperature and promote its evaporation. This method of metal deposition has advantages over other techniques such a sputtering. Sputtering is a technique whereby metal is released from the source by bombardment processes before being deposited onto the target substrate. While this gives good coverage, there is less control over the uniformity of the deposition. This may affect the nanostructures and their resultant enhancement properties. Therefore, e-beam evaporation is a much more suitable method than sputtering for nanoparticle fabrication.

3.2.1.4 Polystyrene removal

Once the metal is deposited, removal of the mask template needs to be carried out effectively to reduce interference of residual polystyrene with the fluorescence enhancement. Various removal techniques have been reported including burning at high temperatures or using organic solvents[161]. Tape stripping removal has also been described[162]–[164]. With this technique adhesive tape is applied to the surface of the substrate holding the PS nanospheres. The tape is removed to lift off the PS nanosphere layer and leaving behind the metal nanotriangles.

While the metal nanotriangles have been successfully used to demonstrate the enhancement of adjacent fluorophores they have not been used for biosensing. Xie et al., have demonstrated

enhancements of 100 fold in the detection of model protein bovine albumin when compared to glass slide controls[152]. Other nanostructures have been applied to biosensing to detect biomarkers including proteins and microRNA. In the next section the use of nanostructures for detecting biomarkers for pancreatic cancer will be described.

3.3 Nanotechnology based biosensors for pancreatic cancer

Different nanostructures have been reported to be useful for pancreatic cancer diagnosis including carbon nanotubes, mesoporous silica nanoparticles, quantum dots and gold nanoparticles[67].

3.3.1 Carbon nanotubes

Carbon nanotubes (CNTs) are comprised of graphene sheet cylinders made of single or multiple walls, known as single-walled carbon nanotubes (SWNTs) and multi-walled carbon nanotubes (MWNTs) respectively. Typical sizes are in the 1-100 nanometre range. They have been used to develop electrochemical immunosensors for the detection of CA 19-9 in the diagnosis of pancreatic cancer[165]. The surface of electrochemical biosensors is functionalised with biomarker binding sites. Electrochemical sensors detect changes in biomarker levels due to a change in the conduction of an electrically conductive surface. Electrochemical sensors that are fabricated using nanoparticles can produce more sensitive changes in their conductivity. The sensor can therefore achieve better sensitivity and can reach lower limits of detection for the biomarkers that they are designed to detect. CNTs in particular are advantageous for use as the electron conductive surface in electrochemical sensors as they have an excellent electron transfer rate and therefore high electrical conductivity. Therefore, they are more sensitive to changes in their conductivity. They also possess high surface areas suitable for binding multiple biomarkers[166]. Furthermore the electrical conductivity may be enhanced by electrodeposition of noble metals to the surface of the CNTs[167]. In the study by Zhuo et al., 2010[113], a sandwich ELISA assay is used to bind CA 19-9 to the surface of CNTs and the change in current response is measured before and after the assay. Due to preparation of the secondary antibodies with insulating SiO_2 nanoparticles the peak current is inversely proportional to the amount

of CA 19-9 in the assay. Hence the impedance (1/conductance) was shown to have a linear relationship with the concentration CA 19-9 between concentrations of CA 19-9 between 0.15 U mL^{-1} and 150 U mL^{-1}. The detection limit was 0.06 U mL^{-1}. The accuracy of the electrochemical sensor was compared with a standard ELISA using clinical samples giving a relative error of less than 3.59%.

3.3.2 Other electrochemical sensors

Other electrochemical sensors have been developed to detect glycans which are glycosylated proteins or oligosaccharide chains attached to proteins. Aberrant glycosylation during cancer progression has been linked to early tumour proliferation and invasion amongst other carcinogenic processes[168]. The impedance to conductivity induced by bound glycans across a nanoporous alumina membrane [169] is used in the Nanomonitor device. The device was able to detect differences in the level of glycans present in normal cells as compared to cancerous human pancreatic cancer cells.

Gold nanoparticles with a yolk-shell configuration have been used to detect CA 19-9[170]. These nanoparticles show high electrocatalytic activity towards hydrogen peroxide reduction to amplify electrochemical signals. Electrocatalysts promote the reaction of substances without getting consumed and produce electrical energy as a by-product. The sensors showed low detection limits and were also transferable to clinical samples.

3.3.3 Quantum dots

Quantum dots (QDs) are nanoparticles with fluorescent properties. In contrast to conventional fluorophores the wavelength of light emission is dependent on the size of the quantum dot and they are excited by a broad wavelength of light. An immunosensor based on a sandwich assay for CA 19-9 has been developed using ZnO quantum dots on a silicon wafer substrate[171]. Antibody to CA 19-9 was conjugated to the QDs and used as capture antibodies. Increasing fluorescence intensity was observed with increasing concentrations of the CA 19-9. The detection limit was 0.25UmL^{-1}.

3.3.4 LSPR-based sensors for microRNA

Biosensors for microRNAs specific to pancreatic cancer are also being developed. If changes in the levels of these miRNAs could be detected, they may be used to profile levels in individuals to give diagnostic and prognostic information about their disease. This could be used for early detection and could also give information to guide treatment for personalised medicine. A biosensor for the detection of microRNA in pancreatic cancer patients has recently been developed[172]. Nanoprisms are fabricated on a substrate and the absorption wavelength at UV-Vis spectroscopy is measured before and after attachment of microRNA. The change in the wavelength is used to detect changes in concentration of the microRNA. This test was successfully used to detect microRNA-21 and -10b and was successfully validated in the plasma from patients with pancreatic cancer.

3.3.5 Metal-enhanced fluorescence-based sensors

While different nanotechnologies are being explored to develop a biosensor, there are no studies to date using MEF to detect biomarkers for pancreatic cancer. Dai's group have published the results of a gold nanoparticle based sensor that detects low levels of carcinoembryonic antigen, CEA[20]. While CEA is not specific for pancreatic cancer it may become elevated in patients with the disease. In clinical practice it may be used in combination with CA 19-9. Fluorescence enhancement of three orders of magnitude was demonstrated taking the limit of detection from the picomolar range ($x10^{-12}$ M) to the femtomolar range ($x10^{-15}$ M) when compared to a standard immunoassay. However, a major disadvantage of the nanoparticles used is that they have a heterogeneous structure. Ideally the nanoparticles should be uniform so that there are minimal confounding effects in the assay and the results are reproducible and reliable.

3.4 Properties of a biosensor platform for pancreatic cancer

While there has been progress with developing highly sensitive biosensors using nanotechnology, several issues still remain. One of the challenges of creating a LSPR bio-sensing device is being able to apply it for the use of detecting clinical biomarkers. Several criteria are required to achieve this[173].

(i) Firstly, the substrate needs to be robust to withstand the applications of biological solutions with strong adhesion of nanoparticles to the substrate,

(ii) They must also be stable in storage without deterioration of function or quality,

(iii) The sensitivity of the sensor must be significantly higher than current methods and ideally be suitable to detect biomarkers at very low concentrations.

In addition to these, a quantitative method and one that allows label free detection whereby the antigen does not need modification by labelling is an attractive attribute of nanotechnology-based biosensors. The use of a fluorescent immunoassay is a suitable method that has been used for protein detection using several nanostructures. The essential components of an immunoassay will be described in the next section.

3.5 Immunoassays

Immunoassays are used to identify and quantify a biomarker of interest. In this technique, a labelled probe is attached to the biomarker and washed to remove the unbound probe. The amount of labelled probe is then measured to quantify the amount that remains attached as a measure of the biomarker present. This simple assay forms the basis of everyday tests, such as pregnancy tests and blood tests and forms the foundations for scientific discoveries including drugs and proteomics. Less than 60 years ago, this method was first used to quantify the amount of insulin in serum[174] and subsequently for the measurement of thyroxine[175]. Since then, the technique has developed greatly and is now used for more complex applications, for example to study protein-protein interactions, to identify drug candidates and for the detection of disease markers in the diagnosis and treatment of disease.

3.5.1 Immunoassay structure

The minimum requirement for an immunoassay is the analyte (antigen) and the detection probe used for quantification. The probe should be sensitive and specific to the antigen but if it is too adherent then it will give an unreliably high background signal. This depends on the nature of the probe and the

washing and blocking technique used. Traditional immunoassays use antibodies for the detection of protein antigens. To facilitate the washing technique, the antigen is immobilised on a solid support. The first immunoassays measured the turbidity of the resulting solution using electrophoresis or light scattering techniques as a measure of the antigen concentration. Modern immunoassays rely on the intensity of fluorescent probes or electrical measurements rather than properties of the assay matrix itself. In a sandwich immunoassay, the capture antibody on the substrate and first level detection antibody are both directed towards the biomarker antigen. They should all come from different species to avoid cross-reaction as much as possible. In particular, this will prevent cross reactivity of the secondary antibody which is key in detection as it is conjugated to the fluorophore. If the capture antibody and primary antibody are both of the same species, this will increase non-specific binding sites and prevent the differentiation of CA 19-9 bound capture antibody from one that is not bound to antigen.

3.5.2 Antigens

An antigen or 'antibody generator' is a molecule against which antibodies are generated. The antigen can be any protein or small molecule (hapten), carbohydrate or nucleic acid. Depending on their size, antigens present one or more epitopes to the antigen recognition site of the antibody. Antibodies can also be raised to detect other antibodies and may therefore also function as antigens.

3.5.3 Antibodies

Antibodies are proteins belonging to the immunoglobin (Ig) class of which there are five subtypes: Immunoglobulin A (IgA), IgD, IgE, IgG and IgM. Immunoglobulin G is the most common subtype found in human serum and constitutes 75% of the total amount. It is also the most common subtype used in immunoassays. Each IgG molecule contains antigen binding sites, F_{ab}. These antigen binding sites contain three different amino acid sequences called compliment determining regions (CDRs) which bind to epitopes on the antigen.

Antibodies can be produced by delivering an antigen to an organism, to induce an immune response, and then retrieving the antibodies specific to that antigen. Antibodies produced in this way are called polyclonal as they have many different epitopes with a range of sensitivities towards the antigen. Monoclonal antibodies have the same epitope, and therefore the same affinity for the antigen. They are produced from a hybrid cell made up of a B-cell (the antibody producing cells of the immune system) and murine myeloma cells which acts to stop gene rearrangement in the B-cells.

3.5.4 Antigen-antibody interactions

Antigen-antibody interactions are important in determining the sensitivity and specificity of the substrate. While an antibody is said to be specific to a certain antigen, this only describes the antigen to which the antibody has the highest affinity[176]. Equation 7 describes the dynamics of the interactions between the antibody, A, antigen, B and antibody-antigen complex, C.

$$A+B \Leftrightarrow C \qquad \textbf{(7)}$$

The interactions between the antibody and antigen are dependent on non-covalent interactions, ionic bonds, hydrogen bonds, van der Waal's forces and hydrophobic interactions. When they bind there is a rapid shift of the equation to the right until the equilibrium is reached. The affinity of the antibody for the antigen is described by the association equilibrium constant which is calculated as the ratio of complex to disassociated antigen and antibody (Equation 8).

$$\frac{[C]}{[A][B]} = K_a \qquad \textbf{(8)}$$

In the context of immunofluorescence, the antibody is saturated at the point of equilibrium and the affinity constant describes the specificity of the antibody. This helps to determine the minimum required antibody concentration for binding. However, as the concentration of antibody increases

there is a greater chance of non-specific interactions with molecules other than the intended antigen. This is because the degree of saturation depends on the affinity and concentration of the antibody so that at high enough concentrations, low-affinity interactions will also occur. Blocking is therefore an essential step during the functionalization. Concentrations of antibody must also be titrated to achieve optimal specificity.

3.5.5 Blocking and non-specific binding

Non-specific binding (NSB) refers to the binding together of components of the immunoassay to each other, which artificially increases the signal of the assay independently of the amount of antigen. This is a result of non-specific interactions such as Van da Waals interactions, hydrophobic forces and electrostatic forces. NSB increases the background signal and therefore the noise-to-signal ratio. The noise-to-signal ratio should be minimised as much as possible to increase the sensitivity of the assay. Variables in the immunoassay affecting the background noise can be controlled such as the concentrations of antibody and the incubation times used. In addition, it is reduced by using a blocking step after applying the capture antibody. The blocking reagent can vary depending on other components in the system. Importantly it must not contain any proteins that the secondary antibody may react with as this will also increase the background fluorescence. Blockers are divided into proteins and detergents. Detergents may be ionic or non-ionic. 1% BSA is commonly used protein blocker as it is effective and widely available. Alternatively, 5-10% solution of serum of the host in which the secondary antibody was produced can also be used. For example, for goat anti–mouse IgG secondary antibodies, 10% goat serum can be used. The IgG in the serum adheres to and blocks NSB sites and prevents the attachment of the labelled secondary antibody. This forces the primary antibody to out-compete the blocking protein for binding. The goat antibodies used in the assay will not cross-react with proteins in the serum used making it a good blocking agent. After the blocking step, washing is crucial to prevent over blocking that will prevent attachment of the required antibody for detection.

3.5.6 Immunoassay support

The immunoassay is usually carried out on a solid support so that it can be handled as a solid rather than solution which makes carrying out the steps of the assay easier and more reliable. The surface of the support is modified for conjugation of the capture probe. The capture ligand is then applied, followed by the antigen of interest. Finally, the detection probe is added, and the sample is measured. The support may also consist of polymer beads, μm in diameter. The beads are suspended in solution and they are then retrieved with gravity or centrifugation. Beads that are magnetic may also be used and these are collected by applying a magnetic field. Large supports such as glass slides and 96-well plates can also be used. The latter are used for microarray technology to detect multiple antigens at the same time.

3.5.7 Fluorescent linked immunosorbent assay (FLISA)

Immunoassays based on the detection of the concentration of a fluorophore detection probe are called fluorescent linked immunosorbent assays (FLISA). These are similar to the well-established ELISA protocol but use a fluorophore probe for detection of the concentration of antigen. The assay may take several forms as shown in Figure 13. Each form has its advantages and disadvantages (Table 2). Ideally the capture antibody should be polyclonal such that it contains antibodies that bind many different epitopes on the antigen to increase the assay sensitivity. This method has been successful for the detection of tumour markers using MEF [121, 123]. The method of conjugation of the immunoassay to the substrate is important and described in the next section.

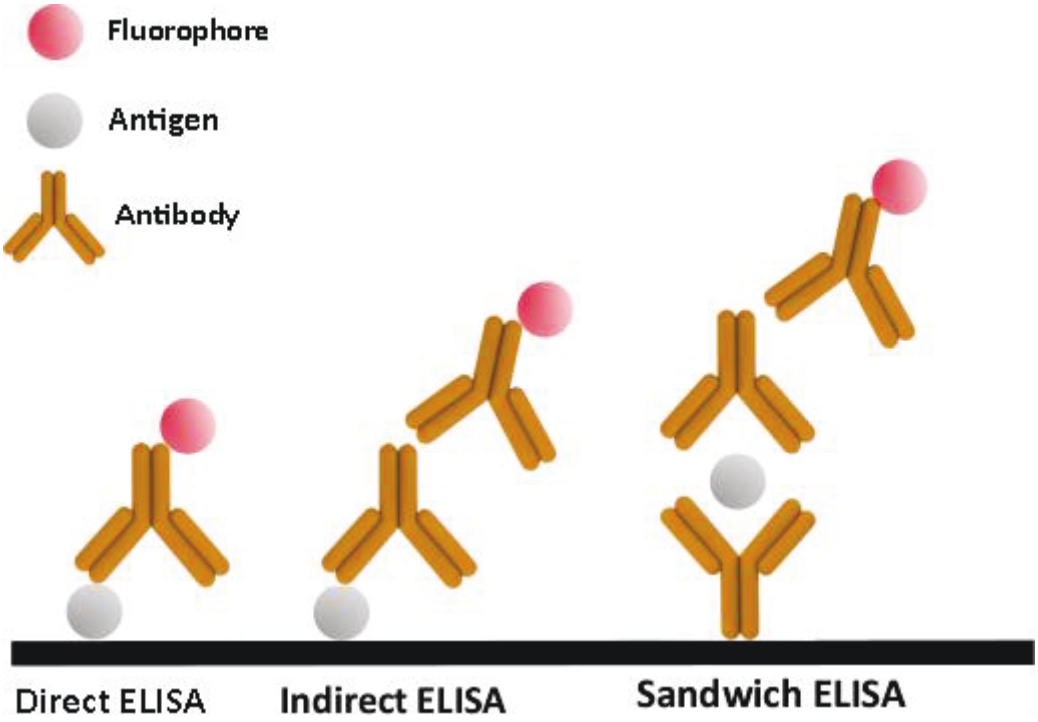


Figure 13: Methods of antibody mediated detection.

Table 2: Advantages and disadvantages of different immunoassay structures

Assay type	Advantages	Disadvantages
Direct ELISA	Fewest conjugation steps Short substrate-fluorophore distance	Lack of capture antibody reduces sensitivity Requires fluorophore conjugation of antigen specific antibody
Indirect ELISA	Fluorophore conjugated secondary antibody widely available	Lack of capture antibody reduces sensitivity
Sandwich ELISA	Capture antibody increases assay sensitivity Fluorophore conjugated secondary antibody widely available	Several conjugation steps-takes longer and more risk of error

3.6 Bioconjugation techniques

Bioconjugation refers to the process of binding two molecules together usually with a covalent bond. One or both molecules are biological or derived from a biomolecule[177]. There are many bioconjugates available and the choice depends on the application. Some examples include the conjugation of drugs to antibodies for targeted therapy or a molecular probe attached to a fluorescent label. Constructing useful biomolecules requires knowledge of coupling chemistry that is used to determine the reactive groups required for certain attachments. Furthermore, the efficiency of the bioconjugation technique will have a significant impact on the fluorescence enhancement efficiency of the substrate. There are a many different molecules used in bioconjugation and the ones relevant to this project will be described in the next section.

3.6.1 PEGylation and chemical coupling

For protein conjugation, polyethylene glycol (PEG) is widely used. PEG is a polymer of ethylene glycol (Figure 14). The number of ethylene glycol units can be changed to alter the molar mass and length of the polymer. Knowledge of coupling chemistries is used to determine suitable end functionalization groups for the PEG[178]. For attachment to gold a thiol group (-SH) is used at one end of the PEG. For protein attachment including antibodies, amine groups in proteins react with hydroxyl-, carboxyl- or aldehyde- functionalised PEG.

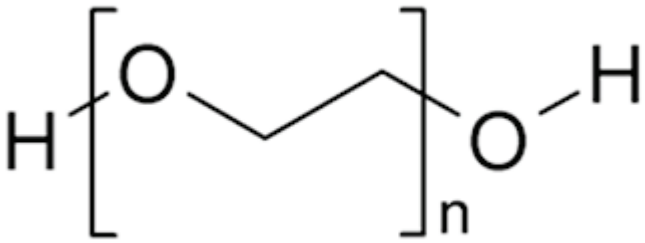


Figure 14: Polyethylene glycol functionalised with end hydroxy groups.

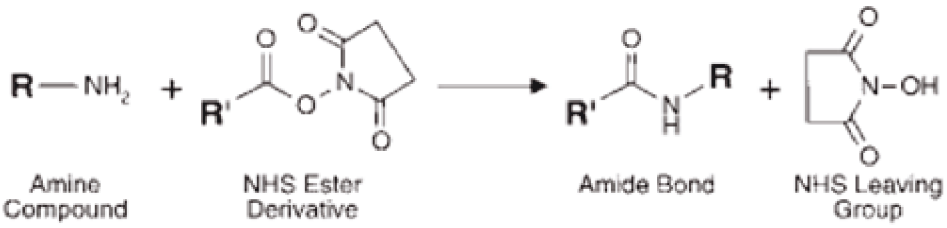


Figure 15: Reaction of amine group with NHS ester to form acylated product

Amide reactions are one of the most commonly used for bioconjugation. Amide groups react with most proteins as well as other macromolecules. The amide groups are firstly modified by either acylation or alkylation. The reactions are rapid and high yield to give rise to stable amide bonds. NHS ester is formed by reaction of NHS with a carboxylate in the presence of a carbodiimide. Carbodiimides are used to mediate the formation of bonds between carboxylates and amine groups. The most commonly used is 1-ethyl-3-(3-dimthylaminopropyl) carbodiimide hydrochloride (EDC). This is also known as a zero-length crosslinker as they form a bond without adding additional atoms. NHS-ester reagents react with nucleophiles (electron donors in a chemical reaction) with release of the NHS leaving group to form an acylated product Figure 14.

3.6.2 Conjugation to glass

(3-Aminopropyl)triethoxysilane (APTES) is a functional silane compound that can be used for conjugation of biomolecules to an inorganic substrate. Once deposited on a substrate, amine groups are available on the surface for further conjugation. For example, carboxyl groups may then be conjugated using a carbodiimide reaction.

3.6.3 Selection of gold nanotriangular arrays

Results from a previous study were used to select the size of PS nanospheres used in the synthesis of the nanotriangular arrays [152]. In this study, modelling was used to predict the correct size of PS nanospheres to produce nanotriangles with absorption wavelength within the biological window. This was then verified experimentally. The ideal diameter of PS nanosphere was 300 nm, with etching times between 0 and 12 seconds. Therefore, in this thesis, nanotriangle arrays were synthesised from PS nanospheres between 280 nm and 500 nm with etching times between 0 and 15 seconds.

3.7 Summary

In summary, nanotechnology biosensors for the detection of pancreatic cancer biomarkers are in the early stages of development. Current sensors use heterogeneous structures and while these may not be ideal for biosensing, the improvement in the detection limits suggest that MEF is a promising strategy that requires exploration. The metal nanotriangular arrays produced by NSL would make ideal platforms for biosensing as the synthesis is highly controlled. This project will focus mainly on the use of such highly ordered arrays to synthesise biosensing platforms for pancreatic cancer. The specific aims of this project are described in the next section.

CHAPTER 4: METHODS

4.1 Materials

Glass microscope slides were obtained from VWR International, USA and sonicated in acetone, 2-propranol and nanopure water before use. Nanopure water (>18.2 MΩ), purified using the Millipore Milli-Q gradient system, was used in all the experiments. Polystyrene (PS) nanospheres with diameters of 280, 400, 500 and 800 nm (10 wt. %) were obtained from Bangs Laboratories Inc., USA. Cysteamine, (3-Aminopropyl)triethoxysilane (APTES), (3-Glycidyloxypropyl)trimethoxysilane (GPTS), 4arm-polyethylene glycol-carboxyl (Mn ~10,000), dimethylformamide (DMF), 1-ethyl-3-[3-(dimethylamino)propyl]-carbodiimide hydrochloride (EDC), N-Hydroxysuccinimide (NHS), 2% sodium dodecyl sulfate, donkey serum, Dylight800^{TM} conjugated polyclonal donkey anti-rabbit antibody and phosphate buffered saline (PBS, pH 7.4) were purchased from Sigma-Aldrich, UK. In addition, for the synthesis of the nanostars, gold chloride trihydrate (HAuCl4·3H2O), sodium citrate tribasic dehydrate, silver nitrate (AgNO3), L-ascorbic acid (AA), hydrogen peroxide solution (H2O2; 30 wt. %), (3-mercaptopropyl) trimethoxysilane (MPTMS; 95%) and biotinylated bovine serum albumin (bBSA) were also purchased from Sigma-Aldrich, UK. For the CA 19-9 assays, purified carbohydrate antigen (CA 19-9) and monoclonal mouse anti-CA 19-9 antibody were purchased from Biospacific, USA. Polyclonal rabbit anti-CA 19-9 antibody was purchased from Lifespan Biosciences, UK. For the GPC-1 assays, monoclonal mouse anti-GPC-1 antibody and polyclonal rabbit anti-GPC-1 antibody were purchased from Lifespan Biosciences, UK. For the microRNA assays, oligonucleotide probes were purchased from Eurofins Genomics, Germany.

4.2 Synthesis and characterization of gold nanotriangular arrays

Monodisperse PS nanospheres with diameters of 280, 400 or 500 nm were diluted with ethanol in a 1:1 ratio. A clean silicon wafer (~ 30 mm × 20 mm) which had been treated with UV ozone was held at a 90-degree angle suspended in a clamp above a bath of water and about 3-5 µL of the above PS nanosphere solutions in ethanol were placed onto the surface of the wafer. With the aid of gravity and surface tension, the PS nanosphere solution migrates down the silicon wafer. As it migrates, ethanol, which is highly volatile, evaporates to leave a monolayer of PS nanospheres. Once the ethanol had evaporated completely, the wafer was subsequently submerged slowly at a 90-degree angle in a 15 cm plastic container filled with 150 mL of nanopure water, causing the PS nanospheres to form a disordered monolayer on the water surface. Incubation overnight and the addition of 4 µL of 2% sodium dodecyl sulfate reduces the surface tension of the water and allows a monolayer with highly ordered areas to be obtained. The PS monolayers were collected from the water surface by hand using UV ozone treated clean glass substrates (10 x 13mm). The glass substrates were left to dry out completely at room temperature. Following formation of the PS nanosphere templates, a Mantis e-beam evaporation system fitted with a deposition monitor quartz crystal microbalance (QCM) was used for the application of a layer of gold with the required thickness. The purpose of the QCM is to measure the thickness of the gold deposition layer allowing highly controlled deposition of a gold metal layer with a thickness of choice. Once the gold had been evaporated on the PS nanosphere template, the PS nanosphere template was removed using a tape stripping removal method. This left behind the gold that had been deposited in the interstices of the PS nanospheres, forming the gold nanotriangular arrays.

The gold nanotriangular arrays were imaged by scanning electron microscopy (SEM) using a LEO Gemini 1525 field emission gun (FEG) SEM (Carl Zeiss Microscopy GmbH, UK). The SEM was operated in secondary electron mode at an accelerating voltage of 5 kV, using the In-Lens detector. The distances were measured using Image J software (National Institutes of Health, 2017). The optical

properties of the gold nanotriangular arrays were measured at room temperature using an Agilent Cary 5000 UV-Vis-NIR spectrophotometer.

4.3 Synthesis and characterization of gold capped polystyrene sphere arrays

To synthesis the gold capped polystyrene arrays; the fishing method described above was used to produce glass substrates lined with a monolayer of PS nanospheres of 280nm. The PS monolayer was treated with UV ozone with etching times of between 0 and 15 seconds and the Mantice e-beam evaporation system was used for the deposition of a gold layer, with a thickness of 60nm.

The gold capped polystyrene arrays were imaged by scanning electron microscopy (SEM) using a LEO Gemini 1525 field emission gun (FEG) SEM (Carl Zeiss Microscopy GmbH, UK). The SEM was operated in secondary electron mode at an accelerating voltage of 5 kV, using the In-Lens detector. The distances were measured using Image J software (National Institutes of Health, 2017). The optical properties of the gold capped polystyrene arrays were measured at room temperature using an Agilent Cary 5000 UV-Vis-NIR spectrophotometer.

4.4 Synthesis and characterization of gold nanostars

Gold nanostars were synthesised by Ioannis Theodorou. Gold nanostars (GNS) of two different sizes, referred to as small (S-GNS) and large (L-GNS) gold nanostars, were synthesized using a seed mediated two-step protocol. Firstly, spherical citrate-stabilized gold nanoparticle (GNP) seeds, with average sizes of 15 nm (GNP_{15}) and 50 nm (GNP_{50}), were prepared by heating 100 mL of a 0.25 mM aqueous $HAuCl_4 \cdot 3H_2O$ solution while stirring. Once the solution reached boiling point, 1 (GNP_{15}) or 0.25 (GNP_{50}) mL of 3.3% (w/v) aqueous sodium citrate solution was rapidly added while stirring vigorously. After 1-3 minutes the solution started to become coloured and the heating was continued until the solution was a stable bright red colour (within 10 min). The solution was cooled in an ice bath and the volume was made up to 100 mL with Milli-Q water and then stored at 4 ^{o}C.

For S-GNS synthesis, 200 µL of GNP_{15} were added to 10 mL of 0.1 mM $HAuCl_4 \cdot 3H_2O$ with 10 µL of 1 M HCl in a 30 mL glass vial at room temperature, under moderate stirring. In the case of L-GNS, 300 µL of GNP_{50} were added to 10 mL of 0.3 mM $HAuCl_4 \cdot 3H_2O$, containing 10 µL of 1 M HCl. Then, 150 µL of 2 mM $AgNO_3$ and 50 µL of 100 mM AA were quickly added for both types of nanostars. The colour of the solution rapidly changed from faint red to blue-green, and stirring was stopped after 30 s.

GNP and GNS were characterized by optical absorption spectroscopy, using an Agilent Cary 5000 UV-Vis-NIR spectrophotometer; and transmission electron microscopy (TEM), using a JEOL JEM-2100F with an accelerating voltage of 200 kV. Size distributions were measured using several TEM images and processed using ImageJ software (National Institutes of Health, 2017).

4.5 Preparation of MPTMS glass slides for synthesis of gold nanostar monolayers on glass

Prior to 3-mercaptopropyltrimethoxysilane (MPTMS) grafting, glass microscopes slides were cut to 10 mm × 12 mm pieces and cleaned by ultrasonication in acetone, Milli-Q water and 2-propanol for 10 minutes each. The slides were dried using compressed air and treated with piranha solution (3:1 v/v H_2SO_4 96%:H_2O_2 30%) for 30 minutes. Then they were washed 3 times by ultrasonication in Milli-Q water for 3 minutes each. The washed slides were dried in an oven at 140 °C for 1 hour and allowed to cool to room temperature. Inside a glass container that had undergone the same cleaning procedure the slides were immersed in a 5% v/v solution of MPTMS in ethanol, sealed and allowed to react for 4 h in a water bath at 40 °C. Silanization of glass surfaces is thought to take place through reaction of surface silanols with the Si-OH groups of MPTMS, leading to formation of Si(surface)-O-Si bridges. The remaining Si-OH groups of MPTMS are positioned in such a way that Si-O-Si bridges can be formed between similar nearby fragments. After 4 hours the MPTMS solution was discarded and the slides were washed 3 times by ultrasonication in ethanol for 3 minutes each. Finally, the slides were dried using compressed air and cured in an oven at 100 ^{o}C for 15 min.

4.6 Formation of GNS self-assembled monolayers on MPTMS glass slides

To form GNS self-assembled monolayers (SAMs), the MPTMS-modified glass slides were placed in glass containers, which had been cleaned with piranha solution as described in the previous section and immersed in solutions of freshly synthesized GNS. The containers were sealed and placed on an orbital shaker (100 rpm) in the dark for 18 hours. The GNS-coated glass slides were rinsed with Milli-Q water 3 times and gently dried using compressed air. They were stored under vacuum and used within 1 week of their fabrication with no changes observed in their optical absorption spectra during this period.

The morphology of the substrates was examined by field emission gun (FEG) scanning electron microscopy (SEM) using a LEO Gemini 1525 (Carl Zeiss Microscopy GmbH, UK). The SEM was operated in secondary electron mode at an accelerating voltage of 5 kV, using the In-Lens detector. The optical properties were measured at room temperature using an Agilent Cary 5000 UV-Vis-NIR spectrophotometer.

4.7 Comparing cysteamine and APTES conjugation methods

To compare the fluorescence intensity after conjugation with APTES, cysteamine and a combination of cysteamine and APTES, the nanotriangular arrays were incubated in either 2% (v/v) solution of APTES in acetone in a water bath at 60°C for 2 hours or incubated in 10mM cysteamine in ethanol overnight and rinsed with ethanol. For the combination, the same protocol for cysteamine was used and followed by that for APTES. After rinsing with ethanol, the amine functionalized substrate was immersed in a solution of 20uM 4-arm poly(ethylene glycol)-carboxylate (Mn~10,000 Da) and 20mM each of 1-ethyl-3-(3-dimethylaminopropyl) carbodiimide and N-hydroxysuccinimide (NHS) in dimethylformamide (DMF) for 2 hours at room temperature. After rinsing again with ethanol, the substrates were incubated with 3 $x10^{-8}$M Dylight800 conjugated IgG for 10 mins followed by washing three times in PBST and once in PBS then the substrates were immersed in nanopure water and dried with compressed air.

4.8 Surface modification of gold nanotriangular arrays

To prepare protein microarrays on the gold nanotriangular films, the array surfaces were first modified with branched poly(ethylene glycol)-carboxylate (PEG-carboxylate), through covalent conjugation to an amine self-assembled monolayer. This amine monolayer was formed by serially incubating the gold nanostructured arrays with cysteamine and (3-Aminopropyl)triethoxysilane (APTES), to ensure coverage of both glass and gold surfaces. The method for this is as follows: the substrates were first treated with UV ozone and then incubated in 10mM cysteamine in ethanol overnight at room temperature. After rinsing with ethanol and drying with compressed air, the substrates were then incubated in a 2% (v/v) solution of APTES in acetone in a water bath at 60°C for 2 hours. After rinsing again in ethanol and drying, the amine-functionalised substrate was immersed in a solution of 20uM 4-arm poly(ethylene glycol)-carboxylate (M_n~10,000 Da) and 20mM each of 1-ethyl-3-(3-dimethylaminopropyl) carbodiimide and N-hydroxysuccinimide (NHS) in dimethylformamide (DMF) at room temperature for 2 hours. After rinsing with ethanol and drying again, the NHS-activated

substrates were ready for treatment with the capture antibody, the first step in the CA 19-9 sandwich assay procedure.

4.9 CA 19-9 sandwich assay procedure

Polyclonal mouse anti-CA 19-9 antibody (capture antibody) was applied at a concentration of 5µM to the substrates and covered and incubated for 1 hour on an orbital shaker at 100 rotations per minute (RPM). The substrates were then uncovered and left on the orbital shaker for a further hour to dry out. Following this the substrates were blocked overnight at 4^{o}C in 3% donkey serum in PBS containing 0.05% tween-20 (PBST) supplemented with 1 mM Tris. Purified carbohydrate antigen 19-9 (CA 19-9) was diluted into PBS at the given concentration and 40 uL was applied to the substrates. PBS was used for the blank control in the place of CA 19-9 antigen. The substrates were incubated at room temperature in a humidified atmosphere for six hours on an orbital shaker (100 RPM) followed by removal of the CA 19-9 by micropipette, two immersions of PBST (five minutes each) followed by a brief immersion in PBS. Polyclonal rabbit anti-CA 19-9 was applied to each substrate at 3 x 10^{-7} M and incubated for 1.5 hours at room temperature on an orbital shaker at 100 RPM. Assays were washed as above. 40µL of 1.6×10^{-8} M of Dylight800 conjugated polyclonal donkey anti-Rabbit IgG was incubated at room temperature on each substrate for 10 minutes. Substrates were washed three times in PBST and once in PBS, followed by immersing in nanopure water and drying with compressed air.

4.10 Tunable fluorescent immunoassay conjugation

After amination and conjugation with branched poly(ethylene glycol)-carboxylate (PEG-carboxylate), the substrates were incubated with monoclonal mouse anti-CA 19-9 immunoglobulin G (IgG) in phosphate buffered saline (PBS), blocked overnight at 4 °C, and incubated with 15.4 U·mL^{-1} of CA 19-9 in PBS. The substrates were then incubated with polyclonal rabbit anti-CA 19-9 antibody, followed

by washing and incubation with DyLight 800 conjugated donkey anti-rabbit antibody, as described above.

4.11 Fluorescence measurement and analysis of CA 19-9 and GPC-1 assays

The fluorescence emission spectra were collected using a Fluorolog Tau 3 system from Horiba Jobin Yvon with a 450 W Xenon lamp excitation. The samples were excited at 755 nm, and their fluorescence was measured in the range of 780–830 nm using 5 nm slits. For the calibration curves, the integrated fluorescence intensity was measured and the mean and standard deviation over four measurements were used. Fluorescence decay curves of Dylight800 conjugated CA 19-9 sandwich assays on nanotriangle substrates and glass controls were measured by time-correlated single photon counting (TCSPC) using the Fluorolog Tau 3 system equipped with a DeltaDiodeTM-C1 controller (Horiba Scientific). Samples were excited using a Delta Diode 723 nm picosecond pulsed diode laser with a 60 ps pulse width, 3.0 mW average power and a 100 MHz repetition rate. Emission was measured at 810 nm for up to 10,000 counts. The fluorescence decay curves were analysed using the DAS6 decay analysis software (Horiba Scientific). The quality of the fits was assessed by the value of the reduced $\chi 2$ value, and a visual inspection of the distribution of the weighted residual. In all cases, the angle of acquisition was set at 30° for accuracy and consistency of the measurements.

4.12 Drop dry calibration

The drop dry calibration was carried out by dropping 30 µL of DyLight 800 conjugated donkey anti-rabbit antibody solution in PBS in concentrations of the given concentration onto the nanostructured arrays and onto glass. Both had been treated with UV ozone first to make the substrates hydrophilic and promote even distribution of the fluorophore.

4.13 Concentration dependent assay at higher concentrations

The initial calibration curve data that was achieved with the CA 19-9 metal enhanced fluorescent immunoassay showing a higher limit of detection was achieved using a higher concentration of the

fluorescent conjugated antibody in the immunoassay. The concentration of Dylight 800 conjugated polyclonal donkey anti-Rabbit IgG was 2.4 x 10^{-7} M. All other steps and concentrations were the same as above.

4.14 Specificity of CA 19-9 fluorescent immunoassay using albumin and GPC-1

For the specificity measurements, albumin or GPC-1 were diluted in PBS and was used as a substitute to CA 19-9 during the assay procedure. Bovine serum albumin (BSA) at concentrations between 10^{-6} and 10^{-13} molL^{-1} were prepared by diluting BSA in PBS. GPC-1 was prepared at concentrations between 10^{-7} and 10^{-14} molL^{-1} also by diluting in PBS. Each dilution was applied to the fluorescent immunoassay to determine the specificity. All other steps were kept the same.

4.15 Immobilization of fluorophore–protein conjugation monolayers onto gold nanostar substrates

The GNS SAMs and clean glass substrates, as a control, were covered by fluorophore monolayers using a biotin-streptavidin conjugation. The fluorophores used in these experiments were two commercially available streptavidin (SA)-conjugated near-infrared dyes (AF750 and AF790). First, to form monolayers of bBSA on the substrates, 26 µL of a 100 mg/mL bBSA solution in PBS was added to their surface and the substrates were incubated for 1 hour in a humidified chamber. bBSA binds to both glass and gold surfaces forming a complete monolayer. In order to be able to quantitatively compare the fluorescence intensity of fluorophore–bBSA conjugates, in the absence and presence of GNS SAMs on glass, the amount of bound bBSA on each substrate was quantified. Therefore, following incubation, the bBSA solution was collected from each substrate. To ensure that most of unbound protein had been removed, the surface of each substrate was rinsed 3 times with 50 µL of PBS, with each rinse being collected for bBSA quantification. The total unbound protein was quantified by measuring the absorbance of the solution at 280 nm, using disposable cuvettes with a 1 cm path length. The amount of bound bBSA on each substrate was calculated by subtraction from the total protein initially added.

Binding of the streptavidin–conjugated fluorophores to bBSA was achieved by adding 37 µL of 25 µg/mL fluorophore solutions onto the substrate surfaces and incubating for 2 hours in humidified chambers in the dark. The substrates were rinsed several times with PBS to remove unbound fluorophores and gently dried using compressed air. Their fluorescence spectra were collected immediately. Clean glass substrates incubated with bBSA only were used to measure the fluorescence background fluorescence intensity.

4.16 Fluorescence measurements and analysis

Fluorescence emission spectra of the Alexa Fluor® organic dyes were collected using a Fluorolog Tau 3 system (Horiba Scientific) with a 450 W Xenon excitation lamp. AF750 and AF790 were excited at 730 and 760 nm, respectively, using a 4 nm slit. Fluorescence emission was measured in the ranges of 760-830 nm and 785-850 nm, respectively, using a 5 nm slit. In all cases, the angle of acquisition was set at 30° for accuracy and consistency of the measurements. For all fluorophores, the fluorescence spectra were averaged over 3 individual spots on each substrate, and over 3 different substrates.

Time-correlated single-photon counting (TCSPC) was applied to acquire fluorescence decay curves for AF750 and AF790. Lifetime data were collected using the Fluorolog Tau 3 system equipped with a DeltaDiode™-C1 controller (Horiba Scientific). Samples were excited using the Delta Diode 730L pulsed laser (Horiba Scientific), which has a peak wavelength at 730 ±10 nm, a 60 ps pulse width, 3.0 mW average power and a 100 MHz repetition rate. Emission was measured at 777 and 805 nm for AF750 and AF790 respectively up to 10,000 counts. The fluorescence decay curves were analysed using the DAS6 decay analysis software (Horiba Scientific). The quality of the fits was assessed by the value of the reduced χ^2 value, and a visual inspection of the distribution of the weighted residual.

4.17 MicroRNA assay procedure

After amination and conjugation with branched poly(ethylene glycol)-carboxylate (PEG-carboxylate), the capture microRNA probe was applied at a concentration of 2.1 x 10^{-7} M to the substrates and incubated for 2 hours on an orbital shaker at 100 RPM. Following this the substrates were blocked overnight at 4°C in 3% donkey serum in PBS containing 0.05% tween-20 (PBST) supplemented with 1 mM tris. The analyte microRNA probe was diluted into PBS at the desired concentration and 40 uL was applied to the substrates. PBS was used for the blank control in the place of the tested miRNA probe. The substrates were incubated at room temperature in a humidified atmosphere for six hours on an orbital shaker (100 RPM). This was followed by removal of the analyte probe by micropipette, two immersions on PBST (five minutes each) and a brief immersion in PBS. The fluorophore conjugated microRNA probe was applied to each substrate at 6 x 10^{-8} M and incubated for 10 minutes at room temperature on an orbital shaker. The fluorophore that was used was Dy782. Substrates were washed three times in PBST and once in PBS, followed by rinsing in nanopure water and drying with compressed air.

4.18 Fluorescence measurement and analysis of microRNA assay

The fluorescence emission spectra were collected using a Fluorolog Tau 3 system from Horiba Jobin Yvon with a 450 W Xenon lamp excitation. For the Dy782 conjugated microRNA probe, the samples were excited at 740 nm, and their fluorescence was measured in the range of 765–815 nm using 5 nm slits. For the calibration curves, the integrated fluorescence intensity was measured and the mean and standard deviation over four measurements were used. In all cases, the angle of acquisition was set at 30° for accuracy and consistency of the measurements.

4.19 Analytical statistics

To demonstrate and compare the properties of a biosensor, several characteristics were measured.

4.19.1 Validation

Validation is evaluation of a test to determine whether it is capable of producing test results that are fit for the purpose that it is intended. This was achieved by comparing the fluorescence enhanced immunoassay with the standard fluorescent immunoassay and calculating the correlation between the results.

4.19.2 Limit of detection

The limit of detection (LOD) is the lowest concentration of analyte that can be reliably detected with a specified level of confidence. The lower the detection limit the greater the sensitivity of the biosensor. This can be calculated by multiplying the standard deviation of the blank recording by a number. This number is determined so that the risk of false positives and false negatives is kept to an acceptable level, and this is usually set at 5% for both types of error. Assuming the results of repeated zero readings follow a normal distribution, by statistical methods the critical value above which the result is considered positive, is *x*blank + 3.3(standard deviation).

4.19.3 Limit of quantification

This is the lowest concentration of analyte that can be determined with an acceptable level of uncertainty. This calculated as 10 x standard deviation of the blank.

4.19.4 Dynamic range

This is the concentration range that the analysis technique produces reliable results. The lower end is the limit of detection, and at the upper end a 'plateauing' of the response is typically observed.

4.19.5 Specificity and sensitivity

In analytics, specificity describes the ability of the assay to produce a response only for the antigen of interest. This is measured by using alternative antigens to test the assay. Specificity is also used to describe a medical test and is calculated as the number of true negatives detected divided by the number in the sample that do not have the disease. Sensitivity is calculated as the number of true positives divided by the number in the sample that have the disease.

4.20 Descriptive statistics

4.20.1 Mean

The mean is a statistic that is used to describe the average of a set of data. It is calculated by adding together the data numbers and dividing by the number of data points.

4.20.2 The null hypothesis, type I and type II errors

When studies are being carried out to determine whether there is an association between two factors, the null hypothesis describes the default position that there is no association between the two variables. In type I errors, there a false positive finding. In other words, the data presented describes that the null hypothesis should be rejected when in actual fact there is no association between the two variables. In type II errors, there is a false negative finding when the null hypothesis is found to be true, but in reality, there is an association between the two factors.

4.20.3 Power calculation

The power of a study describes the probability of a study to correctly reject the null hypothesis. As the power of a study increases, the probability of a type II error decreases. The power of a study is dependent on two factors: the sample size and the effect size. Power analysis is used to determine the sample size required to detect an effect of a given size. For example, power analysis can be used to determine the number of patients needed in a study to determine whether a certain increase in the level of a biomarker is related to a particular disease. One of the problems with biomarker studies is that the number of patients required to prove a biomarker is related to a particular disease is very high. For example, if the power of a study is set at 0.9, and the sensitivity of a test is 0.5, then 435 people would be needed in the study. As the sensitivity of the test is increased, the number of patients also needs to be increased. For clinical validation, a sample size of around 100 would be required to achieve a confidence interval of 95%.

4.20.4 Standard deviation

Standard deviation is a measure that is used to describe the spread of data in relation to the mean. If the standard deviation is low, this indicates that the data points are close to the mean. A higher standard deviation indicates that they are spread further from the mean. Standard deviation is also used to describe a statistically significant result. Data that is greater than two standard deviations away from the default is usually considered to be statistically significant.

4.20.5 Accuracy

Accuracy describes the ability of a test to differentiate between diseased and healthy populations. The accuracy is calculated by measuring the area under the curve (AUC). The curve should be a receiver operating characteristics curve in which the false positive rate is plotted against the true positive rate.

CHAPTER 5: Instrumentation

5.1 Scanning electron microscope

Scanning electron microscopy (SEM) is a form of electron microscopy that uses electron beams to form a black and white image[179]. The advantage of using electrons as opposed to light is that they are able to form images with much higher resolution. The typical resolution of light microscopes is in the range of 200 nanometers compared to around 3 nanometers for a scanning electron microscope. Figure 2.16 shows how an electron microscope is laid out. To create an image, an electron beam is produced from an electron gun and accelerated towards a positive anode. Three different electron guns are currently available each with their advantages and disadvantages as shown in Table 2.1.

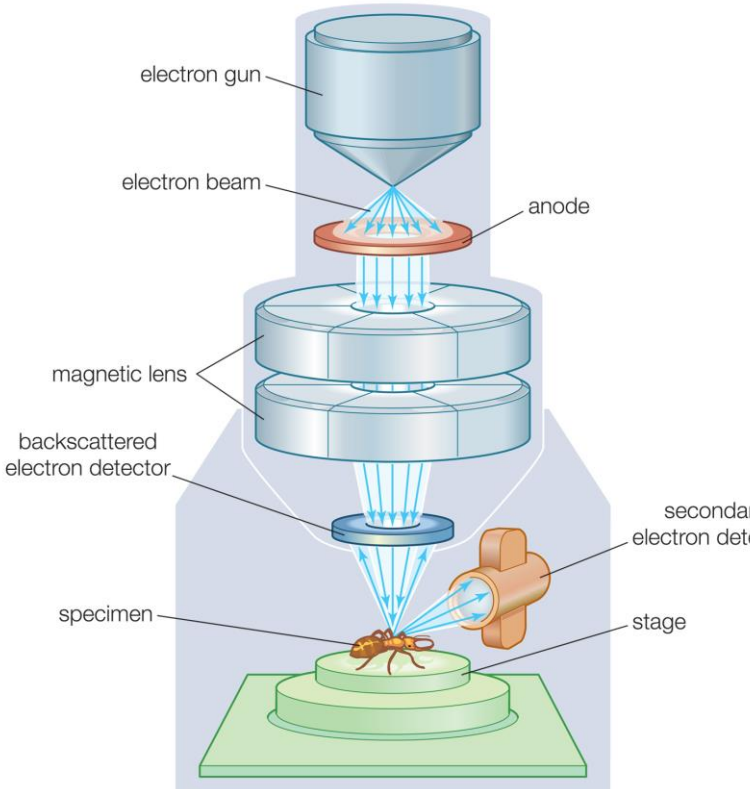


Figure 1: Scanning electron microscope (Taken from Encyclopædia Britannica Online. Web. 24 Apr. 2015).

Table 1: Three main types of electron gun available with their advantages and disadvantages.

Electron gun	Advantages	Disadvantages
Tungsten-Hairpin Gun	Stable source of electrons, inexpensive to replace, does not require ultrahigh vacuum	Short lifetime
Lanthanum-hexaboride Gun	Higher beam brightness, better resolution, longer lifetime	Higher vacuum requirement, needs time to warm up, more expensive to replace
Field-emission Gun	Best resolution, longest lifetime	Not interchangeable, highest vacuum requirement, expensive to produce, electron beam is unstable

After formation of the beam an electromagnetic lens focuses the beam using magnetic forces. The beam then passes through an aperture to control the diameter and remove any scattered electrons. Due to slight imperfections with the electromagnetic lens, the beam that emerges is not perfect and is oval in cross section rather than being round in shape. It is impossible to create a perfect electromagnetic lens and in addition contamination of the lens from the specimen, for example, alters the electromagnetic field and this creates imperfections in the electron beam. The error this creates is known as astigmatism and must be corrected to produce a high-resolution image. This is achieved by manipulating stigmator coils which are smaller electromagnets placed around the column that are controlled by the operator of the microscope and can make small adjustments in the beam to take it back to a round shape.

When electrons hit and interact with the sample they are picked up by a detector and converted into a voltage to produce an image on a cathode ray tube. There are many different interactions that can occur between the electrons and sample. The image of an SEM is produced by the detection of four different types of secondary electron. The first type of secondary electrons produces the highest resolution image. These are produced when the incoming electrons interact with orbital shell electrons of the atoms of the sample causing small angle deflections of the incoming electron and high energy loss. Due to their low energy, most of them are detected despite their varying deflection angles. However, the low energy also means that a lot of these electrons are absorbed by the sample and only those near the surface are able to escape. Projections on the sample have a shorter distance to escape than depressions. Projections therefore appear bright compared to flat or depressed areas that are dark.

The second type of secondary electrons is backscattered electrons which interact with the nucleus of atoms in the sample and as a consequence undergo large angle deflection and low energy loss. This is known as an elastic interaction compared to the inelastic interaction that occurs with the first type of secondary electrons. These electrons provide a low-resolution contribution to the image. They may

then interact with parts in the specimen chamber to produce a third type of secondary electron which have even lower resolution. The fourth type of secondary electron is produced by the scatter of electrons when the primary beam passes through the final aperture. These produce noise and reduce the image resolution. As the detector cannot differentiate between different types of secondary electron these all contribute to the final image.

Due to the way the SEM works the sample must be prepared so that it is electrically conductive. This is achieved by coating with a thin layer of metal such as gold or chromium using a sputter coater. This device uses argon gas in a vacuum chamber to release gold or an alternative metal from a plate on a cathode. The gold atoms are then accelerated towards the specimen which is placed on an anode at the opposite end of the chamber. Prior to this the sample is attached to a stub usually made of aluminium and using an adherent conductive tape, such as carbon tape. After the coating process silver paint is used to create a conductive channel between the edge of the sample and the stub. Without this preparation the SEM produces poor images as electrons from the electron beam collect on the surface of the sample rather than being transmitted through it. This build up in charge then interferes with the deflection of the secondary electrons being scattered from the surface of the sample and distorts the image.

The use of SEM in this project has been invaluable as it aids in the optimisation of structures by providing feedback on sample quality and how imperfections relates to the enhancement efficiency of the samples.

5.2 UV-Visible Spectroscopy

UV-Visible spectroscopy is an essential tool in the evaluation of the plasmonic chip. This is because it is used to determine the resonant wavelength of the nanoparticles and therefore aids in identifying the most suitable matching fluorophore[180]. It was used in this project to help optimise the gold nanotriangles.

Light interacts with matter in several ways. It can either be absorbed, reflected, scattered, transmitted, induce fluorescence or phosphorescence or a photochemical reaction. During fluorescence and phosphorescence, light is absorbed and then re-emitted. This is in contrast to the reflection and scattering processes whereby light is immediately returned. With reflection the incident angle of light is equal to the emission angle, whereas in scattering light is deflected in different angles after interacting with matter. Photochemical reactions involve breaking of chemical bonds. During UV-Vis spectroscopic measurements, the amount of light transmitted by a sample is measured as a proportion of the incident light. The light that is not transmitted is absorbed or scattered. The sum of absorbed and scattered light is known as the extinction. The amount of scattered light is so small that the extinction is presumed equal to the absorption. The wavelength of maximal absorption correlates with the resonant wavelength. The spectroscope measures the absorption at all pre-set wavelengths and expresses this as fraction of 1 or a percentage of the incident light I_0.

5.3 Fluorescence spectroscopy

Fluorescent spectroscopy measurements were carried out using the Fluorolog®-3 Model FL3-22 (Jobin Yvon Horiba). The experiment set-up is shown in figure 2.17.

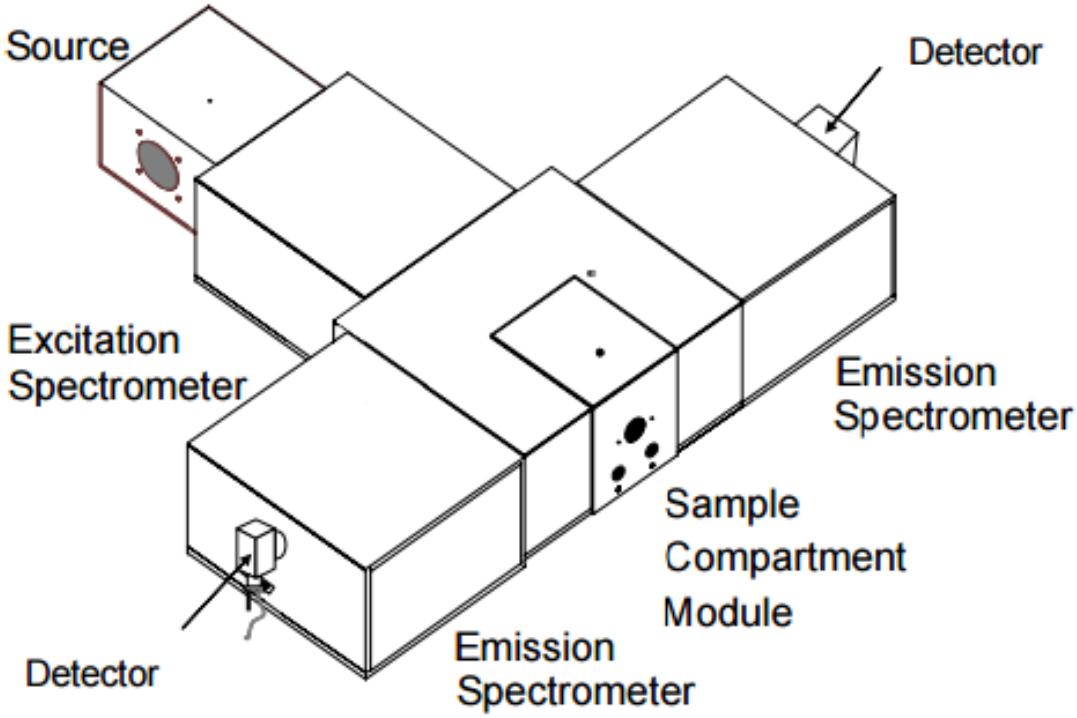


Figure 2: Fluorolog fluorescence spectroscope. (Taken from Fluorolog-3 v. 2.2, Jul 2002).

The sample is placed in the sample holder and into the sample compartment module. For excitation a 450W Xenon lamp is standard. The light is then filtered by an excitation spectrometer that only allows one wavelength to pass through the sample. This light traverses the sample and is filtered by an emission spectrometer that feeds the signal to the detector. The excitation spectrometer passes through a range of pre-set wavelengths and the detector records the spectrum at the given wavelength of emission.

For TCSPC measurements, photon counting allows measurement of the time a molecule stays in the excited state following excitation. After laser excitation, they decay back to the ground state at a certain rate. The reciprocal is the excited state lifetime. These photons are detected using a photomultiplier tube (PMT) and builds up the exponential decay. Fitting this decay gives the excited state lifetime.

CHAPTER 6: SYNTHESIS OF NANOSTRUCTURES FOR USE AS BIOSENSORS

In this chapter, three nanostructures that are suitable for use in a biosensing platform are developed: gold nanotriangular arrays; gold capped polystyrene sphere (GCPS) arrays; and gold nanostars. For each structure, the synthesis method will be described followed by the results of characterisation by scanning electron microscopy (SEM).

6.1 Gold nanotriangular arrays

Nanotriangular arrays are one of the simplest nanostructures. They are versatile structures as they can be synthesised from any metal to provide different optical properties. The regular distribution of the nanoparticles makes them highly suitable for biosensing as the arrays are highly reproducible. The results of assays using these nanoparticles are therefore also expected to be reproducible and precise.

6.1.1 Synthesis of gold nanotriangular arrays

The first step in the synthesis of the regular gold nanotriangular arrays is to produce a regular ordered PS nanosphere template. Using the NSL fishing technique to produce the PS nanosphere template, described in detail in the previous chapter, long range ordered arrays of gold nanotriangles were synthesised. The steps in the fabrication process are shown in Figure 1. Glass substrates 10mm x 13mm in size were chemically cleaned and then treated with UV ozone before the PS nanospheres were applied. The UV ozone removes contaminants from the surface of the glass, such as hydrocarbons, or oils by converting them into volatile substances. The PS nanospheres act as a template prior to the gold layer deposition. Following deposition of the gold layer using e-beam evaporation, the PS nanospheres were removed by tape stripping. Since the interstices between the PS nanospheres as well as the crowns of the PS nanospheres themselves are covered with gold, removal of the PS nanosphere template leaves gold nanotriangles remaining on the

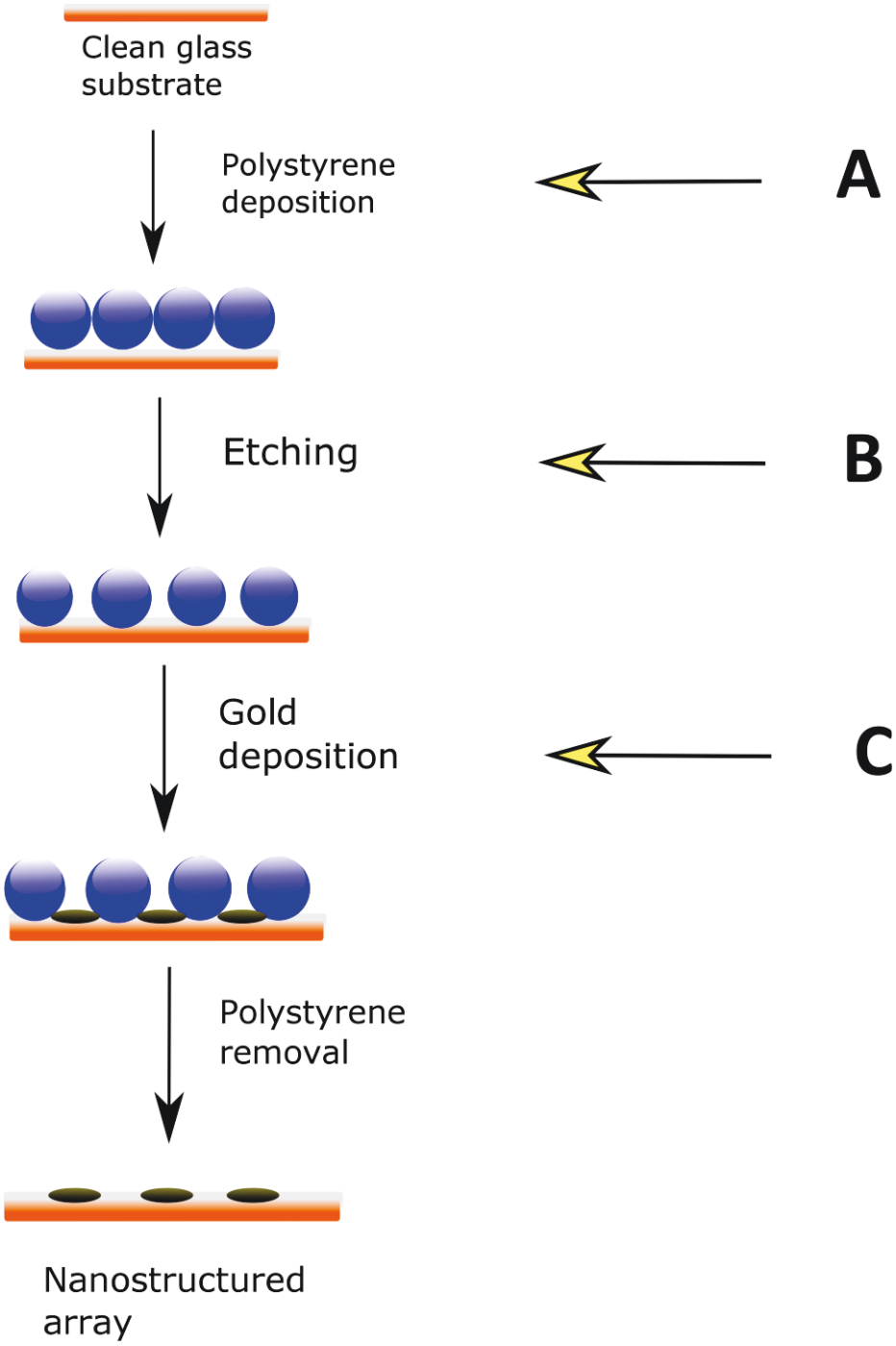


Figure 1: Schematic diagram to show fabrication process of gold nanotriangular arrays. PS nanospheres are used as a template for gold deposition using e-beam evaporation. A, B and C indicate points of intervention to alter size parameters of gold nanotriangles. A: altering PS nanosphere size, B: etching of PS nanospheres C: altering gold layer depth during deposition.

glass surface. The height of the nanotriangles is controlled within the e-beam evaporation system using a quartz crystal monitor (QCM). The gold layer deposited was 100nm in thickness.

Using this synthesis method, certain size parameters of the nanotriangular arrays could be altered. Reactive ion etching (RIE) is a process used in the fabrication of microstructures. It was used to reduce the size of the PS nanospheres prior to deposition of the gold. As described below, this altered the size of the nanoparticles as well as their separation distance, which proved to be a very useful property. In addition, the size of the PS nanospheres could be selected which also altered the size of the nanoparticles and their separation. The effects of RIE and changing the PS nanosphere size were both explored, and the results described below.

6.1.2 SEM characterisation of gold nanotriangular arrays

During the synthesis process the nanotriangular arrays were characterised using SEM. A LEO Gemini 1525 field emission gun scanning electron microscope (FEG-SEM) was used. This allowed the synthesis process to be evaluated and also the quality of the nanostructures to be assessed. The quality of the nanotriangular arrays seen on SEM is important as the success of fluorescence enhancement is closely related to the quality of the nanoparticle structure. Any deviations from the regular ordered array of nanotriangles would have the effect of reducing the amount of fluorescent enhancement. Gold nanotriangular arrays synthesised from 3 different diameter sizes of PS nanospheres were studied: 280 nm, 400 nm and 500 nm. The effect of RIE on nanotriangular arrays synthesised by all 3 sizes of PS nanospheres was also evaluated. The SEM images are shown in figures 2, 3 and 4.

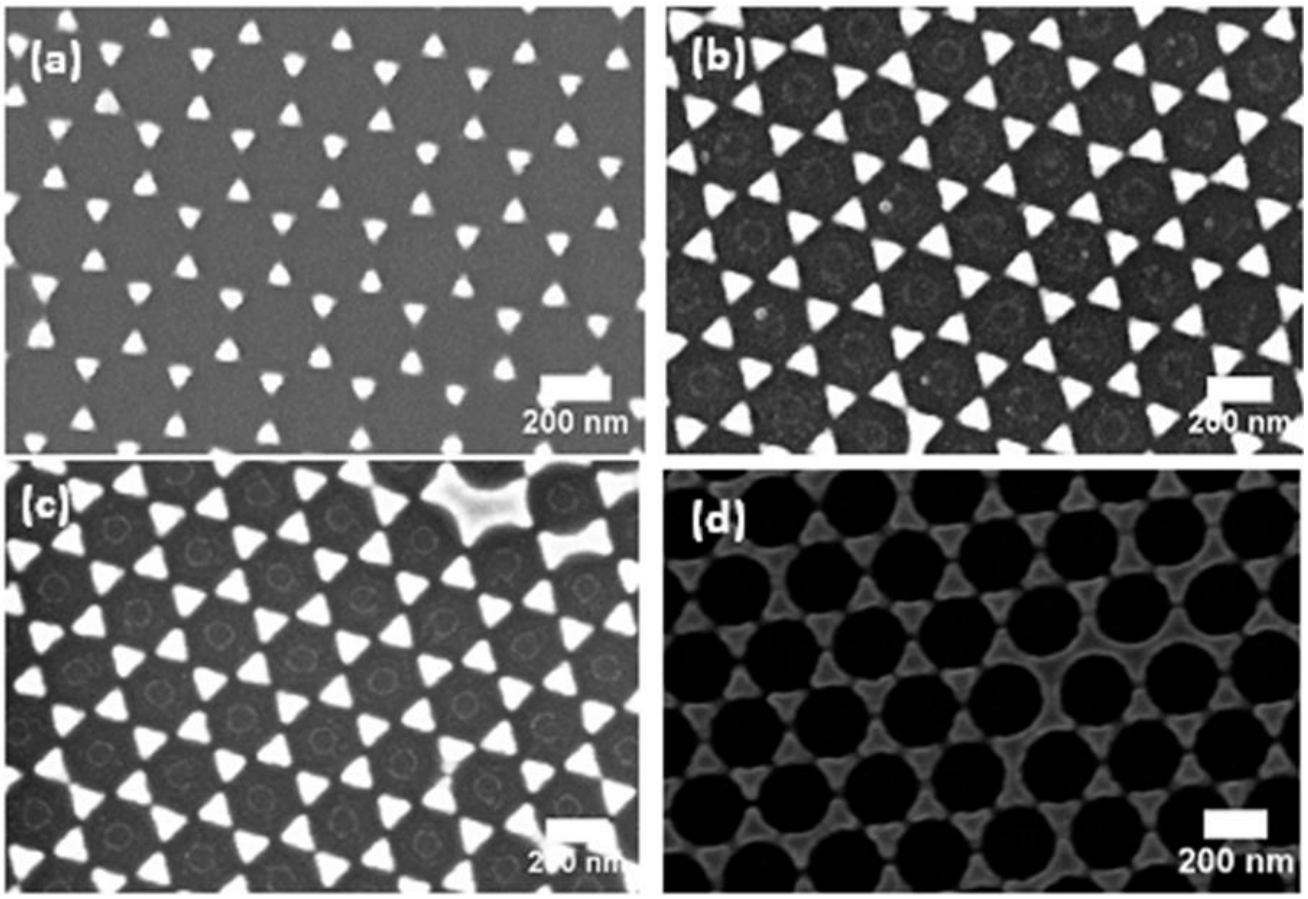


Figure 2: SEM images of nanotriangular arrays synthesised using PS nanospheres of 280 nm in diameter and (a) with no etching (b) with 5 sec etching time (c) with 10 sec etching time (d) with 15 sec etching time.

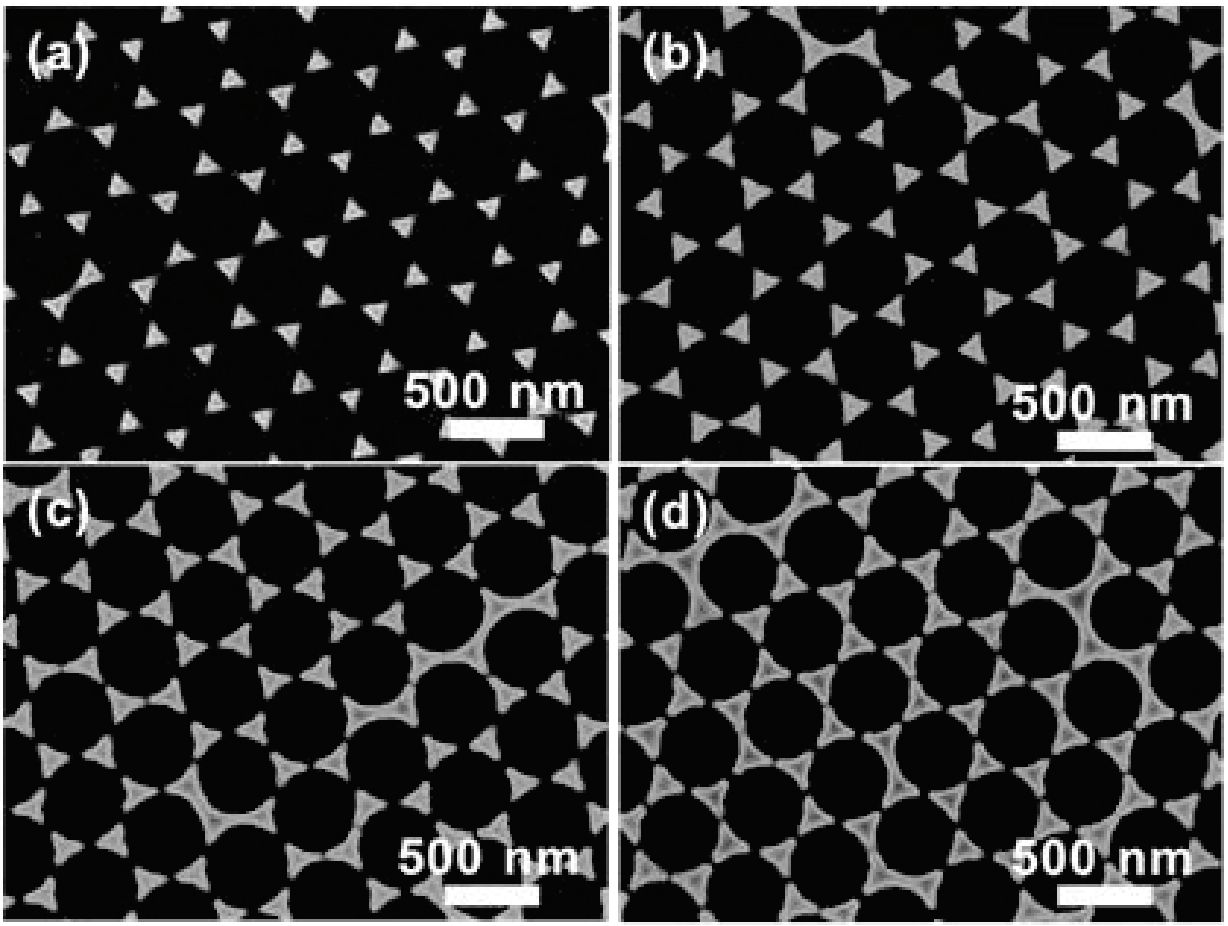


Figure 3: SEM images of nanotriangular arrays synthesised using PS nanospheres of 400 nm in diameter and (a) with no etching (b) with 5 sec etching time (c) with 10 sec etching time (d) with 15 sec etching time.

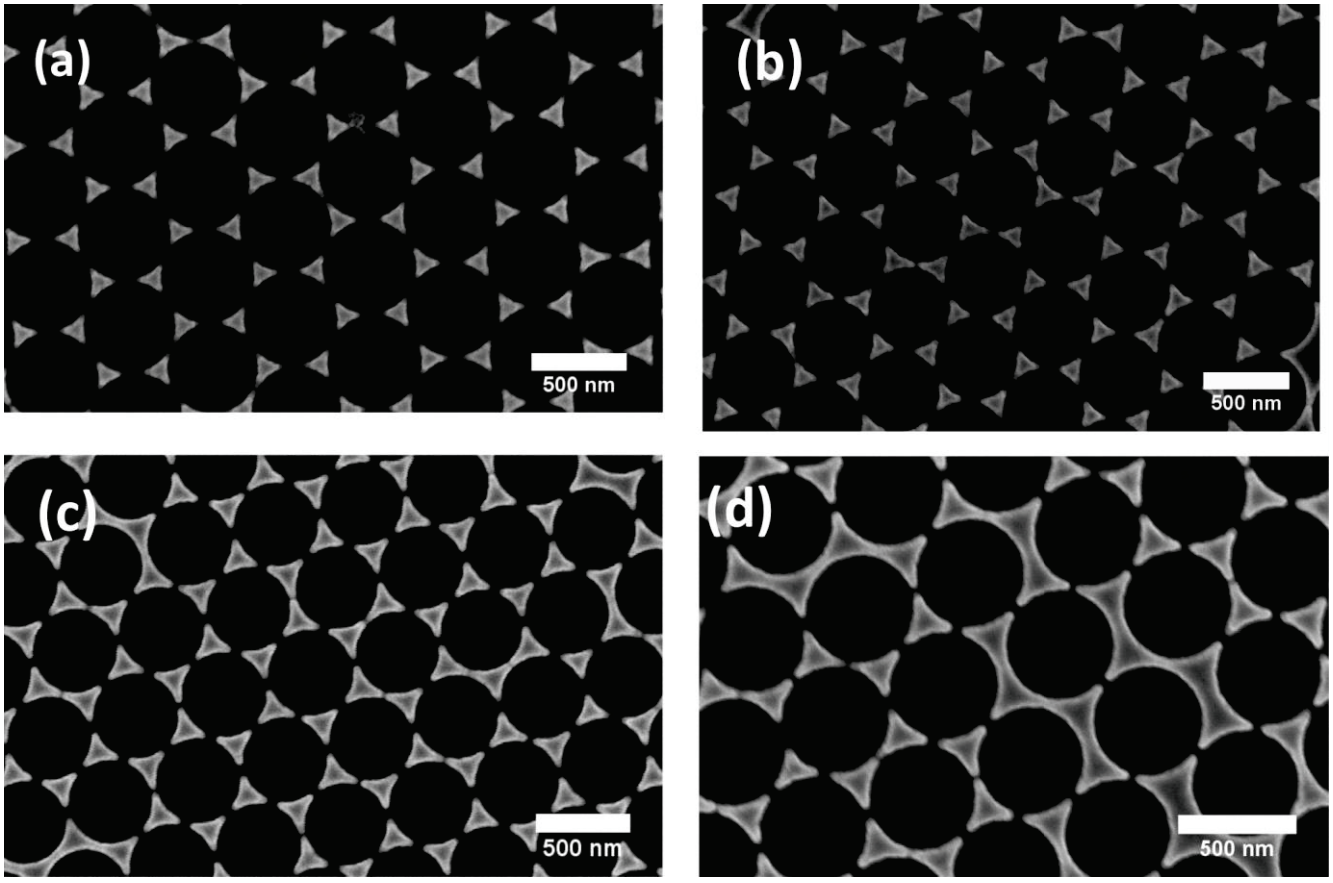


Figure 4: SEM images of nanotriangular arrays synthesised using PS nanospheres of 500 nm in diameter and (a) with no etching (b) with 5 sec etching time (c) with 10 sec etching time (d) with 15 sec etching time.

The SEM images show that the NSL fishing method described produces regular nanotriangular arrays. The images show that the nanotriangular arrays consist of ordered gold nanotriangular shaped particles, arranged with the original hexagonal close packed (HCP) structure of the PS nanosphere template. Increasing the size of the PS nanospheres used as a template, increases the size of the gold nanoparticles. The effects of the RIE are also seen. Applying RIE to the PS nanospheres prior to gold deposition causes a reduction in the PS nanosphere diameter. The position of the PS nanosphere does not change and the interstitial spaces between the PS nanospheres gets larger, therefore the nanotriangles increase in size. As the PS nanospheres get smaller, the contact between them also gets smaller and the distance between the nanoparticles decreases in length. The length of the nanotriangles, and the distance between them was measured using Image J software (National Institute of Health, 2017). These structural characteristics are summarized in Table 1. As expected, the interparticle length decreases and the nanoparticle length increases with increasing etching time. When the nanoparticle length was plotted against the etching time (Figure 5a –c), the line of best fit showed a directly proportional relationship between the two parameters (R= 0.680 for 280nm; R= 0.873 for 400nm; R= 0.966 for 500nm). The use of the NSL fishing technique has distinct advantages, as it is low cost and allows for large area (in the order of cm^2) uniform nanotriangular arrays. These results also demonstrate that control of the size and interparticle separation of the gold nanotriangles can be achieved by selecting the diameter of the PS nanospheres and by applying RIE to the PS nanosphere template prior to gold deposition.

The SEM characterisation highlighted another property of the etching. The maximum etching time used was 15 seconds to synthesise the nanotriangular arrays. If the etching time was increased above 15 secs, the PS nanospheres become so small that nanoholes are formed after gold deposition rather than discrete nanoparticles (Figures 6 and 7). Therefore, 15 secs were the maximum etching time used for synthesis of the nanotriangular arrays.

Table 1: Structural parameters of gold nanotriangular arrays. a is the nanoparticle length and *s* is the inter-particle distance (Figure 5d). Mean value is given and standard deviation of 12 measurements

PS nanosphere diameter (nm)	Etching time (sec)	a, nanoparticle length (nm)	s, interparticle length (nm)
280	0	68±5	77±7
280	5	106±7	42±6
280	10	111±5	34±5
280	15	117 ±12	23 ±6
400	0	134 ± 15	98 ± 15
400	5	164 ± 18	60 ± 10
400	10	179 ± 14	46 ± 5
400	15	186 ± 13	23 ± 10
500	0	149±7	105±30
500	5	170±11	85±13
500	10	202±10	52±7
500	15	215±13	43±4

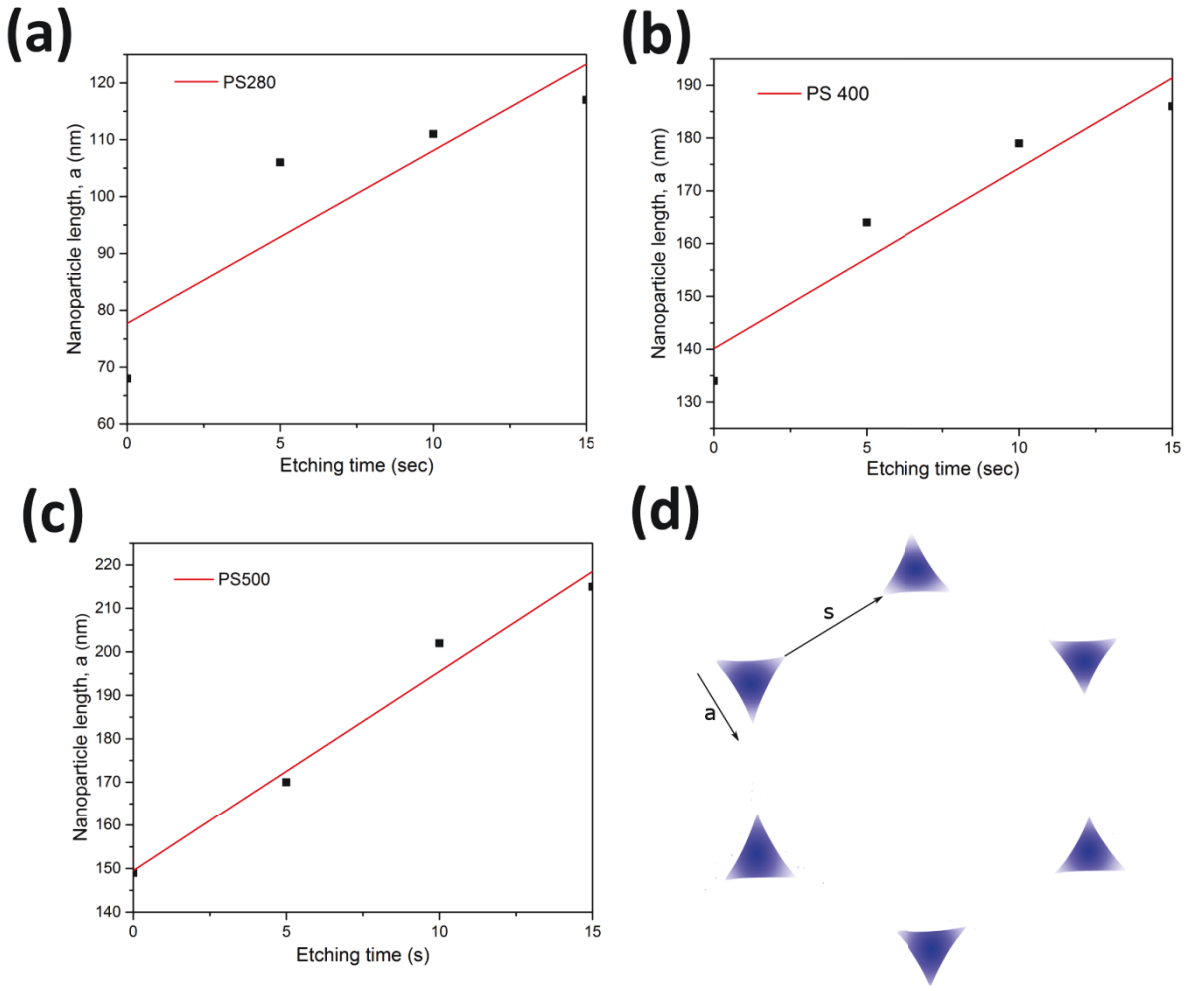


Figure 5: (a)-(c) Scatter plots to show the relationship between the etching time and nanoparticle length, a. Gold nanotriangles were synthesised using PS nanospheres of increasing diameter (a) 280 nm (b) 400 nm (c) 500 nm. (d) Schematic diagram to show the distances measured. a= nanoparticle length s= interparticle distance.

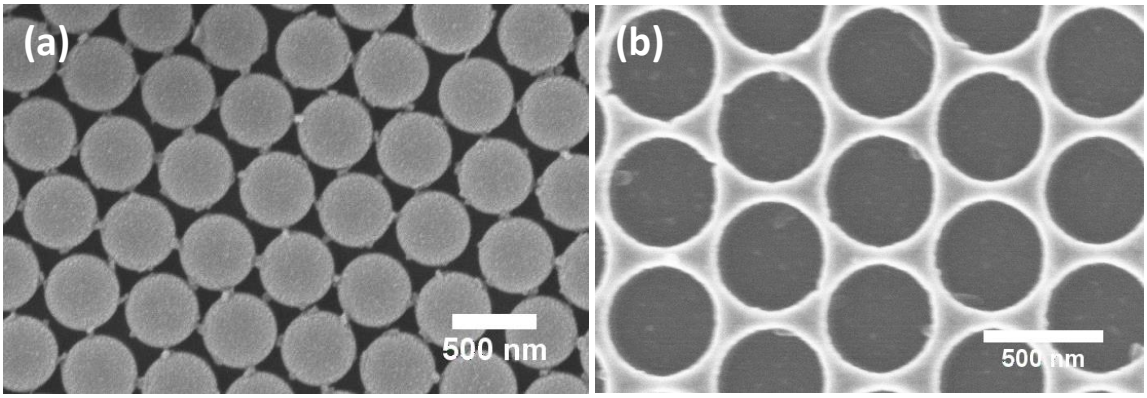


Figure 6: SEM characterisation of polystyrene nanosphere templates and gold nanohole arrays synthesised from 500 nm polystyrene nanospheres etched for 20 secs (a) polystyrene template shows weak crosslinking and reduction in size of PS nanospheres (b) corresponding nanohole array.

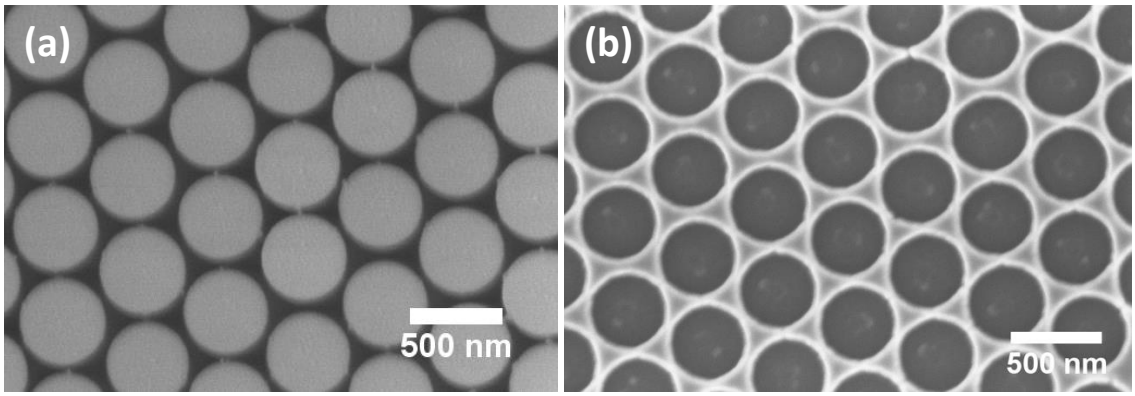


Figure 7: SEM characterisation of PS nanosphere templates and gold nanohole arrays synthesised from 500 nm PS nanospheres etched for 25 secs (a) polystyrene template shows weak crosslinking and reduction in size of PS nanospheres (b) corresponding nanohole array.

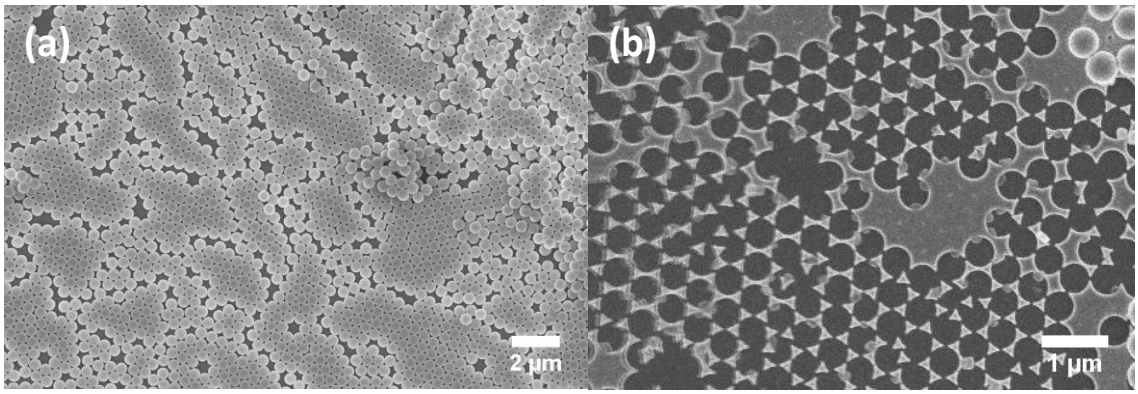


Figure 8: SEM characterisation of (a) PS nanosphere templates and corresponding (b) gold nanotriangular arrays synthesised from 500 nm polystyrene nanospheres demonstrating slip dislocations, vacancies and areas of bilayer and monolayer.

During the fabrication and subsequent SEM characterisation of the nanoparticles some poor quality samples were identified. These displayed defects in the structure of the array (Figure 8). These defects have been described in previous work[181]. Slip dislocations occur where there is misalignment of the rows of PS nanospheres. As a result, the PS nanosphere template may be disrupted producing vacancies in the nanotriangular array. This is because subsequent gold deposition in vacancies produces islands of bulk gold instead of individual nanoparticles. Another type of defect occurs in areas when bilayers or tri-layers of PS nanospheres are deposited on the surface of the glass substrate instead of monolayers. When this happens, the nanotriangle shape is not produced by the gold deposition process. The PS nanosphere deposition step therefore requires care to produce regular and highly ordered monolayers. The area of regular nanotriangular arrays achieved was in the order of centimetres which is sufficient for the intended use.

Many different nanostructures have been described for use in metal enhanced fluorescence. These include silver island films[182] and nanoparticles produced by de-alloying techniques[20]. The disadvantage of these nanostructures is that they are irregular and there is no control over the shape and size of the nanoparticles. Alternative techniques, such as e-beam lithography and nanoprint lithography are precise and controlled methods and the nanostructures they produce are tunable but these methods are low throughput and expensive[17], [183]. NSL and in particular the fishing technique is a useful option for the synthesis of nanoparticle arrays as it produces long range regular ordered arrays that are reproducible and tunable[152]. It is also a cheaper and quicker method compared to its counterparts. These properties are ideal when designing a biosensor platform.

6.2 Gold capped polystyrene sphere (GCPS) arrays

The next nanostructure that was developed and characterised was the gold capped polystyrene sphere (GCPS) arrays. The advantages of GCPS arrays are that they are easy to synthesise, they are ordered, tunable and the production method is low cost. Hollow metal ‘nanocaps’ produced by evaporating metals onto a template of spherical polymer particles, followed by removal of the

template and separation of the nanocaps show a peak optical absorption between 760nm and 915nm that is tunable[184]. The nanocaps produced were the same in shape and size and the absorption spectra could be tuned by changing the fabrication parameters. Similarly Love et al, 2002[185] synthesise metallic half-shells by evaporation of metal onto silica nanospheres. Ordered metal nanostructures produced by sputtering gold onto a monolayer of dielectric microspheres exhibit tunability and high order. Tunability is controlled by changing the size of the microspheres. Variation between silica and polystyrene spheres also changes the way the nanostructures interact with light[186]. Sugawa, 2013[187], demonstrate metal enhanced fluorescence using copper capped silica spheres. An enhancement factor of 89.2 times was observed compared to a bulk copper substrate. While gold capped nanospheres have been used for detection by the other plasmonic methods, they have not been used for metal enhanced fluorescence based detection.

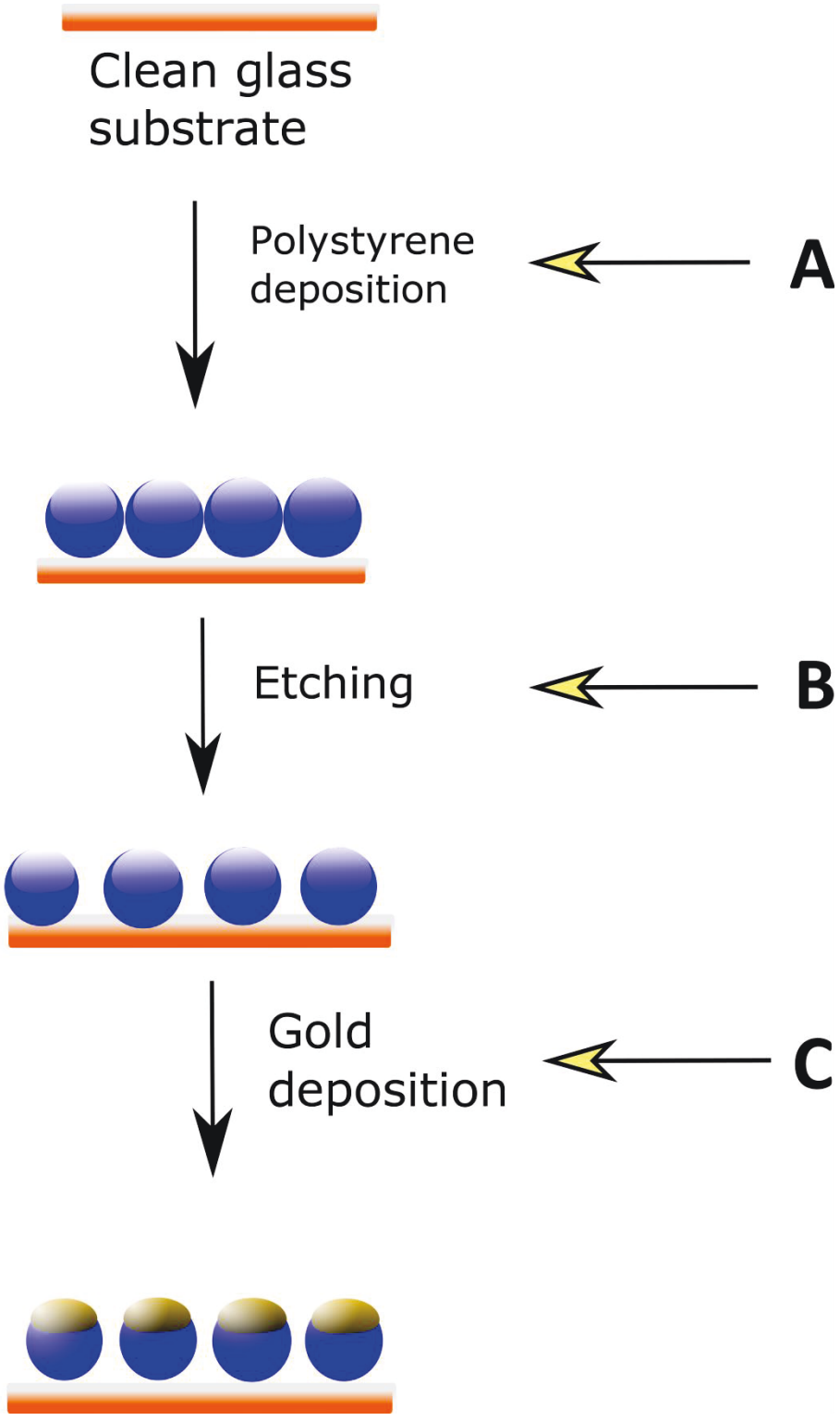


Figure 9: Schematic diagram to show fabrication process of GCPS arrays. PS nanospheres are used as a template for gold deposition using e-beam evaporation. A, B and C indicate points of intervention to alter size parameters of GCPS. A: altering PS nanosphere size, B: etching of PS nanospheres C: altering gold layer depth during deposition.

6.2.1 Synthesis of GCPS arrays

Figure 9 shows the fabrication method of the GCPS arrays. The NSL fishing technique was used to arrange the PS nanosphere template on the surface of glass substrates. The PS nanospheres were then treated with RIE of etching times between 5 secs and 15 secs. The minimum etching time used was 5 seconds to separate the PS nanospheres prior to deposition of the gold. Etching of the PS nanospheres was necessary to ensure the gold nanoparticles remained separate from each other. E-beam evaporation was used to deposit gold on the crowns of the PS nanospheres.

6.2.2 SEM characterisation of GCPS arrays

The arrays were characterised using SEM as shown in Figure 10. The SEM also shows side views of individual GCPS structures that have been tilted relative to their original position. These images show regularly ordered GCPS arrays. They demonstrate that gold deposition occurs on the crown of the PS nanospheres with minimal cross-linking between the caps. The method produces discrete nanoparticles on an isoelectric base of PS nanospheres. The PS nanospheres act as an insulator having a similar function to the silica particles used by Sugawa et al, 2013[187]. Here gold was used instead of copper.

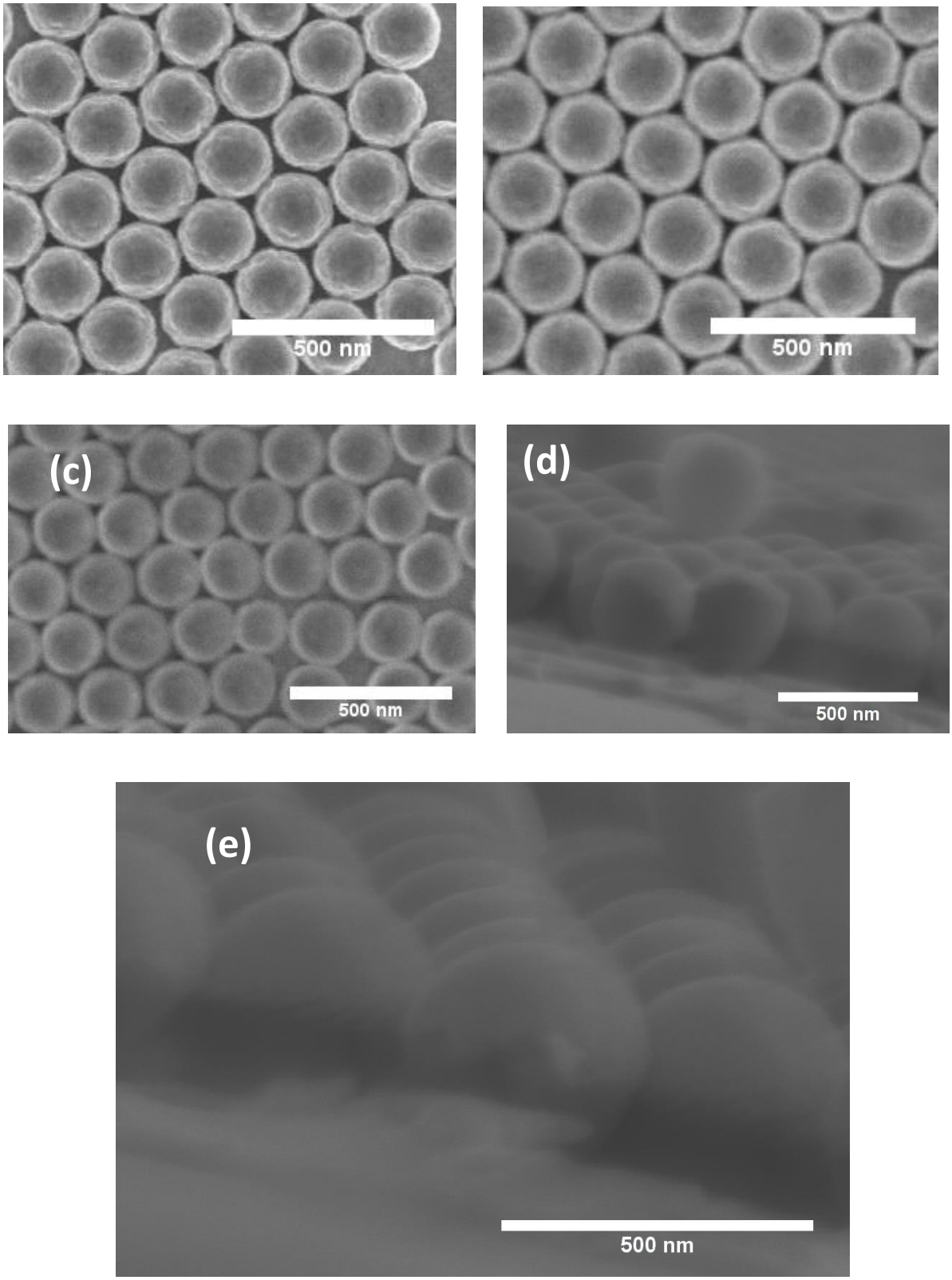


Figure 10: SEM images of GCPS arrays synthesised using PS nanospheres of 280 nm in diameter and (a) with 5 secs etching time (b) with 10 secs etching time (c) with 15 seconds etching time (d) and (e) side view images

6.3 Gold Nanostars (GNS)

Gold nanostars are branched gold nanoparticles with sharp tips. They have large surface areas and complex shapes and display unusual properties due to their nanoscale branches. The nanoparticles can be used in a colloidal phase or they can be grafted to a glass substrate and used in a solid phase.

In the colloidal phase, GNS have been shown to increase tumour detection when used as a contrast agent for imaging[188]. The large surface area of the nanostars makes them suitable for linking to contrast agents for magnetic resonance imaging (MRI) and positron emission tomography (PET) scanning. The small size of the nanostars makes them suitable for uptake into cancer cells. Cellular uptake occurs by two mechanisms. The enhanced permeability and retention (EPR) effect is due to the increased vascular permeability of the blood vessels supplying tumour cells. The nanoparticles preferentially leak into the adjacent tumour tissue and accumulate there. The second mechanism is an active mechanism. The nanoparticles are conjugated with targeting ligands, such as antibodies, which target sites of interest where they are taken up by the tissue. In the colloidal phase, GNS have also been used for the detection of proteins. They could detect binding of the protein streptavidin using a shift in the absorption peak wavelength of the GNS[189]. In the solid phase an GNS biosensor also been used to detect DNA probes[190].

A major advantage of the nanostar structure is that the plasmonic properties are tunable. This is important as the absorption peak wavelength can be tuned so that it falls within the crucial 'biological window'. One of factors that control the peak absorption wavelength of the GNS is the number of spikes, which in turn is controlled by the amount of gold used in the synthesis process[191]. The number of spikes and the sharpness of the tips of GNS can also be changed.

6.3.1 Synthesis of gold nanostars in solution

Several methods of GNS synthesis have been described. For this project the 'seed-mediated' method was used. This method involves two steps. The first step is the synthesis of gold nanoparticles in solution. The general method of producing gold nanoparticles is by reduction of gold compound in the

presence of a stabilising agent[192], which stops nanoparticle growth and prevents aggregation. Most commonly the salt, gold (III) chloride trihydrate ($HAuCl_4$) is reduced by sodium citrate, which also acts as a stabilising agent. In this process Au^{3+} ions are reduced to neutral gold atoms and as the solution becomes supersaturated the gold starts to precipitate to form a coloured solution that contains nanoparticles. In the second step, the seeds are added to a growth solution containing chloroauric acid, $HAuCl_4$. This induces spike growth, which occurs in layers and allows more control over the size and shape of the resulting nanoparticles. A surfactant is usually also required which sticks to facets on the surface of the gold nanoparticles to trigger the growth of the spikes. In most cases, cetyltrimethylammonium bromide (CTAB) is the surfactant used. However, using a surfactant is a problem when producing biocompatible nanoparticles as CTAB is toxic. However, one synthesis method has been reported that that does not use surfactant and allows tunable synthesis[193]. Furthermore, the nanoparticles were tunable to the biological window and could be used for in vivo imaging.

In this project, the surfactant-free seed-mediated method[193] was used to synthesise two different sized nanostars. One is referred to as small (S-GNS) gold nanostars and the other large (L-GNS) gold nanostars. In the 2-step synthesis, the first step was to synthesise gold nanoparticle (GNP) seeds of two sizes, 15 nm and 50 nm termed GNP_{15} and GNP_{50} respectively. This was achieved by heating $HAuCl_4 \cdot 3H_2O$ solution and then adding 2 different volumes of aqueous sodium citrate solution. In the second step, to produce the S-GNS, the GNP_{15} were added to the growth solution of $HAuCl_4 \cdot 3H_2O$ with HCl, $AgNO_3$ and ascorbic acid. For L-GNS, the GNP_{50} were added to the same solution.

6.3.2 TEM characterisation of GNS in solution

The GNS were characterised with transmission electron microscopy (TEM) using a JEOL JEM-2100F with an accelerating voltage of 200 kV (Figure 11).

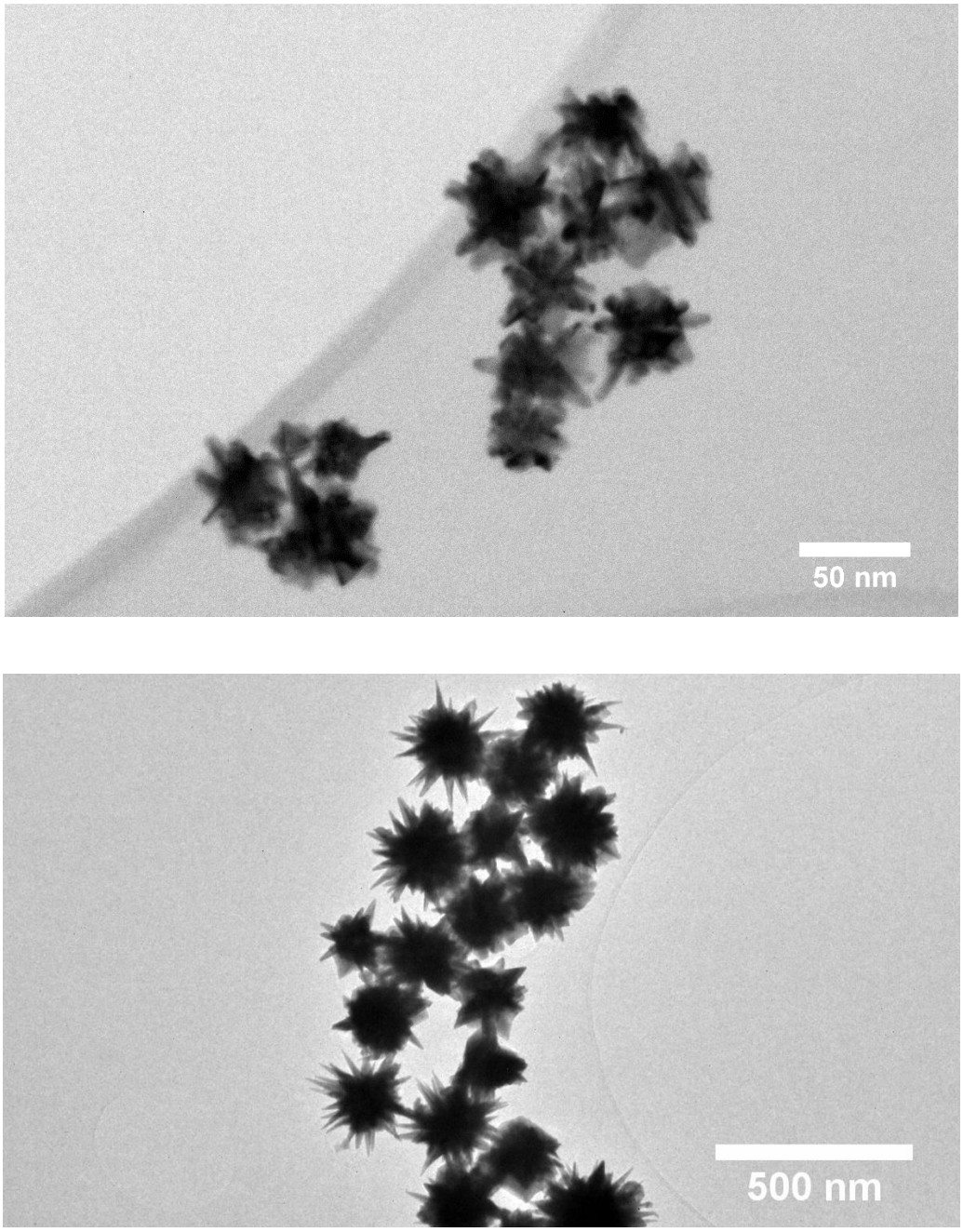


Figure 11: TEM images of (a) S-GNS and (b) L-GNS. Copyright © 2017 American Chemical Society.

Table 2: Morphological characteristics of the GNS. Spike aspect ratio = ratio of width to height.

Copyright © 2017 American Chemical Society.

	Number of spikes	Size (nm)	Core Size (nm)	Spike length (nm)	Spike width (nm)	Spike aspect ratio
S-GNS	8-16	47 ± 17	27 ± 7	10 ± 6	7 ± 3	1.4
L-GNS	14-26	214 ± 90	132 ± 34	60 ± 52	13 ± 12	4.6

GNS of two different sizes were fabricated. TEM characterisation (Figure 11) showed that the GNS had a typical multi-branched shape comprising of a spherical core and several protruding spikes. The morphological characteristics of the GNS, including their overall size (tip-to-tip distance), core size and spike dimensions, were measured using several TEM images using Image J software (National Institutes of Health, 2017) and are summarized in Table 2. For each measurement, 6 nanostars were analysed. The core diameter and tip-to-tip distance were measured twice for each nanostar. Four spikes on each nanostar were chosen at random and the distance between the tip of the spike and its base at the edge of the core was measured as the spike length. The width of the spike was measured at the base. Only nanostars that were clearly defined enough were chosen. The spike aspect ratio describes the ratio of the length of the spike to the width of the spike. In line with previous observations, increasing the size of the gold seed nanoparticles increases the average size of the GNS[193]. Also, the smaller nanostars had fewer spikes with rounder tips compared to the larger nanostars with more spikes that had sharper tips.

6.3.3 Synthesis of self-assembled monolayers of GNS on glass substrates

To be used for a biosensing assay, it was necessary to transfer the nanostars to a glass substrate and investigate their properties in the solid phase. MPTMS modified glass substrates were used to form a monolayer of GNS on the surface of glass substrate surfaces. MPTMS contains Si-OH groups that bind to silanols on the glass surface. The remaining Si-OH groups can bind to other molecules so that the Si-OH groups from a bridge between the glass surface and the attached molecule. To form the self-assembled monolayers, the nanostars were incubated with the MPTMS modified glass slides.

6.3.4 SEM characterisation of GNS on glass substrates

SEM characterisation showed that the GNS were homogenously distributed on the glass substrate (Figure 12). The SEM images show that the L-GNS tended to aggregate more on the glass surface but the nanostars densely populated both surfaces. The nanostars keep their original morphology on the glass substrate.

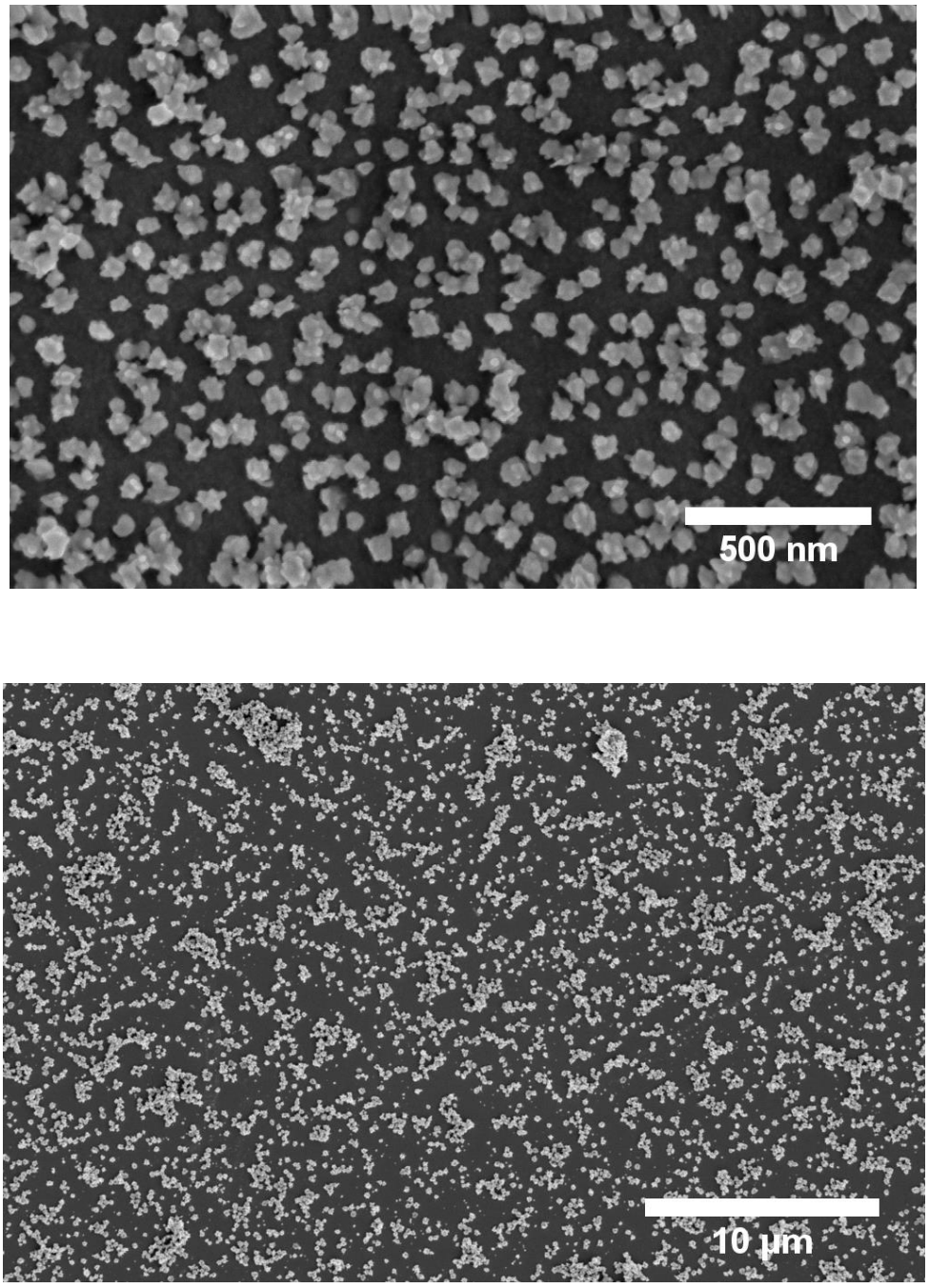


Figure 12: SEM images of GNS substrates fabricated through the self-assembly of (a) S-GNS and (b) L-GNS on MPTMS-coated glass slides. Copyright © 2017 American Chemical Society.

6.4 Summary

In summary, the synthesis of three different nanoscale materials has been demonstrated. The nanotriangular and GCPS arrays were synthesised using the NSL fishing technique. This technique produces a regular ordered PS nanosphere template which is essential for the synthesis of regular nanostructure arrays for biosensing. The structural parameters of all of the nanostructures could be changed by altering steps in the synthesis process. In the next chapter, the way that these nanomaterials interact with light, their optical properties, will be investigated. The impact of altering the structural parameters of the nanostructures on their optical properties will also be demonstrated.

CHAPTER 7: OPTICAL PROPERTIES AND METAL ENHANCED FLUORESCENCE

The optical properties of nanomaterials describe the way the nanomaterials interact with light. Different interactions can be investigated depending on how the nanomaterial is being applied. UV-Vis spectroscopy is a method whereby light is applied to the nanomaterial at a pre-set range of wavelengths. The relative intensity of light that is absorbed at each wavelength can be measured. The peak absorption wavelength is also called the LSPR wavelength as it coincides with the resonant wavelength of the dipole electromagnetic field. In MEF, to achieve the best enhancement factor the LSPR wavelength should be matched to the emission wavelength of the fluorophore.

7.1 Optical properties of gold nanotriangular arrays

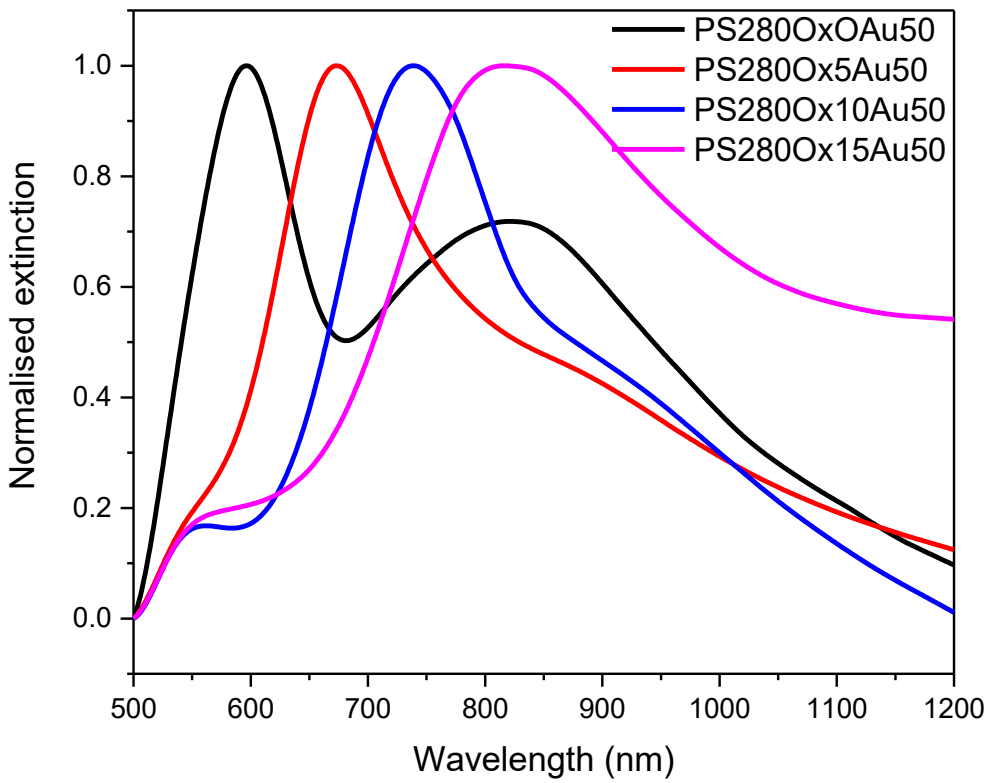
The properties of the nanotriangular arrays were investigated using UV-Vis spectroscopy. The light absorption of the nanotriangular arrays was measured between 400nm and 1200nm using a Cary 5000 spectrometer with baseline correction. The baseline correction is necessary to calibrate the spectroscope. Blank glass was used to calibrate the zero absorption, and a black surface was used to calibrate the 100% absorption level. Nanotriangular arrays made from PS nanospheres of 280, 400 and 500 nm in diameter were studied. The UV-Vis absorption spectrum of the sample provides information about the wavelengths of light that are absorbed by the substrates. The peak absorption wavelength is important for engineering nanomaterials for MEF as it should be matched to the emission wavelength of the fluorophore to give the maximum fluorescence enhancement.

The results of the UV-Vis spectroscopy show that the peak absorption wavelengths of the nanotriangular arrays occur within the visible light (400 to 700 nm) and near infra-red (700 to 2500 nm) regions (Figure 1). Reducing the size of the PS nanospheres with RIE prior to gold deposition, increases the peak absorption wavelength of the nanotriangular array. When the diameter of the PS nanospheres is reduced with RIE, this increases the size of the nanoparticles as the etching process increases the size of the interstices between the PS nanospheres. In other words, increasing the size

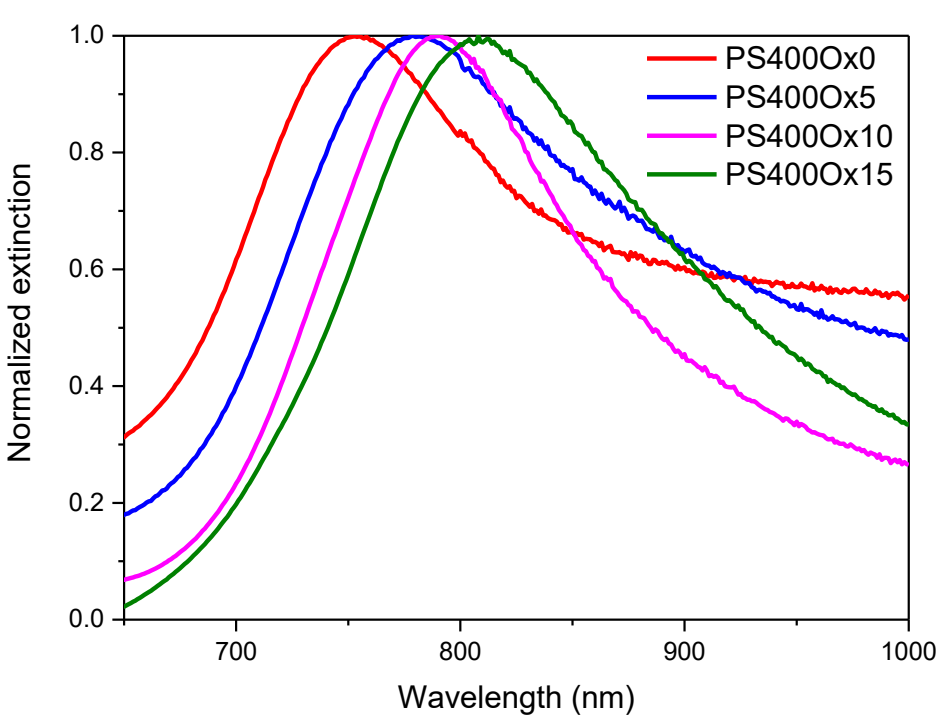
of the nanotriangles causes a red shift in the peak wavelength. The results are summarised in Table 1. As the etching time of the PS nanospheres is increased, the distance between the nanoparticles is also reduced. When the distance between the nanoparticles is reduced, this increases the overlap of the electromagnetic field between adjacent nanoparticles. This is known as a coupling effect. The results of the UV-Vis spectroscopy demonstrate that as the inter-particle distance decreases, there is a red shift in the peak absorption wavelength.

In addition to etching, the size of the nanotriangles can be altered by changing the diameter of the PS nanospheres. Increasing the chosen size of the PS nanospheres also causes a red shift in the absorption wavelength of the nanotriangular array. As the diameter of the PS nanospheres are increased, the area of the interstices between them also increases. Therefore, the size of the nanotriangles increases. Therefore, increasing the size of the nanotriangles by increasing the diameter of the PS nanosphere also leads to a red shift in the peak absorption wavelength of the nanotriangular arrays. These observations correspond with predictions according to Mie theory. The ability to control the peak absorption wavelength by changing the size of the nanoparticles using RIE and selecting the PS nanosphere diameter is a property known as ‘tunability’.

(a)


PS280OxOAu50
PS280Ox5Au50
PS280Ox10Au50
PS280Ox15Au50
Normalised extinction
1.0
0.8
0.6
0.4
0.2
0.0
500
600
700
800
900
1000
1100
1200
Wavelength (nm)

(b)


PS400Ox0
PS400Ox5
PS400Ox10
PS400Ox15
Normalized extinction
1.0
0.8
0.6
0.4
0.2
0.0
700
800
900
1000
Wavelength (nm)

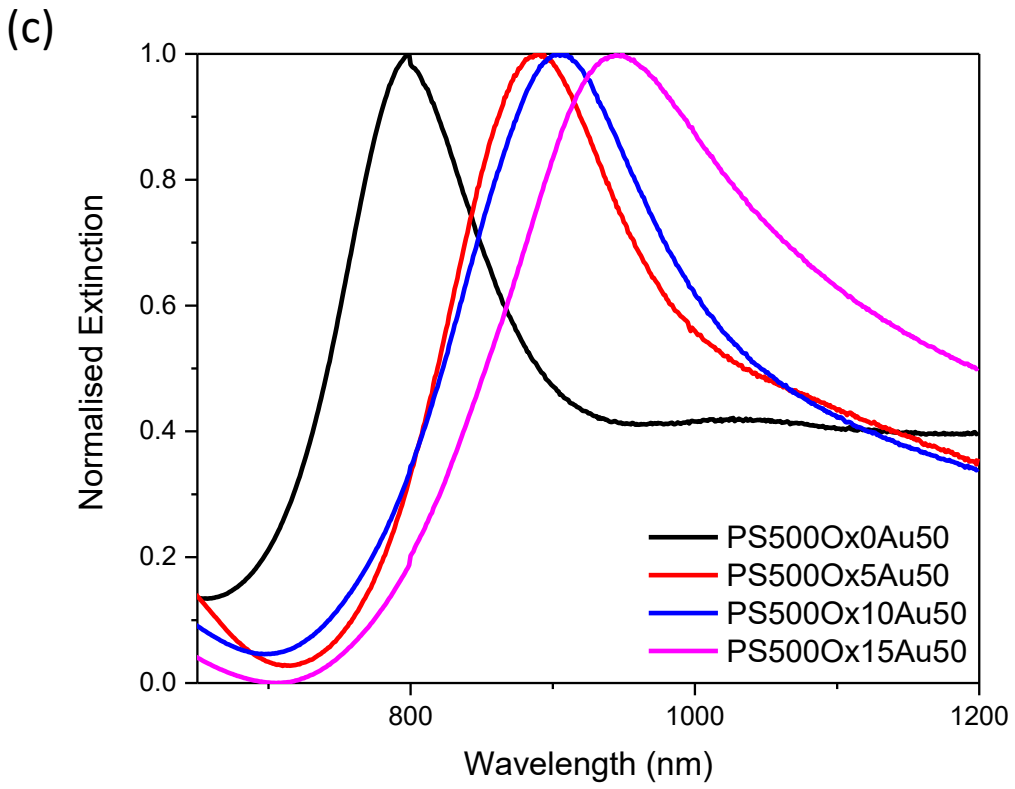


Figure 1: Normalised extinction spectra of Au nanotriangles. (a) 280nm and (b) 400nm (c)500nm polystyrene spheres on glass treated with RIE of duration 0 seconds to 15 seconds were used as a mask template to prepare the nanotriangles on gold. Background absorbance due to glass was measured and subtracted.

Table 1: Extinction peak positions of gold nanotriangular arrays produced with PS nanospheres of different increasing sizes and etching time. Increasing the duration of RIE increases the extinction and causes a monotonic red shift in the plasmon resonance. Increasing the size of the PS nanospheres also causes a red shift in the absorption peak wavelength.

PS size	Etching time (s)	Nanoparticle length (nm)	Extinction peak (nm)
280	0	68	595
280	5	106	674
280	10	111	738
280	15	117	819
400	0	134	756
400	5	164	779
400	10	179	789
400	15	186	808
500	0	149	796
500	5	170	887
500	10	202	904
500	15	215	947

When the oxygen plasma etching time is over 15 seconds, the UV-Vis spectroscopy shows no in-plane dipole peak on the UV-Vis (Figure 2). The SEM characterisation (Chapter 3) shows the reason for this. Instead of separate nanotriangles, a nanohole array is formed. When the PS nanosphere size becomes too small, the interstices between them coalesce and form rings around the PS nanospheres so that nanoholes arrays are formed instead of nanotriangular arrays. The nanohole array does not produce the same absorption peak. The effect is even more pronounced after longer etching times of 30 seconds. To produce nanotriangular arrays, the etching time was limited to 15 seconds.

The optimum increase in etching time was also explored. When measuring the UV-Vis spectroscopy of samples produced by one second intervals of RIE etching time there was an overlap in the absorption peaks (Figure 3). Therefore 5 second increments of etching time were chosen. The overlap is probably due to the quality of the nanoparticle arrays. Therefore, there is no significant detectable difference when the etching time is increase by only one second intervals. As described earlier the sample quality is hindered by defects known as slip dislocations and vacancies and this may be the reason for the lack of differentiation of the peaks seen at one-second increments.

In summary, the ability to tune the absorption wavelength of the nanotriangular arrays by altering the PS nanosphere diameter and the etching time is a very useful property for MEF. To achieve maximum fluorescent enhancement, the peak absorption wavelength should match the emission wavelength of the fluorophore. Therefore, by changing the size of the nanoparticles, the absorption wavelength can be controlled to match the emission of the fluorophore being used. In the next section, the effects of tuning PS nanosphere diameter and etching time on the level of fluorescence enhancement will be explored.

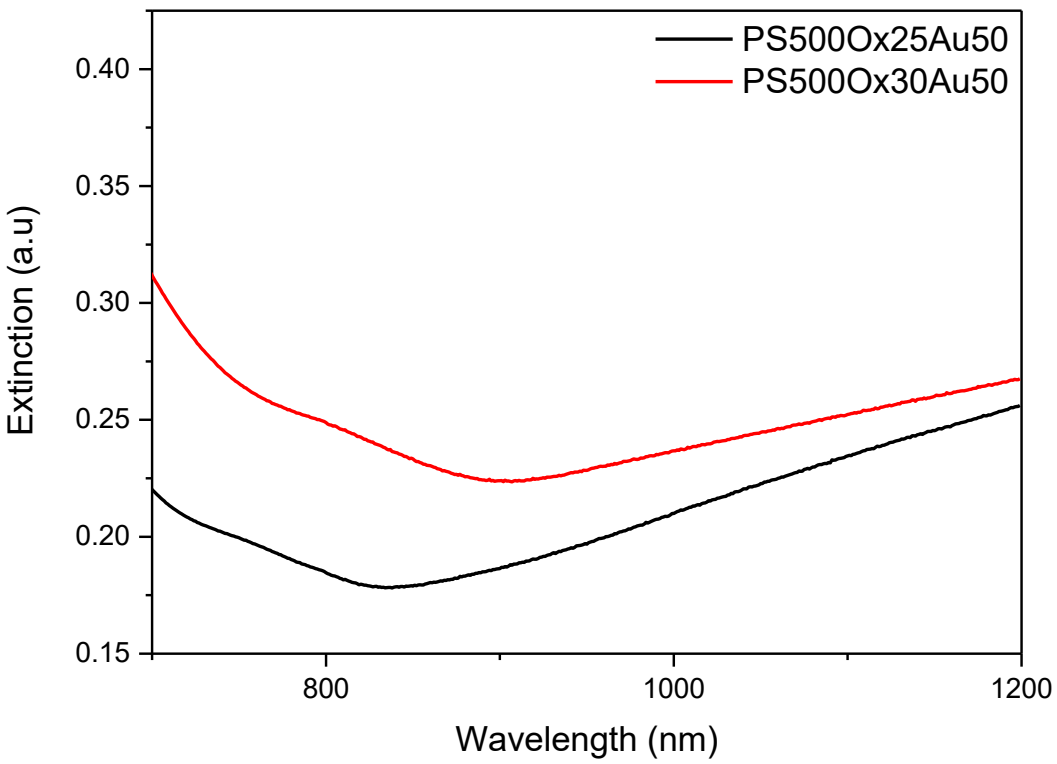


Figure 2: Extinction spectra of Ox25 and Ox30. These show no plasmon resonance peak and this size is therefore the limit of RIE for the use of metal enhanced fluorescence.

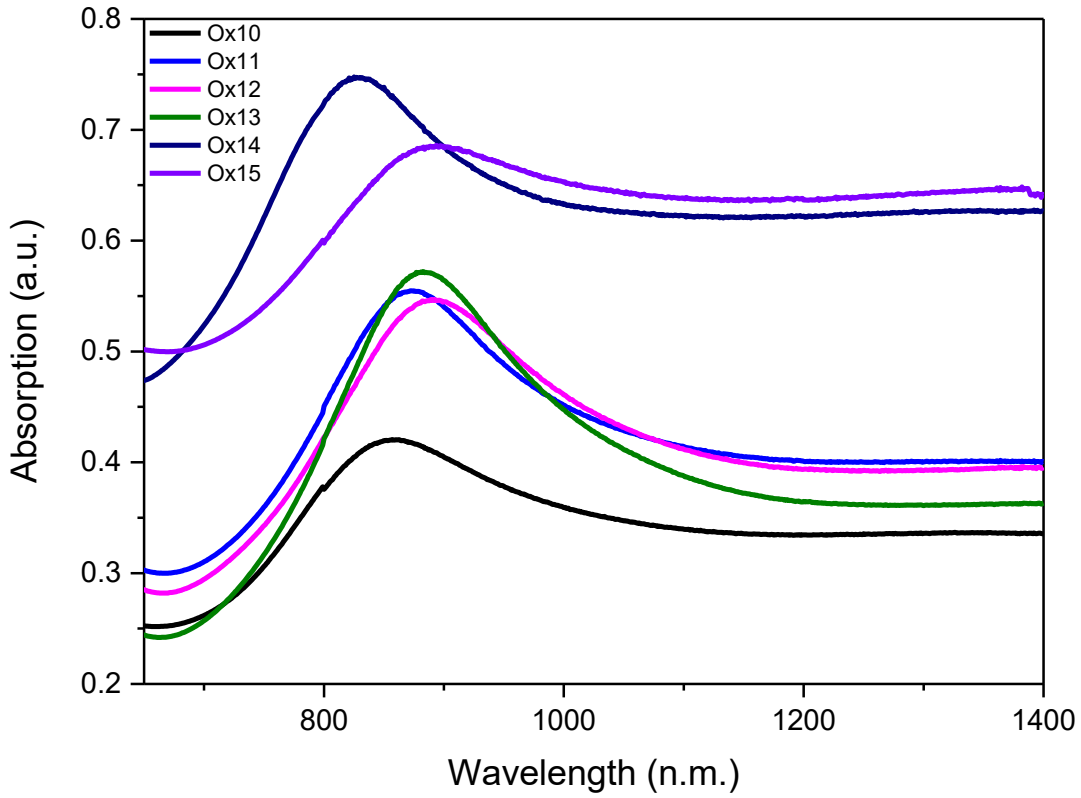


Figure 3: UV-vis of Ox10 to 15 showing no relationship between the size and absorption at this level of optimisation. Absorption spectra were obtained using a Cary 5000i UV-Vis-NIR spectrophotometer equipped with solid sample holder. Background absorbance due to glass was measured and subtracted. Plasmon absorption spectra exhibited only small inter-substrate variation.

7.2 Fluorescence enhancement of nanotriangular arrays

The fluorescence enhancement is a measure that is used to quantify the magnitude of the fluorescence of the nanoparticles when compared to a normal blank glass control that does not contain nanoparticles. It is best tested by attaching a monolayer of fluorophores to both the surface of the nanoparticles and a control substrate and the 2 signals are then compared. A value called the fluorescence enhancement factor is calculated. This value can be used to compare the enhancement factors of different nanostructures. Since a higher enhancement factor should provide a higher detection limit by increasing the sensitivity of a fluorescent assay, the enhancement factor could be selected to produce the detection limit of choice for a given biosensor.

7.2.1 Calculation of fluorescence enhancement factor

Enhancement factor (EF) describes the factor of fluorescence enhancement of the nanoparticle substrate compared to a control substrate, either bulk metal or glass. The derivation of the calculation is described in this section. If the fluorescence intensity of the nanotriangular array is divided by the fluorescence intensity of the control substrate this gives an uncorrected fluorescence enhancement factor:

$$\mathrm{EF} = \frac{\text{Fluorescence intensity (Glass}-\text{nanoparticle}-\text{fluorophore)}}{\text{Fluorescence intensity (Glass}-\text{fluorophore)}} \quad (1)$$

When attaching the fluorophore to the substrate, a spacer molecule is used so create a distance between the fluorophore and the surface of the substrate. If the fluorophore were applied directly to the nanoparticle a quenching effect would be seen. Biotinylated bovine serum albumin (bBSA) has been used as it binds to streptavidin when a streptavidin conjugated fluorophore is used. However,

bBSA is a fluorescent molecule and this background fluorescence needs to be subtracted from the total fluorescent signal when calculating the fluorescence enhancement factor:

$$\mathrm{EF} = \frac{\text{Fluorescence intensity (Glass}-\text{nanoparticle}-\text{bBSA}-\text{AF)}-\text{Fluorescence intensity (Glass}-\text{bBSA)}}{\text{Fluorescence intensity (Glass}-\text{bBSA}-\text{AF)}-\text{Fluorescence intensity (Glass}-\text{bBSA)}} \quad (2)$$

This equation assumes the substrates are of equal size. To counter this, one needs to add in a surface area (SA) correction factor,

$$\mathrm{EF} = \mathrm{SA}\left(\frac{AF}{NP}\right) \times \frac{\text{Fluorescence intensity (Glass}-\text{nanoparticle}-\text{bBSA}-\text{fluorophore)}-\text{Fluorescence intensity (Glass}-\text{nanoparticle}-\text{bBSA)}}{\text{Fluorescence intensity (Glass}-\text{bBSA}-\text{fluorophore)}-\text{Fluorescence intensity (Glass}-\text{bBSA)}} \quad (3)$$

The length of an antibody also provides a suitable spacer distance as the length of an antibody is 10nm [15]. This method was used in some of the experiments. The autofluorescence of the antibodies were measured and found to be negligible. Therefore, the enhancement factor was corrected for the background autofluorescence from the blank glass substrate only as follows:

$$\mathrm{EF} = \mathrm{SA}\left(\frac{AF}{NP}\right) \times \frac{\text{Fluorescence intensity (Glass}-\text{nanoparticle}-\text{fluorophore)}-\text{Fluorescence intensity (Blank glass)}}{\text{Fluorescence intensity (Glass}-\text{fluorophore)}-\text{Fluorescence intensity (Blank glass)}} \quad (4)$$

With bBSA a monolayer of fluorophore is produced. In contrast, the drop drying method causes an uncontrolled distribution of the fluorophore and leads to a mixture of enhancement and quenching effects. Both bBSA and fluorophore conjugated antibodies were used to investigate the enhancement factors of the nanostructures.

7.2.2 Experimental measurement of fluorescence enhancement

The enhancement factor of gold nanotriangular arrays synthesised by NSL has been studied by Xie et al[152]. Three fluorophores were used to investigate the fluorescence enhancement of gold nanotriangular arrays, synthesised with a gold thickness of 100 nm. Biotin was used as a spacer molecule and streptavidin conjugated fluorophores were used. The maximum enhancement factor was 69 times using the fluorophore AlexaFluor 790. The results are summarised in Table 1. With the AF532 fluorophore quenching was observed, i.e. the fluorescence intensity was reduced by the nanotriangular array. This could be accounted by the lack of matching between the peak absorption wavelength of the nanotriangular array and the AF532.

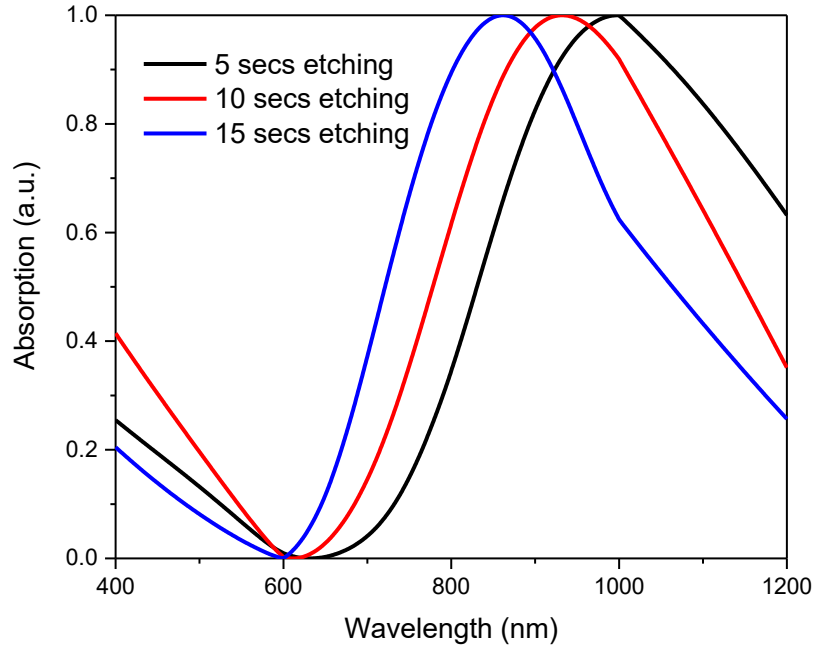
Table 2: Average fluorescence enhancement and quenching factors of streptavidin conjugated Alexa Fluor 532, Alexa Fluor 647, and Alexa Fluor 790 for gold nanotriangular arrays synthesised by NSL (Taken with permission from ref [152]).

Etching time	EF AF532	EF AF647	EF AF790
0 secs	1	2.4	35.8
5 secs	0.6	1.8	48.5
12 secs	0.6	2.0	68.8
30 secs	0.6	1.9	19.2

7.3 Optical properties of gold capped polystyrene sphere arrays

The UV-Vis spectroscopy was carried out for the GCPS arrays synthesised from PS nanospheres of diameters of 280 nm and 400 nm to determine the peak absorption wavelengths. The arrays synthesised using the 280 nm PS nanospheres showed peak absorption mainly in the NIR I (750 to 950 nm) range and the arrays synthesised by the 400 nm diameter PS nanospheres showed peak absorption in the NIR II range (950 to 1400 nm) (Figure 4). For both the 280 nm and 400 nm arrays there was an increase in the peak absorption as the etching time was reduced (Table 3). This is the reverse of the pattern seen with the gold nanotriangular array. This has been observed previously and explained by a coupling effect. In the arrays synthesised with a shorter etching time, the nanoparticles are closer together and this creates a coupling effect between the nanoparticles which causes a red shift in the peak absorption wavelength. It has been reported that etching the PS nanospheres does not affect the size of the nanoparticles on the crown of the PS nanospheres, therefore this is not a factor in the tuning the peak absorption wavelength.

(a)



(b)

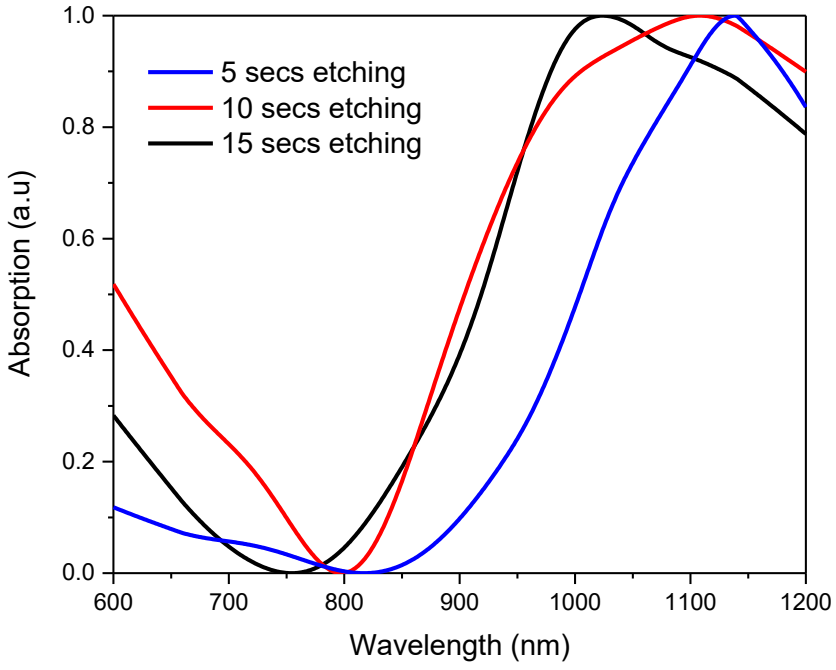


Figure 4: Normalised extinction spectra of GCPS arrays synthesised from (a) 280nm and (b) 400nm polystyrene spheres on glass treated with RIE of duration 0 seconds to 20 seconds. Background absorbance due to glass was measured and subtracted.

Table 3: Measured peak absorption wavelengths and enhancement factors of GCPS arrays.

PS nanosphere diameter (nm)	Etching time	Peak absorption wavelength (nm)	E_f
280	5 secs	997	114
280	10 secs	931	57
280	15 secs	862	45
400	5 secs	1137	n/a
400	10 secs	1111	n/a
400	15 secs	1021	n/a

7.4 Fluorescent enhancement of gold capped polystyrene sphere arrays

The enhancement factor was investigated by drop drying Dylight 800 conjugated IgG to GCPS arrays synthesised from PS nanospheres etched with RIE of increasing etching times. Since the peak absorption wavelengths of the GCPS arrays synthesised with the 280 nm PS nanospheres corresponded with the biological window, only these arrays were investigated (Figure 5). The results show enhancement of the fluorescent signal on all of the GCPS arrays when compared to glass (Figure 6; Table 3). The enhancement factor varies according to the etching time, with the 5 sec etched samples having the best enhancement factor of 114 times.

It has been determined previously that the flat surface area is 2 times smaller than the total surface area of gold deposited on the crowns of PS nanospheres[194]. Therefore, the glass sample used as a control has only half the surface area of the capped nanostructure. The increase in surface area does not account for the enhancement factor of up to 114 times that is observed. The enhancement observed is therefore likely to be a result of a plasmonic effect.

The etching time has an effect on the enhancement factor and therefore there is tunability of the enhancement factor. Etching has an effect on the size of the PS nanospheres. However, using geometrical estimations it has previously been calculated that the diameter of the PS nanospheres does not affect the total exposed area on the PS nanosphere crowns on which gold is deposited. Therefore, the etching time does not affect the size of the gold nanoparticles that are located on the crowns of the PS nanospheres. The change in enhancement factor cannot be attributed to a change in the size of the GCPS array nanoparticles. Also, the change in enhancement factor is not accounted for by the UV-Vis spectroscopy characterisation. The UV Vis spectroscopic characterisation shows that the 5 sec etched array has the longest wavelength peak of 997nm. This is furthest away from the emission wavelength of Dylight 800 at 794nm. Therefore, while the 5 secs etched sample provides the best enhancement factor, this is not explained by matching the emission wavelength of the fluorophore to the absorption peak of the substrate. The presence of ‘hotspots’ between the GCPS

nanoparticles seems to be a prominent factor in determining the enhancement factor. 'Hot spots' can appear in the region between two nanoparticles when two or more nanostructures are within a close distance of each other. These 'hot spots' induce strong electromagnetic fields and in turn they increase the enhancement factor[194]. They occur due the overlapping fields, which produces plasmonic coupling when the nanoparticles are close together. As a result, there is a red shift in the peak absorption wavelength shifts with shorter etching time and larger diameters. As the size of gaps between the nanoparticles is decreased, the number of 'hot spots' also increase to add to the enhancement effect.[194] Furthermore, previous studies also show that as the diameter of the PS nanospheres decreases, the shape of the nanoparticles becomes more planar with a smaller curvature and this has the effect of weakening the field enhancement.

When synthesising the GCPS arrays, the plasmonic effect is thought to be mainly a result of the nanoparticles that are suspended on the insulating PS nanospheres. However, when gold is evaporated onto the PS nanosphere scaffold, gold will invariably become deposited in the interstices between the PS nanospheres as well as on the crowns of the PS nanospheres. Therefore, there may also be a contribution to the enhancement factor by the deposition of gold in the interstices between the PS nanospheres. The deposition of gold in these spaces would produce nanotriangles in a similar way to those produced in the nanotriangular arrays. The possible influence of the interaction between the nanotriangles and capped nanoparticle was evaluated by Zhan et al, 2006[186]. Capped substrates were synthesised and the PS nanosphere template was removed. The absorption of the capped substrate was compared to that of the nanotriangle substrate. The contribution of the nanotriangles was much smaller compared to that of the capped substrate. Any coupling between the capped nanoparticle and nanotriangles should be weak as the distance between them is relatively large. In contrast the distance between the individual capped nanoparticles or nanotriangles is small from where the majority of the plasmonic effect is thought to originate.

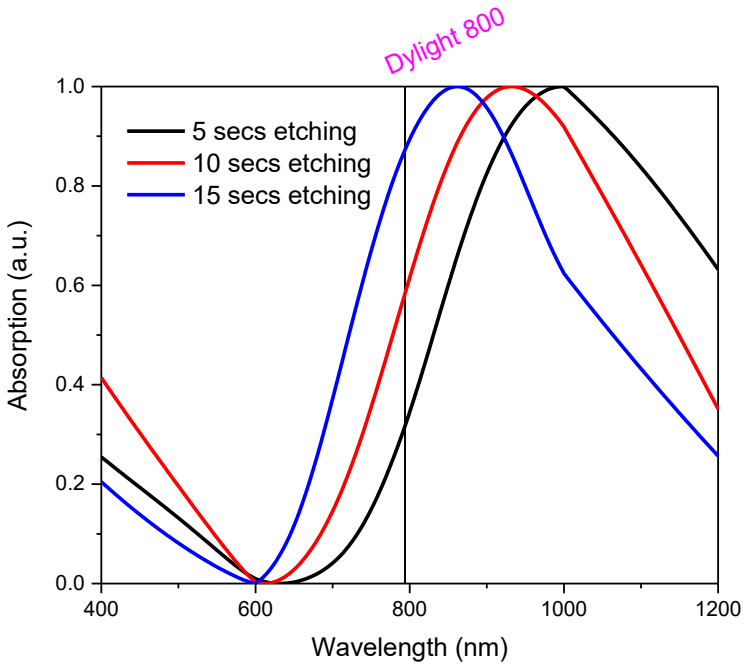


Figure 5: Normalised extinction spectra of GCPS arrays synthesised from 280nm diameter PS nanospheres and increasing etching times. The 794 nm vertical line marks the emission wavelength of Dylight 800.

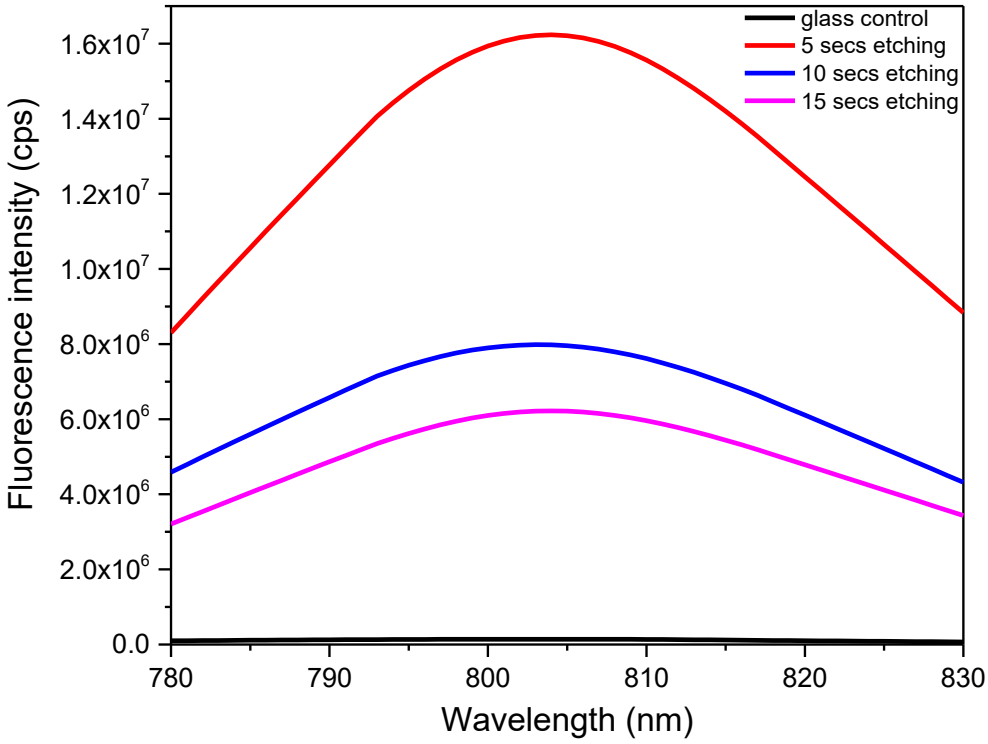


Figure 6: Fluorescence intensity measurements of gold capped polystyrene arrays synthesised with PS nanospheres of 280 nm diameter and increasing etching times.

7.5 Optical properties of gold nanostars

The optical properties of both the pre-cursor gold nanoparticles and gold nanostars were investigated in the colloidal phase (Figure 7). The peak absorption wavelength of the GNPs was both in the visible light region. As expected, the larger nanoparticles had a longer peak absorption wavelength. There was a further red shift in the peak wavelength when the GNPs were converted to GNSs after the growth phase of synthesis. Gold nanostars of two different sizes, S-GNS and L-GNS, were synthesised. The absorption peaks of the S-GNS and L-GNS were 718nm and 1015nm respectively (Figure 7). This is consistent with the results of previous studies[193]. The optical properties of nanostars are thought to be dominated by the tip localised plasmon modes with a contribution from the core structure. This represents two peaks on the absorption spectra. As the contribution from the core plasmon mode is much less, this appears as a shoulder to the main peak originating from the spikes. This occurs at 555nm and 850nm for S-GNS and L-GNS respectively. The main absorption peak that is due to the sharp tips is tunable and dependent on the length and width of the spikes. The longer and wider the average spike length, the higher the peak absorption wavelength. This allowed tuning of the wavelength into the NIR-I region for the smaller GNS and into the NIR-II for the larger GNSs. With absorption peaks within the biological window, such nanoparticles would make ideal candidates for bioimaging and biosensing. To be used for biosensing they were assembled on glass substrates.

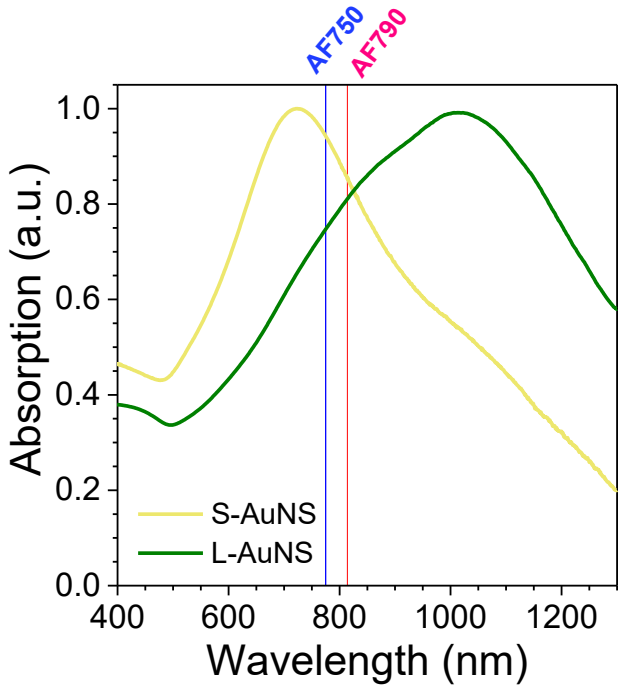


Figure 7: UV-Vis spectroscopy of GNS in solution. Blue and red vertical lines show the emission wavelength of AF750 (blue) and AF790 (red). Copyright © 2017 American Chemical Society.

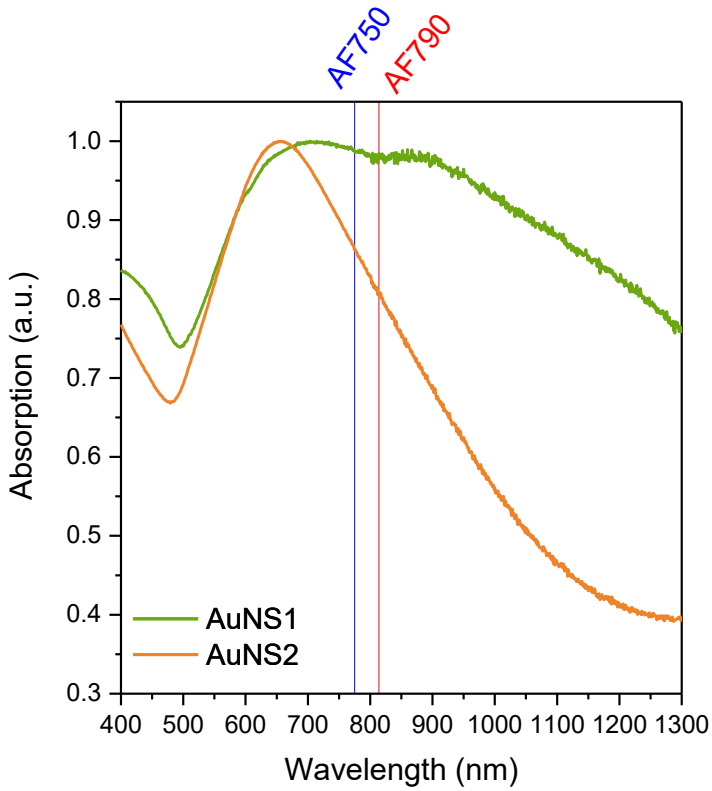


Figure 8: UV-Vis spectrum of S-GNS (green line) and L-GNS (orange) monolayers on glass. Blue and red vertical lines show the emission wavelength of AF750 (blue) and AF790 (red). Copyright © 2017 American Chemical Society.

The optical properties of the dried substrates are shown in Figure 8. Both sizes of nanostars showed a blue shift in the peak wavelength when they were transferred from the solution phase to the solid glass substrate. The peak for the L-GNS became broader possibly due to the greater variability in the distance between the nanostars. The broader wavelength of the L-GNS substrates makes them more compatible for use with fluorophores emitting in the biological window. For S-GNS substrates, the shift was 58 nm on average, which is similar to the blue shift of about 50 nm reported in other studies when monolayers of GNS were grafted onto glass slides[195].

7.6 Fluorescent enhancement of GNS

The fluorescence enhancement of the gold nanostars was measured using the fluorophores AlexaFluor750 and Alexafluor790. The Alexa Fluor dyes are a family of fluorescent dyes that are used commonly used for biological applications[196]. The emission and excitation of these dyes span the visible and near infra-red regions. They can be conjugated to primary or secondary antibodies and therefore may be adapted for use in fluorescent immunoassays.

To measure the fluorescence enhancement, the fluorophores, AlexaFluor750 and Alexafluor790, were conjugated to the surface of the gold nanostars substrates using streptavidin-biotin bonding. Biotinylated albumin consists of albumin protein bound to biotin that is non-specifically attached to amine groups in the albumin. The biotin also binds to gold and glass surfaces by a combination of physioabsorption, electrostatic affinity and covalent binding and it has a strong affinity and specificity for streptavidin. The fluorophores are conjugated to streptavidin, and therefore the function of the biotin is to provide a strong attachment of the fluorophore to the glass and gold surface. It also acts a spacer and provides an optimal distance between the fluorophore and GNS of 8-10nm [143]. If the fluorophore is applied directly to the surface of the GNS, then a quenching effect would occur, and no enhancement would be observed. The enhancement factors were calculated as described in section 7.2.1 and the values are given in Table 4.

The results show that the L-GNS provides the higher enhancement factor with both fluorophores (Figure 9). This is consistent with theoretical calculations that large nanoparticles provide better enhancement. Also, the larger nanostars showed more spikes which are expected to provide a higher

plasmon resonance. A higher enhancement factor was observed when using AF750 compared to AF790. This is likely to be due to the greater overlap of the emission wavelength of AF750 with the absorption peak of the GNS substrate (Figure 8).

The fluorescent enhancement effect is thought to be a result of the electromagnetic resonance near the metallic nanostructure surface. When the metal nanoparticle surface receives energy from external light, electrons within the field oscillate at the same frequency. The electrons are known as surface plasmons and produce another electric field which results in surface plasmon resonance[14]. The enhancement effect is highest at hotspots which occur where the field enhancements of several nanoparticles overlap in small spaces. The sharp branches of nanostars significantly increase the enhancement effect. The improvement in enhancement compared to other types of nanoparticle has led to their use in multiple applications especially in the medical field. The main areas of research are in imaging, biosensing[197], [198][189] and for photothermal transducers in the treatment of cancer[199], [200]. To explore the reason for the enhancement, lifetime measurements were carried out.

7.7 Lifetime measurements of fluorophores conjugated with GNS

The fluorescence decay curves of AF750 and AF790 on the two types of GNS substrates, and control bare glass substrates, are shown in Figure 10. The average fluorescence lifetimes of AF750 and AF790 on blank glass substrates were 0.72 ns and 0.55 ns respectively. The fluorescence lifetimes were reduced for both fluorophores for both types of nanostars. This provides evidence that the enhancement observed is due to a plasmonic effect.

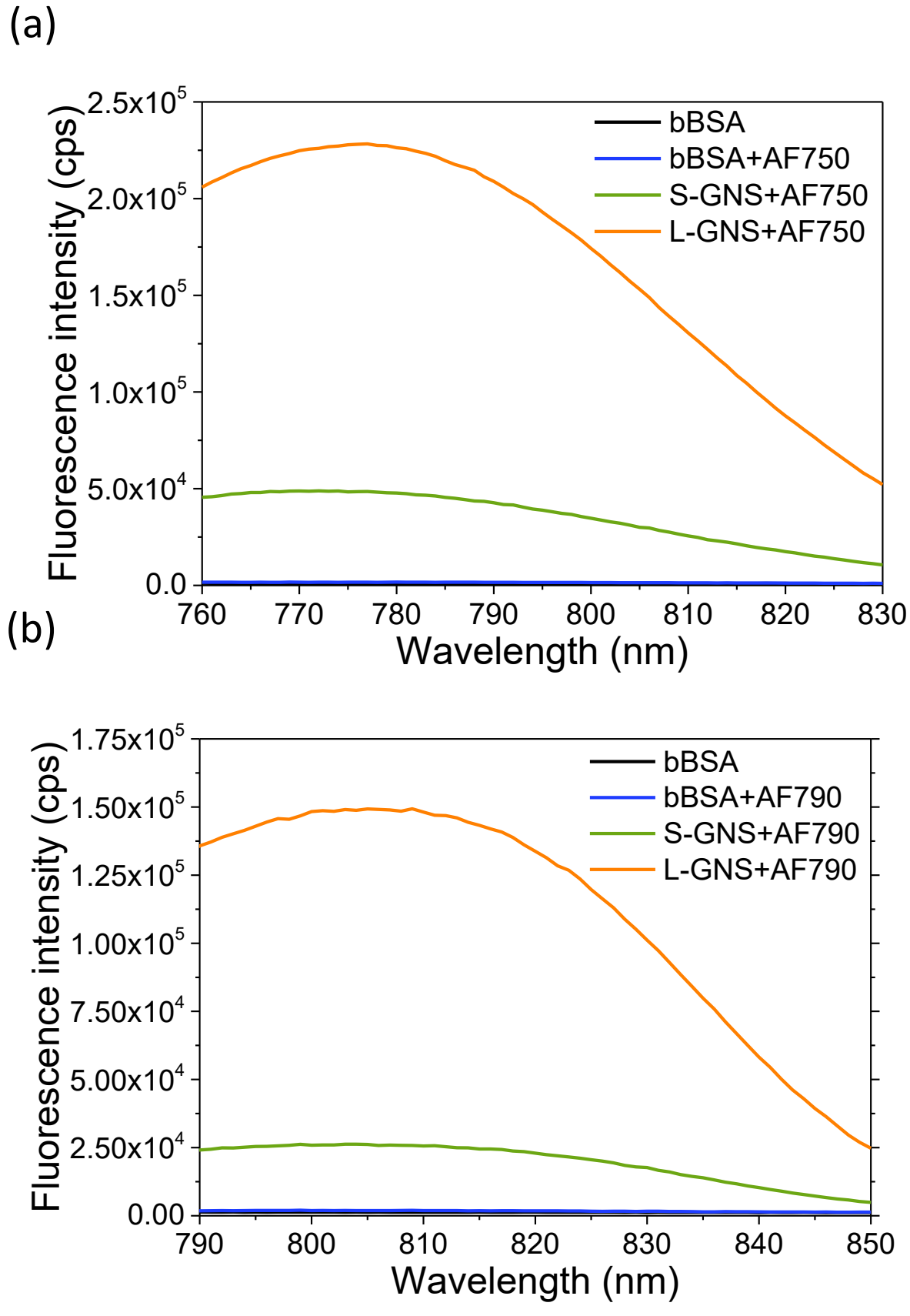
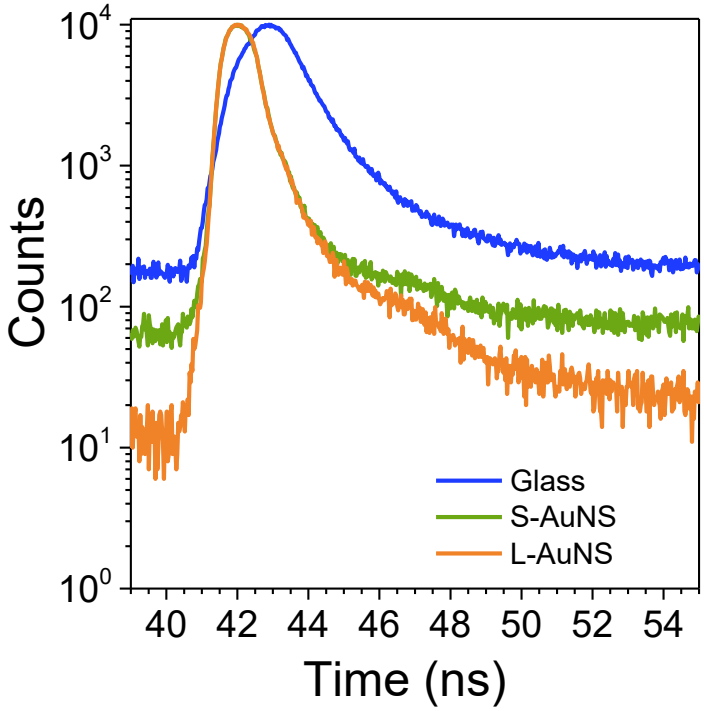


Figure 9: Fluorescence intensity measurements of monolayers of streptavidin-conjugated (a) AF750 and (b) AF790 formed on biotinylated bovine serum albumin (bBSA)-coated glass slides and S- or L-GNS substrates. Copyright © 2017 American Chemical Society.

Table 4: Enhancement factors of gold nanostars using AF750 and AF790 fluorescent dyes. Copyright © 2017 American Chemical Society.

Fluorophore	Substrate	Enhancement Factor (Ef)
AF750	S-GNS	40
	L-GNS	321
AF790	S-GNS	20
	L-GNS	195

(a)



(b)

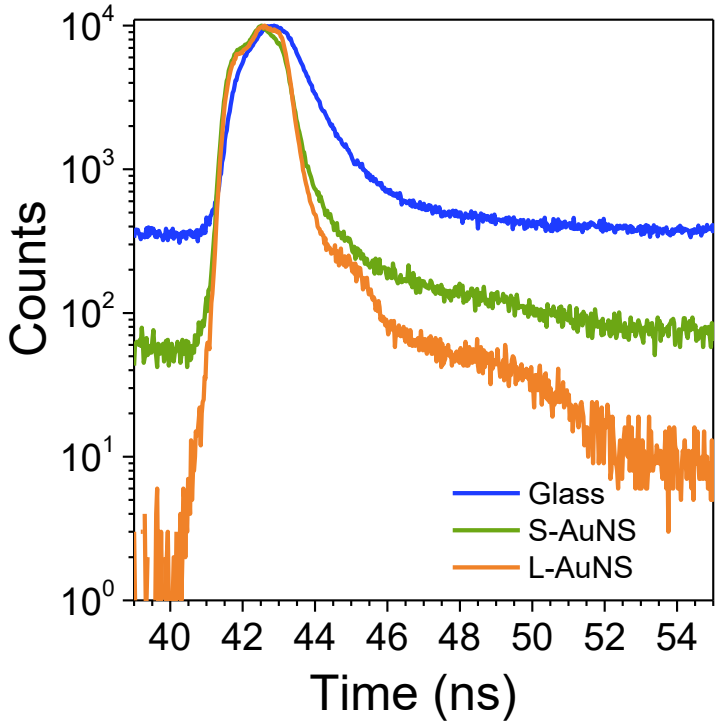


Figure 10: Fluorescence lifetime spectra of streptavidin-conjugated (a) AF750 and (b) AF790 monolayers, immobilized on S- and L-GNS substrates, and on glass surfaces as a control. Copyright © 2017 American Chemical Society.

7.8 Summary

In this chapter, the optical properties and enhancement factors of three different nanostructures has been shown. All structures have the potential to be used for metal enhanced fluorescence on a solid platform which is most useful for immunoassay based sensing. It has also been demonstrated that the gold nanotriangles, GCPS and GNS structures all have optical properties that are tunable. This means the absorption wavelength can be altered so that they fall within the biological window and that they can be matched to the emission wavelength of the fluorophore. In the next chapter, the nanostructures will be used and adapted for biosensing.

CHAPTER 8: PROTEIN ASSAYS

The first step in developing a biosensor is to create a platform for the nanoparticles and the protein of interest. One way of converting the nanoparticles to a platform that is capable of detecting proteins is to develop an analytical protein microarray. Standard analytical protein microarrays consist of a support surface, such as a glass slide, carrying the capture protein. After adding the analyte(s) of interest, a detection probe is added, and this emits a signal according to the amount of protein(s) present. Fluorescent dyes are most commonly used as the detection probe. This method can be converted into a high-throughput process whereby the microarray slide is designed to allow the detection of multiple proteins in parallel. This technique, known as multiplexing, may also be used for detailed analysis of low sample volumes[201], [202], making multiplexing a potentially useful tool for cancer screening. A variety of body fluids could be sampled and tested for the diagnosis of pancreatic cancer including bile and pancreatic cyst fluid, which can only be obtained in small quantities[203]. The expression of a variety of potential candidate biomarkers has already been identified in such fluids that may prove useful for diagnosis of pancreatic cancer[204], [205]. When used in combination, these biomarkers improve the specificity of detecting pancreatic cancer. A multiplexed protein microarray could be designed to detect multiple markers for pancreatic cancer simultaneously. Such a multiplexed microarray would make a highly specific diagnostic test for pancreatic cancer detection.

Unfortunately, current state-of-the-art protein microarrays have low detection limits and therefore lack sensitivity[20][206]. Various methods have been proposed to improve the detection limits of protein microarray assays, based, for example, on enzymatic amplification or carbon nanotube Raman tags[207][208]. Metal enhanced fluorescence (MEF) is emerging as a suitable strategy to improve the sensitivity of protein microarrays. It has been shown that MEF can significantly improve the sensitivity of the protein microarrays. This approach takes advantage of the amplification of fluorescence emission intensity of fluorophores located proximal to plasmonic nanostructures. By selecting

fluorophores emitting in the near infrared range (NIR, 700-900 nm), interference from biomolecule auto-fluorescence is also minimized[137]. Furthermore, the improvement in sensitivity can be achieved without complicating the assay with additional preparation steps or requiring specialized measurement equipment[207] by adding nanoparticles to the support surface platform on which the microarray is based.

Fluorescent enhanced microarrays have been developed for the detection of bowel cancer biomarker, carcinoembryonic antigen (CEA) and three lung cancer biomarkers[20][209]. However, the problem with these fluorescence enhanced microarrays is that they lacked systematic control of the nanoparticle structure and therefore they also lacked control of the corresponding optical properties of the substrate. The microarray substrates used previously were produced using porous gold films formed by using a de-alloying process[20]. In de-alloying, a metal alloy is etched using a corrosive substance to remove one of the constituent metals. This produces pores in the metal surface and, with a sufficient amount of corrosion; the remaining metal is in the form of nanoparticles. Using this synthesis method systematic tuning of the localized surface plasmon resonance (LSPR) of the nanoparticles is limited. Thus, there was no control over the resulting absorption wavelength or fluorescence enhancement factors of the substrate. Being able to control the fluorescence enhancement is the key step for tuning of the wavelength of the substrate so that it falls into the biological window range. It also provides control over maximizing the sensitivity of the substrate as well as controlling the sensitivity of the protein microarray. This is even more important when building a multiplex platform that can detect a combination of proteins. For example, if a multiplex platform were to be built combining the cancer biomarkers carcinoembryonic antigen (CEA) and calcitonin, the nanotriangular array would need to be made from 2 different sized nanotriangles. This is because the normal upper limit for CEA is $3ngmL^{-1}$ and that for calcitonin is $10pgmL^{-1}$. To cover the dynamic range of both biomarkers a substrate would need to be made of 2 different sized nanotriangles. This can be achieved using the NSL method described previously. Having control over the tunability of the

nanotriangular arrays also has another advantage. It provides reproducibility so that there is minimal difference between any two substrates. This is an important property if the substrates are used for diagnostics so that the results are reproducible.

For the first time, the synthesis of tunable protein microarrays is demonstrated using NSL, the method of nanoparticles synthesis used in this project. In this chapter, firstly, the development of a highly sensitive assay for the pancreatic cancer tumour marker CA 19-9 is described using the gold nanotriangular array synthesised using NSL. Secondly, the ability to control the absorption wavelength and therefore the enhancement factor, by changing the size of the gold nanotriangles, is demonstrated. In the second part of this chapter, the tunable GNS are used for CA 19-9 detection.

8.1 Gold nanotriangular array

Firstly, the development of an assay to the pancreatic cancer biomarker CA 19-9 is described using the gold nanotriangular arrays.

8.1.1 Drop-dry calibration of fluorophore conjugated antibody

The fluorescent enhancement of the nanotriangular substrates at different concentrations of fluorophore was determined by drop drying the fluorophore conjugated donkey anti-rabbit antibody onto the substrates. The separation distance provided by the IgG molecule between the fluorophore and nanotriangular substrate is estimated to be between 0 and 10nm and the result is therefore a combination of enhancement and quenching effects[20]. The actual distance is dependent on the orientation of the antibody on the substrate. Fluorescence emission spectra were obtained from unpolarized light using a Fluorolog Tau 3 system from HORIBA Jobin Yvon with 450W Xenon lamp excitation. Fluorescence spectra were corrected for the spectral response. The nanotriangular substrate was compared to glass. Concentrations of between 10^{-6} and 10^{-10} M at 0.5 M intervals were used for the fluorophore conjugated antibody. The results show that the nanotriangular array increases the dynamic range of quantification of the fluorophore concentration when compared to

blank glass (Figure 1). The detection limit was $10^{-8.5}$ M on glass compared to 10^{-9} M on the nanotriangular array. This is a result of both quenching and enhancement as the orientation of the fluorophore cannot be controlled and the distance between the fluorophore and nanotriangular array therefore varies between 0 and 10nm, which is the length of the IgG molecule. Despite this the drop dry calibration curves show a definite improvement in the detection limit of the nanotriangular arrays compared to the glass.

8.1.2 Conjugation of immunoassay to nanotriangular array

Once it was established that the nanotriangular substrates could potentially enhance the fluorescence and the detection limit, a method of conjugation between the nanotriangular array and a protein immunoassay was developed. The aim of using a protein immunoassay in conjugation with the nanoparticles was to make the fluorescence intensity, protein concentration dependent. The nanoparticles could therefore be used to detect the levels of the protein to which the immunoassay is targeting, with the aim of improving the detection limit of such an assay.

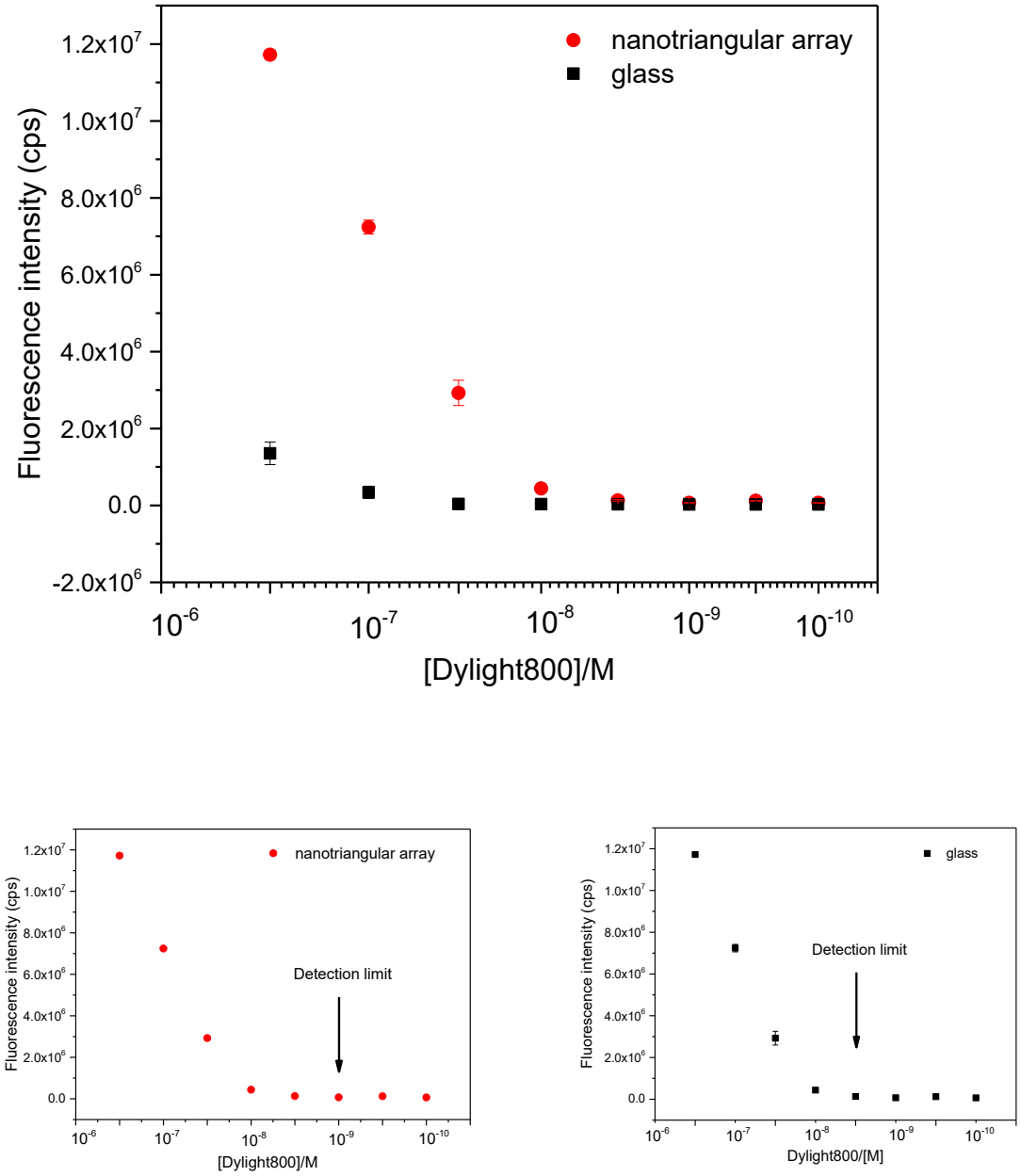


Figure 1: Scatter plots to show the results of the drop dry calibration tests using nanotriangular arrays synthesised from 400 nm diameter PS nanospheres etched for 5 secs. (a) Scatter plot to compare the detection limits on glass and nanotriangular array (b) calibration plot on glass (c) calibration plot on nanotriangular array.

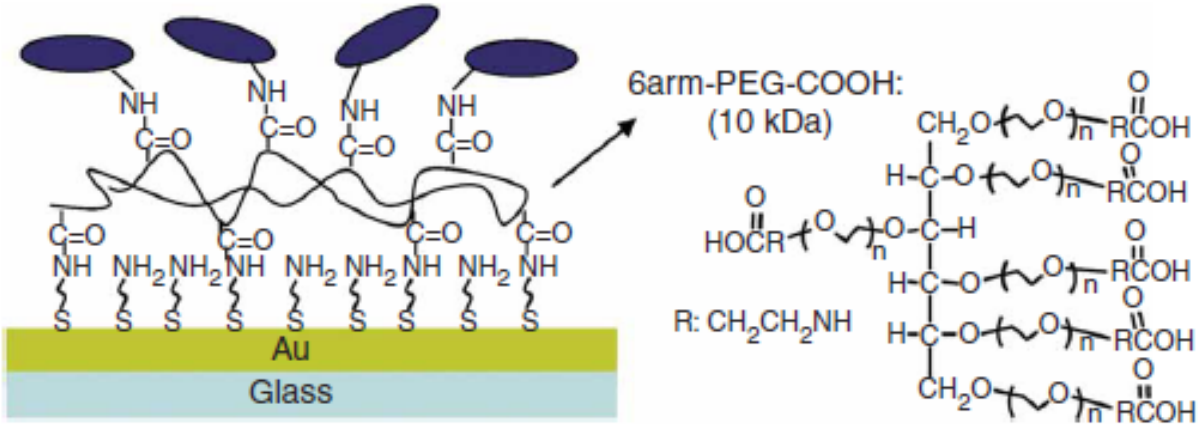


Figure 2: PEG-amine conjugation chemistry of immunoassay with nanostructured substrate (Taken with permission from ref [207]). On the left, the blue ellipses represent the capture antibody, with amine groups binding to carboxylate groups in the PEG.

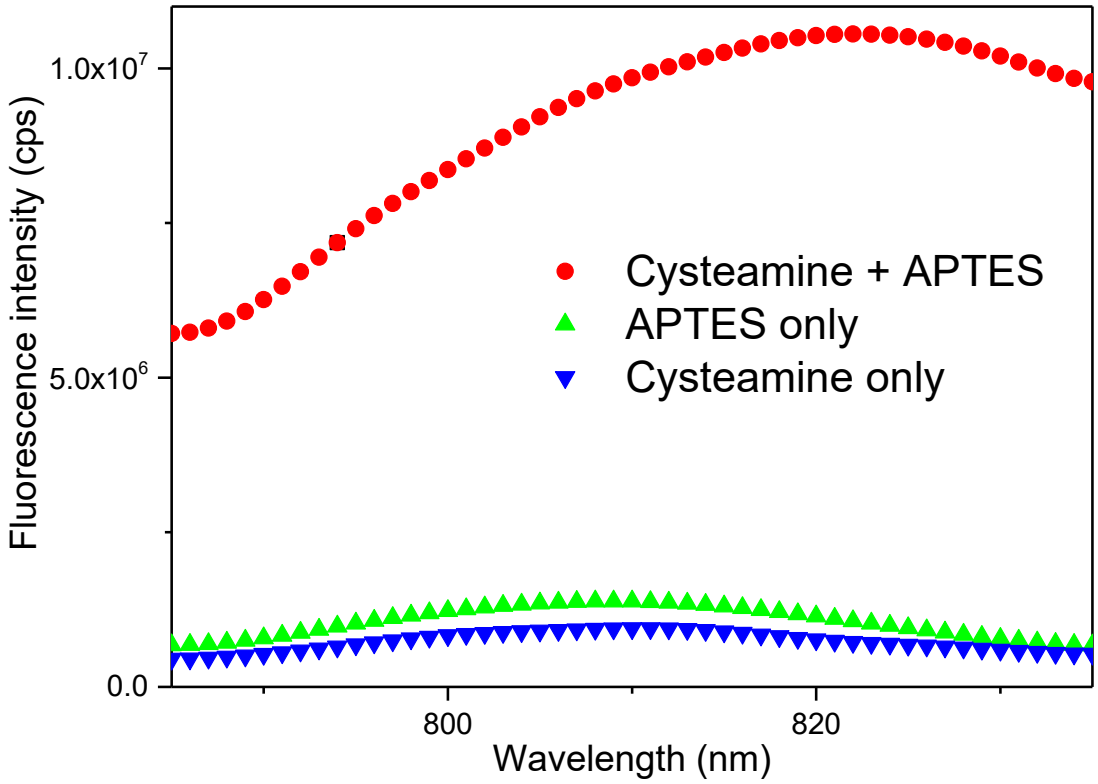


Figure 3: Scatter plot showing the difference in conjugation comparing cysteamine only (blue), APTES only (green) and APTES + cystemine (red). Combination of cysteamine and APTES dramatically improved the level on conjugation.

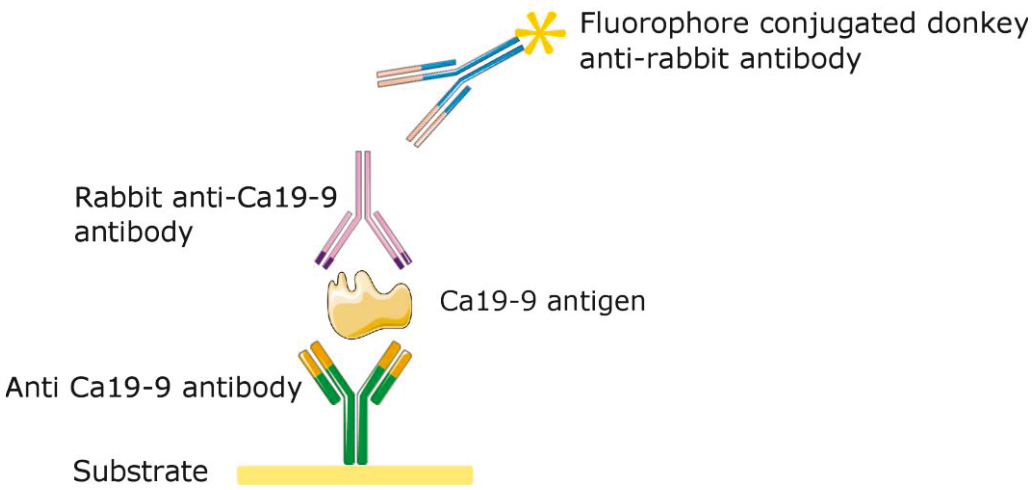


Figure 4: Schematic diagram to show indirect sandwich immunoassay for CA 19-9 conjugated to the nanotriangular substrate.

8.1.3 Traditional immunoassay methods

Immunoassays may be either competitive whereby the antigen of interest is displaced by a label in binding competition, or immunometric where the analyte is labelled directly. Radioimmunoassays, commonly used in clinical laboratories, are an example of a competitive assay. A radioactive labelled antigen competes with an unlabelled antigen in the sample, for binding sites on high affinity antibodies. The radioactive signal is inversely proportional to the amount of antigen in the sample. The immunometric methods are relatively more sensitive than competitive assays and the enzyme-linked immunosorbent assay (ELISA) is an example. In the ELISA method, the capture antibody is immobilised, usually on a 96-well plate. This is followed by a blocking step. After the analyte is added and incubated, the plate is washed. The primary detection antibody is added and then labelled with an enzyme. The most common enzymes used are horseradish peroxidase (HRP) and alkaline phosphatase (ALP). These convert a substrate into a species that can be detected by its change of colour or fluorescence. The enzyme is conjugated to the primary antibody either using biotin and streptavidin binding or using a secondary antibody. ELISA immunoassays are currently used clinically for testing for Hepatitis C, HIV and some tumour markers including prostate specific antigen (PSA) and the pregnancy test that detects human chorionic gonadotrophin. Protein microarrays whereby multiple proteins can be detected simultaneously are being used in proteomics research and also diagnostics. The benefits of ELISA are that the measurement can be automated, but the disadvantage of ELISA is the poor sensitivity, particularly with colorimetric assays. Though the fluorescence ELISA can be used for multiplexing, currently these require large sample volumes of up to 200 µL.

8.1.4 Development of conjugation chemistry

For the conjugation of the protein to the nanoparticle array, poly(ethylene glycol) (PEG) conjugation chemistry was used. PEG is a polymer which has many different uses. It is widely used in bioengineering to create bonds between proteins and synthesised surfaces. PEG can be produced using a range of end molecules depending on the surface chemistry. In Tabakman et al, 2011[20], a six-arm, carboxy-PEG molecule was used. The free carboxy groups on the PEG bind to amine groups

present in proteins (Figure 2). Using a PEG molecule with 6 arms multiplies the number of binding sites for the binding of the capture antibody. Amination is the process of adding amine groups to a surface. Amination of the gold nanotriangular arrays was achieved using cysteamine. The amine groups provide a binding site for the PEG on the surface of the substrate. In this way, the 4-arm PEG binds the substrate and provides three remaining arms to attach to amine groups in the capture antibody. Potentially each 4-arm PEG molecule binds more than one capture antibody, increasing the detection of the antigen further. Experimentation showed that while this was enough to achieve an all or nothing response on the substrate, this did not allow concentration calibration (data not shown). Since a large surface area of the substrate is covered by glass, which is not covered by gold, APTES was also used to aminate the exposed glass surface in combination with cysteamine. APTES is a chemical that is used to aminate the surface of the glass. Combining APTES with cysteamine for the amination process provided a significant improvement in the conjugation of protein. To demonstrate this, the fluorophore conjugated IgG was applied to the nanoparticle array functionalised with cysteamine, APTES and a combination of cysteamine and APTES. After incubation with PEG and then Dylight800 conjugated IgG, the combination gave the highest fluorescence intensity, which demonstrates a higher surface area of conjugation (Figure 3).

8.1.5 Conjugation of sandwich fluorescent immunoassay

Firstly, it was important to evaluate whether the distance provided by the immunoassay would allow enhancement between the fluorophore and the nanoparticle array. This distance was estimated to be 40 nm. The substrates synthesised using 400 nm diameter PS nanospheres were used as the absorption wavelength falls within the biological window. The fluorescent enhancement was investigated at different depths of gold evaporation. One hundred nanometers of gold deposition provided 2 orders of magnitude of enhancement and was used for subsequent experiments. Dylight800 (excitation 777 nm; emission 794 nm) was used as the fluorophore as its emission wavelength falls within the biological window. The chosen wavelength therefore avoids auto-

fluorescence from biological samples while providing matching between the fluorophore and the nanotriangular array.

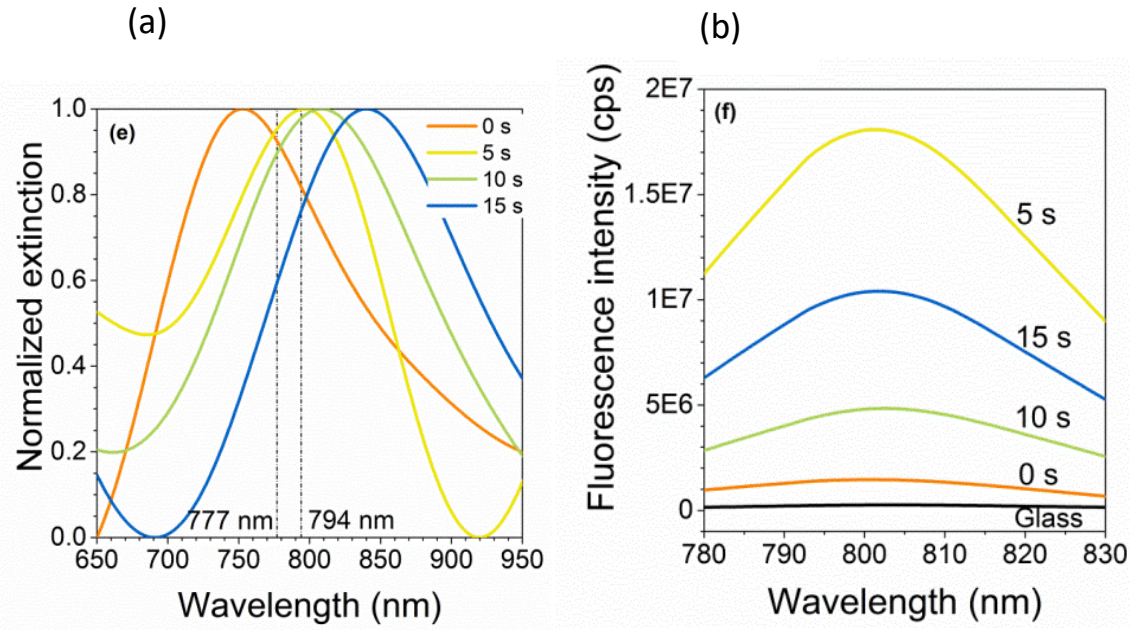


Figure 5: (a) shows the LSPR wavelengths of nanotriangular arrays produced with increasing etching times and excitation/emission wavelength of Dylight 800 (b) shows the relative enhancement produced by these nanotriangular arrays when compared to glass.

Table 1: Structural parameters of nanotriangular arrays synthesised with 400 nm diameter PS nanospheres with increasing etching times. Absorption peak wavelength and corresponding enhancement factors are also given.

Etching time (s)	*α* (nm)	*s* (nm)	Absorption Peak (nm)	Enhancement factor (EF)
0	134 ±15	98 ±15	745	12
5	164 ±18	60 ±10	796	82.5
10	179 ±14	46 ±5	805	29.9
15	186 ±13	23 ±10	846	36.5

8.1.5.1 Sandwich detection immunoassay

Once it was established that IgG antibody could be attached to the nanotriangular substrate and withstand the washing process, an indirect sandwich assay (Figure 4) was developed for CA 19-9. The aim was to investigate whether a fluorescent immunoassay to CA 19-9 could reproduce the fluorescent enhancement seen with the drop drying of fluorophore conjugated antibody . The immunoassay protocol was based on the method published by Tabakman et al, 2011[20], for the detection of CEA (carcinoembryonic antigen). To prepare protein microarrays on the gold nanotriangular arrays, their surfaces were first modified by amination and then 4 arm branched PEG-carboxylate as described in section 6.1.3. The PEGylated substrates were incubated with monoclonal mouse anti-CA 19-9 immunoglobulin G (IgG) which was used as the capture antibody. The substrates were then blocked overnight at 4 °C, and then incubated with 15.4 UmL-1 of CA 19-9 in PBS. The substrates were then incubated with polyclonal rabbit anti-CA 19-9 antibody, followed by washing and incubation with DyLight 800-conjugated donkey anti-rabbit antibody. The fluorescent immunoassay was conjugated to nanotriangles of different sizes for two reasons. Firstly, to check whether there was any enhancement and to investigate whether the enhancement is tunable. Nanotriangles produced using 400 nm PS nanospheres with increasing etching times were used as the peak absorption wavelength of these arrays were within the biological window (Figure 5). The conjugated immunoassay was applied to the substrates and the enhancement factor was found to vary according to the size of the nanoparticle. The best enhancement factor was 82.5 times with nanoparticles that were etched for 5 seconds. The extinction peak of these nanoparticles was 796nm which is closest to the emission peak of the fluorophore used Dylight800 which is 794nm. The 15 second etched sample provided the second best enhancement factor of 36.5 times. The inter-particle distance for nanotriangles produced with 15 second etching time was on average 23 ±10 nm (Table 1) and is the smallest distance for all the nanotriangles. This observation is consistent with theoretical models that describe that the enhancement factor depends on the nanoparticle shape, size and inter-particle separation. The inter-particle separation has an effect on the local electromagnetic field

enhancement. A smaller gap size causes plasmon coupling and significantly enhances the field close to the nanoparticle[210]. Using theoretical calculations, the highest fluorescence enhancement has been observed with a gap size of 10nm, using similarly shaped nanoparticles.

The enhancement factor appears to be dependent on a combination of the absorption peak wavelength and the nanoparticle morphology. The overlap of the emission wavelength of the fluorophore with the LSPR of the metal nanoparticles is essential and the nanoparticles with 5 seconds of etching that meet these criteria give the best enhancement. Those nanoparticles that were produced by etching for 15 seconds have the smallest inter-particle separation but the extinction peak is 846nm and is further away from the emission wavelength of the fluorophore used, Dylight800, 794nm. The enhancement factor is therefore a combination of the optimal wavelength and the nanoparticle size. These results imply that the enhancement factor can be tuned according to the etching time used.

MEF is the most likely reason for the increase in enhancement that is observed. MEF occurs due to coupling between the surface plasmon resonance band of metal nanostructures and the emission band of adjacent fluorophores[180]. The surface plasmon resonance band is a result of charge density oscillations present around metal nanoparticles. This leads to an increased excitation of the fluorophore. The fluorophore exhibits an increased fluorescence quantum yield, decreased lifetime and better photostability[14].

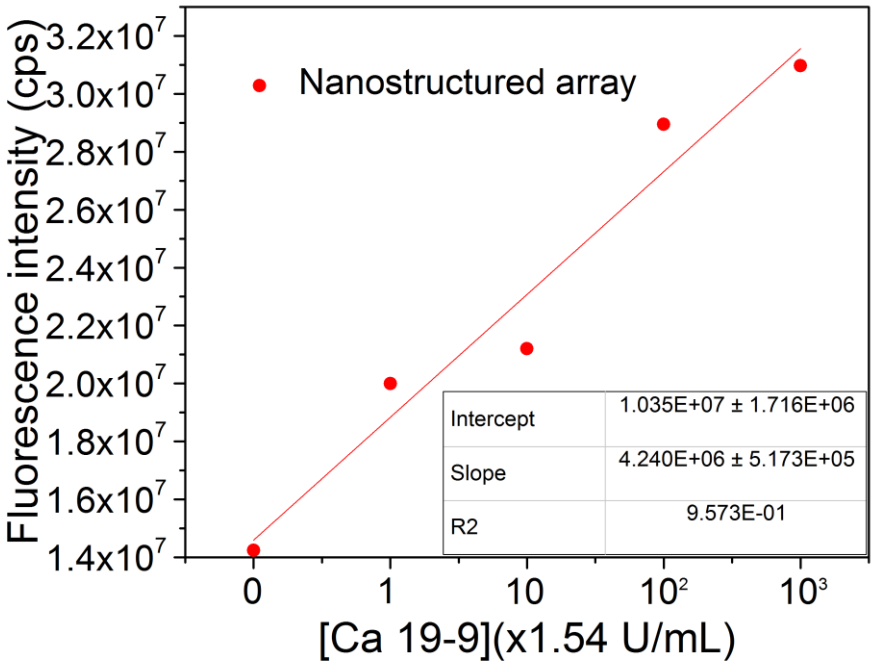
The nanotriangular array has a higher surface area than the blank glass control. The increase in enhancement on the nanotriangular array may be a result of a higher number of fluorophores on the surface of the substrate. However it has been calculated previously that the nanotriangular array has a surface area that is 123% higher than the blank glass control[152]. This would give an increase in enhancement of only 1.23 times. Therefore, the increase in surface area cannot account for all of the increase in enhancement that is observed.

The NSL technique described previously provides a highly controllable method of nanofabrication. This is achieved due to the tunability of the nanoparticles. When the dimensions of the gold nanotriangles are changed by altering the size of the PS nanospheres used, or the oxygen plasma etching time, the peak absorption wavelength is altered. This in turn alters the enhancement factor of the substrate and also the sensitivity.

8.1.5.2 Concentration dependent assay

Once it was established that the immunoassay could produce fluorescent enhancement, the assay was used with increasing concentrations of the antigen CA 19-9 to determine whether the fluorescence intensity is concentration dependent and increases with increasing amount of antigen. Figure 6a shows that between concentrations of 0 and 1540 Uml^{-1} there is a linear relationship between the fluorescence intensity and the concentration of CA 19-9 and the dynamic range is 5 orders (R^2= 9.57). These results show that the limit of detection is 0.4 Uml^{-1}. When the same assay was carried out on glass substrates (Figure 6b) there was also a linear relationship between the signal intensity and the concentration of CA 19-9. However, this was only observed at higher concentrations, between 15.4 and 1540 UmL^{-1}. The background signal was very high, and the detection limit is significantly higher than on the nanoparticle arrays. This can be explained by the presence of metal enhanced fluorescence on the nanoparticle array. This increases the sensitivity of the assay and therefore increases the detection limit on the nanoparticle array when compared to glass.

(a)



(b)

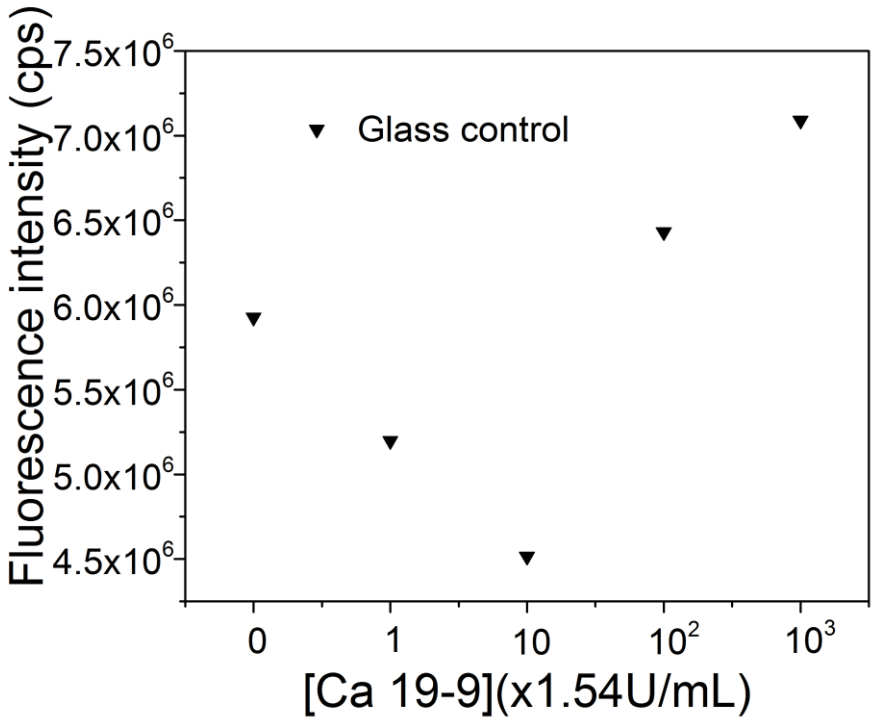


Figure 6: (a) Calibration curve for CA 19-9 immunoassay on nanotriangular array with line of best fit (b) Calibration curve of CA 19-9 immunoassay on blank glass controls.

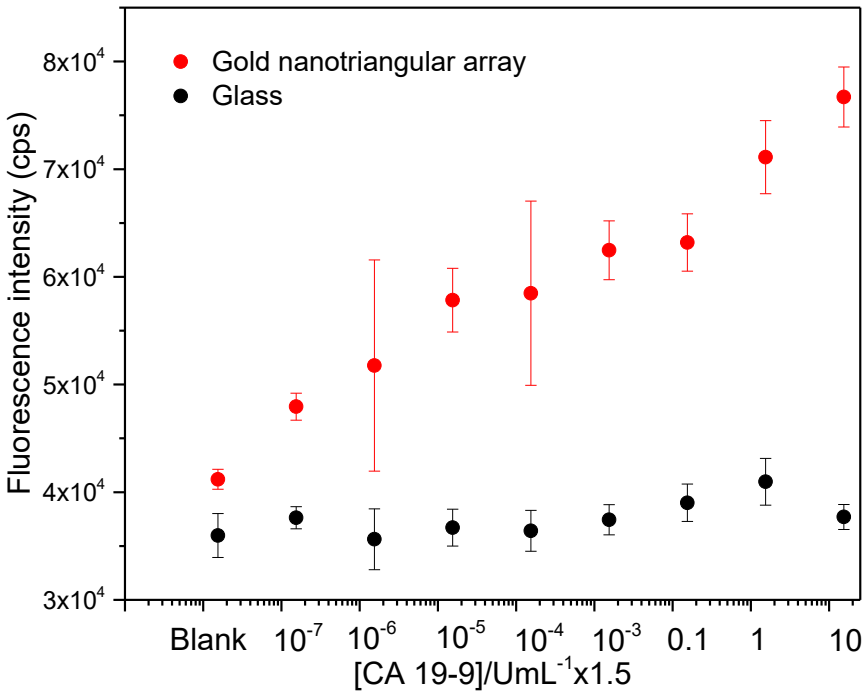


Figure 7. The relationship between fluorescence intensity and CA 19-9 concentration using glass compared to gold nanotriangular arrays. Integrated fluorescent intensity was calculated and points represent the mean of four measurements.

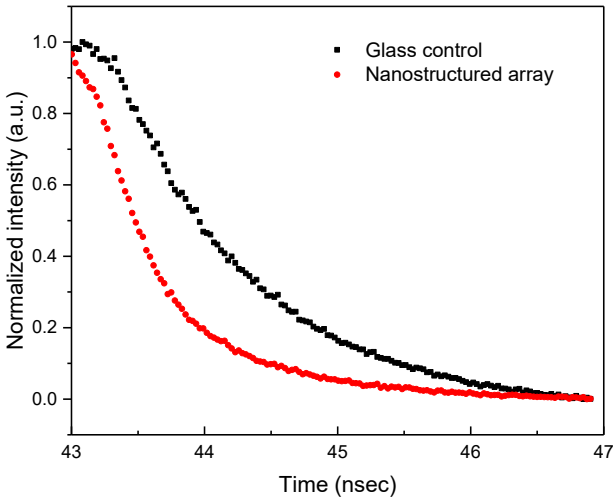


Figure 8: Fluorescence decay curves of Dylight800 on nanostructured array (red) and glass slide (black).

8.1.5.3 Lowering the detection limit

To increase the sensitivity of the substrate further it was necessary to reduce the background signal. One way to do this was to reduce the amount of fluorophore used in the assay; another way was to improve the blocking technique. The results are shown in Figure 7.

By reducing the fluorophore concentration and optimising the concentrations of the other components in the assay, the sensitivity of the substrate increased. Based on these results, the limit of detection improved by six orders of magnitude, to 0.0000005 UmL^{-1}. The linear range was between 10^{-7} and 10^{-1} UmL^{-1}. This detection limit is the lowest reported for CA 19-9.

8.1.5.4 Excited state lifetime analysis

To investigate the mechanism of fluorescence enhancement, the excited-state lifetime for the fluorophore used in the immunoassay was measured by time-correlated single photon counting (TCSPC). In fluorescence enhancement a reduction in the lifetime is expected. The quantum yield of a fluorophore (Q_0) is defined as the ratio of the radiative decay rate (k_{rad}) to the total excited state decay rate,

$$Q_0=k_{rad}/[k_{rad} + k_{nr}] \qquad (1)$$

where k_{nr} is the non-radiative decay rate and the excited state lifetime is given by

$$(k_{rad} + K_{nr})^{-1} \qquad (2)$$

When the Dylight800 conjugated immunoassay was used to determine the lifetime, a reduction in the lifetime was observed from 880 ps in free space, to 58 ps (Figure 8). This decrease may be due to an increase in radiative decay due to fluorophores coupling to the gold nanotriangular array to increase the quantum yield. This provides further evidence that the observed enhancement is a result of metal enhanced fluorescence.

8.1.5.5 Specificity

To evaluate the specificity of the fluorescent immunoassay, the assay was tested using both albumin and GPC-1 as the antigen instead of CA 19-9 (Figure 9). GPC-1 has been recently been identified as another biomarker with levels that increase in pancreatic cancer[5].

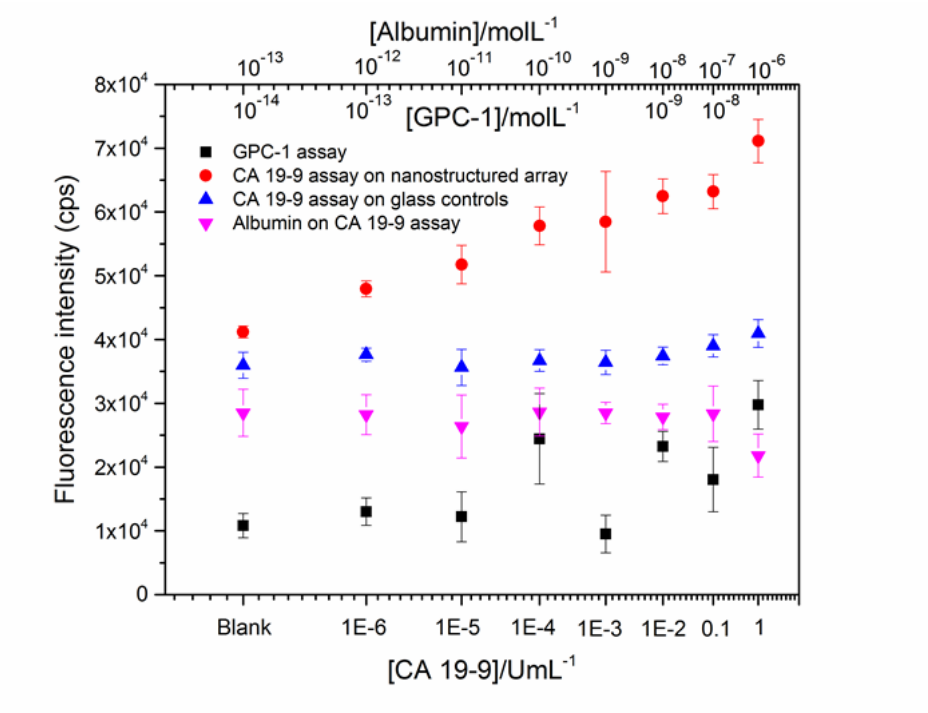


Figure 9: Specificity test of CA 19-9 assay using albumin and GPC-1 as antigens.

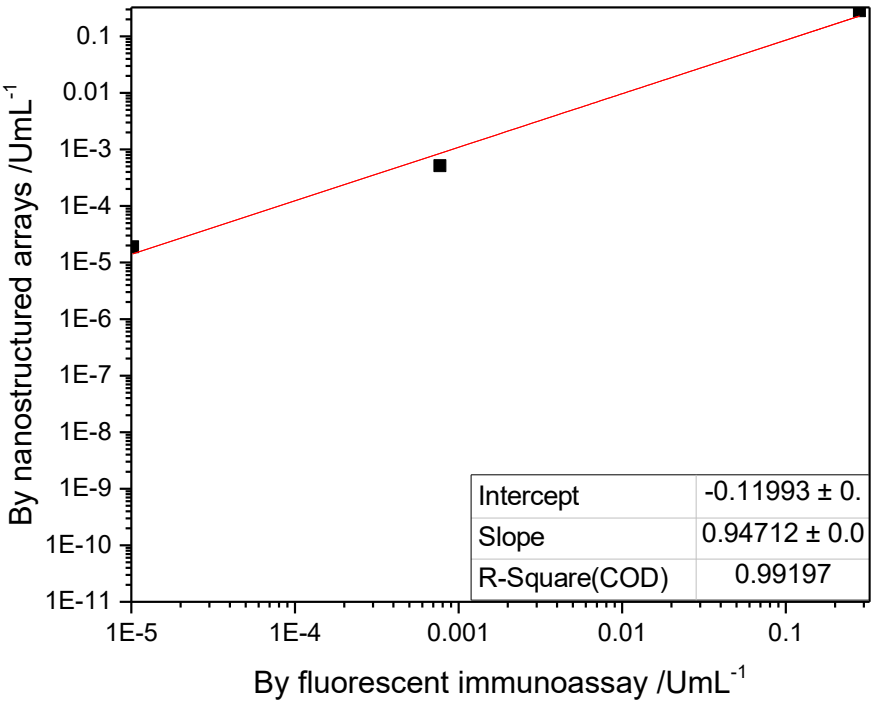


Figure 10: Preliminary clinical validation in three donkey serum samples spiked with CA 19-9.

Albumin was used at concentrations between 10^{-6} M and 10^{-13}M and GPC-1 between 10^{-7} M and 10^{-14} M. The results show that there is a low fluorescent intensity at all tested concentrations of both albumin and GPC-1. In addition, there is no linear relationship between either the concentrations of albumin and GPC-1, and the fluorescence intensity seen with the CA 19-9 assay. The specificity of the assay is due to the use of antibodies which are highly specific for detection of the antigen protein. Also, a sandwich assay was used where a capture antibody is used to anchor the protein and a second antibody is used to complete the sandwich. Therefore, two epitopes were used to detect the antigen, CA 19-9. If the protein was anchored directly onto the substrate, the specificity of the assay would be expected to be lower. It was important to ensure that the capture and primary antibodies do not recognise the same epitope, however.

The fluorescence intensity of the albumin assay was lower than that for the glass control. Therefore, the CA 19-9 assay on glass produced a higher signal than that produced by the albumin assay. This would be expected as the glass control assay would produce a higher background signal than the signal produced when albumin is used.

8.1.5.6 Clinical detection of CA 19-9 protein

While the previous experiments have been carried out using CA 19-9 diluted in a PBS buffer, it is important to test the assay using CA 19-9 in serum, as it would be used clinically. Serum contains other background proteins that may affect the assay results and is therefore referred to as a complex matrix. To evaluate the use of the nanotriangular arrays to detect the CA 19-9 antigen within a complex matrix, donkey serum spiked with CA 19-9 antigen at three different concentrations was used as the analyte. The results obtained with the nanotriangular array were compared with those obtained using a standard fluorescent immunoassay conducted on glass (Figure 10). The reason for using a fluorescent immunoassay as the gold standard was to reduce any confounding factors by making the methodology across the techniques as consistent as possible.

The results show a good correlation between the two tests (R^2=0.992) in the range 1 x 10^{-5}UmL^{-1} and 0.1 UmL^{-1} (Figure 10). Since the CA 19-9 was spiked into donkey serum, these results show that the assay can detect CA 19-9 in a complex matrix that consists of other serum proteins. These results also show that the assay produces results that are in good correlation with a gold standard test that is known to be valid. However, only three samples were used so the sample size is small, and the experiment needs to be repeated with more samples.

In summary, metal enhanced fluorescence has been observed using the nanotriangular arrays by placing fluorophores adjacent to the gold nanoparticles. Using this enhancement, it has been possible to increase the sensitivity of detection of CA 19-9 and to lower the detection limit. This was successfully validated in spiked serum samples. Further validation needs to be done using a larger number of clinical patient samples.

8.1.5.7 GPC-1 assay

For the purposes of multiplexing, the nanotriangular assay was conjugated to GPC-1, a protein that may also be a useful biomarker for pancreatic cancer. The results of the calibration curve show a detection limit of 10^{-15}M (Figure 11). It is thought that this could be used with CA 19-9 and other biomarkers for pancreatic cancer to create a multiplex biosensor to increase the specificity of detection.

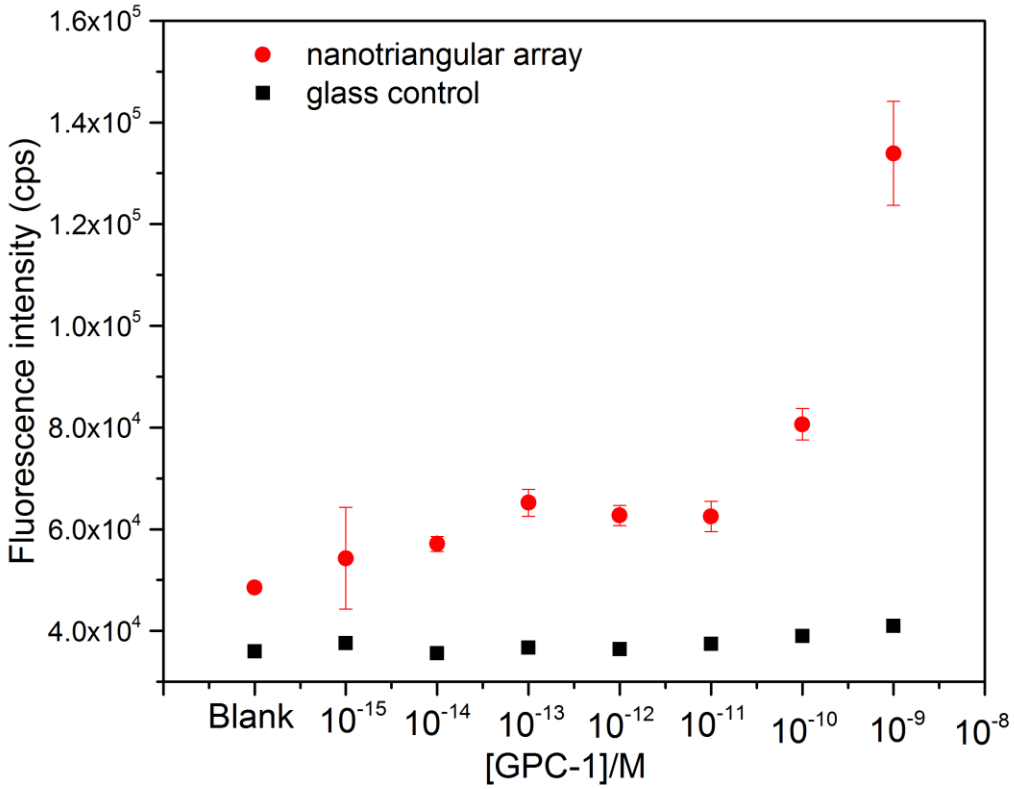


Figure 11: Calibration curve for GPC-1 fluorescent immunoassay on gold nanotriangular substrates. Glass control arrays have also been plotted for comparison.

8.2 Gold nanostars

The gold nanostars were also investigated for their use as biosensors. The fluorescence enhancement was investigated first.

8.2.1 Drop dry calibration

To determine whether the nanostars substrates could be used to detect different protein concentrations, drop dry calibration experiments were carried out (Figure 12). The same protocol that was used with the gold nanotriangular arrays was used for the gold nanostars. In brief, 30uL of Dylight800 conjugated IgG in reducing concentrations was drop dried onto substrates synthesised from the smaller gold nanostars. The IgG provides a spacer distance of approximately 10 nm between the fluorophore and nanoparticles. However, since the orientation of the antibodies is not controlled, the fluorescence intensity that is observed is a combination of quenching and enhancement effects of the nanoparticle on fluorophore. The results show that the fluorescence intensity of the gold nanostars is proportional to the concentration of Dylight800-IgG. The lowest concentration of Dylight800 that could be detected was $10^{-9.5}$ M. This was 10 times higher than the concentration that could be detected on glass, which was $10^{-8.5}$ M. This shows that the gold nanostars substrates could potentially be used to increase the detection limit of the fluorescent immunoassay for CA 19-9.

8.2.2 Enhancement of fluorescent immunoassay using gold nanostars

The gold nanostars substrates were investigated for their use with the CA 19-9 fluorescent immunoassay. The same conjugation chemistry that was used for the gold nanotriangles was used for the gold nanostars. The protocol was slightly modified due to the synthesis process of the gold nanostars substrates. MPTMS was used for binding of the gold nanostars to the glass substrates during the synthesis of the gold nanostar substrates. Therefore, the MPTES step was not repeated for the conjugation of the 4-arm carboxy- PEG to the glass surface. Cysteamine incubation only was carried out to allow conjugation of the 4-arm carboxy-PEG to the remaining gold covered surface of the

substrate. The small nanostars were used as this provided a more homogeneous monolayer on the glass substrates than the large gold nanostars.

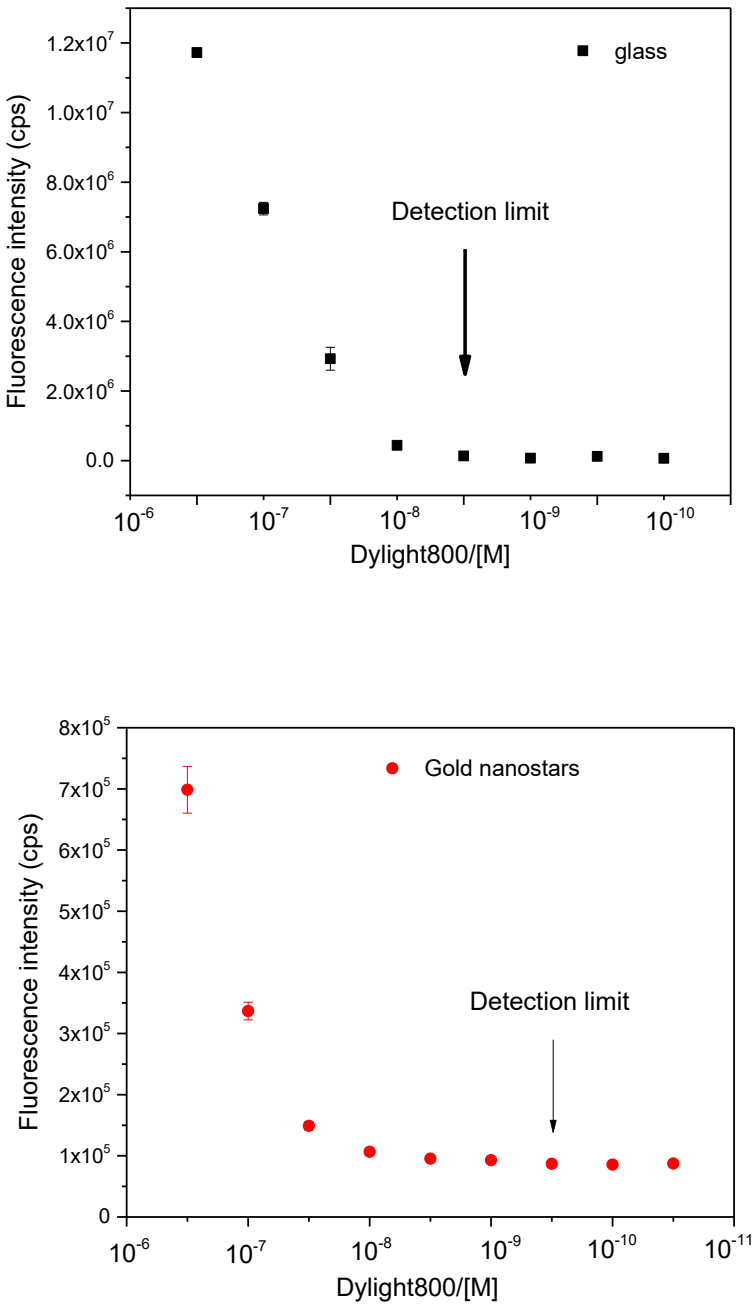


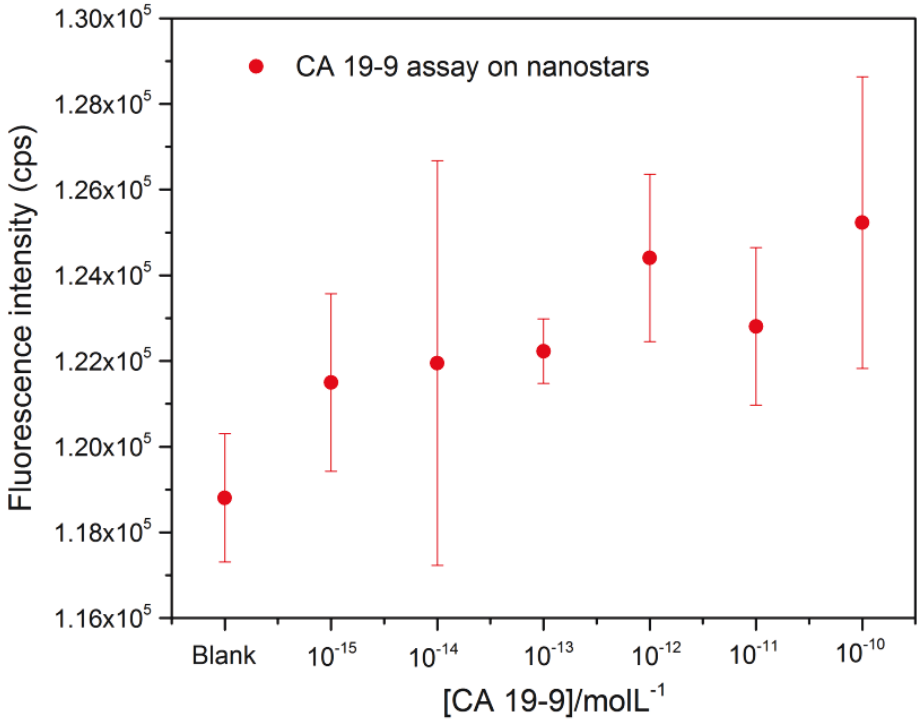
Figure 12: Scatter plots to show the results of the drop dry calibration tests using gold nanostar substrates synthesised from S-GNSs (a) calibration plot on glass (b) calibration plot on nanotriangular array.

The calibration curve achieved for CA 19-9 was carried out and is shown in Figure 13. This shows that concentration dependence can be achieved by applying the fluorescent immunoassay to the nanostars substrates. The results show a linear relationship between the concentration of the CA 19-9 and the fluorescence intensity of the substrates between 1543 UmL^{-1} and 1.5 x 10^{-5} UmL^{-1} M. The limit of detection was 1.5 10^{-2} UmL^{-1} calculated as 3 times the standard deviation of the blank plus the blank reading.

8.3 Summary

When comparing the nanotriangular arrays to the gold nanostars certain differences were seen. Firstly, the detection limit of the gold nanostars was lower than that of the gold nanotriangular arrays. This could be explained by the lower enhancement factor that was observed with the gold nanostars compared to the gold nanotriangular arrays. Secondly the error bars observed with the gold nanostar substrates were much wider than those seen with the gold nanotriangular arrays. This seems to suggest that the nanostars produce a noisier, background signal. The increase in noise is related to the lower detection limit. The higher the background noise, the lower the limit of detection. This difference in noise may be explained by the structural differences between the two types of nanoparticles. The nanotriangular arrays consist of regular repeated arrays that in turn produce an electromagnetic field that is consistent across substrate. The variation of the electromagnetic field is therefore expected to be minimal. This is one of the benefits of using NSL for the synthesis of the nanoparticles. In contrast, the nanostar substrates were synthesised by immersion of MPTMS-modified glass slides in gold nanostar solution. Using this technique, the gold nanostars would be randomly distributed on the surface of the substrate. In addition, the gold nanostars were seen to aggregate when characterised by SEM (Figure 14). This would cause further inconsistencies in the distribution of the nanostars and hence disrupt the consistency of the electromagnetic field.

(a)



(b)

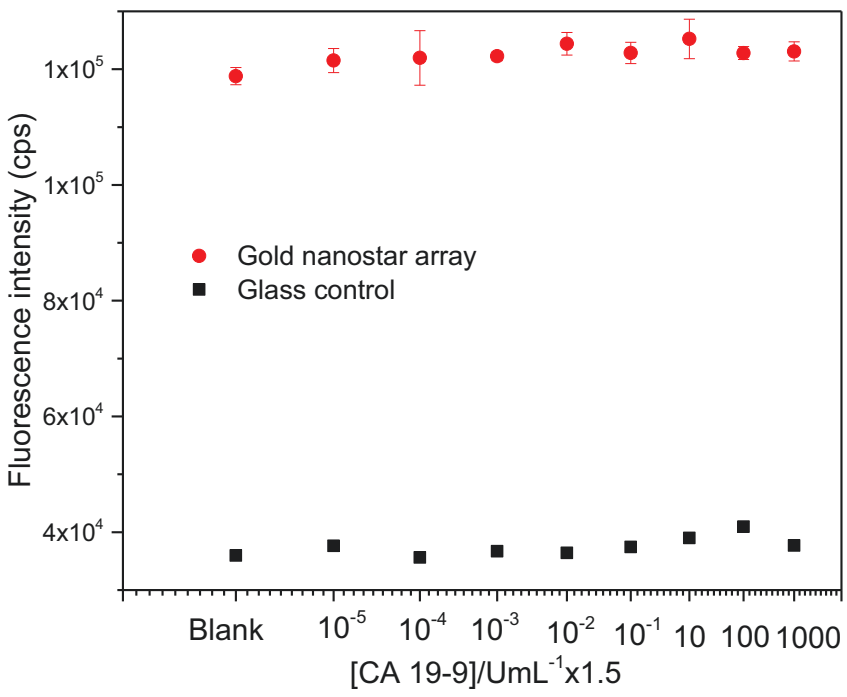


Figure 13: (a) Calibration curve for CA 19-9 fluorescent immunoassay on gold nanostar substrates (b) in comparison with glass control assay.

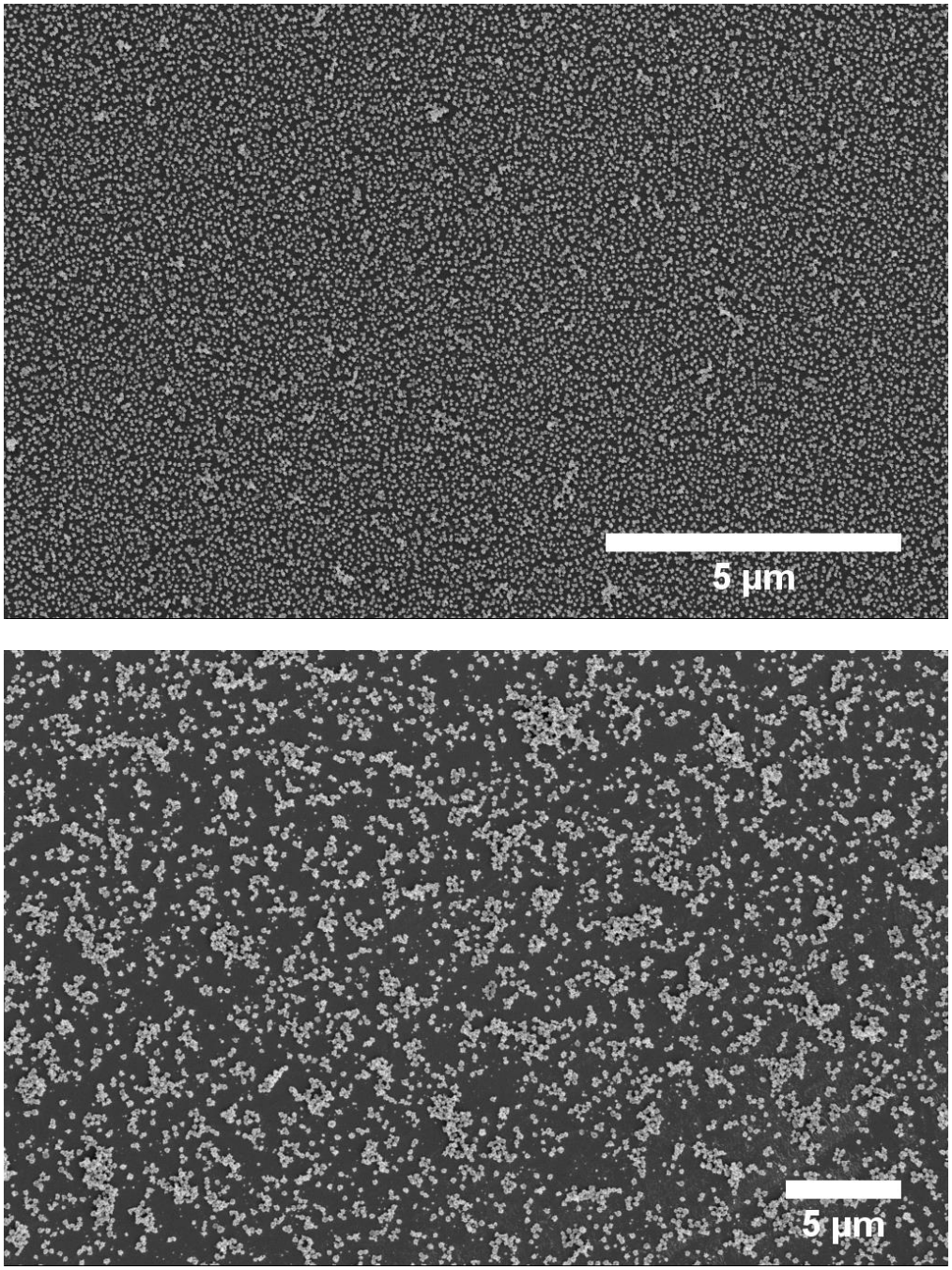


Figure 14: SEM images of GNS self-assembled monolayers on glass of (a) S-NS (b) L-NS showing greater aggregation of L-NS compared to S-NS. Copyright © 2017 American Chemical Society.

CHAPTER 9: MICRORNA ASSAYS

Recent studies have shown that microRNA expression differs between cancer types. Combined with their stability in tissue and body fluids, microRNAs are being investigated for their use as biomarkers for disease diagnosis and treatment response[82]. In pancreatic cancer, differential microRNA expression has been shown in pancreatic cancer tissue specimens when compared with normal pancreatic tissue[211], [212]. However, the detection of different levels of microRNA in blood is a more attractive option as this would be a less invasive strategy for obtaining a diagnosis and may eventually be used as a screening tool to detect early stage disease before symptoms occur. It could also be used to characterise tumours to provide information about prognosis as well as the types of therapy to which a tumour may respond. Currently, CA 19-9 is the only validated biomarker for pancreatic cancer but suffers from high false negative rates, in the Lewis negative phenotype and high false positive rates as it may also be expressed in benign diseases. MicroRNAs could provide an earlier and more precise diagnosis as well as more specific information about tumours in individual patients.

Due to their small size and low abundance, current available methods to detect microRNA require amplification steps which are time consuming and labour intensive[213]. Biosensors based on plasmonic mechanisms have been used to detect microRNA in pancreatic cancer and avoid the need for an additional amplification step. Surface plasmon resonance (SPR) relies on a shift in the LSPR wavelength seen during UV-Vis spectroscopic characterisation to detect the presence of microRNA. Gold nanoprisms were immobilised onto a glass substrate and these were then functionalised with complementary DNA probes[172], [214] using a mixture with a 1:1 ratio of the complementary DNA probe and a PEG_6-thiol spacer. The thiol group at the terminus of the PEG promotes attachment of the PEG to gold. The PEG spacer keeps the complementary DNA probes separated to allow space for the matching miRNA to interact and bind. After hybridisation with the microRNA probe, the change in LSPR wavelength was recorded and plotted against the known concentration of microRNA to produce a calibration curve. The biosensors were able to detect miR-21 and miR-10b in plasma from patients

with pancreatic cancer with a detection limit of ~35 x 10^{-15} M (35 femtomolar). By increasing the size of the nanoprisms, the detection limit was optimised to 83 x10^{-18} (attomolar). While the limit of detection demonstrated using this technique is very low, the actual shifts in the LSPR after binding of the microRNA were small at less than 15 nm. The biosensor was tested on a small sample of 6 patients with pancreatic cancer and 6 normal controls and needs further clinical validation. Furthermore, the gold nanoparticles are synthesised in solution phase and conjugated to glass slides. Therefore, there is no control over the placement of the nanoparticles on the glass substrate. Similarly, to the gold nanostars synthesised in this project, these would be expected to lack the regularity that is important to achieve consistent results. Huertas et al, 2016[215], achieve an even lower detection limit for miR-181a (LOD=23aM) using a nanophotonic biosensor in commercial samples and human urine samples from patients with bladder carcinoma. This was also achieved without a purification or amplification step.

MEF has also been successfully used for the detection of RNA probes[216]. Fluorescent conjugated RNA probes were used in combination with silver island films. The detection limit was 25 femtomolar and was lower than that of the reverse transcriptase polymerase chain reaction (RT-PCR). As there is no additional amplification step, this MEF based assay was also quicker and simpler to carry out than RT-PCR.

9.1 Gold capped polystyrene sphere (GCPS) arrays

The GCPS arrays produced in this project were investigated for their use in the detection of microRNA by MEF. While similar arrays made of silver[194] and gold[186] have been explored previously, nanostructures of this type have not been used for the detection of microRNA. The first step was to evaluate the enhancement factor using a drop-drying method.

9.1.1 Drop dry calibration

The experiments of drop dry calibration were also carried out using the Dylight800 conjugated IgG. However, the results showed no relationship between the fluorescence intensity and the

concentration of the fluorophore (data given in appendix). This was thought to be because of the surface area and density of the nanoparticles causing a high concentration of fluorophore to remain on the surface and leading to a prominent quenching effect. Next, the calibration using a microRNA assay was carried out.

9.1.2 Calibration curve using microRNA assay for miR-21

To determine whether the assay could be used as a diagnostic platform to detect microRNA, an assay was developed using oligonucleotide probes (Figure 1). The oligonucleotide probes used are given in Table 1. The assay that was developed was based on that used for CA 19-9 and uses the same conjugation chemistry with attachment of 4-arm PEG to allow adherence of the capture probe. The capture probe was made of a synthetic oligonucleotide probe with a sequence that is complementary to the analyte, miR-21. The capture probe terminated in an amine group to allow chemical conjugation to the carboxyl group exposed on the surface of the 4-arm PEG. After incubation with miR-21, the analyte of interest, a second microRNA probe was used for detection. This oligonucleotide probe used for detection was conjugated to the Dy782 fluorophore (excitation/ emission; 783 nm / 800 nm). Each oligonucleotide base has a length of a third of a nanometre. The length of the assay probes therefore provides an ideal distance between the fluorophore and the nanoparticle for fluorescent enhancement of around 7 nm [9]. miR-21 was chosen as the analyte as it has been shown to be highly expressed in the blood of patients with pancreatic cancer.

The results of the calibration tests show that there is a linear relationship between the concentration of miR-21 and the fluorescence intensity of the final assay (Figure 2). The background count was initially very high. When this was repeated with excessive washing (blank reading shown in Figure 4a) the signal was reduced. While the assay needs further work, these preliminary results show that the GPCS arrays may be useful for miRNA quantification. In addition, the GCPS arrays demonstrated morphological stability throughout the conjugation process and the assay procedure without the need for chemical binding between the gold and polystyrene spheres. This is an improvement on the

previously published capped nanoparticles that required chemical binding between the gold and polymer scaffold so that the array could withstand the assay binding and washing steps.

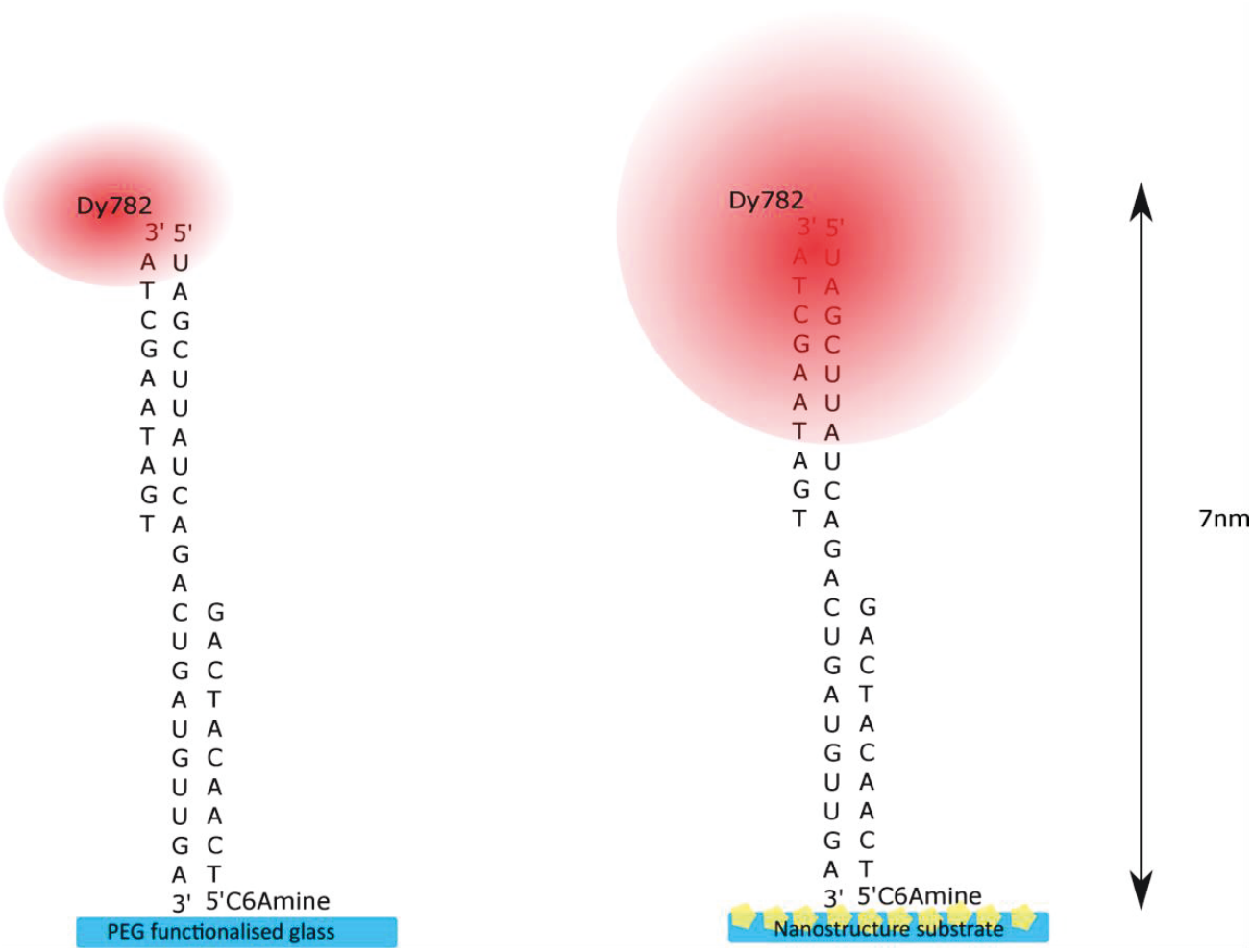
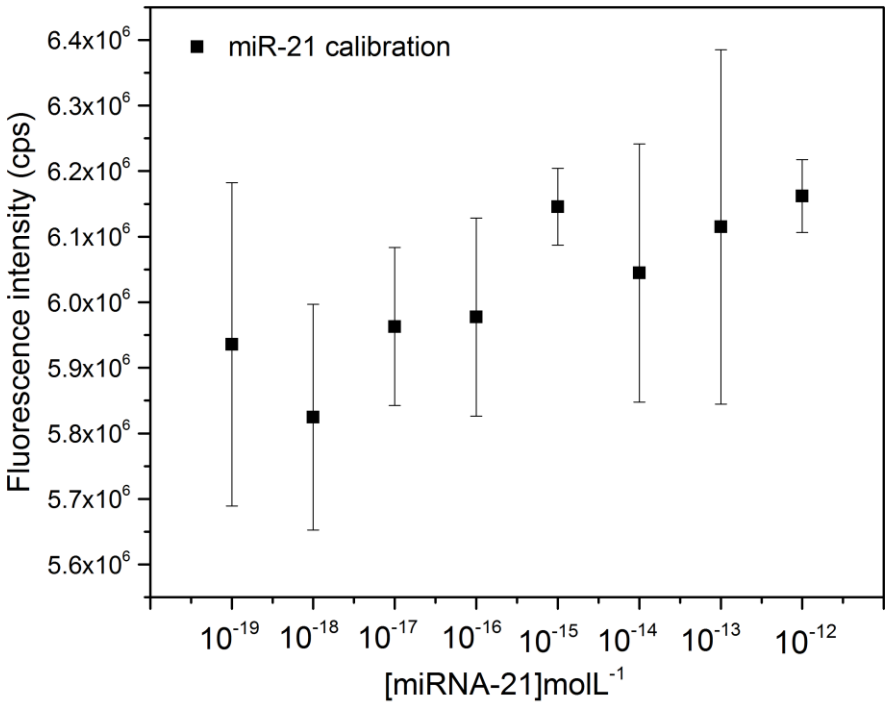


Figure 1: Schematic diagram to show microRNA probe assay set-up for miR-21.

Table 1: Oligonucleotide probe sequences used in the microRNA assays

Class	Assay	Sequence	MW (g/mol)	Modification
Analyte	miR-21	5'-UAGCUUAUCAGACUGAUGUUGA-3'	7004	none
Capture probe	miR-21	5'-TCAACATCAG-3'	3175	5'-AmineC_6
Fluorophore conjugated	miR-21	5'-TGATAAGCTA-3'	4046	3'-DY782
Analyte	miR-10b	5'-UACCCUGAGAACCGAAUUUGUG-3'	7308	none
Capture probe	miR-10b	5'-CACAAATTCG-3'	3175	5'-AmineC6
Fluorophore	miR-10b	5'-CTACAGGGTA-3'	4047	3'-DY782
Analyte miR-10a (specificity)	miR-10b	'5-UACCCUGUAGAUCCGAAUUUGUG-3'	7285	none

(a)



(b)

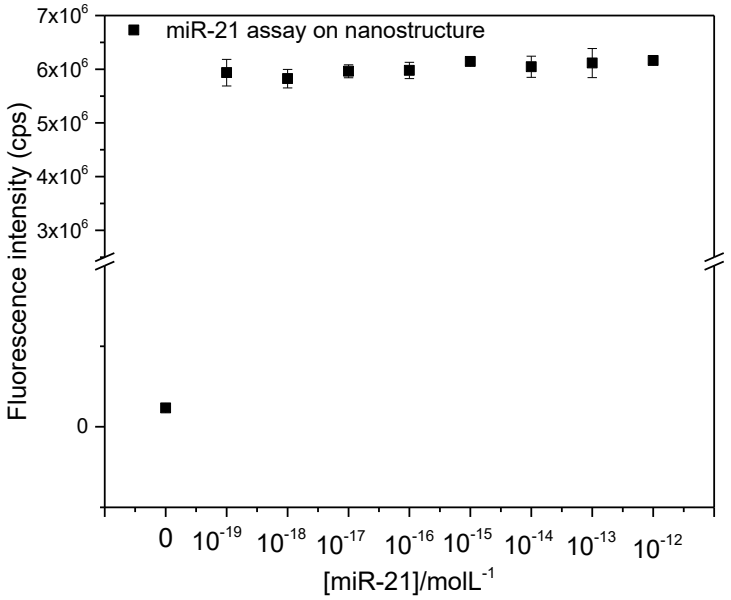


Figure 2: Calibration curve of miRNA miR-21 assay on GCPS assay shows linear relationship between the concentration of the miR-21 and the fluorescence intensity of the assay (a) without blank reading (b) with blank reading.

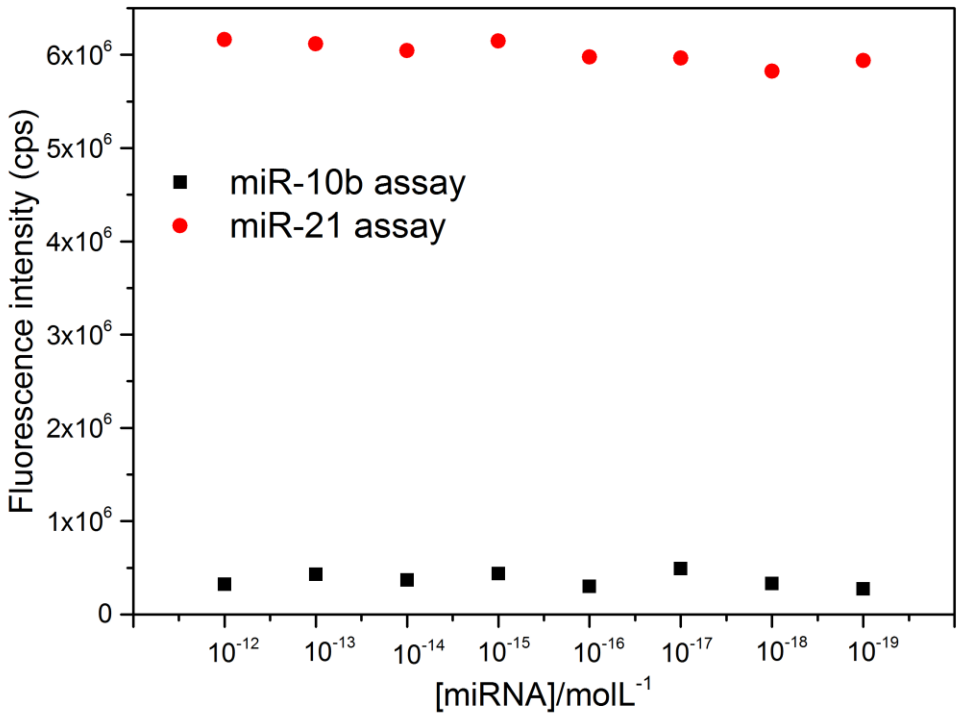


Figure 3: Specificity test for miR-21 assay using miR-10b as the substitute analyte.

9.1.3 Specificity of miR-10b on miR-21 assay

To test the specificity of the microRNA assay, the protocol was repeated using miR-10b as the test miRNA instead of miR-21 (Figure 3). The structure of miR-10b is given in Table 1. The reason for testing miR-10b on the miR-21 assay is that it is also expressed at high levels in the blood of patients with pancreatic cancer. Therefore, it would be important to know whether the assay can distinguish between raised levels of miR-21 and miR-10b. The results show that the fluorescent intensity of the assay is significantly lower than that of miRNA-21 when it is used in the assay. There was no concentration dependence of the assay when the miR-21 assay is used to measure miR-10b. The signal with miR-10b is comparable to the background signal of the assay with miR-21. Therefore, the assay can distinguish miR-21 from miR-10b which has a different oligonucleotide sequence.

9.2 Summary

The highly sensitive detection of microRNA using GCPS arrays has been demonstrated using a fluorescent assay. Fluorescent enhancement is thought to be the method of amplification of the fluorophore probes and improvement in sensitivity. Due to the naturally low levels of microRNA in clinical specimens, an amplification step is required when assays for microRNA are currently used in clinical laboratories. Using fluorescence enhancement means that an additional amplification step is not required to detect the microRNA. Furthermore, the nanostructure used was both robust and stable under the processing and washing steps of the assay and were cheap and easy to produce. It may also be adapted to detect multiple microRNAs simultaneously for multiplexing. These nanostructures need further validation in clinical samples, but it would be a very good candidate for a multiplex microRNA biosensing platform in future.

CHAPTER 10: CONCLUSIONS AND FUTURE WORK

In this project, three different metallic nanomaterials have been synthesised, optimised and evaluated for their use in biosensing using metal enhanced fluorescence. The level of fluorescence enhancement observed was up to 321 times using the large gold nanostar substrates, suggesting that these nanomaterials could be used to improve the detection limits of fluorescence based biological assays. Indeed, these nanomaterials have been successfully used for the detection of pancreatic cancer biomarkers, Ca 19-9 and GPC-1. As predicted, a significant improvement in the detection limit of these assays was observed when compared to the standard fluorescent immunoassays for these biomarkers. Furthermore, when these nanomaterials were conjugated to a fluorescent microRNA assay for miR-21, a linear relationship was observed between the fluorescence intensity of the assay and the concentration of microRNA. This result suggests that the enhancement provided by these nanomaterials could circumvent the need for amplification of these genetic materials using PCR prior to their measurement. To evaluate the usefulness of these assays for biosensing, CA 19-9 spiked donkey serum was used as the test medium for the CA 19-9 assay. Although the sample number is small, the results indicate that the nanomaterials could reliably determine the levels of CA 19-9 in a complex matrix. Furthermore, the specificity tests demonstrate that the fluorescent enhanced assays are highly specific for the protein of interest CA 19-9.

When considering the properties of a biosensor, each of the nanomaterials used have their advantages and disadvantages. The main advantage of the nanotriangular arrays is that the synthesis is a highly controllable process. This provides nanotriangular arrays that are regular and highly ordered. It also means the nanotriangular arrays can be tuned so that the enhancement factor can be altered by changing the structural parameters of the arrays. This not only allows the enhancement factor to be optimised so that the optical properties match the chosen fluorophore to provide the lowest detection limit, but it also means that the enhancement factor and hence the detection limit can be selected according to the requirements of the assay. The GCPS arrays displayed higher

enhancement factors and tunability but high background noise. This is likely to be due to the highly packed arrangement of the nanoparticles. Similarly, the gold nanostars lack the regular distribution and control of the gold nanotriangular arrays as they are synthesised in the solution phase and then distributed onto glass substrates by hand. One of the major advantages of all three nanomaterials is that they can be used to synthesise multiplex diagnostic platforms which would be useful for the diagnosis of pancreatic cancer.

Multiplexing describes the ability of a device to detect more than one signal at the same time. It is a technique that has been used to diagnosis certain diseases, such as autoimmune disease and certain cancers where the signals from multiple biomarkers are used to detect disease[20]. Zhang et al, 2012[217] demonstrate the detection of six cytokines (vascular endothelial growth factor (VEGF), Interleukin 1β (IL-1β), Interleukin 4 (IL-4), Interleukin 6 (IL-6), Interferon γ (IFN-γ), and Tumour necrosis factor (TNF)) in the culture media of cancer cells on a metal enhanced fluorescence biosensing chip that could be used to detect early stage cancer. Tabakman et al, 2011[20], use the same biosensing chip to detect multiple human autoantibodies that could be used to detect autoimmune disorders such as systemic lupus erythematosus (SLE) and polymyositis.

The advantage of multiplexing with certain diseases is that detecting more than one biomarker can increase the sensitivity of diagnosis of the disease and possibly detect the disease at an earlier stage. For the detection of pancreatic cancer, it has been established that the use of CA 19-9 as a standalone biomarker for diagnosis and screening is not useful due to the high false positive and false negative rates. However, it has been demonstrated in several studies that combining CA 19-9 with other biomarkers increases the sensitivity and specificity of detecting pancreatic cancer. Therefore, multiplexing would be a suitable approach to the early detection of pancreatic cancer. Furthermore, nanotechnology based platforms would be particularly useful to increase the sensitivity of detecting these markers. For example, microRNAs are likely to be future candidates as biomarkers for pancreatic cancer and if the detection of these could be enhanced using nanotechnology and combined with

established markers such as CA 19-9, then these could be incorporated onto a multiplex platform. Thus, by producing a nanotechnology based multiplex platform, the specificity of detecting pancreatic cancer could be increased by combining several markers. Therefore, for future work, the results of this project could be used to develop a multiplex platform based on MEF for pancreatic cancer biomarkers.

Currently, there is only one report of a nanotechnology based multiplex platform being used for the detection of pancreatic cancer. The platform described is based on surface-enhanced Raman spectroscopy (SERS) technology instead of MEF. SERS is a technique whereby nanoparticles are used to increase the sensitivity of Raman spectroscopy. Raman spectroscopy is an analytical technique used to provide information about the composition of materials. It was first described by CV Raman in 1929[218]. The way materials interact with light, in particular, the effects on light scattering is the technique that is used to study the materials. A database of known scattering properties is used as a reference. Both the intensity and the wavelength of scattered light are the variables that are characteristic for different materials. With standard Raman spectroscopy, the low intensity of scattering signals makes it very difficult to detect low levels of molecules. Enhancement of the signals using nearby resonant metal nanoparticles in the SERS technique has made it possible to detect single molecules. Using SERS in combination with an immunoassay, Banaei et al., present a multiplex platform for detecting pancreatic cancer using three proteins: CA 19-9, matrix metalloproteinase 7 (MMP 7) and mucin 4 (MUC4). The platform was used on 15 patient serum samples. The levels of CA 19-9 were most useful for differentiating patients with pancreatic cancer from those with pancreatitis and normal controls. Although a formal clinical validation was not carried out, all three markers were useful for differentiating these three groups of patients.

MEF has been used to build multiplex platforms for diseases other than cancer. Toxoplasma gondii is a potentially fatal parasitic infection in patients with reduced immunity and in new-born babies. Pomares et al successfully validate a multiplex test using MEF, comparing this to current commercial

test using serum from 244 patients[219]. Similarly, as described above Tabakman et al, 2011[20] use a metal enhancing platform to detect human autoantibodies in autoimmune disease.

By far, the greatest impact of this technology on future work would be to detect pancreatic cancer at an early stage, and before a patient becomes asymptomatic. The methods used in this project could be used to build a multiplex platform that combines CA 19-9 with pancreatic cancer specific microRNA. Using the tuning properties, the platform could be produced with different sensitivities. The nanotriangles could be combined with the GCPS arrays to detect both CA 19-9 and microRNA using the nanolithography, etching and gold evaporation processes described herein. This would be validated in serum samples from patients with pancreatic cancer and compared to patients with benign pancreatic disease and normal controls. The demand for such technology for diagnosing pancreatic cancer is clear and the same technology is easily transferable to other diseases.

Increasing the sensitivity of detecting markers of infection is another useful application of this technology. Early detection of infection would reduce morbidity and mortality of this disease by allowing early treatment. A classic example is human immunodeficiency virus (HIV). Early detection of the disease is limited by the sensitivity of detecting diagnostic HIV proteins in serum. It has been reported that early detection and treatment of HIV could be curative in certain cases. De la Rica et al[220], have used a plasmonic immunoassay to increase the detection of the disease using a visual sensor. However, the assay described was unstable and although it was highly sensitive for the detection of p24, a HIV capsid antigen that is present in the very early stages of the disease, the assay cannot be used for multiplexing.

In conclusion, metallic nanomaterials have been developed and adapted for biosensing using metal enhanced fluorescence. Due to the fluorescence enhancement, the sensitivity of fluorescence based assays have been significantly enhanced. A detection limit of $5 \times 10^{-7} UmL^{-1}$ has been achieved for CA 19-9 and 1×10^{-15} M for GPC-1 proteins. A microRNA assay to miR-21 could also be achieved on the metal enhancing platforms. The multiplexing capabilities of this platform offer potential use to detect

early stage pancreatic cancer by detecting several biomarkers for the disease with adaptability to the earlier detection of other diseases, for earlier treatment and better patient outcomes.

REFERENCES

[1] CancerResearch, "Cancer statistics for the UK," *Cancer Research UK*. pp. 1–4, 2016.

[2] D. P. Ryan, T. S. Hong, and N. Bardeesy, "Pancreatic Adenocarcinoma," *N. Engl. J. Med.*, vol. 371, no. 11, pp. 1039–1049, 2014.

[3] U. K. Ballehaninna and R. S. Chamberlain, "Serum CA 19-9 as a Biomarker for Pancreatic Cancer-A Comprehensive Review," *Indian J. Surg. Oncol.*, vol. 2, no. 2, pp. 88–100, 2011.

[4] U. K. Ballehaninna and R. S. Chamberlain, "The clinical utility of serum CA 19-9 in the diagnosis, prognosis and management of pancreatic adenocarcinoma: An evidence based appraisal," *J. Gastrointest. Oncol.*, vol. 3, no. 2, pp. 105–119, 2012.

[5] S. A. Melo *et al.*, "Glypican-1 identifies cancer exosomes and detects early pancreatic cancer," *Nature*, vol. 523, no. 7559, pp. 177–182, 2015.

[6] R. Liu *et al.*, "Serum microRNA expression profile as a biomarker in the diagnosis and prognosis of pancreatic cancer," *Clin. Chem.*, vol. 58, no. 3, pp. 610–618, 2012.

[7] T. Setoyama, X. Zhang, S. Natsugoe, and G. A. Calin, "microRNA-10b: A new marker or the marker of pancreatic ductal adenocarcinoma?," *Clinical Cancer Research*, vol. 17, no. 17. pp. 5527–5529, 2011.

[8] X. Kong *et al.*, "Detection of differentially expressed microRNAs in serum of pancreatic ductal adenocarcinoma patients: MiR-196a could be a potential marker for poor prognosis," *Dig. Dis. Sci.*, vol. 56, no. 2, pp. 602–609, 2011.

[9] J. Liu *et al.*, "Combination of plasma microRNAs with serum CA 19-9 for early detection of pancreatic cancer," *Int. J. Cancer*, vol. 131, no. 3, pp. 683–691, 2012.

[10] B. Haley and E. Frenkel, "Nanoparticles for drug delivery in cancer treatment," *Urologic Oncology: Seminars and Original Investigations*, vol. 26, no. 1. pp. 57–64, 2008.

[11] A. Fabi *et al.*, "Prospective study on nanoparticle albumin-bound paclitaxel in advanced breast cancer: Clinical results and biological observations in taxane-pretreated patients," *Drug Des. Devel. Ther.*, vol. 9, pp. 6177–6183, 2015.

[12] D. Kalita, D. Shome, V. G. Jain, K. Chadha, and J. R. Bellare, "In vivo intraocular distribution and safety of periocular nanoparticle carboplatin for treatment of advanced retinoblastoma in humans," *American Journal of Ophthalmology*, vol. 157, no. 5. 2014.

[13] K. Aslan, I. Gryczynski, J. Malicka, E. Matveeva, J. R. Lakowicz, and C. D. Geddes, "Metal-enhanced fluorescence: An emerging tool in biotechnology," *Current Opinion in Biotechnology*, vol. 16, no. 1 SPEC. ISS. pp. 55–62, 2005.

[14] D. Darvill, A. Centeno, and F. Xie, "Plasmonic fluorescence enhancement by metal nanostructures: shaping the future of bionanotechnology," *Phys. Chem. Chem. Phys.*, vol. 15, no. 38, p. 15709, 2013.

[15] A. Kinkhabwala, Z. Yu, S. Fan, Y. Avlasevich, K. Müllen, and W. E. Moerner, "Large single-molecule fluorescence enhancements produced by a bowtie nanoantenna," *Nat. Photonics*, vol. 3, no. 11, pp. 654–657, 2009.

[16] T. D. Corrigan, S. Guo, R. J. Phaneuf, and H. Szmacinski, "Enhanced fluorescence from periodic

arrays of silver nanoparticles," *J. Fluoresc.*, vol. 15, no. 5, pp. 777–784, 2005.

[17] P. P. Pompa *et al.*, "Metal-enhanced fluorescence of colloidal nanocrystals with nanoscale control," *Nat. Nanotechnol.*, vol. 1, no. 2, pp. 126–130, 2006.

[18] A. I. Dragan *et al.*, "Distance Dependence of Metal-Enhanced Fluorescence," *Plasmonics*, vol. 7, no. 4, pp. 739–744, 2012.

[19] K. Ray, R. Badugu, and J. R. Lakowicz, "Distance-dependent metal-enhanced fluorescence from Langmuir-Blodgett monolayers of Alkyl-NBD derivatives on silver island films," *Langmuir*, vol. 22, no. 20, pp. 8374–8378, 2006.

[20] S. M. Tabakman *et al.*, "Plasmonic substrates for multiplexed protein microarrays with femtomolar sensitivity and broad dynamic range," *Nat. Commun.*, vol. 2, no. 1, 2011.

[21] D. Yadav and A. B. Lowenfels, "The epidemiology of pancreatitis and pancreatic cancer," *Gastroenterology*, vol. 144, no. 6. pp. 1252–1261, 2013.

[22] A. Vincent, J. Herman, R. Schulick, R. H. Hruban, and M. Goggins, "Pancreatic cancer," in *The Lancet*, 2011, vol. 378, no. 9791, pp. 607–620.

[23] M. Ilic and I. Ilic, "Epidemiology of pancreatic cancer," *World Journal of Gastroenterology*, vol. 22, no. 44. pp. 9694–9705, 2016.

[24] T. P. Yeo and A. B. Lowenfels, "Demographics and epidemiology of pancreatic cancer," *Cancer Journal (United States)*, vol. 18, no. 6. pp. 477–484, 2012.

[25] G. J. Krejs, "Pancreatic cancer: Epidemiology and risk factors," *Digestive Diseases*, vol. 28, no. 2. pp. 355–358, 2010.

[26] T. Kolodecik, C. Shugrue, M. Ashat, and E. C. Thrower, "Risk factors for pancreatic cancer: Underlying mechanisms and potential targets," *Front. Physiol.*, vol. 4 JAN, 2014.

[27] C. Bosetti *et al.*, "Cigarette smoking and pancreatic cancer: An analysis from the International Pancreatic Cancer Case-Control Consortium (PANC4)," *Ann. Oncol.*, vol. 23, no. 7, pp. 1880–1888, 2012.

[28] V. L. W. Go, A. Gukovskaya, and S. J. Pandol, "Alcohol and pancreatic cancer," in *Alcohol*, 2005, vol. 35, no. 3, pp. 205–211.

[29] E. Lucenteforte *et al.*, "Alcohol consumption and pancreatic cancer: A pooled analysis in the International Pancreatic Cancer Case-Control Consortium (PanC4)," *Ann. Oncol.*, vol. 23, no. 2, pp. 374–382, 2012.

[30] S. M. Gapstur, E. J. Jacobs, A. Deka, M. L. McCullough, A. V. Patel, and M. J. Thun, "Association of alcohol intake with pancreatic cancer mortality in never smokers," *Arch. Intern. Med.*, vol. 171, no. 5, pp. 444–451, 2011.

[31] A. Berrington de Gonzalez, S. Sweetland, and E. Spencer, "A meta-analysis of obesity and the risk of pancreatic cancer," *Br J Cancer*, vol. 89, no. 3, pp. 519–523, 2003.

[32] R. Z. Stolzenberg-Solomon *et al.*, "Meat and meat-mutagen intake and pancreatic cancer risk in the NIH-AARP cohort," *Cancer Epidemiol. Biomarkers Prev.*, vol. 16, no. 12, pp. 2664–2675, 2007.

[33] J. T. Magruder, D. Elahi, and D. K. Andersen, "Diabetes and pancreatic cancer: Chicken or egg?,"

Pancreas, vol. 40, no. 3. pp. 339–351, 2011.

[34] D. Li, "Diabetes and pancreatic cancer," *Mol Carcinog*, vol. 51, no. 1, pp. 64–74, 2012.

[35] S. Gupta *et al.*, "New-onset diabetes and pancreatic cancer.," *Clin. Gastroenterol. Hepatol.*, vol. 4, no. 11, pp. 1301–1366, 2006.

[36] Q. Ben *et al.*, "Diabetes mellitus and risk of pancreatic cancer: A meta-analysis of cohort studies.," *Eur. J. Cancer*, vol. 47, no. 13, pp. 1928–37, 2011.

[37] A. V. Pinho, L. Chantrill, and I. Rooman, "Chronic pancreatitis: A path to pancreatic cancer," *Cancer Letters*, vol. 345, no. 2. pp. 203–209, 2014.

[38] J. Ueda, M. Tanaka, T. Ohtsuka, S. Tokunaga, and T. Shimosegawa, "Surgery for chronic pancreatitis decreases the risk for pancreatic cancer: a multicenter retrospective analysis.," *Surgery*, vol. 153, no. 3, pp. 357–64, 2013.

[39] S. Raimondi, A. B. Lowenfels, A. M. Morselli-Labate, P. Maisonneuve, and R. Pezzilli, "Pancreatic cancer in chronic pancreatitis; aetiology, incidence, and early detection," *Best Pract. Res. Clin. Gastroenterol.*, vol. 24, no. 3, pp. 349–358, 2010.

[40] R. H. Hruban, G. M. Petersen, P. K. Ha, and S. E. Kern, "Genetics of pancreatic cancer. From genes to families," *Surg Oncol Clin N Am*, vol. 7, no. 1, pp. 1–23, 1998.

[41] D. K. Bartsch, T. M. Gress, and P. Langer, "Familial pancreatic cancerĝ"current knowledge," *Nature Reviews Gastroenterology and Hepatology*, vol. 9, no. 8. pp. 445–453, 2012.

[42] R. H. Hruban, M. I. Canto, M. Goggins, R. Schulick, and A. P. Klein, "Update on familial pancreatic cancer," *Advances in Surgery*, vol. 44, no. 1. pp. 293–311, 2010.

[43] D. E. Jenne *et al.*, "Peutz-Jeghers syndrome is caused by mutations in a novel serine threonine kinase.," *Nat. Genet.*, vol. 18, no. 1, pp. 38–43, 1998.

[44] A. M. Goldstein, "Familial melanoma, pancreatic cancer and germline CDKN2A mutations," *Hum. Mutat.*, vol. 23, no. 6, pp. 630–630, 2004.

[45] H. F. A. Vasen, N. A. Gruis, R. R. Frants, P. A. Van Der Velden, E. T. M. Hille, and W. Bergman, "Risk of developing pancreatic cancer in families with familial atypical multiple mole melanoma associated with a specific 19 deletion of p16 (p16-Leiden)," *Int. J. Cancer*, vol. 87, no. 6, pp. 809–811, 2000.

[46] T. Breast Cancer Linkage Consortium, "Cancer Risks in BRCA2 Mutation Carriers," *JNCI J. Natl. Cancer Inst.*, vol. 91, no. 15, pp. 1310–1316, 1999.

[47] C. J. Van Asperen *et al.*, "Cancer risks in BRCA2 families: Estimates for sites other than breast and ovary," *J. Med. Genet.*, vol. 42, no. 9, pp. 711–719, 2005.

[48] F. Kastrinos *et al.*, "Risk of pancreatic cancer in families with Lynch syndrome.," *Jama*, vol. 302, no. 16, pp. 1790–5, 2009.

[49] F. M. Giardiello *et al.*, "Increased risk of thyroid and pancreatic carcinoma in familial adenomatous polyposis.," *Gut*, vol. 34, no. 10, pp. 1394–6, 1993.

[50] D. C. Whitcomb *et al.*, "Hereditary pancreatitis is caused by a mutation in the cationic trypsinogen gene," *Nat. Genet.*, vol. 14, no. 2, pp. 141–145, 1996.

[51] R. E. Brand *et al.*, “Advances in counselling and surveillance of patients at risk for pancreatic cancer,” *Gut*, vol. 56, no. 10. pp. 1460–1469, 2007.

[52] H. T. Lynch *et al.*, “Familial pancreatic cancer: clinicopathologic study of 18 nuclear families,” *Am. J. Gastroenterol.*, vol. 85, no. 1, pp. 54–60, 1990.

[53] R. Schneider *et al.*, “German national case collection for familial pancreatic cancer (FaPaCa): Ten years experience,” *Fam. Cancer*, vol. 10, no. 2, pp. 323–330, 2011.

[54] S. Yachida *et al.*, “Distant metastasis occurs late during the genetic evolution of pancreatic cancer,” *Nature*, vol. 467, no. 7319, pp. 1114–1117, 2010.

[55] M. Distler, D. Aust, J. Weitz, C. Pilarsky, and R. Grützmann, “Precursor lesions for sporadic pancreatic cancer: PanIN, IPMN, and MCN,” *BioMed Research International*, vol. 2014. 2014.

[56] J. B. M. Koorstra, G. Feldmann, N. Habbe, and A. Maitra, “Morphogenesis of pancreatic cancer: Role of pancreatic intraepithelial neoplasia (PanINs),” *Langenbeck’s Arch. Surg.*, vol. 393, no. 4, pp. 561–570, 2008.

[57] A. M. Lennon *et al.*, “The early detection of pancreatic cancer: What will it take to diagnose and treat curable pancreatic neoplasia?,” *Cancer Research*, vol. 74, no. 13. pp. 3381–3389, 2014.

[58] S. J. Murphy *et al.*, “Genetic alterations associated with progression from pancreatic intraepithelial neoplasia to invasive pancreatic tumor,” *Gastroenterology*, vol. 145, no. 5, 2013.

[59] G. Feldmann, R. Beaty, R. H. Hruban, and A. Maitra, “Molecular genetics of pancreatic intraepithelial neoplasia,” *Journal of Hepato-Biliary-Pancreatic Surgery*, vol. 14, no. 3. pp. 224–232, 2007.

[60] P. Cancer and G. Project, “Pancreatic cancer genomes reveal aberrations in axon guidance pathway genes,” *Nature*, vol. 491, no. 7424, pp. 399–405, 2012.

[61] T. A. Laffan *et al.*, “Prevalence of unsuspected pancreatic cysts on MDCT,” *Am. J. Roentgenol.*, vol. 191, no. 3, pp. 802–807, 2008.

[62] V. M. Kim and N. Ahuja, “Early detection of pancreatic cancer,” *Chinese J. Cancer Res.*, vol. 27, no. 4, pp. 321–331, 2015.

[63] A. Jemal, R. Siegel, E. Ward, Y. Hao, J. Xu, and M. J. Thun, “Cancer Statistics, 2009,” *CA. Cancer J. Clin.*, vol. 59, no. 4, pp. 225–249, 2009.

[64] K. J. Ruddy *et al.*, “Breast cancer presentation and diagnostic delays in young women,” *Cancer*, vol. 120, no. 1, pp. 20–25, 2014.

[65] C. Burgess, A. Ramirez, M. Richards, and S. Love, “Who and what influences delayed presentation in breast cancer?,” *Br. J. Cancer*, vol. 77, no. 8, pp. 1343–1348, 1998.

[66] B. Sa *et al.*, “The role of surgery for pancreatic cancer: a 12-year review of patient outcome,” *Ulster Med J*, vol. 79, no. 2, pp. 70–75, 2010.

[67] A. Săftoiu and P. Vilmann, “Role of endoscopic ultrasound in the diagnosis and staging of pancreatic cancer.,” *J. Clin. Ultrasound*, vol. 37, no. 1, pp. 1–17, 2009.

[68] E. E. Long, J. Van Dam, S. Weinstein, B. Jeffrey, T. Desser, and J. A. Norton, “Computed tomography, endoscopic, laparoscopic, and intra-operative sonography for assessing

resectability of pancreatic cancer," *Surg. Oncol.*, vol. 14, no. 2, pp. 105–113, 2005.

[69] P. Legmann *et al.*, "Pancreatic tumors: Comparison of dual-phase helical CT and endoscopic sonography," *Am. J. Roentgenol.*, vol. 170, no. 5, pp. 1315–1322, 1998.

[70] D. S. Lu, S. Vedantham, R. M. Krasny, B. Kadell, W. L. Berger, and H. A. Reber, "Two-phase helical CT for pancreatic tumors: pancreatic versus hepatic phase enhancement of tumor, pancreas, and vascular structures," *Radiology*, vol. 199, no. 3, pp. 697–701, 1996.

[71] J. G. Fletcher *et al.*, "Pancreatic malignancy: value of arterial, pancreatic, and hepatic phase imaging with multi-detector row CT.," *Radiology*, vol. 229, no. 1, pp. 81–90, 2003.

[72] J. A. Pietryga and D. E. Morgan, "Imaging preoperatively for pancreatic adenocarcinoma," *Journal of Gastrointestinal Oncology*, vol. 6, no. 4. pp. 343–357, 2015.

[73] R. W. Prokesch, L. C. Chow, C. F. Beaulieu, R. Bammer, and R. B. Jeffrey, "Isoattenuating pancreatic adenocarcinoma at multi-detector row CT: secondary signs.," *Radiology*, vol. 224, no. 3, pp. 764–8, 2002.

[74] J. H. Kim *et al.*, "Visually Isoattenuating Pancreatic Adenocarcinoma at Dynamic-Enhanced CT: Frequency, Clinical and Pathologic Characteristics, and Diagnosis at Imaging Examinations," *Radiology*, vol. 257, no. 1, pp. 87–96, 2010.

[75] S. H. Yoon *et al.*, "Small (≤ 20 mm) pancreatic adenocarcinomas: analysis of enhancement patterns and secondary signs with multiphasic multidetector CT.," *Radiology*, vol. 259, no. 2, pp. 442–452, 2011.

[76] M. Del Chiaro *et al.*, "Short-term results of a magnetic resonance imaging-based Swedish screening program for individuals at risk for pancreatic cancer," *JAMA Surg.*, vol. 150, no. 6, pp. 512–518, 2015.

[77] T. Rosch *et al.*, "Endoscopic ultrasound in pancreatic tumor diagnosis," *Gastrointest Endosc*, vol. 37, no. 3, pp. 347–352, 1991.

[78] M. R. Zavon, "Principles and Practice of Screening for Disease.," *Arch. Intern. Med.*, vol. 123, no. 3, p. 349, 1969.

[79] M. I. Canto *et al.*, "International cancer of the pancreas screening (CAPS) consortium summit on the management of patients with increased risk for familial pancreatic cancer," *Gut*, vol. 62, no. 3, pp. 339–347, 2013.

[80] M. Herreros-Villanueva and L. Bujanda, "Non-invasive biomarkers in pancreatic cancer diagnosis: what we need versus what we have," *Ann. Transl. Med.*, vol. 4, no. 7, pp. 134–134, 2016.

[81] Z. Huang and F. Liu, "Diagnostic value of serum carbohydrate antigen 19-9 in pancreatic cancer: a meta-analysis.," *Tumour Biol.*, pp. 7459–7465, 2014.

[82] M. D. Jansson and A. H. Lund, "MicroRNA and cancer," *Molecular Oncology*, vol. 6, no. 6. pp. 590–610, 2012.

[83] W. Filipowicz, S. N. Bhattacharyya, and N. Sonenberg, "Mechanisms of post-transcriptional regulation by microRNAs: Are the answers in sight?," *Nature Reviews Genetics*, vol. 9, no. 2. pp. 102–114, 2008.

[84] C. M. Croce, "Causes and consequences of microRNA dysregulation in cancer," *Nature Reviews*

Genetics, vol. 10, no. 10. pp. 704–714, 2009.

[85] R. C. Lee, R. L. Feinbaum, and V. Ambros, "The C. elegans heterochronic gene lin-4 encodes small RNAs with antisense complementarity to lin-14," *Cell*, vol. 75, no. 5, pp. 843–854, 1993.

[86] B. Wightman, I. Ha, and G. Ruvkun, "Posttranscriptional regulation of the heterochronic gene lin-14 by lin-4 mediates temporal pattern formation in C. elegans," *Cell*, vol. 75, no. 5, pp. 855–862, 1993.

[87] B. J. Reinhart *et al.*, "The 21-nucleotide let-7 RNA regulates developmental timing in Caenorhabditis elegans," *Nature*, vol. 403, no. 6772, pp. 901–906, 2000.

[88] S. Bagga *et al.*, "Regulation by let-7 and lin-4 miRNAs results in target mRNA degradation," *Cell*, vol. 122, no. 4, pp. 553–563, 2005.

[89] S. A. Muljo, C. Kanellopoulou, and L. Aravind, "MicroRNA targeting in mammalian genomes: Genes and mechanisms," *Wiley Interdisciplinary Reviews: Systems Biology and Medicine*, vol. 2, no. 2. pp. 148–161, 2010.

[90] G. Raposo and W. Stoorvogel, "Extracellular vesicles: Exosomes, microvesicles, and friends," *Journal of Cell Biology*, vol. 200, no. 4. pp. 373–383, 2013.

[91] C. D'Souza-Schorey Crislyn and J. W. Clancy, "Tumor-derived microvesicles: Shedding light on novel microenvironment modulators and prospective cancer biomarkers," *Genes Dev.*, vol. 26, no. 12, pp. 1287–1299, 2012.

[92] N. Javeed *et al.*, "Pancreatic cancer-derived exosomes cause paraneoplastic β-cell dysfunction," *Clin. Cancer Res.*, vol. 21, no. 7, pp. 1722–1733, 2015.

[93] H. Valadi, K. Ekström, A. Bossios, M. Sjöstrand, J. J. Lee, and J. O. Lötvall, "Exosome-mediated transfer of mRNAs and microRNAs is a novel mechanism of genetic exchange between cells," *Nat. Cell Biol.*, vol. 9, no. 6, pp. 654–659, 2007.

[94] C. Tetta, E. Ghigo, L. Silengo, M. C. Deregibus, and G. Camussi, "Extracellular vesicles as an emerging mechanism of cell-to-cell communication," *Endocrine*, vol. 44, no. 1. pp. 11–19, 2013.

[95] C. Z. Chen, L. Li, H. F. Lodish, and D. P. Bartel, "MicroRNAs Modulate Hematopoietic Lineage Differentiation," *Science (80-.).*, vol. 303, no. 5654, pp. 83–86, 2004.

[96] P. S. Mitchell *et al.*, "Circulating microRNAs as stable blood-based markers for cancer detection," *Proc. Natl. Acad. Sci.*, vol. 105, no. 30, pp. 10513–10518, 2008.

[97] J. L. Eun *et al.*, "Expression profiling identifies microRNA signature in pancreatic cancer," *Int. J. Cancer*, vol. 120, no. 5, pp. 1046–1054, 2007.

[98] M. Dillhoff, J. Liu, W. Frankel, C. Croce, and M. Bloomston, "MicroRNA-21 is overexpressed in pancreatic cancer and a potential predictor of survival," *J. Gastrointest. Surg.*, vol. 12, no. 12, pp. 2171–2176, 2008.

[99] N. Kosaka, H. Iguchi, and T. Ochiya, "Circulating microRNA in body fluid: A new potential biomarker for cancer diagnosis and prognosis," *Cancer Science*, vol. 101, no. 10. pp. 2087–2092, 2010.

[100] C. Wan, Y. Shen, T. Yang, T. Wang, L. Chen, and F. Wen, "Diagnostic value of microRNA for pancreatic cancer: a meta-analysis.," *Arch. Med. Sci.*, vol. 8, pp. 749–55, 2012.

[101] J. Wang *et al.*, “MicroRNAs in plasma of pancreatic ductal adenocarcinoma patients as novel blood-based biomarkers of disease.,” *Cancer Prev. Res. (Phila).*, vol. 2, no. 9, pp. 807–813, 2009.

[102] Q. Chen, L. Yang, Y. Xiao, J. Zhu, and Z. Li, “Circulating microRNA-182 in plasma and its potential diagnostic and prognostic value for pancreatic cancer,” *Med. Oncol.*, vol. 31, no. 11, p. 225, 2014.

[103] C. Zhao *et al.*, “Diagnostic and biological significance of microRNA-192 in pancreatic ductal adenocarcinoma,” *Oncol. Rep.*, vol. 30, no. 1, pp. 276–284, 2013.

[104] R. Morimura *et al.*, “Novel diagnostic value of circulating miR-18a in plasma of patients with pancreatic cancer,” *Br. J. Cancer*, vol. 105, no. 11, pp. 1733–1740, 2011.

[105] S. Ali, K. Almhanna, W. Chen, P. A. Philip, and F. H. Sarkar, “Differentially expressed miRNAs in the plasma may provide a molecular signature for aggressive pancreatic cancer,” *Am. J. Transl. Res.*, vol. 3, no. 1, pp. 28–47, 2011.

[106] G. A. Cote *et al.*, “A pilot study to develop a diagnostic test for pancreatic ductal adenocarcinoma based on differential expression of select miRNA in plasma and bile,” *Am. J. Gastroenterol.*, vol. 109, no. 12, pp. 1942–1952, 2014.

[107] M. Kojima *et al.*, “MicroRNA markers for the diagnosis of pancreatic and biliary-tract cancers,” *PLoS One*, vol. 10, no. 2, 2015.

[108] J. Xu *et al.*, “Plasma miRNAs effectively distinguish patients with pancreatic cancer from controls a multicenter study,” *Ann. Surg.*, vol. 263, no. 6, pp. 1173–1179, 2016.

[109] N. A. Schultz *et al.*, “MicroRNA biomarkers in whole blood for detection of pancreatic cancer,” *JAMA - J. Am. Med. Assoc.*, vol. 311, no. 4, pp. 392–404, 2014.

[110] S. Atarod, H. Smith, A. Dickinson, and X. N. Wang, “MicroRNA levels quantified in whole blood varies from PBMCs,” *F1000Research*, vol. 3, p. 183, 2014.

[111] J. Kleeff *et al.*, “Plasma microRNA panels to diagnose pancreatic cancer: Results from a multicenter study,” *Oncotarget*, vol. 7, no. April, pp. 28000–28012, 2016.

[112] W. Yuan *et al.*, “New combined microRNA and protein plasmatic biomarker panel for pancreatic cancer.,” *Oncotarget*, vol. 7, no. 48, pp. 80033–80045, 2016.

[113] L. Gao, S. B. He, and D. C. Li, “Effects of miR-16 plus CA 19-9 detections on pancreatic cancer diagnostic performance,” *Clin. Lab.*, vol. 60, no. 1, pp. 73–77, 2014.

[114] T. Deng *et al.*, “Identification of Circulating miR-25 as a Potential Biomarker for Pancreatic Cancer Diagnosis,” *Cell. Physiol. Biochem.*, vol. 39, no. 5, pp. 1716–1722, 2016.

[115] B. Alemar *et al.*, “MiRNA-21 and miRNA-34a Are Potential Minimally Invasive Biomarkers for the Diagnosis of Pancreatic Ductal Adenocarcinoma,” *Pancreas*, vol. 45, no. 1, pp. 84–92, 2016.

[116] A. Li *et al.*, “MicroRNA array analysis finds elevated serum miR-1290 accurately distinguishes patients with low-stage pancreatic cancer from healthy and disease controls,” *Clin. Cancer Res.*, vol. 19, no. 13, pp. 3600–3610, 2013.

[117] N. A. E. M. Hussein, Z. A. E. Kholy, M. M. Anwar, M. A. Ahmad, and S. M. Ahmad, “Plasma miR-22-3p, miR-642b-3p and miR-885-5p as diagnostic biomarkers for pancreatic cancer,” *J. Cancer Res. Clin. Oncol.*, vol. 143, no. 1, pp. 83–93, 2017.

[118] F. Yang *et al.*, “Liposome based delivery systems in pancreatic cancer treatment: From bench to bedside,” *Cancer Treatment Reviews*, vol. 37, no. 8. pp. 633–642, 2011.

[119] C. Li *et al.*, “Identification of pancreatic cancer stem cells,” *Cancer Res.*, vol. 67, no. 3, pp. 1030–1037, 2007.

[120] S. Egawa *et al.*, “Japan pancreatic cancer registry; 30th year anniversary: Japan pancreas society,” *Pancreas*, vol. 41, no. 7. pp. 985–992, 2012.

[121] A. Richter, M. Niedergethmann, J. W. Sturm, D. Lorenz, S. Post, and M. Trede, “Long-term results of partial pancreaticoduodenectomy for ductal adenocarcinoma of the pancreatic head: 25-Year experience,” *World J. Surg.*, vol. 27, no. 3, pp. 324–329, 2003.

[122] D. H. Li, K. P. Xie, R. Wolff, and J. L. Abbruzzese, “Pancreatic cancer,” *Lancet*, vol. 363, pp. 1049–1057, 2004.

[123] K. D. Piatkevich, V. N. Malashkevich, K. S. Morozova, N. A. Nemkovich, S. C. Almo, and V. V. Verkhusha, “Extended stokes shift in fluorescent proteins: Chromophore-protein interactions in a near-infrared TagRFP675 variant,” *Sci. Rep.*, vol. 3, 2013.

[124] D. Dressman, H. Yan, G. Traverso, K. W. Kinzler, and B. Vogelstein, “Transforming single DNA molecules into fluorescent magnetic particles for detection and enumeration of genetic variations,” *Proc. Natl. Acad. Sci.*, vol. 100, no. 15, pp. 8817–8822, 2003.

[125] M. Xiao *et al.*, “Rapid DNA mapping by fluorescent single molecule detection,” *Nucleic Acids Res.*, vol. 35, no. 3, 2007.

[126] C. Chakraborty, C.-H. Hsu, Z.-H. Wen, and C.-S. Lin, “Recent Advances of Fluorescent Technologies for Drug Discovery and Development,” *Curr. Pharm. Des.*, vol. 15, no. 30, pp. 3552–3570, 2009.

[127] M. Hall, I. Kazakova, and Y. M. Yao, “High sensitivity immunoassays using particulate fluorescent labels,” *Anal. Biochem.*, vol. 272, no. 2, pp. 165–170, 1999.

[128] B. A. Robbins and R. M. Nakamura, “Current status of fluorescent immunoassays,” *Journal of Clinical Laboratory Analysis*, vol. 2, no. 1. pp. 62–67, 1988.

[129] S. Cesaro-Tadic *et al.*, “High-sensitivity miniaturized immunoassays for tumor necrosis factor alpha using microfluidic systems.,” *Lab Chip*, vol. 4, pp. 563–569, 2004.

[130] H. G. Pfeiffer and H. a. Liebhafsky, “The Origins of Beer’s Law,” *J. Chem. Educ.*, vol. 28, p. 123, 1951.

[131] M. N. Berberan-Santos, “Beer’s law revisited,” *Journal of Chemical Education*, vol. 67. p. 757, 1990.

[132] J. R. Lakowicz, *Principles of fluorescence spectroscopy*. 2006.

[133] Z. L. Zhang, Y. R. Fang, W. H. Wang, L. Chen, and M. T. Sun, “Propagating surface plasmon polaritons: Towards applications for remote-excitation surface catalytic reactions,” *Adv. Sci.*, vol. 3, no. 1, 2015.

[134] S. A. Maier, *Plasmonics: Fundamentals and applications*. 2007.

[135] T. W. Odom and G. C. Schatz, “Introduction to plasmonics,” *Chemical Reviews*, vol. 111, no. 6, pp. 3667–3668, 2011.

[136] D. a Weitz, S. Garoff, C. D. Hanson, T. J. Gramila, and J. I. Gersten, “Fluorescent lifetimes of molecules on silver-island films.,” *Opt. Lett.*, vol. 7, no. 2, pp. 89–91, 1982.

[137] J. V. Frangioni, “In vivo near-infrared fluorescence imaging,” *Current Opinion in Chemical Biology*, vol. 7, no. 5. pp. 626–634, 2003.

[138] S. Kühn, U. Håkanson, L. Rogobete, and V. Sandoghdar, “Enhancement of single-molecule fluorescence using a gold nanoparticle as an optical nanoantenna,” *Phys. Rev. Lett.*, vol. 97, no. 1, 2006.

[139] J. C. Love, L. A. Estroff, J. K. Kriebel, R. G. Nuzzo, and G. M. Whitesides, “Self-assembled monolayers of thiolates on metals as a form of nanotechnology,” *Chemical Reviews*, vol. 105, no. 4. pp. 1103–1169, 2005.

[140] E. Hao and G. C. Schatz, “Electromagnetic fields around silver nanoparticles and dimers,” *J. Chem. Phys.*, vol. 120, no. 1, pp. 357–366, 2004.

[141] A. J. Haes, C. L. Haynes, A. D. McFarland, G. C. Schatz, R. P. Van Duyne, and S. Zou, “Plasmonic Materials for Surface-Enhanced Sensing and Spectroscopy,” *MRS Bull.*, vol. 30, no. 5, pp. 368–375, 2005.

[142] Z. Zhou, H. Huang, Y. Chen, F. Liu, C. Z. Huang, and N. Li, “A distance-dependent metal-enhanced fluorescence sensing platform based on molecular beacon design,” *Biosens. Bioelectron.*, vol. 52, pp. 367–373, 2014.

[143] A. I. Dragan and C. D. Geddes, “Excitation volumetric effects (EVE) in metal-enhanced fluorescence,” *Phys. Chem. Chem. Phys.*, vol. 13, no. 9, p. 3831, 2011.

[144] N. Akbay, J. R. Lakowicz, and K. Ray, “Distance-dependent intrinsic fluorescence of proteins on aluminum nanostructures,” *Prog. Biomed. Opt. Imaging - Proc. SPIE*, vol. 8234, pp. 1–8, 2012.

[145] N. Akbay, J. R. Lakowicz, and K. Ray, “Distance-dependent metal-enhanced intrinsic fluorescence of proteins using polyelectrolyte layer-by-layer assembly and aluminum nanoparticles,” *J. Phys. Chem. C*, vol. 116, no. 19, pp. 10766–10773, 2012.

[146] J. Kummerlen, A. Leitner, H. Brunner, F. R. Aussenegg, and A. Wokaun, “Enhanced dye fluorescence over silver island films: Analysis of the distance dependence,” *Mol. Phys.*, vol. 80, no. 5, pp. 1031–1046, 1993.

[147] T. Ito and S. Okazaki, “Pushing the limits of lithography,” *Nature*, vol. 406, no. 6799. pp. 1027–1031, 2000.

[148] U. C. Fischer, “Submicroscopic pattern replication with visible light,” *J. Vac. Sci. Technol.*, vol. 19, no. 4, p. 881, 1981.

[149] H. W. Deckman and J. H. Dunsmuir, “Natural lithography,” *Appl. Phys. Lett.*, vol. 41, no. 4, pp. 377–379, 1982.

[150] J. C. Hulteen and R. P. Van Duyne, “Nanosphere lithography: A materials general fabrication process for periodic particle array surfaces,” *J. Vac. Sci. Technol. A Vacuum, Surfaces, Film.*, vol. 13, no. 3, pp. 1553–1558, 1995.

[151] R. Micheletto, H. Fukuda, and M. Ohtsu, “A Simple Method for the Production of a Two-Dimensional, Ordered Array of Small Latex Particles,” *Langmuir*, vol. 11, no. 9, pp. 3333–3336, 1995.

[152] F. Xie, A. Centeno, M. R. Ryan, D. J. Riley, and N. M. Alford, “Au nanostructures by colloidal lithography: from quenching to extensive fluorescence enhancement,” *J. Mater. Chem. B*, vol. 1, no. 4, pp. 536–543, 2013.

[153] X. Liu, B. Choi, N. Gozubenli, and P. Jiang, “Periodic arrays of metal nanorings and nanocrescents fabricated by a scalable colloidal templating approach,” *J. Colloid Interface Sci.*, vol. 409, pp. 52–58, 2013.

[154] L. Y. Wu, B. M. Ross, and L. P. Lee, “Optical properties of the crescent-shaped nanohole antenna,” *Nano Lett.*, vol. 9, no. 5, pp. 1956–1961, 2009.

[155] A. Kosiorek, W. Kandulski, H. Glaczynska, and M. Giersig, “Fabrication of nanoscale rings, dots, and rods by combining shadow nanosphere lithography and annealed polystyrene nanosphere masks,” *Small*, vol. 1, no. 4, pp. 439–444, 2005.

[156] J.-F. Masson, M.-P. Murray-Méthot, and L. S. Live, “Nanohole arrays in chemical analysis: manufacturing methods and applications,” *Analyst*, vol. 135, no. 7, p. 1483, 2010.

[157] C. L. Haynes and R. P. Van Duyne, “Nanosphere lithography: A versatile nanofabrication tool for studies of size-dependent nanoparticle optics,” *J. Phys. Chem. B*, vol. 105, no. 24, pp. 5599–5611, 2001.

[158] J. Yu, Q. Yan, and D. Shen, “Co-Self-Assembly of Binary Colloidal Crystals at the Air−Water Interface,” *ACS Appl. Mater. Interfaces*, vol. 2, no. 7, pp. 1922–1926, 2010.

[159] E. Sirotkin, J. D. Apweiler, and F. Y. Ogrin, “Macroscopic ordering of polystyrene carboxylate-modified nanospheres self-assembled at the water-air interface,” *Langmuir*, vol. 26, no. 13, pp. 10677–10683, 2010.

[160] E. M. Hicks *et al.*, “Plasmonic properties of film over nanowell surfaces fabricated by nanosphere lithography,” *J. Phys. Chem. B*, vol. 109, no. 47, pp. 22351–22358, 2005.

[161] Y. Lei, S. Yang, M. Wu, and G. Wilde, “Surface patterning using templates: concept, properties and device applications,” *Chem. Soc. Rev.*, vol. 40, no. 3, pp. 1247–1258, 2011.

[162] T. Rindzevicius, Y. Alaverdyan, A. Dahlin, F. Höök, D. S. Sutherland, and M. Käll, “Plasmonic sensing characteristics of single nanometric holes,” *Nano Lett.*, vol. 5, no. 11, pp. 2335–2339, 2005.

[163] A. Dmitriev *et al.*, “Enhanced nanoplasmonic optical sensors with reduced substrate effect,” *Nano Lett.*, vol. 8, no. 11, pp. 3893–3898, 2008.

[164] J. Zhao, B. Frank, S. Burger, and H. Giessen, “Large-area high-quality plasmonic oligomers fabricated by angle-controlled colloidal nanolithography,” *ACS Nano*, vol. 5, no. 11, pp. 9009–9016, 2011.

[165] F. Yang *et al.*, “Emerging inorganic nanomaterials for pancreatic cancer diagnosis and treatment,” *Cancer Treatment Reviews*, vol. 38, no. 6. pp. 566–579, 2012.

[166] S. Ji *et al.*, “Carbon nanotubes in cancer diagnosis and therapy,” *Biochim. Biophys. Acta - Rev. Cancer*, vol. 1806, no. 1, pp. 29–35, 2010.

[167] B. M. Quinn, C. Dekker, and S. G. Lemay, “Electrodeposition of noble metal nanoparticles on carbon nanotubes,” *J. Am. Chem. Soc.*, vol. 127, no. 17, pp. 6146–6147, 2005.

[168] D. H. Dube and C. R. Bertozzi, “Glycans in cancer and inflammation--potential for therapeutics

and diagnostics.," *Nat. Rev. Drug Discov.*, vol. 4, pp. 477–488, 2005.

[169] V. J. Nagaraj, S. Aithal, S. Eaton, M. Bothara, P. Wiktor, and S. Prasad, "NanoMonitor: a miniature electronic biosensor for glycan biomarker detection.," *Nanomedicine (Lond).*, vol. 5, no. 3, pp. 369–378, 2010.

[170] A. Guo *et al.*, "An electrochemical immunosensor for ultrasensitive detection of carbohydrate antigen 199 based on Au@CuxOS yolk-shell nanostructures with porous shells as labels," *Biosens. Bioelectron.*, vol. 63, pp. 39–46, 2015.

[171] B. Gu, C. Xu, C. Yang, S. Liu, and M. Wang, "ZnO quantum dot labeled immunosensor for carbohydrate antigen 19-9," *Biosens. Bioelectron.*, vol. 26, no. 5, pp. 2720–2723, 2011.

[172] G. K. Joshi, S. Deitz-Mcelyea, M. Johnson, S. Mali, M. Korc, and R. Sardar, "Highly specific plasmonic biosensors for ultrasensitive MicroRNA detection in plasma from pancreatic cancer patients," *Nano Lett.*, vol. 14, no. 12, pp. 6955–6963, 2014.

[173] Y. Zhang *et al.*, "Towards a high-throughput label-free detection system combining localized-surface plasmon resonance and microfluidics," *Lab Chip*, vol. 12, no. 17, p. 3012, 2012.

[174] R. S. Yalow and S. A. Berson, "Immunoassay of endogenous plasma insulin in man," *Obes. Res.*, vol. 4, no. 6, pp. 583–600, 1996.

[175] P. M. Keane, P. J. Pegg, and E. Johnson, "Estimation of thyroxine binding protein capacities using a non-electrophoretic technique.," *J. Clin. Endocrinol. Metab.*, vol. 29, no. 8, pp. 1126–1130, 1969.

[176] H. Byrne, P. J. Conroy, J. C. Whisstock, and R. J. O'Kennedy, "A tale of two specificities: Bispecific antibodies for therapeutic and diagnostic applications," *Trends in Biotechnology*, vol. 31, no. 11. pp. 621–632, 2013.

[177] G. T. Hermanson, *Bioconjugate Techniques: Third Edition*. 2013.

[178] I. W. Hamley, "PEG-peptide conjugates," *Biomacromolecules*, vol. 15, no. 5. pp. 1543–1559, 2014.

[179] K. D. Vernon-Parry, "Scanning electron microscopy: an introduction," *III-Vs Rev.*, vol. 13, no. 4, pp. 40–44, 2000.

[180] J. R. Lakowicz, "Radiative decay engineering 5: Metal-enhanced fluorescence and plasmon emission," *Anal. Biochem.*, vol. 337, no. 2, pp. 171–194, 2005.

[181] R. K. Kannadorai, U. S. Dinish, C. Y. Fu, G. Hegde, M. Olivo, and A. Asundi, "Nanosphere templated metallic grating assisted enhanced fluorescence," *J. Fluoresc.*, vol. 22, no. 2, pp. 609–614, 2012.

[182] J. R. Lakowicz *et al.*, "Radiative decay engineering: 2. Effects of silver island films on fluorescence intensity, lifetimes, and resonance energy transfer," *Anal. Biochem.*, vol. 301, no. 2, pp. 261–277, 2002.

[183] B. Yang *et al.*, "Tuning the intensity of metal-enhanced fluorescence by engineering silver nanoparticle arrays," *Small*, vol. 6, no. 9, pp. 1038–1043, 2010.

[184] J. Liu, A. I. Maaroof, L. Wieczorek, and M. B. Cortie, "Fabrication of hollow metal 'nanocaps' and their red-shifted optical absorption spectra," *Adv. Mater.*, vol. 17, no. 10, pp. 1276–1281, 2005.

[185] J. C. Love, B. D. Gates, D. B. Wolfe, K. E. Paul, and G. M. Whitesides, “Fabrication and Wetting Properties of Metallic Half-Shells with Submicron Diameters,” *Nano Lett.*, vol. 2, no. 8, pp. 891–894, 2002.

[186] P. Zhan *et al.*, “The anomalous infrared transmission of gold films on two-dimensional colloidal crystals,” *Adv. Mater.*, vol. 18, no. 12, pp. 1612–1616, 2006.

[187] K. Sugawa *et al.*, “Metal-enhanced fluorescence platforms based on plasmonic ordered copper arrays: Wavelength dependence of quenching and enhancement effects,” *ACS Nano*, vol. 7, no. 11, pp. 9997–10010, 2013.

[188] V. Raghavan *et al.*, “Dual plasmonic gold nanostars for photoacoustic imaging and photothermal therapy,” *Nanomedicine*, vol. 12, no. 5, pp. 457–471, 2017.

[189] S. K. Dondapati, T. K. Sau, C. Hrelescu, T. A. Klar, F. D. Stefani, and J. Feldmann, “Label-free biosensing based on single gold nanostars as plasmonic transducers,” *ACS Nano*, vol. 4, no. 11, pp. 6318–6322, 2010.

[190] S. Mariani, S. Scarano, J. Spadavecchia, and M. Minunni, “A reusable optical biosensor for the ultrasensitive and selective detection of unamplified human genomic DNA with gold nanostars,” *Biosens. Bioelectron.*, vol. 74, pp. 981–988, 2015.

[191] Y. Liu, H. Yuan, F. R. Kersey, J. K. Register, M. C. Parrott, and T. Vo-Dinh, “Plasmonic gold nanostars for Multi-Modality sensing and diagnostics,” *Sensors (Switzerland)*, vol. 15, no. 2. pp. 3706–3720, 2015.

[192] G. Chirico, M. Borzenkov, and P. Pallavicini, *Gold nanostars: Synthesis, properties and biomedical application*. 2015.

[193] H. Yuan, C. G. Khoury, H. Hwang, C. M. Wilson, G. A. Grant, and T. Vo-Dinh, “Gold nanostars: Surfactant-free synthesis, 3D modelling, and two-photon photoluminescence imaging,” *Nanotechnology*, vol. 23, no. 7, 2012.

[194] C. Farcău and S. Aştilean, “Silver half-shell arrays with controlled plasmonic response for fluorescence enhancement optimization,” *Appl. Phys. Lett.*, vol. 95, no. 19, 2009.

[195] P. Pallavicini *et al.*, “Self-assembled monolayers of gold nanostars: a convenient tool for near-IR photothermal biofilm eradication,” *Chem. Commun.*, vol. 50, no. 16, pp. 1969–1971, 2014.

[196] N. Panchuk-Voloshina *et al.*, “Alexa Dyes, a Series of New Fluorescent Dyes that Yield Exceptionally Bright, Photostable Conjugates,” *J. Histochem. Cytochem.*, vol. 47, no. 9, pp. 1179–1188, 1999.

[197] B. Bassi *et al.*, “Tunable coating of gold nanostars: Tailoring robust SERS labels for cell imaging,” *Nanotechnology*, vol. 27, no. 26, 2016.

[198] M. Schütz, D. Steinigeweg, M. Salehi, K. Kömpe, and S. Schlücker, “Hydrophilically stabilized gold nanostars as SERS labels for tissue imaging of the tumor suppressor p63 by immuno-SERS microscopy,” *Chem. Commun.*, vol. 47, no. 14, p. 4216, 2011.

[199] H. Yuan, C. G. Khoury, C. M. Wilson, G. A. Grant, A. J. Bennett, and T. Vo-Dinh, “In vivo particle tracking and photothermal ablation using plasmon-resonant gold nanostars,” *Nanomedicine Nanotechnology, Biol. Med.*, vol. 8, no. 8, pp. 1355–1363, 2012.

[200] S. Liang *et al.*, “CD44v6 monoclonal antibody-conjugated gold nanostars for targeted

photoacoustic imaging and plasmonic photothermal therapy of gastric cancer stem-like cells," *Theranostics*, vol. 5, no. 9, pp. 970–984, 2015.

[201] D. M. Rissin *et al.*, "Single-molecule enzyme-linked immunosorbent assay detects serum proteins at subfemtomolar concentrations," *Nat. Biotechnol.*, vol. 28, no. 6, pp. 595–599, 2010.

[202] L. A. Liotta *et al.*, "Protein microarrays: Meeting analytical challenges for clinical applications," *Cancer Cell*, vol. 3, no. 4. pp. 317–325, 2003.

[203] M. Hartmann, J. Roeraade, D. Stoll, M. F. Templin, and T. O. Joos, "Protein microarrays for diagnostic assays," *Anal. Bioanal. Chem.*, vol. 393, no. 5, pp. 1407–1416, 2009.

[204] J. K. Ryu *et al.*, "Elevated microRNA miR-21 levels in pancreatic cyst fluid are predictive of mucinous precursor lesions of ductal adenocarcinoma," *Pancreatology*, vol. 11, no. 3, pp. 343–350, 2011.

[205] A. Farina, "Proximal fluid proteomics for the discovery of digestive cancer biomarkers," *Biochimica et Biophysica Acta - Proteins and Proteomics*, vol. 1844, no. 5. pp. 988–1002, 2014.

[206] R. L. Woodbury, S. M. Varnum, and R. C. Zangar, "Elevated HGF levels in sera from breast cancer patients detected using a protein microarray ELISA," *J. Proteome Res.*, vol. 1, no. 3, pp. 233–237, 2002.

[207] Z. Chen *et al.*, "Protein microarrays with carbon nanotubes as multicolor Raman labels," *Nat. Biotechnol.*, vol. 26, no. 11, pp. 1285–1292, 2008.

[208] B. Schweitzer *et al.*, "Multiplexed protein profiling on microarrays by rolling-circle amplification," *Nat. Biotechnol.*, vol. 20, no. 4, pp. 359–365, 2002.

[209] B. Liu *et al.*, "High Performance, Multiplexed Lung Cancer Biomarker Detection on a Plasmonic Gold Chip," *Adv. Funct. Mater.*, vol. 26, no. 44, pp. 7994–8002, 2016.

[210] P. K. Jain and M. A. El-Sayed, "Plasmonic coupling in noble metal nanostructures," *Chem. Phys. Lett.*, vol. 487, no. 4–6, pp. 153–164, 2010.

[211] E. J. Lee *et al.*, "Expression profiling identifies microRNA signature in pancreatic cancer.," *Int. J. Cancer*, vol. 120, no. 5, pp. 1046–54, 2007.

[212] N. a Schultz *et al.*, "MicroRNA expression profiles associated with pancreatic adenocarcinoma and ampullary adenocarcinoma.," *Mod. Pathol.*, vol. 25, no. 12, pp. 1609–22, 2012.

[213] T. D. Schmittgen *et al.*, "Real-time PCR quantification of precursor and mature microRNA," *Methods*, vol. 44, no. 1, pp. 31–38, 2008.

[214] G. K. Joshi *et al.*, "Label-Free Nanoplasmonic-Based Short Noncoding RNA Sensing at Attomolar Concentrations Allows for Quantitative and Highly Specific Assay of MicroRNA-10b in Biological Fluids and Circulating Exosomes," *ACS Nano*, vol. 9, no. 11, pp. 11075–11089, 2015.

[215] C. S. Huertas, D. Fariña, and L. M. Lechuga, "Direct and Label-Free Quantification of Micro-RNA-181a at Attomolar Level in Complex Media Using a Nanophotonic Biosensor," *ACS Sensors*, vol. 1, no. 6, pp. 748–756, 2016.

[216] Y. Fu and J. R. Lakowicz, "Single-molecule studies of enhanced fluorescence on silver island films," *Plasmonics*, vol. 2, no. 1, pp. 1–4, 2007.

[217] B. Zhang *et al.*, "Multiplexed cytokine detection on plasmonic gold substrates with enhanced

near-infrared fluorescence," *Nano Res.*, vol. 6, no. 2, pp. 113–120, 2013.

[218] C. V. RAMAN and K. S. KRISHNAN, "A New Type of Secondary Radiation," *Nature*, vol. 121, no. 3048, pp. 501–502, 1928.

[219] C. Pomares *et al.*, "Validation of IgG, IgM multiplex plasmonic gold platform in French clinical cohorts for the serodiagnosis and follow-up of Toxoplasma gondii infection," *Diagn. Microbiol. Infect. Dis.*, vol. 87, no. 3, pp. 213–218, 2017.

[220] R. De La Rica and M. M. Stevens, "Plasmonic ELISA for the ultrasensitive detection of disease biomarkers with the naked eye," *Nat. Nanotechnol.*, vol. 7, no. 12, pp. 821–824, 2012.

APPENDICIES

CHAPTER 7: OPTICAL PROPERTIES AND METAL ENHANCED FLUORESCENCE

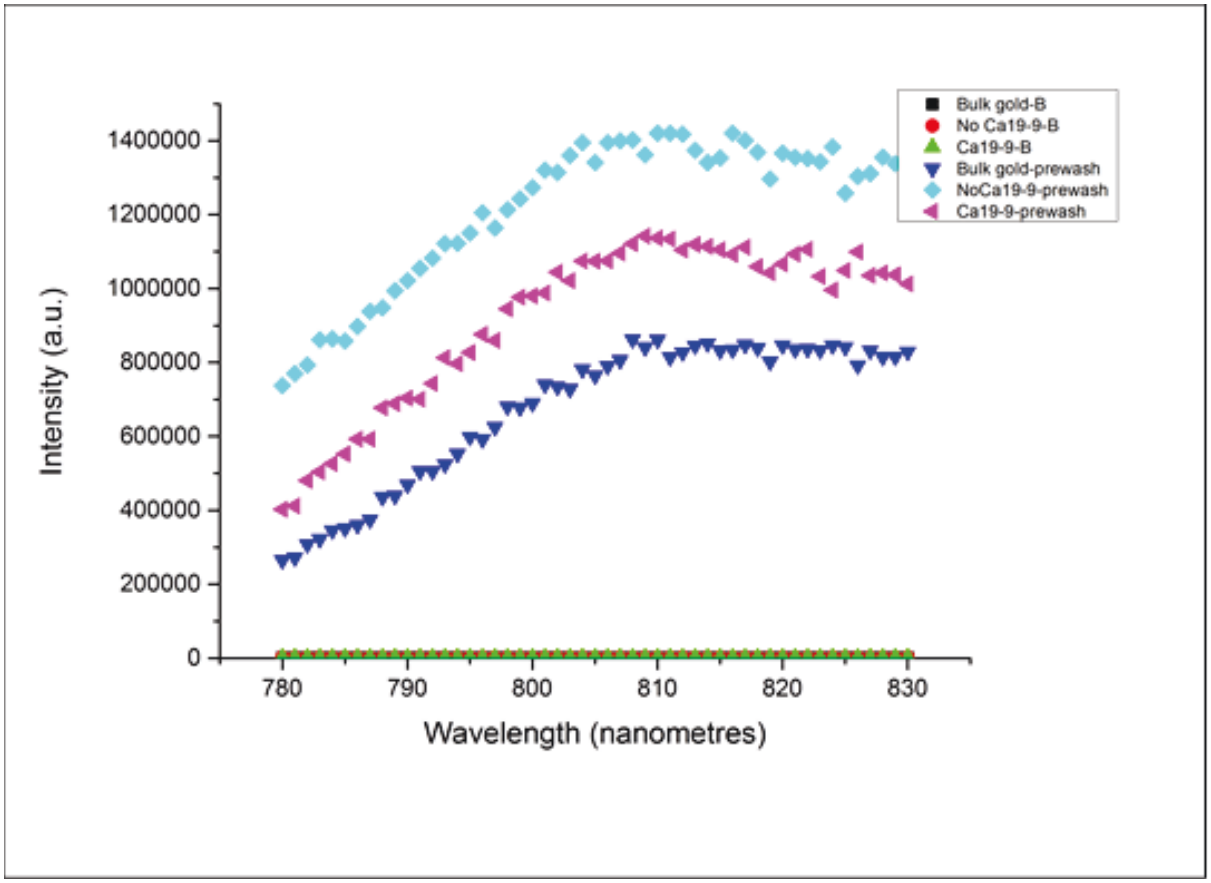


Figure 1: Calibration of CA 19-9 assay on bulk gold and glass showing limited calibration when using only gold conjugation.

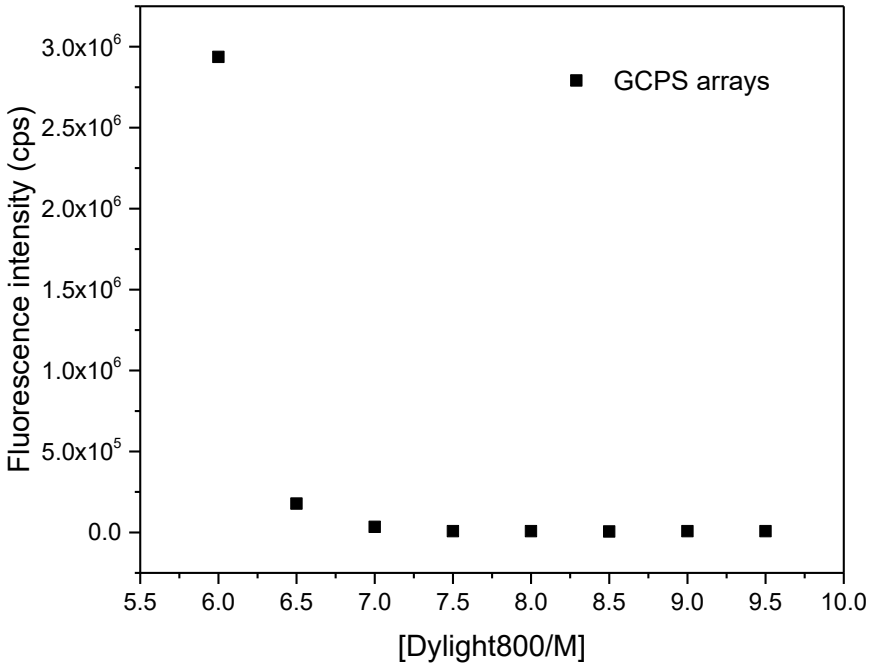


Figure 2: Drop dry calibration of Dylight 800 on GCPS arrays.

Copyright Clearance Center RightsLink®

Home | Create Account | Help

ACS Publications
Most Trusted. Most Cited. Most Read.

Title: Gold Nanostar Substrates for Metal-Enhanced Fluorescence through the First and Second Near-Infrared Windows

Author: Ioannis G. Theodorou, Zaynab A. R. Jawad, Qianfan Jiang, et al

Publication: Chemistry of Materials

Publisher: American Chemical Society

Date: Aug 1, 2017

Copyright © 2017, American Chemical Society

LOGIN

If you're a copyright.com user, you can login to RightsLink using your copyright.com credentials. Already **a RightsLink user** or want to learn more?

PERMISSION/LICENSE IS GRANTED FOR YOUR ORDER AT NO CHARGE

This type of permission/license, instead of the standard Terms & Conditions, is sent to you because no fee is being charged for your order. Please note the following:

- Permission is granted for your request in both print and electronic formats, and translations.
- If figures and/or tables were requested, they may be adapted or used in part.
- Please print this page for your records and send a copy of it to your publisher/graduate school.
- Appropriate credit for the requested material should be given as follows: "Reprinted (adapted) with permission from (COMPLETE REFERENCE CITATION). Copyright (YEAR) American Chemical Society." Insert appropriate information in place of the capitalized words.
- One-time permission is granted only for the use specified in your request. No additional uses are granted (such as derivative works or other editions). For any other uses, please submit a new request.

BACK | CLOSE WINDOW

Copyright © 2017 Copyright Clearance Center, Inc. All Rights Reserved. Privacy statement. Terms and Conditions.
Comments? We would like to hear from you. E-mail us at customercare@copyright.com